

# The Quantum Three-Dimensional Sinai Billiard — a Semiclassical Analysis

Harel Primack

*Fakultät für Physik, Albert-Ludwigs Universität Freiburg,  
Hermann-Herder-Str. 3, D-79104 Freiburg, Germany*  
email: harel@physik.uni-freiburg.de

and

Uzy Smilansky

*Department of Physics of Complex Systems,  
The Weizmann Institute, Rehovot 76100, Israel*  
email: fnsmla1@weizmann.weizmann.ac.il

Submitted to Physics Reports, 1.6.99

## Abstract

We present a comprehensive semiclassical investigation of the three-dimensional Sinai billiard, addressing a few outstanding problems in “quantum chaos”. We were mainly concerned with the accuracy of the semiclassical trace formula in two and higher dimensions and its ability to explain the universal spectral statistics observed in quantized chaotic systems. For this purpose we developed an efficient KKR algorithm to compute an extensive and accurate set of quantal eigenvalues. We also constructed a systematic method to compute millions of periodic orbits in a reasonable time. Introducing a proper measure for the semiclassical error and using the quantum and the classical databases for the Sinai billiards in two and three dimensions, we concluded that the semiclassical error (measured in units of the mean level spacing) is independent of the dimensionality, and diverges at most as  $\log \hbar$ . This is in contrast with previous estimates. The classical spectrum of lengths of periodic orbits was studied and shown to be correlated in a way which induces the expected (random matrix) correlations in the quantal spectrum, corroborating previous results obtained in systems in two dimensions. These and other subjects discussed in the report open the way to extending the semiclassical study to chaotic systems with more than two freedoms.

PACS numbers: 05.45.+b, 03.65.Sq

Keywords: Quantum chaos, billiards, semiclassical approximation, Gutzwiller trace formula.

# Contents

<b>1</b>	<b>Introduction</b>	<b>5</b>
<b>2</b>	<b>Quantization of the 3D Sinai billiard</b>	<b>14</b>
2.1	The KKR determinant . . . . .	14
2.2	Symmetry considerations . . . . .	16
2.2.1	Group-theoretical resummations . . . . .	16
2.2.2	Number-theoretical resummations . . . . .	17
2.2.3	Desymmetrization . . . . .	18
2.3	Numerical aspects . . . . .	19
2.4	Verifications of low-lying eigenvalues . . . . .	23
2.5	Comparing the exact counting function with Weyl's law . . . . .	25
<b>3</b>	<b>Quantal spectral statistics</b>	<b>27</b>
3.1	The integrable $R = 0$ case . . . . .	27
3.1.1	Two-point statistics of the integrable case . . . . .	28
3.2	Nearest-neighbour spacing distribution . . . . .	31
3.3	Two-point correlations . . . . .	33
3.4	Auto-correlations of spectral determinants . . . . .	37
<b>4</b>	<b>Classical periodic orbits</b>	<b>42</b>
4.1	Periodic orbits of the 3D Sinai torus . . . . .	42
4.2	Periodic Orbits of the 3D Sinai billiard — Classical desymmetrization	46
4.3	The properties and statistics of the set of periodic orbits . . . . .	50
4.4	Periodic orbit correlations . . . . .	60
4.4.1	Numerical tests . . . . .	63
4.4.2	The dynamical origin of the correlations . . . . .	65
4.4.3	Length correlations in the 3-Torus . . . . .	69
<b>5</b>	<b>Semiclassical analysis</b>	<b>71</b>
5.1	Semiclassical desymmetrization . . . . .	72
5.2	Length spectrum . . . . .	75
5.3	A semiclassical test of the quantal spectrum . . . . .	76
5.4	Filtering the bouncing-balls I: Dirichlet–Neumann difference . . . . .	77
5.5	Filtering the bouncing-balls II: Mixed boundary conditions . . . . .	83
<b>6</b>	<b>The accuracy of the semiclassical energy spectrum</b>	<b>89</b>
6.1	Measures of the semiclassical error . . . . .	90
6.2	Numerical results . . . . .	100
<b>7</b>	<b>Semiclassical theory of spectral statistics</b>	<b>117</b>
<b>8</b>	<b>Summary</b>	<b>126</b>

<b>A</b>	<b>Efficient quantization of billiards: BIM vs. full diagonalization</b>	<b>129</b>
<b>B</b>	<b>Symmetry reduction of the numerical effort in the quantization of billiards</b>	<b>131</b>
<b>C</b>	<b>Resummation of <math>D_{LM}</math> using the Ewald summation technique</b>	<b>132</b>
<b>D</b>	<b>“Physical” Ewald summation of <math>G_0^T(\vec{q})</math></b>	<b>136</b>
<b>E</b>	<b>Calculating <math>D_{00}^{(3)}</math></b>	<b>139</b>
<b>F</b>	<b>The “cubic harmonics” <math>Y_{LJK}^{(\gamma)}</math></b>	<b>140</b>
	F.1 Calculation of the transformation coefficients $a_{\gamma JK,M}^{(L)}$ . . . . .	140
	F.2 Counting the $Y_{LJ}^{(\gamma)}$ ’s . . . . .	142
<b>G</b>	<b>Evaluation of <math>l(\vec{\rho}_p)</math></b>	<b>143</b>
	G.1 Proof of equation (10) . . . . .	143
	G.2 Calculating $l(\vec{\rho}_p)$ . . . . .	144
<b>H</b>	<b>Number theoretical degeneracy of the cubic lattice</b>	<b>145</b>
	H.1 First moment . . . . .	145
	H.2 Second moment . . . . .	145
<b>I</b>	<b>Weyl’s law</b>	<b>147</b>
<b>J</b>	<b>Calculation of the monodromy matrix</b>	<b>150</b>
	J.1 The 3D Sinai torus case . . . . .	150
	J.2 The 3D Sinai billiard case . . . . .	152

# 1 Introduction

The main goal of “quantum chaos” is to unravel the special features which characterize the quantum description of classically chaotic systems [1, 2]. The simplest time independent systems which display classical chaos are two dimensional, and therefore most of the research in the field focused on systems in 2D. However, there are very good and fundamental reasons for extending the research to higher number of dimensions. The present paper reports on our study of a paradigmatic three-dimensional system: The 3D Sinai billiard. It is the first analysis of a system in 3D which was carried out in depth and detail comparable to the previous work on systems in 2D.

The most compelling motivation for the study of systems in 3D is the lurking suspicion that the semiclassical trace formula [2] — the main tool for the theoretical investigations of quantum chaos — fails for  $d > 2$ , where  $d$  is the number of freedoms. The grounds for this suspicion are the following [2]. The semiclassical approximation for the propagator does not exactly satisfy the time-dependent Schrödinger equation, and the error is of order  $\hbar^2$  *independently of the dimensionality*. The semiclassical energy spectrum, which is derived from the semiclassical propagator by a Fourier transform, is therefore expected to deviate by  $\mathcal{O}(\hbar^2)$  from the exact spectrum. On the other hand, the mean spacing between adjacent energy levels is proportional to  $\hbar^d$  [3] for systems in  $d$  dimensions. Hence, the figure of merit of the semiclassical approximation, which is the expected error expressed in units of the mean spacing, is  $\mathcal{O}(\hbar^{2-d})$ , which diverges in the semiclassical limit  $\hbar \rightarrow 0$  when  $d > 2$ ! If this argument were true, it would have negated our ability to generalize the large corpus of results obtained semiclassically, and checked for systems in 2D, to systems of higher dimensions. Amongst the primary victims would be the semiclassical theory of spectral statistics, which attempts to explain the universal features of spectral statistics in chaotic systems and its relation to random matrix theory (RMT) [4, 5]. RMT predicts spectral correlations on the range of a single spacing, and it is not likely that a semiclassical theory which provides the spectrum with an uncertainty which exceeds this range, can be applicable or relevant. The available term by term generic corrections to the semiclassical trace formula [6, 7, 8] are not sufficient to provide a better estimate of the error in the semiclassically calculated energy spectrum. To assess the error, one should substitute the term by term corrections in the trace formula or the spectral  $\zeta$  function which do not converge in the absolute sense on the real energy axis. Therefore, to this date, this approach did not provide an analytic estimate of the accuracy of the semiclassical spectrum.

Under these circumstances, we initiated the present work which addressed the problem of the semiclassical accuracy using the approach to be described in the sequel. Our main result is that in contrast with the estimate given above, the semiclassical error (measured in units of the mean spacing) is *independent* of the dimensionality. Moreover, a conservative estimate of the upper bound

for its possible divergence in the semiclassical limit is  $\mathcal{O}(|\log \hbar|)$ . This is a very important conclusion. It allows one to extend many of the results obtained in the study of quantum chaos in 2D to higher dimensions, and justifies the use of the semiclassical approximation to investigate special features which appear only in higher dimensions. We list a few examples of such effects:

- The dual correspondence between the spectrum of quantum energies and the spectrum of actions of periodic orbits [9, 10, 11] was never checked for systems in more than 2D. However, if the universality of the *quantum* spectral correlations is independent of the number of freedoms, the corresponding range of correlations in the spectrum of *classical* actions is expected to depend on the dimensionality. Testing the validity of this prediction, which is derived by using the trace formula, is of great importance and interest. It will be discussed at length in this work.
- The full range of types of stabilities of classical periodic orbits that includes also the loxodromic stability [2] can be manifest only for  $d > 2$ .
- Arnold’s diffusion in the KAM regime is possible only for  $d > 2$  (even though we do not encountered it in this work).

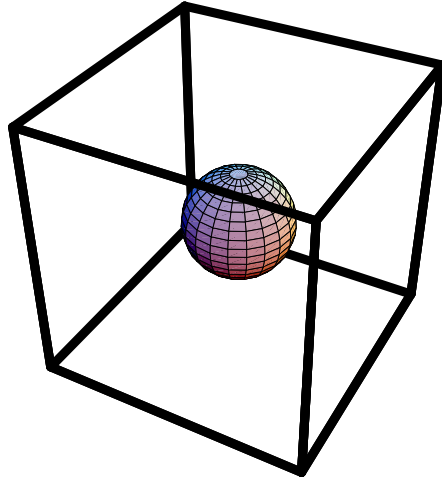
Having stated the motivations and background for the present study, we shall describe the strategy we chose to address the problem, and the logic behind the way we present the results in this report.

The method we pursued in this first exploration of quantum chaos in 3D, was to perform a comprehensive semiclassical analysis of a *particular* yet typical system in 3D, which has a well studied counterpart in 2D. By comparing the exact quantum results with the semiclassical theory, we tried to identify possible deviations which could be attributed to particular failures of the semiclassical approximation in 3D. The observed deviations, and their dependence on  $\hbar$  and on the dimensionality, were used to assess the semiclassical error and its dependence on  $\hbar$ . Such an approach requires the assembly of an accurate and complete databases for the quantum energies and for the classical periodic orbits. This is a very demanding task for chaotic systems in 3D, and it is the main reason why such studies were not performed before.

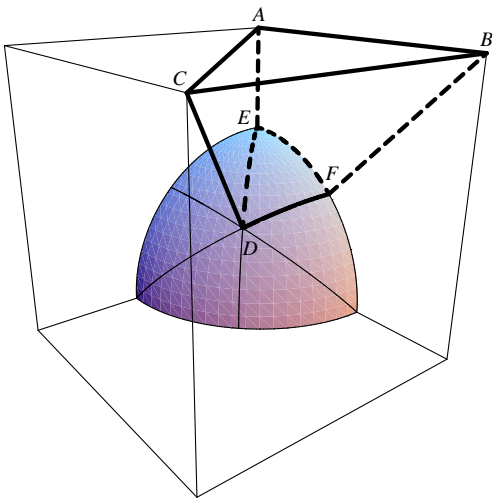
When we searched for a convenient system for our study, we turned immediately to billiards. They are natural paradigms in the study of classical and quantum chaos. The classical mechanics of billiards is simpler than for systems with potentials: The energy dependence can be scaled out, and the system can be characterized in terms of purely geometric data. The dynamics of billiards reduces to a mapping through the natural Poincaré section which is the billiard’s boundary. Much is known about classical billiards in the mathematical literature (e.g. [12]), and this information is crucial for the semiclassical application. Billiards are also very convenient from the quantal point of view. There are specialized methods to quantize them which are considerably simpler than those for

potential systems [13]. Some of them are based on the Boundary Integral Method (BIM) [14], the KKR method [15], the scattering approach [16, 17] and various improvements thereof [18, 19, 20]. The classical scaling property is manifest also quantum mechanically. While for potential systems the energy levels depend in a complicated way on  $\hbar$  and the classical actions are non-trivial functions of  $E$ , in billiards, both the quantum energies and the classical actions scale trivially in  $\hbar$  and  $\sqrt{E}$ , respectively, which simplifies the analysis considerably.

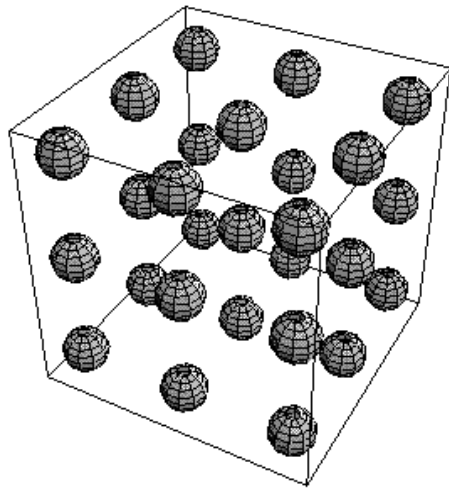
The particular billiard we studied is the *3D Sinai billiard*. It consists of the free space between a 3-torus of side  $S$  and an inscribed sphere of radius  $R$ , where  $2R < S$ . It is the natural extension of the familiar 2D Sinai billiard, and it is shown in figure 1 using three complementary representations. The classical dynamics consists of specular reflections from the sphere. If the billiard is desymmetrized, specular reflections from the symmetry planes exist as well. The 3D Sinai billiard has several advantages. It is one of the very few systems in 3D which are rigorously known to be ergodic and mixing [21, 22, 23]. Moreover, since its introduction by Sinai and his proof of its ergodicity [21], the 2D Sinai billiard was subject to thorough classical, quantal and semiclassical investigations [21, 15, 24, 25, 26, 22, 17, 27]. Therefore, much is known about the 2D Sinai billiard and this serves us as an excellent background for the study of the 3D counterpart. The symmetries of the 3D Sinai billiard greatly facilitate the quantal treatment of the billiard. Due to the spherical symmetry of the inscribed obstacle and the cubic-lattice symmetry of the billiard (see figure 1(c)) we are able to use the KKR method [28, 29, 30, 15] to numerically compute the energy levels. This method is superior to the standard methods of computing generic billiard's levels. In fact, had we used the standard methods with our present computing resources, it would have been possible to obtain only a limited number of energy levels with the required precision. The KKR method enabled us to compute many thousands of energy levels of the 3D Sinai billiard. The fact that the billiard is symmetric means that the Hamiltonian is block-diagonalized with respect to the irreducible representations of the symmetry group [31]. Each block is an independent Hamiltonian which corresponds to the desymmetrized billiard (see figure 1(b)) for which the boundary conditions are determined by the irreducible representations. Hence, with minor changes one is able to compute a few independent spectra that correspond to the same 3D desymmetrized Sinai billiard but with different boundary conditions — thus one can easily accumulate data for spectral statistics. On the classical level, the 3D Sinai billiard has the great advantage of having a symbolic dynamics. Using the centers of spheres which are positioned on the infinite  $\mathbb{Z}^3$  lattice as the building blocks of this symbolic dynamics, it is possible to uniquely encode the periodic orbits of the billiard [27, 32]. This construction, together with the property that periodic orbits are the single minima of the length (action) function [27, 32], enables us to systematically find all of the periodic orbits of the billiard, which is crucial for the application of the semiclassical periodic orbit theory. We emphasize that



(a)



(b)



(c)

Figure 1: Three representations of the 3D Sinai billiard: (a) original, (b) 48-fold desymmetrized (maximal desymmetrization) into the fundamental domain, (c) unfolded to  $\mathbb{R}^3$ .



performing a systematic search of periodic orbits of a given billiard is far from being trivial (e.g. [2, 33, 34, 35, 36]) and there is no general method of doing so. The existence of such a method for the 3D Sinai billiard was a major factor in favour of this system.

The advantages of the 3D Sinai billiard listed above are gained at the expense of some problematic features which emerge from the cubic symmetry of the billiard. In the billiard there exist families of periodic, neutrally stable orbits, the so called “bouncing-ball” families that are illustrated in figure 2. The bouncing-ball families are well-known from studies of, e.g., the 2D Sinai and the stadium billiards [15, 17, 37, 38]. These periodic manifolds have zero measure in phase space (both in 2D and in 3D), but nevertheless strongly influence the dynamics. They are responsible for the long (power-law) tails of some classical distributions [39, 40]. They are also responsible for non-generic effects in the quantum spectral statistics, e.g., large saturation values of the number variance in the 2D Sinai and stadium billiards [37]. The most dramatic visualization of the effect of the bouncing-ball families appears in the function  $D(l) \equiv \sum_n \cos(k_n l)$  — the “quantal length spectrum”. The lengths  $l$  that correspond to the bouncing-ball families are characterized by large peaks that overwhelm the generic contributions of unstable periodic orbits [38] (as is exemplified by figure 28). In the 3D Sinai billiard the undesirable effects are even more apparent than for the 2D billiard. This is because, in general, they occupy 3D volumes rather than 2D areas in configuration space and consequently their amplitudes grow as  $k^1$  (to be contrasted with  $k^0$  for unstable periodic orbits). Moreover, for  $R < S/2$  there is always an infinite number of families present in the 3D Sinai billiard compared to the finite number which exists in the 2D Sinai and the stadium billiards. The bouncing balls are thoroughly discussed in the present work, and a large effort was invested in devising methods by which their effects could be filtered out.

After introducing the system to be studied, we shall explain now the way by which we present the results. The semiclassical analysis is based on the exact quantum spectrum, and on the classical periodic orbits. Hence, the first sections are dedicated to the discussion of the exact quantum and classical dynamics in the 3D Sinai billiard, and the semiclassical analysis is deferred to the last sections. The sections are grouped as follows:

- Quantum mechanics and spectral statistics (sections 2 and 3).
- Classical periodic orbits (section 4).
- Semiclassical analysis (sections 5, 6, 7).

In section 2 we describe the KKR method which was used to numerically compute the quantum spectrum. Even though it is a rather technical section, it gives a clear idea of the difficulties encountered in the quantization of this system, and how we used symmetry considerations and number-theoretical arguments to

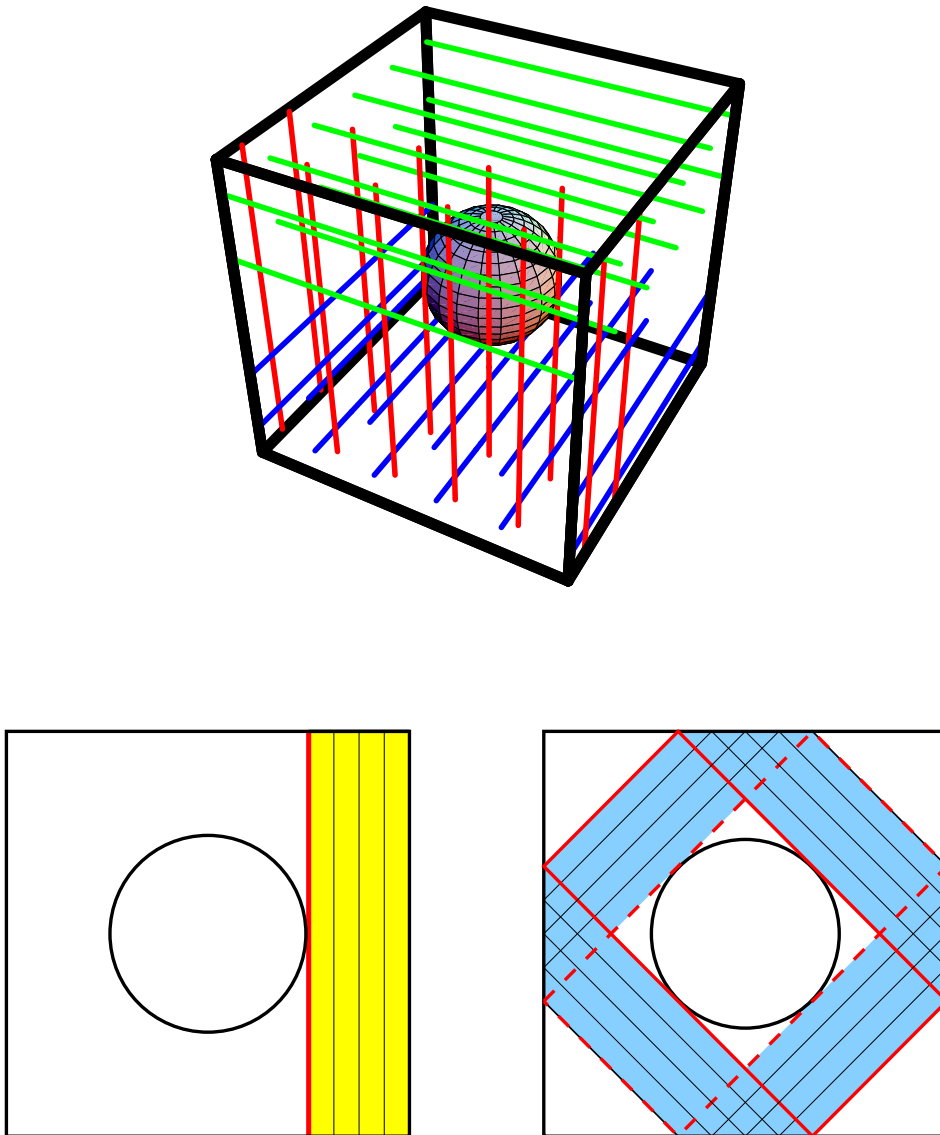


Figure 2: Some bouncing-ball families in the 3D Sinai billiard. Upper figure: Three families parallel to the  $x, y$  and  $z$  axes. Lower figure: Top view of two families.

reduce the numerical effort considerably. The desymmetrization of the billiard according to the symmetry group is worked out in detail. This section ends with a short explanation of the methods used to ensure the completeness and the accuracy of the spectrum.

The study of spectral statistics, section 3, starts with the analysis of the integrable billiard ( $R = 0$ ) case. This spectrum is completely determined by the underlying classical bouncing-ball manifolds which are classified according to their dimensionality. The two-point form factor in this case is *not* Poissonian, even though the system is integrable. Rather, it reflects the number-theoretical degeneracies of the  $\mathbb{Z}^3$  lattice resulting in non-generic correlations. Turning to the chaotic ( $R > 0$ ) cases, we investigate some standard statistics (nearest-neighbor, number variance) as well as the auto-correlations of the spectral determinant, and compare them to the predictions of RMT. The main conclusion of this section is that the spectral fluctuations in the 3D Sinai billiard belong to the same universality class as in the 2D analogue.

Section 4 is devoted to the systematic search of the periodic orbits of the 3D Sinai billiard. We rely heavily on a theorem that guarantees the uniqueness of the coding and the variational minimality of the periodic orbit lengths. The necessary generalizations for the desymmetrized billiard are also explained. Once the algorithm for the computation of periodic orbits is outlined, we turn to the definition of the spectrum of lengths of periodic orbits and to the study of its statistics. The number of periodic orbits with lengths smaller than  $L$  is shown to proliferate exponentially. We check also classical sum rules which originate from ergodic coverage, and observe appreciable corrections to the leading term due to the infinite horizon of the Sinai billiard. Turning our attention to the two-point statistics of the classical spectrum, we show that it is not Poissonian. Rather, there exist correlations which appear on a scale larger than the nearest spacing. This has very important consequences for the semiclassical analysis of the spectral statistics. We study these correlations and offer a dynamical explanation for their origin.

The semiclassical analysis of the billiard is the subject of section 5. As a prelude, we propose and use a new method to verify the completeness and accuracy of the quantal spectrum, which is based on a “universal” feature of the classical length spectrum of the 3D Sinai billiard. The main purpose of this section is to compare the quantal computations to the semiclassical predictions according to the Gutzwiller trace formula, as a first step in our study of its accuracy. Since we are interested in the generic unstable periodic orbits rather than the non-generic bouncing balls, special effort is made to eliminate the effects of the latter. This is accomplished using a method that consists of taking the derivative with respect to a continuous parameterization of the boundary conditions on the sphere.

In section 6 we embark on the task of estimating the semiclassical error of energy levels. We first define the measures with which we quantify the semiclas-

sical error, and demonstrate some useful statistical connections between them. We then show how these measures can be evaluated for a given system using its quantal and semiclassical length spectra. We use the databases of the 2D and 3D Sinai billiards to derive the estimate of the semiclassical error which was already quoted above: The semiclassical error (measured in units of the mean spacing) is *independent* of the dimensionality, and a conservative estimate of the upper bound for its possible divergence in the semiclassical limit is  $\mathcal{O}(|\log \hbar|)$ .

Once we are reassured of the reliability of the trace formula in 3D, we return in section 7 to the spectral statistics of the quantized billiard. The semiclassical trace formula is interpreted as an expression of the duality between the quantum spectrum and the classical spectrum of lengths. We show how the length correlations in the classical spectrum induce correlations in the quantum spectrum, which reproduce rather well the RMT predictions.

The work is summarized in section 8.

To end the introductory notes, a review of the existing literature is in order. Only very few systems in 3D were studied in the past. We should first mention the measurements of 3D acoustic cavities [41, 42, 43, 44, 45] and electromagnetic (microwaves) cavities [46, 47, 48, 49]. The measured frequency spectra were analyzed and for irregular shapes (notably the 3D Sinai billiard) the level statistics conformed with the predictions of RMT. Moreover, the length spectra showed peaks at the lengths of periodic manifolds, but no further quantitative comparison with the semiclassical theory was attempted. However, none of the experiments is directly relevant to the quantal (scalar) problem since the acoustic and electromagnetic vector equations cannot be reduced to a scalar equation in the configurations chosen. Therefore, these experiments do not constitute a direct analogue of quantum chaos in 3D. This is in contrast with flat and thin microwave cavities which are equivalent (up to some maximal energy) to 2D quantal billiards.

A few 3D billiards were discussed theoretically in the context of quantum chaos. Polyhedral billiards in the 3D hyperbolic space with constant negative curvature were investigated by Aurich and Marklof [50]. The trace formula in this case is exact rather than semiclassical, and thus the issue of the semiclassical accuracy is not relevant. Moreover, the tetrahedron that was treated had exponentially growing multiplicities of lengths of classical periodic orbits, and hence cannot be considered as generic. Prosen considered a 3D billiard with smooth boundaries and 48-fold symmetry [19, 20] whose classical motion was almost completely (but not fully) chaotic. He computed many levels and found that level statistics reproduce the RMT predictions with some deviations. He also found agreement with Weyl's law (smooth density of states) and identified peaks of the length spectrum with lengths of periodic orbits. The majority of high-lying eigenstates were found to be uniformly extended over the energy shell, with notable exceptions that were "scarred" either on a classical periodic orbit or on a symmetry plane. Henseler, Wirzba and Guhr treated the  $N$ -sphere scattering

systems in 3D [51] in which the quantum mechanical resonances were compared to the predictions according to the Gutzwiller trace formula. A good agreement was observed for the uppermost band of resonances and no agreement for other bands which are dominated by diffraction effects. Unfortunately, conclusive results were given only for non-generic configurations of two and three spheres for which all the periodic orbits are planar. In addition, it is not clear whether one can infer from the accuracy of complex scattering resonances to the accuracy of real energy levels in bound systems. Recently, Sieber [52] calculated the  $4 \times 4$  stability (monodromy) matrices and the Maslov indices for general 3D billiards and gave a practical method to compute them, which extended our previous results for the 3D Sinai billiard [53, 54].

## 2 Quantization of the 3D Sinai billiard

In the present section we describe the KKR determinant method [28, 29, 55, 30] to compute the energy spectrum of the 3D Sinai billiard, and the results of the numerical computations. The KKR method, which was used by Berry for the 2D Sinai billiard case [15], is most suitable for our purpose since it allows to exploit the symmetries of the billiard to reduce the numerical effort considerably. The essence of the method is to convert the Schrödinger equation and the boundary conditions into a *single* integral equation. The spectrum is then the set of real wavenumbers  $k_n$  where the corresponding secular determinant vanishes. As a matter of fact, we believe that only with the KKR method could we obtain a sufficiently accurate and extended spectrum for the quantum 3D Sinai billiard. We present in this section also some numerical aspects and verify the accuracy and completeness of the computed levels.

We go into the technical details of the quantal computation because we wish to show the high reduction factor which is gained by the KKR method. Without this significant reduction the numerical computation would have resulted in only a very limited number of levels [46, 48]. The reader who is not interested in these technical details should proceed to subsection 2.4. To avoid ambiguities, we strictly adhere to the conventions of [56].

### 2.1 The KKR determinant

We first consider the 3D “Sinai torus”, which is the free space outside of a sphere of radius  $R$  embedded in a 3-torus of side length  $S$  (see fig. 1). The Schrödinger equation of an electron of mass  $m$  and energy  $E$  is reduced to the Helmholtz equation:

$$\nabla^2\psi + k^2\psi = 0, \quad k \equiv \sqrt{2mE}/\hbar. \quad (1)$$

The boundary conditions on the sphere are taken to be the general linear (self-adjoint) conditions:

$$\kappa \cos \alpha \cdot \psi + \sin \alpha \cdot \partial_{\hat{n}}\psi = 0, \quad (2)$$

where  $\hat{n}$  is the normal pointing outside the billiard,  $\kappa$  is a parameter with dimensions of  $k$ , and  $\alpha \in [0, \pi/2]$  is an angle that interpolates between Dirichlet ( $\alpha = 0$ ) and Neumann ( $\alpha = \pi/2$ ) conditions. These “mixed” boundary conditions will be needed in section 5 when dealing with the semiclassical analysis. Applying the KKR method, we obtain the following quantization condition (see [54] for a derivation and for details):

$$\det [A_{lm,l'm'}(k) + kP_l(kR; \kappa, \alpha)\delta_{ll'}\delta_{mm'}] = 0, \quad (3)$$

$$l, l' = 0, 1, 2, \dots, \quad 0 \leq m \leq l, 0 \leq m' \leq l',$$

where  $k$  is the wavenumber under consideration and:

$$A_{lm,l'm'}(k) \equiv 4\pi i^{l-l'} \sum_{LM} i^{-L} C_{LM,lm,l'm'} D_{LM}(k) ,$$

$$L = 0, 1, 2, \dots , M = 0, \dots, L , \quad (4)$$

$$D_{LM}(k) \equiv (-ik) \left[ \sum_{\vec{\rho} \in \mathbf{Z}^3 / \{\vec{0}\}} h_L^+(kS\rho) Y_{LM}^*(\Omega_{\vec{\rho}}) + \frac{1}{\sqrt{4\pi}} \delta_{L0} \right] , \quad (5)$$

$$C_{LM,lm,l'm'} \equiv \int_0^\pi d\theta \int_0^{2\pi} d\phi Y_{LM}(\theta, \phi) Y_{lm}^*(\theta, \phi) Y_{l'm'}(\theta, \phi) , \quad (6)$$

$$P_l(kR; \kappa, \alpha) \equiv \frac{\kappa R \cos \alpha \cdot n_l(kR) - kR \sin \alpha \cdot n_l'(kR)}{\kappa R \cos \alpha \cdot j_l(kR) - kR \sin \alpha \cdot j_l'(kR)} \quad (7)$$

$$= \cot[\eta_l(kR; \kappa, \alpha)] . \quad (8)$$

In the above  $j_l$ ,  $n_l$ ,  $h_l^+$  are the spherical Bessel, Neumann and Hankel functions, respectively [56],  $Y_{lm}$  are the spherical harmonics [56] with argument  $\Omega_{\vec{\rho}}$  in the direction of  $\vec{\rho}$ , and  $\eta_l$  are the scattering phase shifts from the sphere, subject to the boundary conditions (2).

The physical input to the KKR determinant is distributed in a systematic way: The terms  $A_{lm,l'm'}(k)$  contain information only about the structure of the underlying  $\mathbf{Z}^3$  lattice, and are independent of the radius  $R$  of the inscribed sphere. Hence they are called the “structure functions” [28, 30]. Moreover, they depend on a smaller number of “building block” functions  $D_{LM}(k)$  which contain the infinite lattice summations. The diagonal term  $kP_l(kR)\delta_{ll'}\delta_{mm'}$  contains the information about the inscribed sphere, and is expressed in terms of the scattering phase shifts from the sphere. This elegant structure of the KKR determinant (3) prevails in more general situations and remains intact even if the  $\mathbf{Z}^3$  lattice is replaced by a more general one, or if the “hard” sphere is replaced by a “soft” spherical potential with a finite range (“muffin-tin” potential) [28, 30, 29]. This renders the KKR a powerful quantization method. In all these cases the structure functions  $A_{lm,l'm'}$  depend only on the underlying lattice, and the relation (8) holds with the appropriate scattering matrix. Thus, in principle, the structure functions (or rather  $D_{LM}$ ) can be tabulated once for a given lattice (e.g. cubic) as functions of  $k$ , and only  $P_l$  need to be re-calculated for every realization of the potential (e.g. changing  $R$ ). This makes the KKR method very attractive also for a large class of generalizations of the 3D Sinai billiard.

The determinant (3) is not yet suitable for numerical computations. This is because the lattice summations in  $D_{LM}$  are only *conditionally convergent* and have to be resummed in order to give absolutely and rapidly convergent sums. This is done using the Ewald summation technique, which is described in appendices C–E. The further symmetry reductions of the KKR determinant, which are one of the most important advantages of this method, are discussed in the following.

## 2.2 Symmetry considerations

As can be seen from equations (4–8) and from appendix C, the main computational effort involved in computing the KKR determinant is consumed in the lattice sums  $D_{LM}(k)$  which need to be evaluated separately for every  $k$ . Therefore, it is imperative to use every possible means to economize the computational effort invested in calculating these functions. For this purpose, we shall exploit the cubic symmetry of the 3D Sinai billiard as well as other relations that drastically reduce the computational effort.

### 2.2.1 Group–theoretical resummations

For the practical (rapidly convergent) computation, the functions  $D_{LM}$  are decomposed into three terms which are given in appendix C (see also appendix D). Equations (211)–(214) express  $D_{LM}^{(2)}$  as a sum over the direct cubic lattice, whereas,  $D_{LM}^{(1)}$  is a sum over the reciprocal cubic lattice, which is also a cubic lattice. Thus, both sums can be represented as:

$$D_{LM}^{(j)}(k) = \sum_{\vec{\rho} \in \mathbf{Z}^3} f^{(j)}(\rho; k) Y_{LM}^*(\Omega_{\vec{\rho}}), \quad j = 1, 2. \quad (9)$$

We show in appendix G that lattice sums of this kind can be rewritten as:

$$D_{LM}^{(j)}(k) = \sum_{\vec{\rho}_p} \frac{f^{(j)}(\rho_p; k)}{l(\vec{\rho}_p)} \sum_{\hat{g} \in O_h} Y_{LM}^*(\Omega_{\hat{g}\vec{\rho}_p}), \quad (10)$$

where  $O_h$  is the cubic symmetry group [31], and  $\vec{\rho}_p \equiv (i_1, i_2, i_3)$  resides in the *fundamental section*  $0 \leq i_1 \leq i_2 \leq i_3$ . The terms  $l(\vec{\rho}_p)$  are integers which are explicitly given in appendix G. The inner sums are independent of  $k$ , and can thus be tabulated once for all. Hence the computation of the  $k$  dependent part becomes 48 times more efficient (for large, finite lattices) when compared to (9) due to the restriction of  $\vec{\rho}_p$  to the fundamental section.

A further reduction can be achieved by a unitary transformation from the  $\{Y_{LM}\}$  basis to the more natural basis of the irreducible representations (irreps) of  $O_h$ :

$$Y_{LJK}^{(\gamma)}(\Omega) \equiv \sum_M a_{\gamma JK, M}^{(L)*} Y_{LM}(\Omega), \quad (11)$$

where  $\gamma \in [1, \dots, 10]$  denotes the irrep under consideration,  $J$  counts the number of the inequivalent irreps  $\gamma$  contained in  $L$ , and  $K = 1, \dots, \dim(\gamma)$  is the row index within the irrep. The functions  $Y_{LJK}^{(\gamma)}$  are known as the “cubic harmonics” [57]. Combining (10) and (11), and using the unitarity of the transformation as well as the “great orthonormality theorem” of group theory [31] we arrive at:

$$D_{LM}^{(j)}(k) = \sum_J a_{sJ, M}^{(L)*} D_{LJ}^{(j)}(k) \quad (12)$$



$$D_{LJ}^{(j)}(k) , = 48 \sum_{\vec{\rho}_p} \frac{f^{(j)}(\rho_p; k)}{l(\vec{\rho}_p)} Y_{LJ}^{(s)*}(\Omega_{\vec{\rho}_p}) . \quad (13)$$

The superscript ( $s$ ) denotes the totally symmetric irrep. The constant coefficients  $a_{sJ,M}^{(L)*}$  can be taken into the (constant) coefficients  $C_{LM,lm,l'm'}$  resulting in:

$$A_{lm,l'm'}(k) = 4\pi i^{l-l'} \sum_{LJ} i^{-L} D_{LJ}(k) C_{LJ,lm,l'm'} \quad (14)$$

$$D_{LJ}(k) = D_{LJ}^{(1)}(k) + D_{LJ}^{(2)}(k) + D_{00}^{(3)}(k) \delta_{L0} \quad (15)$$

$$C_{LJ,lm,l'm'} = \sum_M a_{sJ,M}^{(L)*} C_{LM,lm,l'm'} . \quad (16)$$

We show in appendix F that for large  $L$  the number of  $D_{LJ}(k)$ 's is smaller by a factor  $\approx 1/48$  than the number of  $D_{LM}(k)$ 's. This means that the entries of the KKR determinant are now computed using a substantially smaller number of building blocks for which lattice summations are required. Thus, in total, we gain a saving factor of  $48^2 = 2304$  over the more naive scheme (4–6).

### 2.2.2 Number–theoretical resummations

In the above we grouped together lattice vectors with the same magnitude, using the geometrical symmetries of the cubic lattice. One can gain yet another reduction factor in the computational effort by taking advantage of a phenomenon which is particular to the cubic lattice and stems from *number theory*. The lengths of lattice vectors in the fundamental sector show an appreciable degeneracy, which is not connected with the  $O_h$  symmetry. For example, the lattice vectors (5, 6, 7) and (1, 3, 10) have the same magnitude,  $\sqrt{110}$ , and are not geometrically conjugate by  $O_h$ . This number–theoretical degeneracy is both frequent and significant, and we use it in the following way. Since the square of the magnitude is an integer we can write:

$$D_{LJ}^{(j)}(k) = \sum_{n=1}^{\infty} f^{(j)}(\rho_p = \sqrt{n}; k) \left[ \sum_{\rho_p^2=n} \frac{48}{l(\vec{\rho}_p)} Y_{LJ}^{(s)*}(\Omega_{\vec{\rho}_p}) \right] . \quad (17)$$

The inner sums incorporate the number theoretical degeneracies. They are  $k$  independent, and therefore can be tabulated once for all.

To show the efficiency of (17) let us restrict our lattice summation to  $\rho_p \leq \rho_{\max}$  (which we always do in practice). For large  $\rho_{\max}$  the number of lattice vectors in the fundamental domain is  $\pi \rho_{\max}^3 / 36$ , and the number of summands in (17) is at most  $\rho_{\max}^2$ . Thus, the saving factor is at least  $\pi \rho_{\max} / 36$ . In fact, as shown in appendix H, there are only (asymptotically)  $(5/6) \rho_{\max}^2$  terms in (17), which sets the saving factor due to number–theoretical degeneracy to be  $\pi \rho_{\max} / 30$ . In practice,  $\rho_{\max} = \mathcal{O}(100)$  and this results in a reduction factor of about 10, which is very significant.

### 2.2.3 Desymmetrization

The symmetry of the 3D Sinai torus implies that the wavefunctions can be classified according to the irreps of  $O_h$  [31]. Geometrically, each such irrep corresponds to specific boundary conditions on the symmetry planes that define the desymmetrized 3D Sinai billiard (see figure 1). This allows us to “desymmetrize” the billiard, that is to restrict ourselves to the fundamental domain with specific boundary conditions instead of considering the whole 3–torus. We recall that the boundary conditions on the sphere are determined by  $P_l(k)$  and are independent of the irrep under consideration. For simplicity, we shall restrict ourselves to the two simplest irreps which are both one–dimensional:

$\gamma = a$ : This is the totally antisymmetric irrep, which corresponds to Dirichlet boundary conditions on the planes.

$\gamma = s$ : This is the totally symmetric irrep, which corresponds to Neumann boundary conditions on the planes.

The implementation of this desymmetrization is straightforward (see [54] for details) and results in a new secular equation:

$$\det \left[ A_{lj,l'j'}^{(\gamma)}(k) + kP_l(kR)\delta_{ll'}\delta_{jj'} \right] = 0 \quad (18)$$

where  $\gamma$  is the chosen irrep and:

$$A_{lj,l'j'}^{(\gamma)}(k) = 4\pi i^{l-l'} \sum_{LJ} i^{-L} D_{LJ}(k) C_{LJ,lj,l'j'}^{(\gamma)} \quad (19)$$

$$C_{LJ,lj,l'j'}^{(\gamma)} = \sum_{mm'} a_{\gamma j,m}^{(l)} a_{\gamma j',m'}^{(l')*} C_{LJ,lm,l'm'} \quad (20)$$

$$= \sum_{Mmm'} a_{sJM}^{(L)*} a_{\gamma j,m}^{(l)} a_{\gamma j',m'}^{(l')*} C_{LM,lm,l'm'} . \quad (21)$$

The desymmetrization of the problem has a few advantages:

**Computational efficiency:** In appendix F we show that for large  $L$ 's the number of cubic harmonics  $Y_{LJK}^{(\gamma)}$  that belong to a one–dimensional irrep is 1/48 of the number of the spherical harmonics  $Y_{LM}$ . Correspondingly, if we truncate our secular determinant such that  $L \leq L_{\max}$ , then the dimension of the new determinant (18) is only 1/48 of the original one (3) for the fully symmetric billiard. Indeed, the desymmetrized billiard has only 1/48 of the volume of the symmetric one, and hence the density of states is reduced by 48 (for large  $k$ ). However, due to the high cost of computing a determinant (or performing a Singular Value Decomposition) [58] the reduction in the density of states is over-compensated by the reduction of the matrix size, resulting in a saving factor of 48. This is proven in appendix B, where it

is shown in general that levels of desymmetrized billiards are computationally cheaper than those of billiards which possess symmetries. Applied to our case, the computational effort to compute a given number  $N$  of energy levels of the desymmetrized billiard is 48 times cheaper than computing  $N$  levels of the fully symmetric billiard.

**Statistical independence of spectra:** For each irrep the spectrum is statistically independent of the others, since it corresponds to different boundary conditions. Thus, if the fully symmetric billiard is quantized, the resulting spectrum is the union of 10 independent spectra (there are 10 irreps of  $O_h$  [31]), and significant features such as level rigidity will be severely blurred [59]. To observe generic statistical properties and to compare with the results of RMT, one should consider each spectrum separately, which is equivalent to desymmetrizing the billiard.

**Rigidity:** The statistical independence has important practical consequences. Spectral rigidity implies that it is unlikely to find levels in close vicinity of each other. Moreover, the fluctuations in the spectral counting functions are bounded. Both features of rigidity are used in the numerical algorithm which computes the spectrum, and is described in more detail in section 2.3.

To summarize this subsection, we have demonstrated that the high symmetry features of the 3D Sinai billiard are naturally incorporated in the KKR method. This renders the computation of its spectrum much more efficient than in the case of other, less symmetric 3D billiards. Thus, we expect to get many more levels than the few tens that can be typically obtained for generic billiards [46, 48]. In fact, this feature is the key element which brought this project to a successful conclusion. We note that other specialized computation methods, which were applied to highly symmetric 3D billiards, also resulted in many levels [19, 20].

This completes the theoretical framework established for the efficient numerical computation of the energy levels. In the following we discuss the outcome of the actual computations.

## 2.3 Numerical aspects

We computed various energy spectra, defined by different combinations of the physically important parameters:

1. The radius  $R$  of the inscribed sphere (the side  $S$  was always taken to be 1).
2. The boundary conditions on the sphere: Dirichlet / Neumann / mixed:  
 $0 \leq \alpha \leq \pi/2$ .

3. The boundary conditions on the symmetry planes of the cube: Dirichlet / Neumann. These boundary conditions correspond to the antisymmetric / symmetric irrep of  $O_h$ , respectively. Due to the lattice periodicity, Dirichlet (Neumann) boundary conditions on the symmetry planes induce Dirichlet (Neumann) also on the planes between neighbouring cells.

The largest spectral stretch that was obtained numerically corresponded to  $R = 0.2$  and Dirichlet boundary condition everywhere. It consisted of 6697 levels in the interval  $0 < k \leq 281.078$ . We denote this spectrum in the following as the “longest spectrum”.

The practical application of (18) brings about many potential sources of divergence: The KKR matrix is infinite dimensional in principle, and each of the elements is given as an infinite sum over the cubic lattice. To regulate the infinite dimension of the matrix we use a physical guideline, namely, the fact that for  $l > kR$  the phase shifts decrease very rapidly toward zero, and the matrix becomes essentially diagonal. Therefore, a natural cutoff is  $l_{\max} = kR$ , which is commonly used (e.g. [17]). In practice one has to go slightly beyond this limit, and to allow a few evanescent modes:  $l_{\max} = kR + l_{\text{evan}}$ . To find a suitable value of  $l_{\text{evan}}$  we used the parameters of the longest spectrum and computed the 17 eigenvalues in the interval  $199.5 < k < 200$  with  $l_{\text{evan}} = 0, 2, 4, 6, 8, 10$  ( $l_{\max}$  has to be odd). We show in figure 3 the successive accuracy of the computed eigenvalues between consecutive values of  $l_{\text{evan}}$ . The results clearly indicate a 10-fold increase in accuracy with each increase of  $l_{\text{evan}}$  by 2. A moderately high accuracy of  $O(10^{-4})$  relative to level spacing requires  $l_{\text{evan}} = 8$  which was the value we used in our computations.

To regulate the infinite lattice summations in  $D_{LJ}$  we used successively larger subsets of the lattice. The increase was such that at least twice as many lattice points were used. Our criterion of convergence was that the maximal absolute value of the difference between successive computations of  $D_{LJ}$  was smaller than a prescribed threshold:

$$\max_{LJ} |D_{LJ}^i - D_{LJ}^{i+1}| < \epsilon. \quad (22)$$

The threshold  $\epsilon = 10^{-6}$  was found to be satisfactory, and we needed to use a sub-lattice with maximal radius of 161.

The KKR program is essentially a loop over  $k$  which sweeps the  $k$ -axis in a given interval. At each step the KKR matrix  $M(k)$  is computed, and then its determinant is evaluated. In principle, eigenvalues are obtained whenever the determinant vanishes. In practice, however, the direct evaluation of the determinant suffers from two drawbacks:

- The numerical algorithms that are used to compute  $\det M(k)$  are frequently unstable. Hence, it is impossible to use them beyond some critical  $k$  which is not very large.

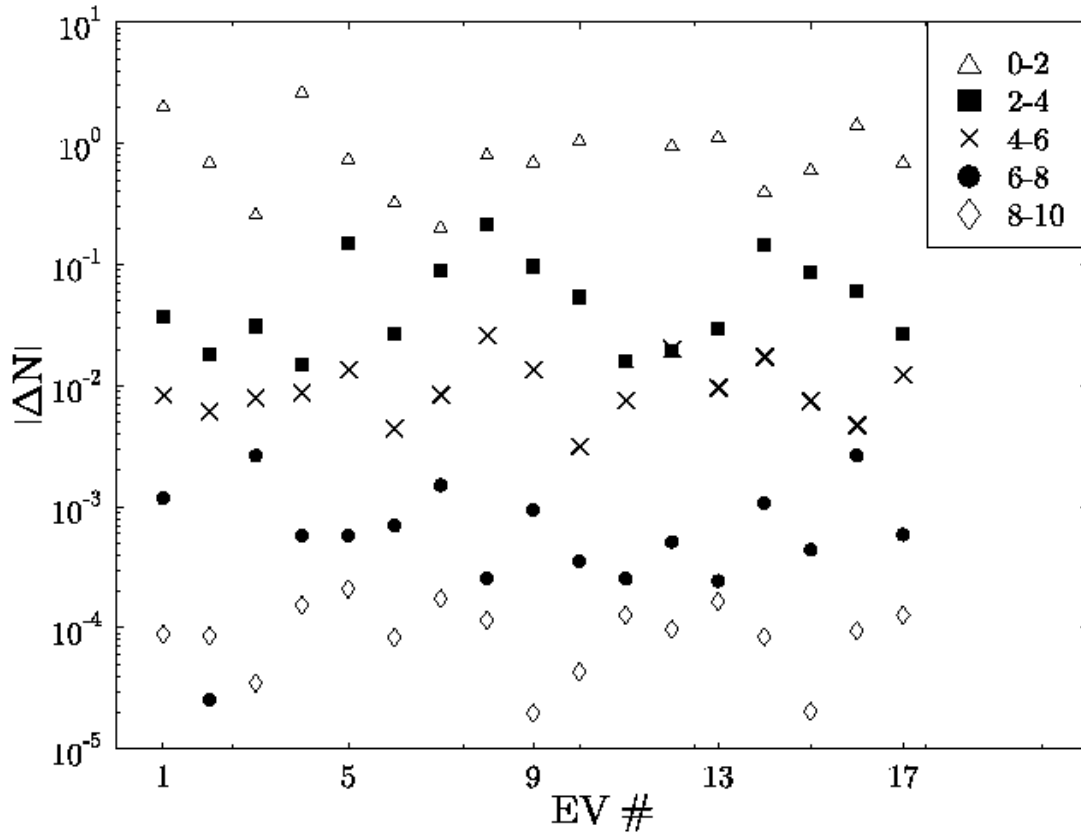


Figure 3: Accuracy of eigenvalues as a function of the number of evanescent modes  $l_{\text{evan}}$ . The case considered was  $R = 0.2$  and Dirichlet boundary conditions everywhere. The figure shows the absolute differences of the eigenvalues between two successive values of  $l_{\text{evan}}$ , multiplied by the smooth level density. That is, “0-2” means  $\bar{d}(k_n) |k_n(l_{\text{evan}}=2) - k_n(l_{\text{evan}}=0)| \equiv |\Delta N_n|$ . We show 17 eigenvalues in the interval  $199.5 < k < 200$ .

- For moderately large  $k$ 's, the absolute values of  $\det M(k)$  are very small numbers that result in computer underflows (in double precision mode), even for  $k$ -values which are not eigenvalues.
- Due to finite precision and rounding errors,  $\det M(k)$  never really vanishes for eigenvalues.

A superior alternative to the direct calculation of the determinant is to use the Singular Value Decomposition (SVD) algorithm [58], which is stable under any circumstances. In our case,  $M$  is real and symmetric, and the output are the “singular values”  $\sigma_i$  which are the absolute values of the eigenvalues of  $M$ . The product of all of the singular values is equal to  $|\det M|$ , which solves the stability problem. To cure the other two problems consider the following “conditioning measure”:

$$r(k) \equiv \sum_{i=1}^{\dim M(k)} \ln \sigma_i(k). \quad (23)$$

The use of the logarithm circumvents the underflow problem. Moreover, we always expect some of the smallest singular values to reflect the numerical noise, and the larger ones to be physically relevant. Near an eigenvalue, however, one of the “relevant” singular values must approach zero, resulting in a “dip” in the graph of  $r(k)$ . Hence, by tracking  $r$  as a function of  $k$ , we locate its dips and take as the eigenvalues the  $k$  values for which the local minima of  $r$  are obtained. Frequently one encounters very shallow dips (typically  $\ll 1$ ) which are due to numerical noise and should be discarded.

To ensure the location of all of the eigenvalues in a certain  $k$  interval, the  $k$ -axis has to be sampled densely. However, oversampling should be avoided to save computer resources. In order to choose the sampling interval  $\Delta k$  in a reasonable way, we suggest the following. If the system is known to be classically chaotic, then we expect the quantal nearest-neighbour distribution to follow the prediction of Random Matrix Theory (RMT) [2]. In particular, for systems with time reversal symmetry:

$$P(s) \approx \frac{\pi}{2}s, \quad s \ll 1, \quad s \equiv (k_{n+1} - k_n) \bar{d}((k_n + k_{n+1})/2) \quad (24)$$

where  $\bar{d}(k)$  is the smooth density of states. The chance of finding a pair of energy levels in the interval  $[s, s + ds]$  is  $P(s) ds$ . The cumulative probability of finding a pair in  $[0, s]$  is therefore crudely given by:

$$I(s) \approx \int_0^s P(s') ds' \approx \frac{\pi}{4}s^2, \quad s \ll 1. \quad (25)$$

A more refined calculation, taking into account all the possible relative configurations of the pair in the interval  $[0, s]$  gives:

$$Q(s) \approx \frac{\pi}{6}s^2, \quad s \ll 1. \quad (26)$$

If we trace the  $k$ -axis with steps  $\Delta k$  and find an eigenvalue, then the chance that there is *another* one in the same interval  $\Delta k$  is  $Q(\Delta k \bar{d}(k))$ . If we prescribe our tolerance  $Q$  to lose eigenvalues, then we should choose:

$$\Delta k = \frac{s(Q)}{\bar{d}(k)} \approx \frac{1}{\bar{d}(k)} \sqrt{\frac{6Q}{\pi}}. \quad (27)$$

In the above, we assumed that the dips in  $r(k)$  are wide enough, such that they can be detected over a range of several  $\Delta k$ 's. If this is not the case and the dips are very sharp, we must refine  $\Delta k$ . In our case dips were quite sharp, and in practice we needed to take  $Q$  of the order  $10^{-5} \div 10^{-6}$ .

## 2.4 Verifications of low-lying eigenvalues

After describing some numerical aspects of the computation, we turn to various tests of the integrity and completeness of the computed spectra. In this subsection we compare the computed low-lying eigenvalues for  $R > 0$  with those of the  $R = 0$  case. In the next one we compare the computed stair-case function to Weyl's law.

The theoretical background for the comparison between low-lying eigenvalues to those of the  $R = 0$  case is as follows. The lowest  $l$  value, for which there exist antisymmetric cubic harmonics, is  $l = 9$  [57]. Consequently, for cases with Dirichlet conditions on the symmetry planes, the lowest  $l$ -values in the KKR matrix is  $l = 9$ . Thus, for  $kR < 9$  the terms  $P_l(kR)$  in equation (18) are very small, and the matrix is essentially as if the inscribed sphere was not present. In that case of the "empty tetrahedron" the eigenvalues can be calculated analytically:

$$k_n^{R=0} = \frac{2\pi}{S} \sqrt{l^2 + m^2 + n^2}, \quad 0 < l < m < n. \quad (28)$$

We hence expect:

$$k_n \approx k_n^{R=0} \quad \text{for } k_n \lesssim 9/R. \quad (29)$$

Similar considerations were used by Berry [15] for the 2D Sinai billiard, where he also calculated the corrections to the low-lying eigenvalues. In figure 4 we plot the unfolded difference  $\Delta N_n \equiv \bar{d}(k_n) |k_n - k_n^{R=0}|$  for the longest spectrum ( $R = 0.2$ , Dirichlet everywhere). One clearly observes that indeed the differences are very small up to  $k = 9/0.2 = 45$ , and they become of order 1 afterwards, as expected. This confirms the accuracy and completeness of the low-lying levels. Moreover, it verifies the correctness of the rather complicated computations of the terms  $A_{l_j, l'_j}$  which are due to the cubic lattice.

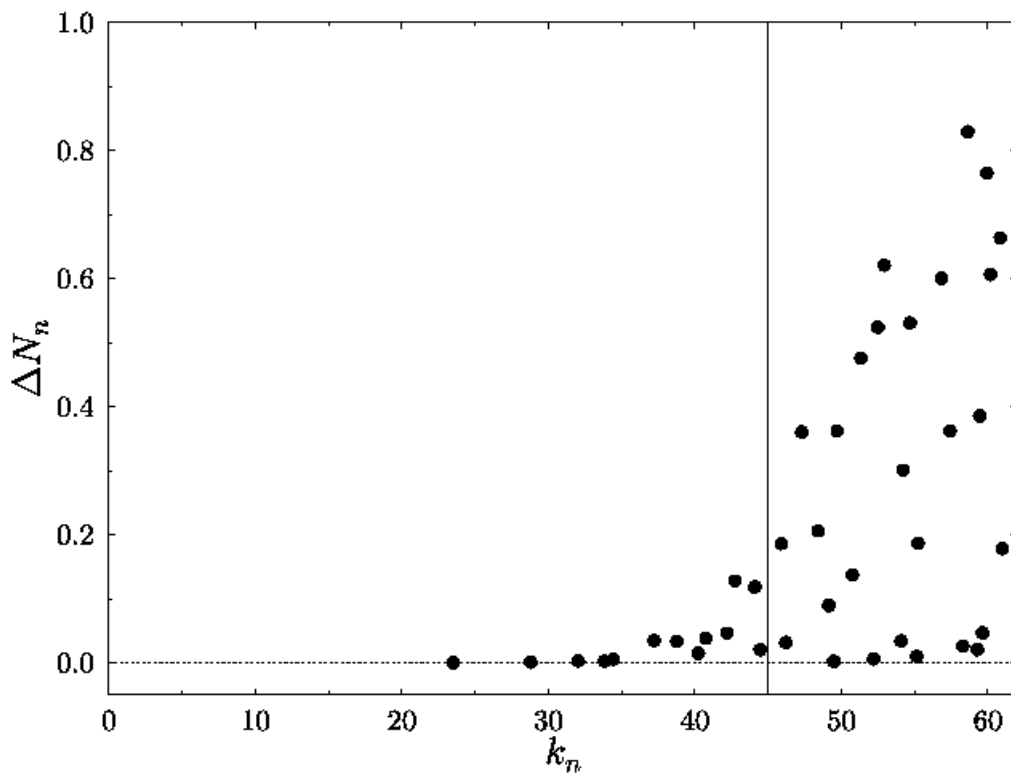


Figure 4: The unfolded differences  $\Delta N_n$  for the low-lying levels of the 3D Sinai billiard with  $R = 0.2$  and Dirichlet everywhere. We indicated by the vertical line  $k = 45$  the theoretical expectation for transition from small to large  $\Delta N$ . The line  $\Delta N = 0$  was slightly shifted upwards for clarity.



## 2.5 Comparing the exact counting function with Weyl's law

It is by now a standard practice (see e.g. [17]) to verify the completeness of a spectrum by comparing the resulting stair-case function  $N(k) \equiv \#\{k_n \leq k\}$  to its smooth approximation  $\bar{N}(k)$ , known as “Weyl’s law”. In appendix I we derived Weyl’s law for the 3D Sinai billiard (equation (290)), and now consider the difference  $N_{osc}(k) \equiv N(k) - \bar{N}(k)$ . Any jump of  $N_{osc}$  by  $\pm 1$  indicates a redundant or missing eigenvalue. In fact, this tool is of great help to locating missing eigenvalues. In figure 5 we plot  $N_{osc}$  for the longest spectrum. It is evident that the curve fluctuates around 0 with no systematic increase/decrease trends, which verifies the completeness of the spectrum. The average of  $N_{osc}$  over the available  $k$ -interval is  $(-4) \cdot 10^{-4}$  which is remarkably smaller than any single contribution to  $\bar{N}$  (note that we had no parameters to fit). This is a very convincing verification both of the completeness of the spectrum as well as the accuracy of the Weyl’s law (290). We also note that the typical fluctuations grow quite strongly with  $k$ . This is due to the effects of the bouncing-ball families (see section 1) and will be discussed further in section 3.3.

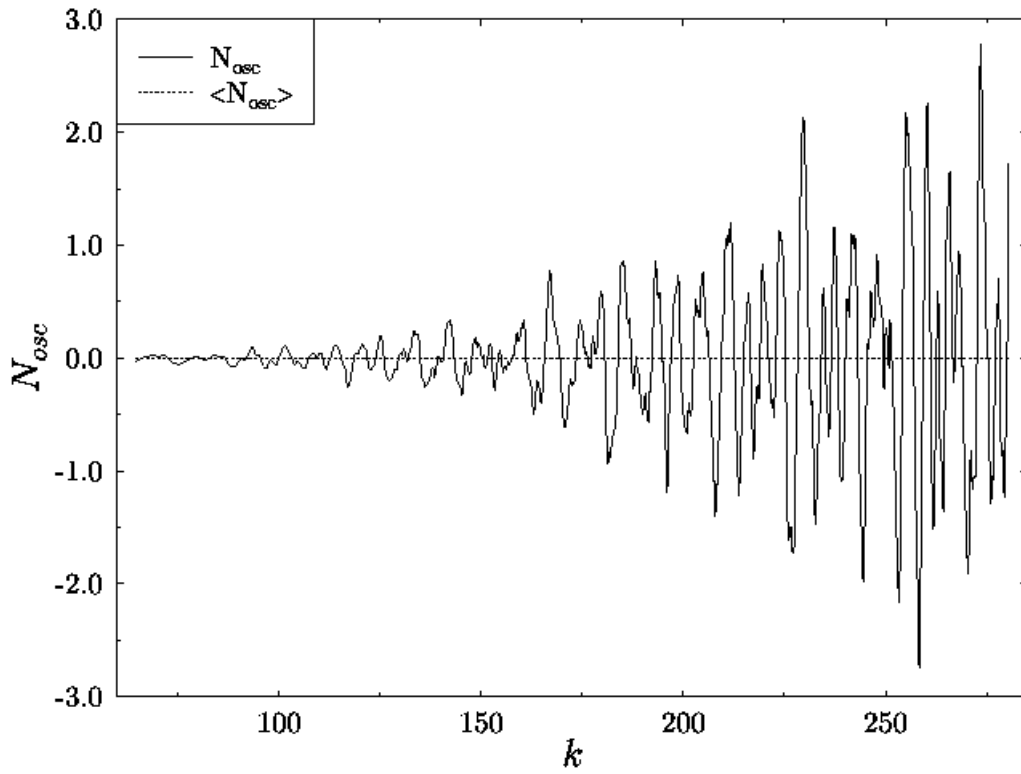


Figure 5:  $N_{osc}(k)$  for the longest spectrum of the 3D billiard. The data are smoothed over 50 level intervals.

### 3 Quantal spectral statistics

Weyl’s law predicts the smooth behaviour of the quantal density of states. There is a wealth of information also in the fluctuations, and their investigation is usually referred to as “spectral statistics”. Results of spectral statistics that comply with the predictions of Random Matrix Theory (RMT) are generally considered as a hallmark of the underlying classical chaos [24, 59, 2, 60, 17].

In the case of the Sinai billiard we are plagued with the existence of the non-generic bouncing–ball manifolds. They influence the spectral statistics of the 3D Sinai billiard. It is therefore desirable to study the bouncing balls in some detail. This is done in the first subsection, where we discuss the integrable case ( $R = 0$ ) that contains only bouncing–ball manifolds.

For the chaotic cases  $R > 0$  we consider the two simplest spectral statistics, namely, the nearest–neighbour distribution and two–point correlations. We compute these statistics for the levels of the 3D Sinai billiard, and compare them to RMT predictions. In addition, we discuss the two–point statistics of spectral determinants that was recently suggested by Kettemann, Klakow and Smilansky [61] as a characterization of quantum chaos.

#### 3.1 The integrable $R = 0$ case

If the radius of the inscribed sphere is set to 0, we obtain an integrable billiard which is the irreducible domain whose volume is  $1/48$  of the cube. It is plotted in figure 6. This tetrahedron billiard is a convenient starting point for analyzing the bouncing–ball families, since it contains no unstable periodic orbits but only bouncing balls. Quantum mechanically, the eigenvalues of the tetrahedron are given explicitly as:

$$k_{(nml)} = \frac{2\pi}{S} \sqrt{n^2 + m^2 + l^2}, \quad 0 < n < m < l \in \mathbb{N}. \quad (30)$$

The spectral density  $d_{R=0}(k) = \sum_{0 < n < m < l} \delta(k - k_{(nml)})$  can be Poisson resummed to get:

$$\begin{aligned} d_{R=0}(k) &= \frac{S^3 k^2}{96\pi^2} \sum_{pqr \in \mathbb{Z}} \text{sinc} \left( kS \sqrt{p^2 + q^2 + r^2} \right) \\ &- \frac{S^2 k}{32\pi} \sum_{pq \in \mathbb{Z}} J_0 \left( kS \sqrt{p^2 + q^2} \right) - \frac{S^2 k}{16\sqrt{2}\pi} \sum_{pq \in \mathbb{Z}} J_0 \left( kS \sqrt{p^2 + \frac{q^2}{2}} \right) \\ &+ \frac{3S}{16\pi} \sum_{p \in \mathbb{Z}} \cos(kSp) + \frac{S}{8\sqrt{2}\pi} \sum_{p \in \mathbb{Z}} \cos \left( k \frac{S}{\sqrt{2}} p \right) \\ &+ \frac{S}{6\sqrt{3}\pi} \sum_{p \in \mathbb{Z}} \cos \left( k \frac{S}{\sqrt{3}} p \right) - \frac{5}{16} \delta(k - 0). \end{aligned} \quad (31)$$

In the above  $\text{sinc}(x) \equiv \sin(x)/x$ ,  $\text{sinc}(0) \equiv 1$ , and  $J_0$  is the zeroth order Bessel function. Let us analyze this expression in some detail. Terms which have all summation indices equal to 0 give the *smooth* part of the density, and all the remaining terms constitute the *oscillatory* part. Collecting the smooth terms together we get:

$$\bar{d}_{R=0}(k) = \frac{S^3 k^2}{96\pi^2} - \frac{S^2 k}{32\pi}(1 + \sqrt{2}) + \frac{S}{144\pi}(27 + 9\sqrt{2} + 8\sqrt{3}) - \frac{5}{16}\delta(k - 0). \quad (32)$$

This is Weyl's law for the tetrahedron, which exactly corresponds to (290) with  $R = 0$  (except the last term for which the limit  $R \rightarrow 0$  is different).

As for the oscillatory terms, it is first useful to replace  $J_0(x)$  by its asymptotic approximation [62] which is justified in the semiclassical limit  $k \rightarrow \infty$ :

$$J_0(x) \approx \sqrt{\frac{2}{\pi x}} \cos\left(x - \frac{\pi}{4}\right), \quad x \rightarrow \infty. \quad (33)$$

Using this approximation we observe that all of the oscillatory terms have phases which are of the form  $(k \times \text{length} + \text{phase})$ . This is the standard form of a semiclassical expression for the density of states of a billiard. To go a step further we notice that the leading-order terms, which are proportional to  $k^1$  (first line of (31)), have lengths of  $S\sqrt{p^2 + q^2 + r^2}$  which are the lengths of the periodic orbits of the 3-torus, and therefore of its desymmetrization into the tetrahedron. This conforms with the expressions derived by Berry and Tabor [63, 64] for integrable systems. The other, sub-leading, oscillatory contributions to (31) correspond to “improper” periodic manifolds, in the sense that their dynamics involves non-trivial limits. Some of these periodic orbits are restricted to symmetry plane or go along the edges. Of special interest are the periodic orbits that are shown in figure 6. They are isolated, but are neutrally stable and hence are non-generic. Their contributions are contained in the last two terms of (31), and the one with length  $S/\sqrt{3}$  is the shortest neutral periodic orbit. Other sub-leading oscillatory contributions are discussed in [54]. We therefore established an interpretation in terms of (proper or improper) classical periodic orbits of the various terms of (31).

### 3.1.1 Two-point statistics of the integrable case

We continue by investigating the two-point statistics of the tetrahedron, which will be shown to provide some nontrivial and interesting results. Since we are interested in the limiting statistics as  $k \rightarrow \infty$  we shall consider only the leading term of (31), which is the first term. Up to a factor of 48, this is exactly the density of states  $d_{T^3}$  of the cubic 3-torus, and thus for simplicity we shall dwell on the 3-torus rather than on the tetrahedron:

$$d_{T^3}(k) = \sum_{\vec{\rho} \in \mathbf{Z}^3} \delta\left(k - \frac{2\pi}{S}\rho\right) = \frac{S^3 k^2}{2\pi^2} \sum_{\vec{\rho} \in \mathbf{Z}^3} \text{sinc}(kS\rho). \quad (34)$$

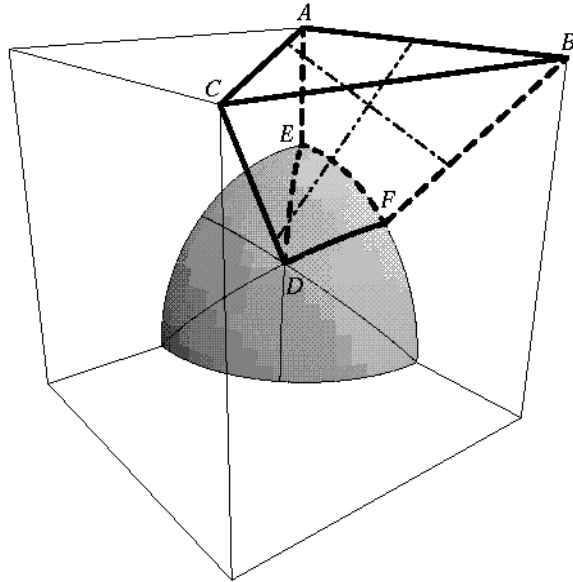
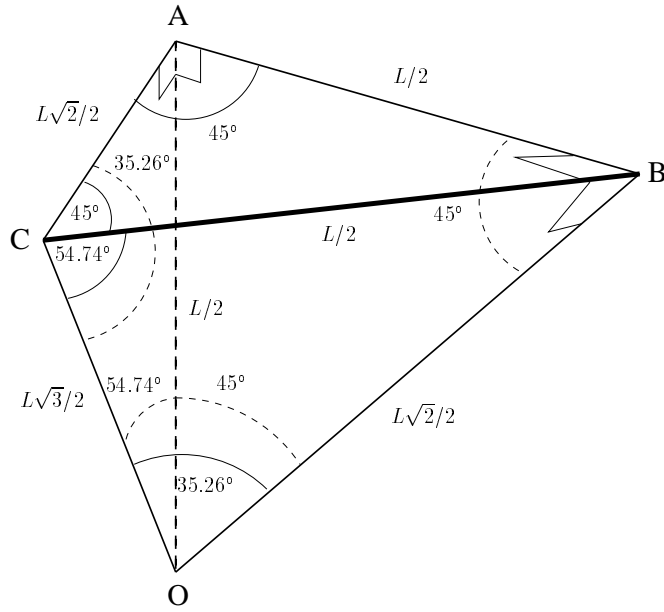


Figure 6: Upper: Geometry of the tetrahedron ( $R = 0$ ) billiard. Lower: Neutral periodic orbits in the desymmetrized 3D Sinai. The billiard is indicated by bold-face edges. Dot-dash line: The shortest neutral periodic orbit of length  $S/\sqrt{3}$ . Double dot-dash line: Neutral periodic orbit of length  $S/\sqrt{2}$ .

We observe that both the quantal spectrum and the classical spectrum (the set of lengths of periodic orbits) are supported on the cubic lattice  $\mathbf{Z}^3$ , and this strong duality will be used below.

The object of our study is the spectral form factor, which is the Fourier transform of the two-point correlation function of the energy levels [59]. For billiards it is more convenient to work with the eigenwavenumbers  $k_n$  rather than with the eigenenergies  $E_n$ . Here the form factor is given by:

$$K(\tau; k) = \frac{1}{N} \left| \sum_{n=n_1}^{n_2} \exp [2\pi i \bar{d}(k) k_n \tau] \right|^2 \quad (35)$$

In the above  $N \equiv n_2 - n_1 + 1$ , and  $k_n$  are the eigenvalues in the interval  $[k_{n_1}, k_{n_2}]$  centered around  $k = (k_{n_1} + k_{n_2})/2$ . It is understood that the interval contains many levels but is small enough such that the average density is almost a constant and is well approximated by  $\bar{d}(k)$ .

In the limit  $\tau \rightarrow \infty$  the phases in (35) become random in the generic case, and therefore  $K(\tau) \rightarrow 1$ . However, if the levels are degenerate, more care should be exercised, and one obtains:

$$K(\tau; k) = \frac{1}{N} \sum_n g_k(k_n) = \frac{1}{N} \sum_i' g_k^2(k_i), \quad \tau \rightarrow \infty, \quad (36)$$

where  $g_k(k_n)$  is the degeneracy of  $k_n$  and the primed sum is only over distinct values of  $k_i$ . Since  $N = \sum_i' g_k(k_i)$  we obtain:

$$K(\tau; k) = \frac{\sum_i' g_k^2(k_i)}{\sum_i' g_k(k_i)} = \frac{\langle g_k^2(k) \rangle}{\langle g_k(k) \rangle}, \quad \tau \rightarrow \infty, \quad (37)$$

where  $\langle \cdot \rangle$  denotes an averaging over  $k_i$ 's near  $k$ . In the case of a constant  $g$  the above expression reduces to  $K(\tau \rightarrow \infty) = g$ , but it is important to note that  $K(\tau \rightarrow \infty) \neq \langle g \rangle$  for non-constant degeneracies. Using the relation  $\rho = kS/(2\pi)$  (see equation (34)) and equations (274), (276) in appendix H we get:

$$K_{T^3}(\tau; k) = \frac{\langle g_\rho^2(kS/(2\pi)) \rangle}{\langle g_\rho(kS/(2\pi)) \rangle} = \frac{\beta S}{2\pi} k, \quad \tau \rightarrow \infty, \quad (38)$$

where  $\beta \approx 9.8264$  is a constant. That is, contrary to the generic case, the saturation value of the form factor grows linearly with  $k$  due to number-theoretical degeneracies.

Turning to the form factor in the limit  $\tau \rightarrow 0$ , we first rewrite (34) as  $d_{T^3}(k) = \bar{d}(k) + \sum_j A_j \sin(kL_j)$ . Then, using the diagonal approximation as suggested by Berry [4, 65], and taking into account the degeneracies  $g_\ell(L_j)$  of the lengths we have:

$$K(\tau; k) = \frac{1}{4\bar{d}^2(k)} \sum_j' g_\ell^2(L_j) |A_j|^2 \delta(\tau - L_j/L_H), \quad \tau \ll 1. \quad (39)$$

In the above the prime denotes summation only over *distinct* classical lengths, and  $L_{\text{H}} \equiv 2\pi\bar{d}(k)$  is called the Heisenberg length. The coefficients  $A_j$  are functions of  $L_j$  and therefore can be replaced by the function  $A(\tau)$ . For  $\tau$  large enough such that the periodic manifolds have a well-defined classical density  $\bar{d}_{\text{cl}}(\ell)$ , the summation over delta functions can be replaced by multiplication with  $L_{\text{H}}\bar{d}_{\text{cl}}(\ell)/\langle g_{\ell}(\ell) \rangle$  with  $\ell = L_{\text{H}}\tau$  such that:

$$K(\tau; k) = \left( \frac{\pi |A^2(\tau)| \bar{d}_{\text{cl}}(\ell)}{2\bar{d}(k)} \right) \frac{\langle g_{\ell}^2(\ell) \rangle}{\langle g_{\ell}(\ell) \rangle}, \quad \tau \ll 1. \quad (40)$$

A straightforward calculation shows that the term in brackets is simply 1, which is the generic situation for the integrable case (Poisson statistics) [4, 66]. Hence, we obtain:

$$K(\tau; k) = \frac{\langle g_{\ell}^2(\ell) \rangle}{\langle g_{\ell}(\ell) \rangle}, \quad \tau \rightarrow 0. \quad (41)$$

Since, as we noted above, the lengths of the classical periodic orbits are supported on the  $\mathbb{Z}^3$  lattice, we can write using  $\ell = S\rho$ :

$$K(\tau; k) = \frac{\langle g_{\rho}^2(\ell/S) \rangle}{\langle g_{\rho}(\ell/S) \rangle} = \frac{\beta k^2 S^2}{\pi} \tau, \quad \tau \rightarrow 0. \quad (42)$$

where we used again equations (274), (276). This is a very surprising result, since it implies that contrary to the generic integrable systems, which display Poisson level statistics with  $K = 1$ , here  $K \propto \tau$  which is typical to chaotic systems! This peculiarity is manifestly due to the number theoretical degeneracies of  $\mathbb{Z}^3$ .

If we now combine the two limiting behaviours of the form factor in the simplest way, we can express it as a scaled RMT-GUE form factor:

$$K_{\mathcal{T}^3}(\tau; k) \approx K_{\infty} \cdot K_{\text{GUE}}(\gamma\tau) \quad (43)$$

where  $K_{\infty} = S\beta k/(2\pi)$  and  $\gamma = 2Sk$ . For the tetrahedron we have the same result with  $K_{\infty} \rightarrow K_{\infty}/48$  and  $\gamma \rightarrow \gamma/48$ . This prediction is checked and verified numerically in figure 7 where we computed the quantal form factor of the tetrahedron around various  $k$ -values. The agreement of the two asymptotes to the theoretical prediction (43) is evident and the difference from Poisson is well beyond the numerical fluctuations.

### 3.2 Nearest-neighbour spacing distribution

We now turn to the chaotic case  $R > 0$ . One of the most common statistical measures of a quantum spectrum is the nearest-neighbour distribution  $P(s)$ . In fact, it is the simplest statistics to compute from the numerical data. We need only to consider the distribution of the scaled (unfolded) spacings between neighbouring levels:

$$s_n \equiv \bar{N}(k_{n+1}) - \bar{N}(k_n) \approx \bar{d}(k_n)(k_{n+1} - k_n). \quad (44)$$

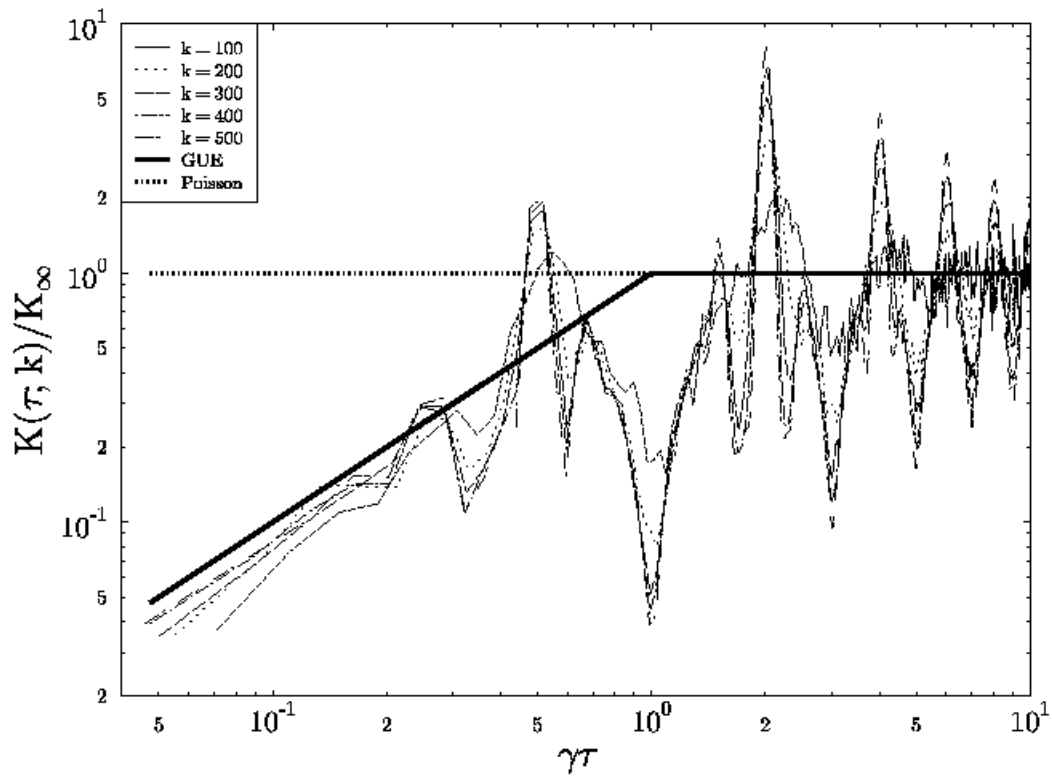


Figure 7: The scaled quantal form factor of the tetrahedron for various  $k$ -values compared with GUE and Poisson. Note the log-log scales.



It is customary to plot a histogram of  $P(s)$ , but it requires an arbitrary choice of the bin size. To avoid this arbitrariness, we consider the cumulant distribution:

$$I(s) \equiv \int_0^s ds' P(s') \quad (45)$$

for which no bins are needed. Usually, the numerical data are compared not to the exact  $P_{\text{RMT}}(s)$  but to Wigner's surmise [2], which provides an accurate approximation to the exact  $P_{\text{RMT}}(s)$  in a simple closed form. In our case, since we found a general agreement between the numerical data and Wigner's surmise, we choose to present the differences from the exact expression for  $I_{\text{GOE}}(s)$  taken from Dietz and Haake [67]. In figure 8 we show these differences for  $R = 0.2, 0.3$  and Dirichlet boundary conditions (6697 and 1994 levels, respectively). The overall result is an agreement between the numerical data and RMT to better than 4%. This is consistent with the general wisdom for classically chaotic systems in lower dimensions, and thus shows the robustness of the RMT conjecture [24] for higher-dimensional systems (3D in our case).

Beyond this general good agreement it is interesting to notice that the differences between the data and the exact GOE for  $R = 0.2$  seem to indicate a systematic modulation rather than a statistical fluctuation about the value zero. The same qualitative result is obtained for other boundary conditions with  $R = 0.2$ , substantiating the conjecture that the deviations are systematic and not random. For  $R = 0.3$  the differences look random and show no particular pattern. However, for the upper third of the spectrum one observes structures which are similar to the  $R = 0.2$  case (see figure 8, lower part).

Currently, we have no theoretical explanation of the above mentioned systematic deviations. They might be due to the non-generic bouncing balls. To assess this conjecture we computed  $P(s)$  for  $R = 0.2, 0.3$  with Dirichlet boundary conditions in the spectral interval  $150 < k < 200$ . The results (not shown) indicate that the deviations are smaller for the larger radius. This is consistent with the expected weakening of the bouncing-ball contributions as the radius grows, due to larger shadowing and smaller volumes occupied by the bouncing-ball families. Hence, we can conclude that the bouncing balls are indeed prime candidates for causing the systematic deviations of  $P(s)$ . It is worth mentioning that a detailed analysis of the  $P(s)$  of spectra of quantum graphs show similar deviations from  $P_{\text{RMT}}(s)$  [68].

### 3.3 Two-point correlations

Two-point statistics also play a major role in quantum chaos. This is mainly due to their analytical accessibility through the Gutzwiller trace formula as demonstrated by Berry [4, 65]. There is a variety of two-point statistical measures which are all related to the pair-correlation function [59]. We chose to focus on  $\Sigma^2(l)$  which is the local variance of the number of levels in an energy interval

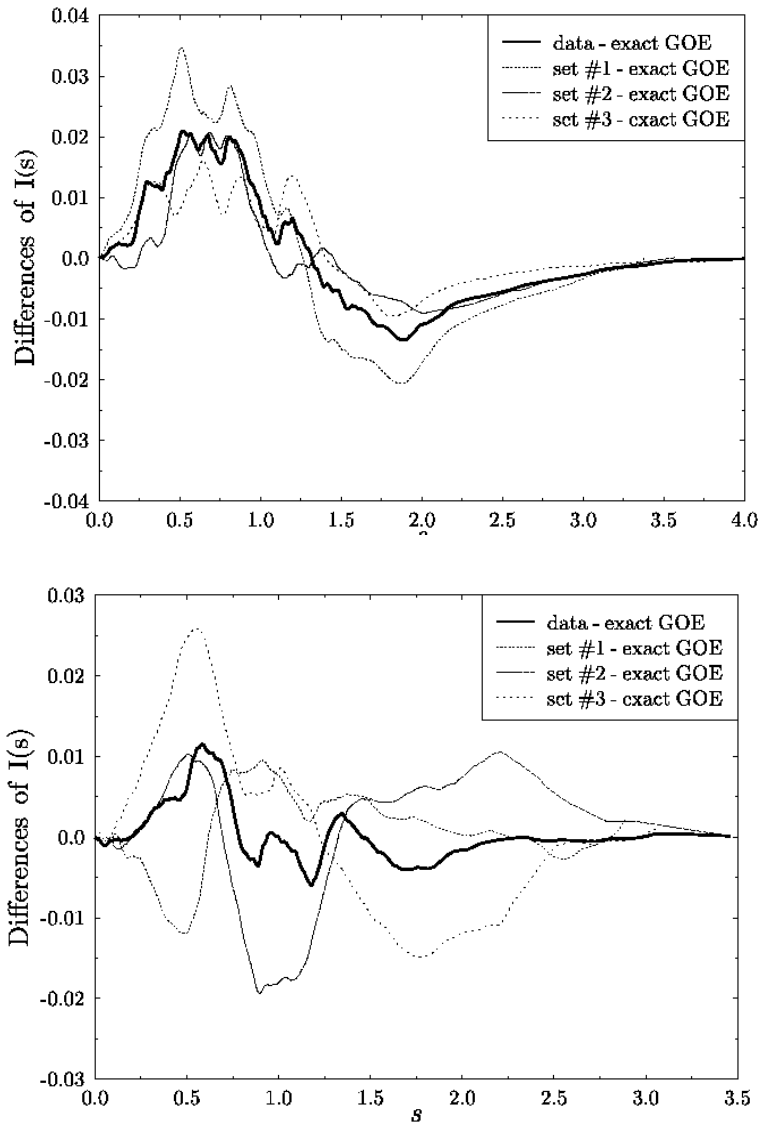


Figure 8: Differences of integrated nearest-neighbour distribution for  $R = 0.2$  (up) and  $R = 0.3$  (down). Set #1, 2, 3 refer to the division of the spectrum into 3 domains. Data are slightly smoothed for clarity.

that has the size of  $l$  mean spacings. The general expectation for generic systems, according to the theory of Berry [4, 65], is that  $\Sigma^2$  should comply with the predictions of RMT for small values of  $l$  (universal regime) and saturate to a non-universal value for large  $l$ 's due to the semiclassical contributions of short periodic orbits. The saturation value in the case of generic billiards is purely classical ( $k$ -independent). The effect of the non-generic bouncing-ball manifolds on two-point spectral statistics was discussed in the context of 2D billiards by Sieber et al. [37] (for the case of the stadium billiard). They found that  $\Sigma^2$  can be decomposed into two parts: A generic contribution due to unstable periodic orbits and a non-generic contribution due to bouncing balls:

$$\Sigma^2(l) \approx \Sigma_{\text{UPO}}^2(l) + \Sigma_{\text{bb}}^2(l). \quad (46)$$

The term  $\Sigma_{\text{bb}}^2$  has the structure:

$$\Sigma_{\text{bb}}^2(l) = kF_{\text{stadium}}(l/\bar{d}(k)), \quad (47)$$

where  $F_{\text{stadium}}$  is a function which is determined by the bouncing balls of the stadium billiard, and is given explicitly in [37]. In particular, for large values of  $l$  the term  $\Sigma_{\text{bb}}^2$  fluctuated around an asymptotic value:

$$\Sigma_{\text{bb}}^2(l) \approx kF_{\text{stadium}}(\infty), \quad l \rightarrow \infty. \quad (48)$$

One can apply the arguments of Sieber et al. [37] to the case of the 3D Sinai billiard and obtain for the leading order bouncing balls (see (34)):

$$\Sigma_{\text{bb}}^2(l) \approx k^2F_{\text{3Dsb}}(l/\bar{d}(k)), \quad (49)$$

with  $F_{\text{3Dsb}}$  characteristic to the 3D Sinai billiard. Asymptotically, we expect:

$$\Sigma_{\text{bb}}^2(l) \approx k^2F_{\text{3Dsb}}(\infty), \quad l \rightarrow \infty. \quad (50)$$

The function  $F_{\text{3Dsb}}$  can be written down, albeit it contains the areas of the cross-sections of the various bouncing-ball manifolds, for which we have no explicit expressions. Therefore, we shall investigate the scaling features of  $\Sigma_{\text{bb}}^2$  without insisting on its explicit form.

The numerical computations of  $\Sigma^2$  for the longest spectrum ( $R = 0.2$ , Dirichlet everywhere) are shown in figure 9. We divided the spectrum into 4 intervals such that  $\bar{d}$  did not vary much within each interval. This is a pre-requisite for a meaningful semiclassical analysis. It is evident from the figure that for small values of  $l$  (up to  $\approx 1$ ) there is an agreement with GOE. Moreover, the agreement with GOE is much better than with either GUE or Poisson, as expected. This is in agreement with the common knowledge in quantum chaos [59], and again, substantiates the RMT conjecture also for chaotic systems in 3D. For larger  $l$  values there are marked deviations which saturate into oscillations around a  $k$ -dependent

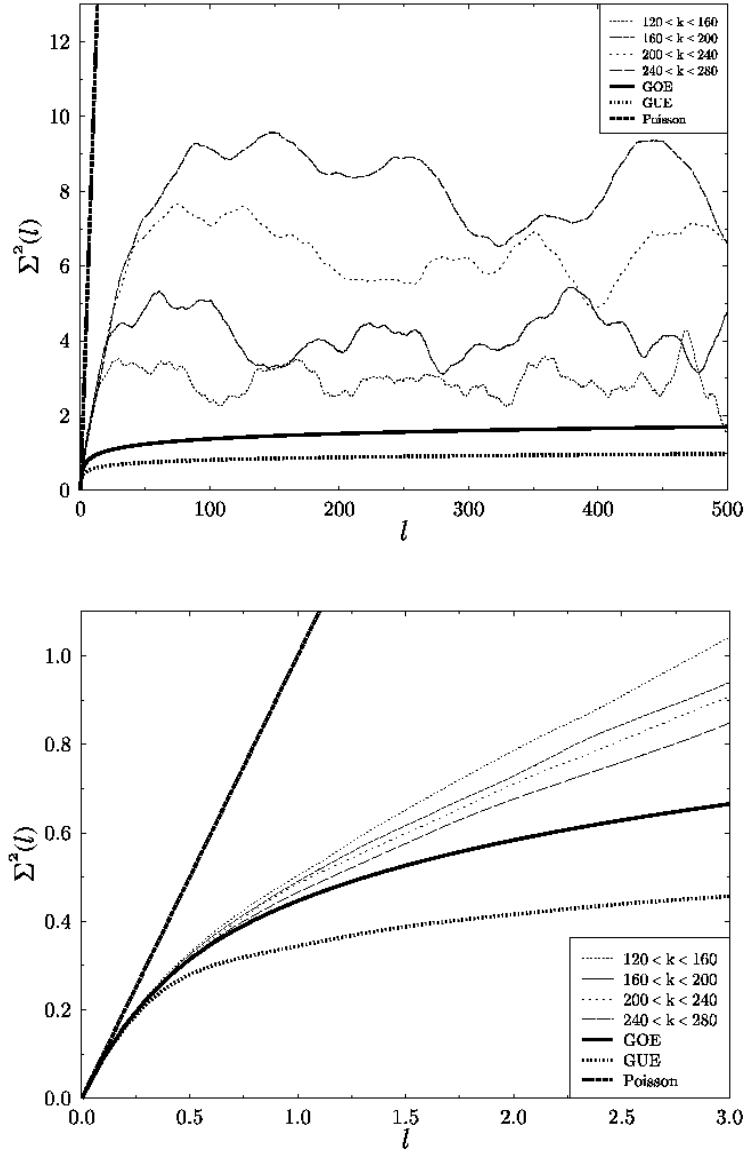


Figure 9: The number variance  $\Sigma^2(l)$  for the longest spectrum. Upper plot: Full  $l$ -range, lower plot: A magnification of small  $l$  range.

asymptotic values. It is clearly seen that the saturation values grow faster than  $k$ , which is consistent with (50). To test (49) quantitatively, we plotted in figure 10 the rescaled function:

$$S_{\text{bb}}^2(q; k) \equiv \frac{1}{k^2} [\Sigma^2(q\bar{d}(k)) - \Sigma_{\text{GOE}}^2(q\bar{d}(k))] \quad (51)$$

which according to (49) is the  $k$ -independent function  $F_{3\text{Dsb}}(q)$ . Indeed, there is a clear data collapse for  $q \lesssim 5$ , and the saturation values of  $S_{\text{bb}}^2$  are of the same magnitude for all values of  $k$ . This verifies (49) and demonstrates the important part which is played by the bouncing balls in the two-point (long range) statistics.

For generic systems the agreement between  $\Sigma^2$  and RMT should prevail up to  $l^*$ , where:

$$l^* = \frac{L_{\text{H}}(k)}{L_{\text{min}}} = \frac{2\pi\bar{d}(k)}{L_{\text{min}}}. \quad (52)$$

In the above  $L_{\text{H}}$  is Heisenberg length and  $L_{\text{min}}$  is the length of the shortest periodic orbit. For the cases shown in figure 9 the value of  $l^*$  is of the order of 100. Nevertheless, the deviations from the universal predictions start much earlier. This is again a clear sign of the strong effect of the bouncing-balls. To substantiate this claim, we compare in figure 11 the number variances for  $R = 0.2$  and  $R = 0.3$  in the same  $k$  interval and with the same boundary conditions (Dirichlet). The influence of the bouncing-balls is expected to be less dominant in the  $R = 0.3$  case, since there are fewer of them with smaller cross sections. This is indeed verified in the figure: The agreement with GOE predictions lasts much longer (up to  $l \approx 6$ ) in the  $R = 0.3$  case, and the saturation value is smaller, as expected.

### 3.4 Auto-correlations of spectral determinants

The two-point correlations discussed above are based on the quantal *spectral densities*. Kettmann, Klakow and Smilansky [61] introduced the auto-correlations of quantal *spectral determinants* as a tool for the characterization of quantum chaos. Spectral determinants are defined as:

$$Z(E) = 0 \iff E = E_n, \quad (53)$$

that is, they are 0 iff  $E$  is an eigenenergy. The (unnormalized) correlation function of a spectral determinant is defined as:

$$C(\omega; E) \equiv \frac{1}{\Delta E} \int_{E-\Delta E/2}^{E+\Delta E/2} dE' Z\left(E' + \frac{\omega}{2d}\right) Z^*\left(E' - \frac{\omega}{2d}\right), \quad \omega \ll \Delta E. \quad (54)$$

There are various motivations to study the function  $C(\omega)$  [61]:

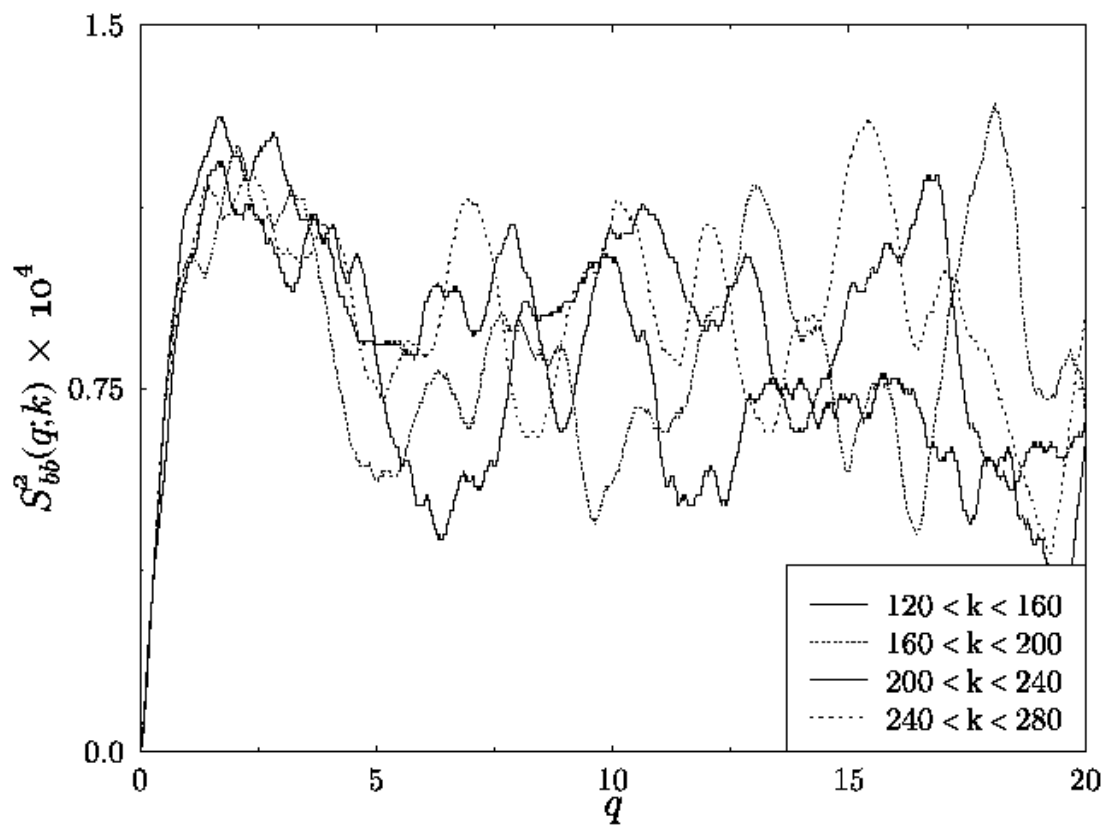


Figure 10: Rescaled number variance (51) for the longest spectrum.

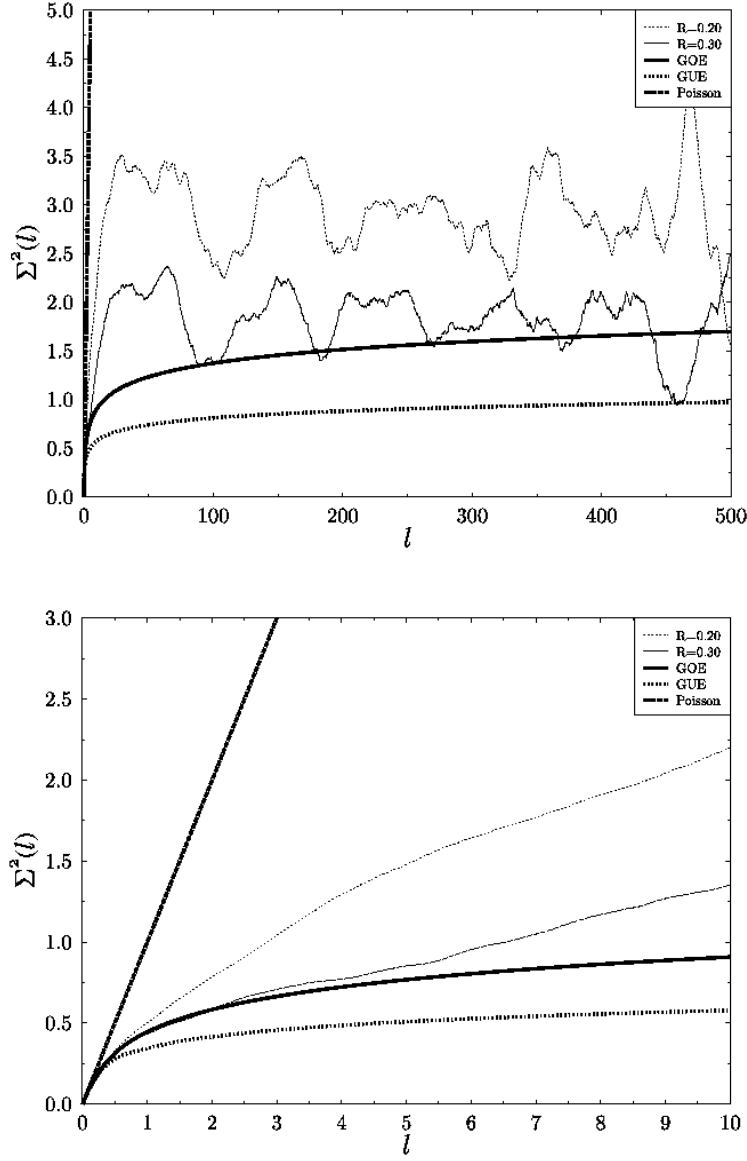


Figure 11: Comparison between the number variances for two different radii  $R = 0.2, 0.3$  of the inscribed sphere of the 3D Sinai billiard. In both cases we considered the spectral interval  $120 < k < 160$  and used Dirichlet boundary conditions.

1. There is a marked difference in the behaviour of  $C(\omega)$  for rigid and non-rigid spectra. For completely rigid spectra the function  $C(\omega)$  is oscillatory, while for Poissonian spectra it rapidly decays as a Gaussian. For the RMT ensembles it shows damped oscillations which are due to rigidity.
2. The function  $C(\omega)$  contains information about all  $n$ -point correlations of the spectral densities. Thus, it is qualitatively distinct from the two-point correlations of spectral densities and contains new information.
3. The Fourier transform of  $C(\omega)$  exhibit in an explicit and simple way symmetry properties which are due to the reality of the energy levels.
4. In contrast to spectral densities, the semiclassical expressions for spectral determinants can be regularized using the method of Berry and Keating [69]. Regularized semiclassical spectral determinants contain a finite number of terms, and are manifestly real for real energies.
5. The semiclassical expression for  $C(\omega)$  is closely related to the classical Ruelle zeta function.

To study  $C(\omega)$  numerically, regularizations are needed. For the 3D Sinai billiard the longest spectrum was divided into an ensemble of 167 intervals of  $N = 40$  levels, and each interval was unfolded to have mean spacing 1 and was centered around  $E = 0$ . For each unfolded interval  $I_j$  the function  $C_j(\omega)$  was computed using equation (69) of [61], with  $\Delta E = \sqrt{N}$ . The ensemble average function  $C(\omega)$  was normalized such that  $C(0) = 1$ . The results of the computation are shown in figure 12. The agreement with RMT is quite good up to  $\omega \approx 3$ , that is for short energy scales for which we indeed expect universality to hold.



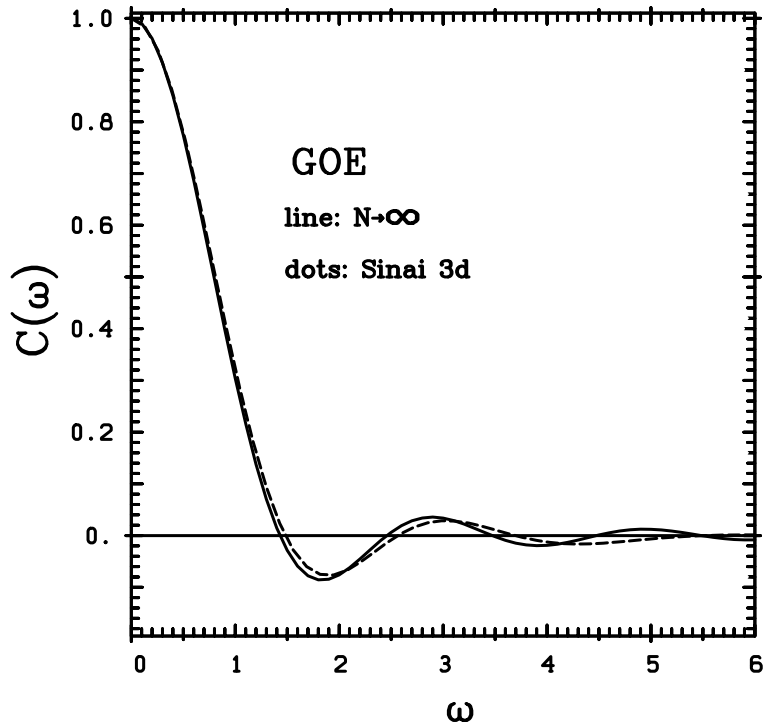


Figure 12: The two-point correlation function of spectral determinants  $C(\omega)$  for the 3D Sinai billiard (longest spectrum). The spectrum was divided into 167 intervals of 40 levels each and the average correlation function is shown. The continuous line is the RMT-GOE theoretical curve, and the dashed line is the numerical correlation. The correlation function is normalized to 1 for  $\omega = 0$ . With kind permission from the authors of [61].

## 4 Classical periodic orbits

In this section we present a comprehensive study of the periodic orbits of the 3D Sinai billiard. By “periodic orbits” we mean throughout this section generic, isolated and unstable periodic orbits which involve at least one bounce from the sphere. Thus, bouncing-ball orbits are not treated in this section. The classical periodic orbits are the building blocks for the semiclassical Gutzwiller trace formula, and are therefore needed for the semiclassical analysis to be presented in the next section.

### 4.1 Periodic orbits of the 3D Sinai torus

We found it necessary and convenient to first identify the periodic orbits of the **symmetric** 3D Sinai billiard on the torus, and to compute their lengths and stabilities. The periodic orbits of the **desymmetrized** 3D Sinai billiard could then be derived by an appropriate classical desymmetrization procedure.

The basic problem is how to find in a systematic (and efficient) way all the periodic orbits of the 3D Sinai billiard up to a given length  $L_{\max}$ . In dealing with periodic orbits of the Sinai billiard it is very helpful to consider its unfolded representation that tessellates  $\mathbb{R}^3$  — as is shown in figure 1. We start by considering the periodic orbits of the fully symmetric 3D Sinai billiard on the torus (ST). This case is simpler than the desymmetrized billiard, since it contains no boundaries and the tiling of the  $\mathbb{R}^3$  space is achieved by simple translations along the cubic lattice  $\mathbb{Z}^3$ . In the unfolded representation every orbit is described by a collection of straight segments which connect spheres. At a sphere, the incident segment reflects specularly. A *periodic* orbit of period  $n$  is not necessarily periodic in the unfolded representation, but rather, it obeys the restriction that the segments repeat themselves after  $n$  steps *modulo* a translation by a lattice vector (see figure 13). If we fix an origin for the lattice, we can assign to every orbit (not necessarily periodic) a “code word” by concatenating the “addresses” (locations of the centers on the  $\mathbb{Z}^3$  lattice) of the spheres from which it reflects. The code word can consist of either the *absolute* addresses of the spheres or alternatively, the address of the sphere *relative* to the previous one. We shall adopt the latter convention and use the relative addresses as the “letters” from which the code word is composed. This relative coding has the advantage that a periodic orbit is represented by a periodic code word. The number of possible letters (“alphabet”) is obviously infinite and the letter  $(0, 0, 0)$  is excluded. A periodic orbit can be represented by any cyclic permutation of its code. To lift this ambiguity, we choose a convenient (but otherwise arbitrary) lexical ordering of the letters and use the code word which is *lexically maximal* as the unique representative of the

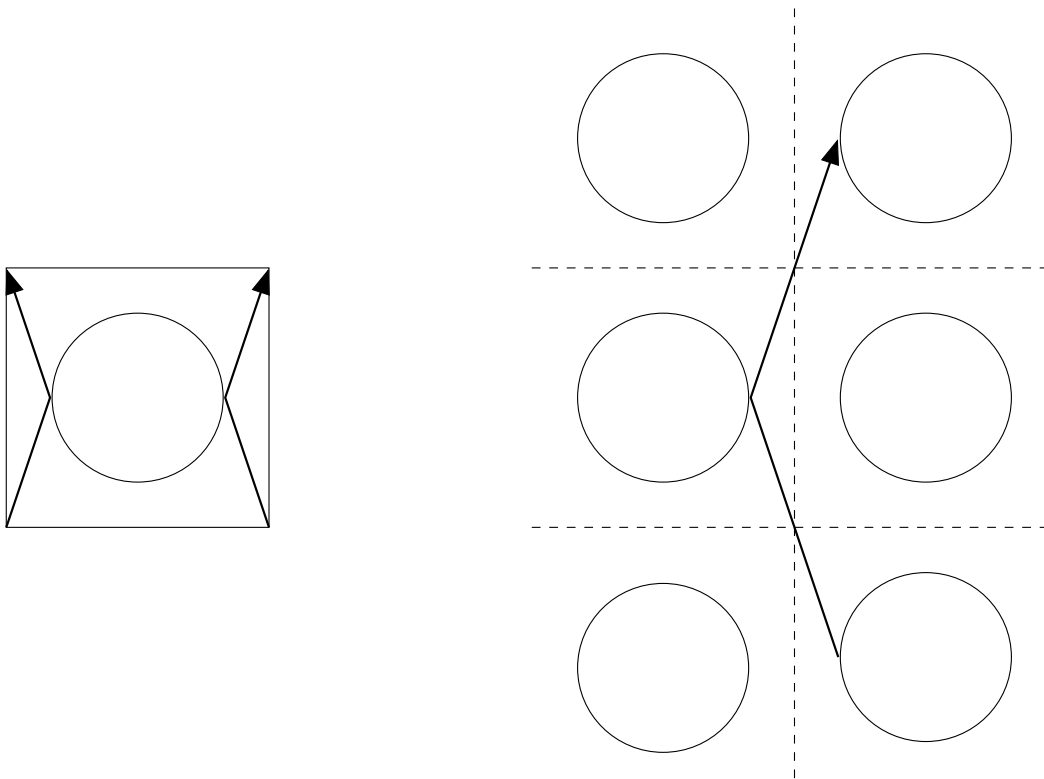


Figure 13: Representation of a periodic orbit of the Sinai 2-torus. Left: One cell representation, Right: Unfolded representation.

periodic orbit:

$$\begin{aligned}
 (\text{periodic orbit of ST}) &\longmapsto W = (w_1, w_2, \dots, w_n), w_i \in \mathbb{Z}^3 \setminus (0, 0, 0) \\
 W &= \max\{W, \hat{P}W, \hat{P}^2W, \dots, \hat{P}^{n-1}W\},
 \end{aligned} \tag{55}$$

where  $\hat{P}W = (w_2, w_3, \dots, w_n, w_1)$  is the operation of a cyclic permutation of the code word.

Let us consider the code word  $W$  with  $n$  letters:

$$W = (w_1, w_2, \dots, w_n), \quad w_i = (w_{ix}, w_{iy}, w_{iz}). \tag{56}$$

It relates to the  $n + 1$  spheres centered at  $c_1 = (0, 0, 0)$ ,  $c_2 = w_1$ ,  $c_3 = w_1 + w_2, \dots, c_{n+1} = w_1 + \dots + w_n$ . Let us choose arbitrary points on each of the spheres, and connect them by straight segments. We get a piecewise straight line which leads from the first to the last sphere, which, in general, is not a classical orbit because the specular reflection conditions are not satisfied. To find a periodic orbit, we specify the positions of the points on each sphere by two angles  $\theta_i, \varphi_i$ . The length of the line is a function of  $\{(\theta_i, \varphi_i) |_{i=1, \dots, n}\}$ . Periodic orbits on the ST must have identical coordinates for the first and the last points (modulo a lattice translation), hence  $\theta_{n+1} = \theta_1, \varphi_{n+1} = \varphi_1$  and we have only  $2n$  independent variables to completely specify a periodic set of segments, with length:

$$L_W(\theta_1, \dots, \theta_n, \varphi_1, \dots, \varphi_n) = \sum_{i=1}^n L_i(\theta_i, \theta_{i+1}, \varphi_i, \varphi_{i+1}), \tag{57}$$

where  $L_i$  are the lengths of the segments that correspond to the letter  $w_i$ . To satisfy the condition of specular reflection we require that the length  $L_W$  is extremal with respect to any variation of its variables.

The following theorem guarantees two essential properties of the coding and of the periodic orbits which are identified as the extrema of (57) [27, 32]:

**Theorem:** To each code word  $W$  of the 3D ST there corresponds *at most* one periodic orbit which is the only minimum of  $L_W$ .

The theorem contains two statements: First, that periodic orbits are necessarily minima of the length, and not saddles or maxima. Second, that there are no local minima besides the global one. The phrase “at most” in the theorem above needs clarification: For each code word  $W$  the length function  $L_W$  is a continuous function in all of its variables over the compact domain which is the union of the spheres. Therefore  $L_W$  must have a global minimum within this domain. This minimum can be, however, classically forbidden, meaning that at least one of its segments cuts through one or more spheres in the lattice (that might or might not be a part of the code) rather than reflecting from the outside. This is called “shadowing”. An example is shown in figure 14. The forbidden periodic orbits

are excluded from the set of classical periodic orbits. (They also do not contribute to the leading order of the trace formula [70, 15] and therefore are of no interest in our semiclassical analysis.) If all the segments are classically allowed, then we have a valid classical periodic orbit. Finally we would like to mention that the minimality property was already implied in the work of Sieber [60], and the explicit versions of the theorem were proved simultaneously by Bunimovich [27] (general formulation, applies in particular to the 3D case) and Schanz [32] (restricted to the 2D Sinai billiard).

The number of letters in the codes of periodic orbits of length less than  $L_{\max}$  can be bounded from above by the following argument. To each letter  $w$  there corresponds a minimal segment length  $L_{\min}(w) > 0$  which is the minimum distance between the spheres centered at  $(0, 0, 0)$  and at  $w = (w_x, w_y, w_z)$ :

$$L_{\min}(w) = S\sqrt{w_x^2 + w_y^2 + w_z^2} - 2R. \quad (58)$$

In the above,  $S$  is the lattice constant (torus's side) and  $R$  is the radius of the sphere. The smallest possible  $L_{\min}(w)$  is obtained for  $w = (1, 0, 0)$  and equals  $S - 2R \equiv L_{\min}$ . We readily conclude that the code word cannot contain more letters than the integer part of  $L_{\max}/L_{\min}$ .

We are now in a position to formulate an algorithm for a systematic search of *all* the periodic orbits of length up to  $L_{\max}$  of the 3D Sinai torus:

1. Collect all of the admissible letters into an alphabet. An admissible letter  $w$  satisfies:
  - (a)  $w \neq (0, 0, 0)$ .
  - (b)  $w$  is not trivially impossible due to complete shadowing, e.g., like  $(2, 0, 0) = 2 \times (1, 0, 0)$ .
  - (c)  $L_{\min}(w) \leq L_{\max}$ .
2. Define an arbitrary lexical order of the letters.
3. From the admissible alphabet construct the set of admissible code words  $W = (w_1, \dots, w_n)$ , such that:
  - (a)  $L_{\min}(W) \equiv \sum_{i=1}^n L_{\min}(w_i) \leq L_{\max}$ .
  - (b)  $w_i \neq w_{i+1}$  — no a-priori complete shadowing.
  - (c)  $W$  is lexically maximal with respect to cyclic permutations:  $W = \max\{\hat{P}^i W, i = 0, \dots, n - 1\}$ .
4. For each candidate code word  $W$  minimize numerically the function  $L_W$ . According to the theorem, there should be exactly one minimum, which is the global one.

5. Check whether the resulting periodic orbit is shaded. Accept only periodic orbits which are not shaded.

Once the periodic orbit is identified, its monodromy (stability) matrix is computed according to the recipe given in appendix J.

## 4.2 Periodic Orbits of the 3D Sinai billiard — Classical desymmetrization

If we desymmetrize the ST into the Sinai billiard (SB), we still find that the SB tessellates the  $\mathbb{R}^3$  space. Hence, each periodic orbit of the ST is necessarily also a periodic orbit of the SB. The converse is not true, i.e., periodic orbits of the SB are not necessarily periodic in ST. However, it is easy to be convinced that if a periodic orbit of SB is repeated sufficiently many times, it becomes also periodic in ST. An example is shown in figure 15. From a more abstract point of view, this is because the cubic group  $O_h$  is finite. Thus in principle one could use the algorithm given above to systematically find all the periodic orbits of the SB. This is, however, highly inefficient because by analyzing the group  $O_h$  we find that in order to find all the periodic orbits of the SB up to  $L_{\max}$  we must find all of the periodic orbits of ST up to  $6L_{\max}$ . Due to the exponential proliferation of periodic orbits this would be a colossal waste of resources which would diminish our ability to compute periodic orbits almost completely. To circumvent this difficulty, without losing the useful uniqueness and minimality properties which apply to the ST, we make use of the property that periodicity in the SB is synonymous to periodicity in ST *modulo* an element  $\hat{g} \in O_h$ . This simple geometrical observation is a manifestation of the fact that the tiling of  $\mathbb{R}^3$  by the SB is generated by the group  $O_h \otimes \mathbb{Z}^3$ . Thus, we can represent the periodic orbits of the SB by using their unfolded representation, augmented by the symmetry element  $\hat{g}$  according to which the periodic orbits closes:

$$\text{Periodic orbit of SB} \mapsto \hat{W} \equiv (W; \hat{g}) = (w_1, w_2, \dots, w_n; \hat{g}). \quad (59)$$

The coding is not yet well-defined since a given periodic orbit can in general be represented by several codes. Similarly to the case of the ST, there is a degeneracy with respect to the starting point. However, in the case of the SB this is not simply related to cyclic permutations. Rather, if a periodic orbit is described by  $(w_1, w_2, \dots, w_n; \hat{g})$  then it is also described by:

$$\begin{aligned} & (w_2, w_3, \dots, w_n, \hat{g}w_1; \hat{g}), (w_3, w_4, \dots, \hat{g}w_1, \hat{g}w_2; \hat{g}), \dots, \\ & (\hat{g}w_1, \hat{g}w_2, \dots, \hat{g}w_n; \hat{g}), (\hat{g}w_2, \hat{g}w_3, \dots, \hat{g}^2w_1; \hat{g}), \dots \\ & \vdots \\ & (\hat{g}^{\phi(\hat{g})-1}w_1, \hat{g}^{\phi(\hat{g})-1}w_2, \dots, \hat{g}^{\phi(\hat{g})-1}w_n; \hat{g}), \dots, (\hat{g}^{\phi(\hat{g})-1}w_n, w_1, w_2, \dots, w_{n-1}; \hat{g}). \end{aligned} \quad (60)$$

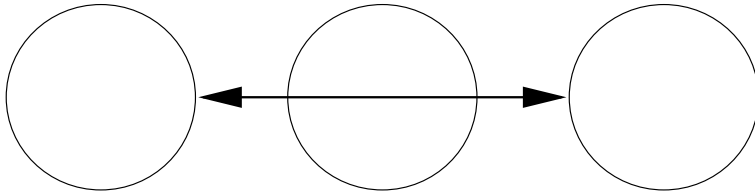


Figure 14: A shadowed (classically forbidden) periodic orbit of the Sinai 3-torus.

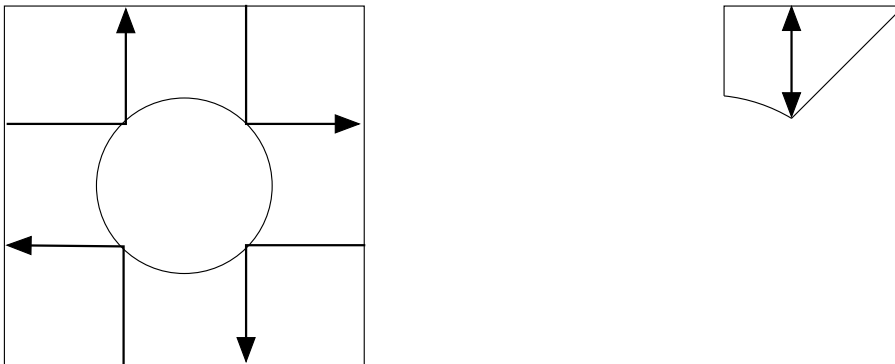


Figure 15: Desymmetrization of orbits from the Sinai torus to the Sinai billiard. For clarity we show an example in 2D. Left: A primitive periodic orbit in the ST. Right: The corresponding periodic orbit in the SB. We observe that the latter is 4 times shorter than the former.

In the above  $\phi(\hat{g})$  is the *period* of  $\hat{g}$ , which is defined as the smallest natural number for which  $\hat{g}^{\phi(\hat{g})} = \hat{e}$ , where  $\hat{e}$  is the identity operation. For  $O_h$  in particular  $\phi(\hat{g}) \in \{1, 2, 3, 4, 6\}$ . The above generalized cyclic permutation invariance is due to the periodicity modulo  $\hat{g}$  of the periodic orbits of the SB in the unfolded representation. In addition to the generalized cyclic invariance there is also a geometrical invariance of orbits of the SB in the unfolded representation. Indeed, if we operate on an orbit in the unfolded representation with any  $\hat{h} \in O_h$  we obtain the same orbit in the SB. This symmetry is carried over also to the codes. If a periodic orbit is described by  $(w_1, w_2, \dots, w_n; \hat{g})$  then it is also described by:

$$(\hat{h}w_1, \hat{h}w_2, \dots, \hat{h}w_n; \hat{h}\hat{g}\hat{h}^{-1}) \quad \forall \hat{h} \in O_h. \quad (61)$$

To summarize, a periodic orbit of the SB can be encoded into a code word up to degeneracies due to generalized cyclic permutations and geometrical operations. The set of operations which relate the various codes for a given periodic orbit is a group to which we refer as the invariance group.

In order to lift this degeneracy and to obtain a unique mapping of periodic orbits of the SB to code words we need to specify a criterion for choosing exactly one representative. There are many ways of doing this, but we found it convenient to apply the natural mapping of periodic orbits of the SB to those of the ST, and there, to choose the maximal code. More specifically:

1. Select the alphabet according to the rules prescribed in the preceding subsection, and define ordering of letters.
2. Extend the word  $\hat{W}$  into  $\tilde{W}$ :

$$\tilde{W} \equiv (w_1, w_2, \dots, w_n, \hat{g}w_1, \hat{g}w_2, \dots, \hat{g}w_n, \hat{g}^2w_1, \dots, \hat{g}^{\phi(\hat{g})-1}w_1, \dots, \hat{g}^{\phi(\hat{g})-1}w_n). \quad (62)$$

The code  $\tilde{W}$  describes the periodic orbit of the SB which is continued  $\phi(\hat{g})$  times to become periodic in the ST. Applying a generalized cyclic permutation on  $\hat{W}$  is equivalent to applying the standard cyclic permutation on  $\tilde{W}$ . Applying a geometrical operation  $\hat{h}$  on  $\hat{W}$  is equivalent to operating letter by letter with  $\hat{h}$  on  $\tilde{W}$ . The invariance group corresponding to  $\tilde{W}$  is  $\mathcal{H} = \mathcal{C} \otimes O_h$ , where  $\mathcal{C}$  is the group of cyclic permutations of order  $n \cdot \phi(\hat{g})$ . The simple decomposition of  $\mathcal{H}$  is due to the commutativity of  $\mathcal{C}$  and  $O_h$ , and it greatly facilitates the computations.

3. If  $\tilde{W}$  is maximal with respect to the invariance group  $\mathcal{H}$ , then the corresponding  $\hat{W}$  is the representative of the periodic orbit.

A comment on the uniqueness of this selection process is appropriate at this point. For any  $\hat{W}$  we can uniquely construct the corresponding  $\tilde{W}$  and the invariance group and check the maximality of  $\tilde{W}$ . Hence, we are able to uniquely



decide whether  $\hat{W}$  is a valid representative code or not. However, there are cases in which more than one  $\hat{W}$  correspond to the *same maximal*  $\tilde{W}$ . It is straightforward to show that in these cases the basic code word  $W$  is symmetric under some operation(s):  $W = \hat{k}W$ ,  $\hat{k} \in O_h$ . To such symmetric codes must correspond symmetric periodic orbits, which is necessitated by the uniqueness theorem for the ST. But for the SB the symmetry of the orbit means that it is wholly contained in a symmetry plane, and therefore is not a proper classical orbit. Such orbits are nevertheless required for the semiclassical analysis and will be treated in the next section when dealing with semiclassical desymmetrization. In summary, we have shown so far that the mapping of a given *proper* periodic orbit to a code is well-defined and unique.

In order for the coding to be useful and powerful, we need to establish uniqueness in the opposite direction, that is to show that for a given (unsymmetrical)  $\hat{W}$  there corresponds at most one (proper) classical periodic orbit. The mapping  $\hat{W} \mapsto \tilde{W}$  is very useful in that respect. Indeed, if there were two distinct periodic orbits of the SB with the same coding  $\hat{W}$ , then we could repeat them  $\phi(\hat{g})$  times to get two distinct periodic orbits of the ST with the same code  $\tilde{W}$ , which is in contradiction with the theorem above. This proves the uniqueness of the relation between codes and periodic orbits.

To facilitate the actual computation of periodic orbits of the SB, we have to establish their minimality property, similarly to the ST case. We need to prove that the length of a periodic orbit is a minimum, and that it is the only minimum. The minimality of a periodic orbit of the SB is proven by using again the unfolding to periodic orbits of ST, and noting that a minimum of  $L_{\tilde{W}}$  is necessarily also a minimum of  $L_{\hat{W}}$ , since the latter is a constrained version of the former. Thus, periodic orbits of the SB are minima of  $L_{\hat{W}}$ . We finally have to show that there exists only a single minimum of  $L_{\hat{W}}$ . The complication here is that, in principle, a minimum of  $L_{\hat{W}}$  does not necessarily correspond to a minimum of  $L_{\tilde{W}}$ , since there are, in general, more variables in the latter. We resolve this difficulty by using arguments from the proof of Schanz [32] as follows. A necessary condition for minimality is that orbits are either externally reflected from the scatters or cut through them in straight segments. Internal reflections are not allowed for a minimum. Thus, if we extend a minimum of SB to ST, we necessarily get an orbit with no internal reflections. According to Schanz [32], there is exactly one such orbit, which is the minimum in ST. This proves the uniqueness of the (global) minimum of  $L_{\hat{W}}$  in SB.

These results allow us to use essentially the same algorithm as for the ST for the systematic search of periodic orbits of the SB. We need to extend the codes and the length functions to include a group element  $\hat{g}$ , and to modify the rules according to which we choose an admissible and lexically maximal code word  $\hat{W}$ . One also has to modify the computations of the monodromy matrix, as described in appendix J.

### 4.3 The properties and statistics of the set of periodic orbits

The algorithm described above is capable of finding all of the periodic orbits up to any desired length. Before discussing the properties of this set, we find it appropriate to display a few typical periodic orbits, which were computed for the desymmetrized billiard with  $R = 0.2$  (and  $S = 1$ ). The orbits are represented in an unfolded way in figures 16–19.

In this subsection we shall study in detail the spectrum of lengths of periodic orbits, a small interval thereof is shown in figure 20. Each horizontal strip provides the lower end of the length spectrum of Sinai billiards with  $0.02 \leq R \leq 0.36$ . The spectrum corresponding to the lowest value of  $R$  shows clustering of the lengths near the typical distances of points of the  $\mathbb{Z}^3$  lattice  $(1, \sqrt{2}, \sqrt{3}, 2, \dots)$ . Once  $R$  is increased, some of the periodic orbits which were allowed for the smaller  $R$  are decimated because of the increased effect of shadowing. However, their lengths become shorter, resulting in the proliferation of the periodic orbits with their length. This is best seen in the spectrum which corresponds to the largest value of  $R$  — the graphics is already not sufficiently fine to resolve the individual lengths.

After these introductory comments, we now study the length spectrum in detail, and compare the theoretical expectations with the numerical results. The exponential proliferation of the periodic orbits puts a severe limit on the length range which we could access with our finite computer resources. However, we were able to compute the periodic orbits for a few values of the radius  $R$ , and concentrated on the  $R = 0.2$  case in order to be able to perform a semiclassical analysis of the longest quantal spectrum (see next section). For this radius we found all the 586,965 periodic orbits up to length 5. This number of periodic orbits includes repetitions and time-reversed conjugates. We also computed for this radius all the 12,928,628 periodic orbits up to length 10 which have no more than 3 reflections. This comprises the database on which we based our further numerical studies and illustrations. The systematic algorithm which was used to produce this data set, together with a few tests which will be described here and in the next section, lead us to believe that the data set is both accurate and complete.

Periodic orbits are expected to proliferate exponentially (e.g., [2]). That is, the number  $N_{\text{len}}(l)$  of periodic orbits of length less than  $l$  should approach asymptotically [2]:

$$N_{\text{len}}(l) \approx \frac{\exp(\lambda l)}{\lambda l}, \quad l \rightarrow \infty, \quad (63)$$

where  $\lambda$  is the topological entropy (per unit length). To examine the validity of

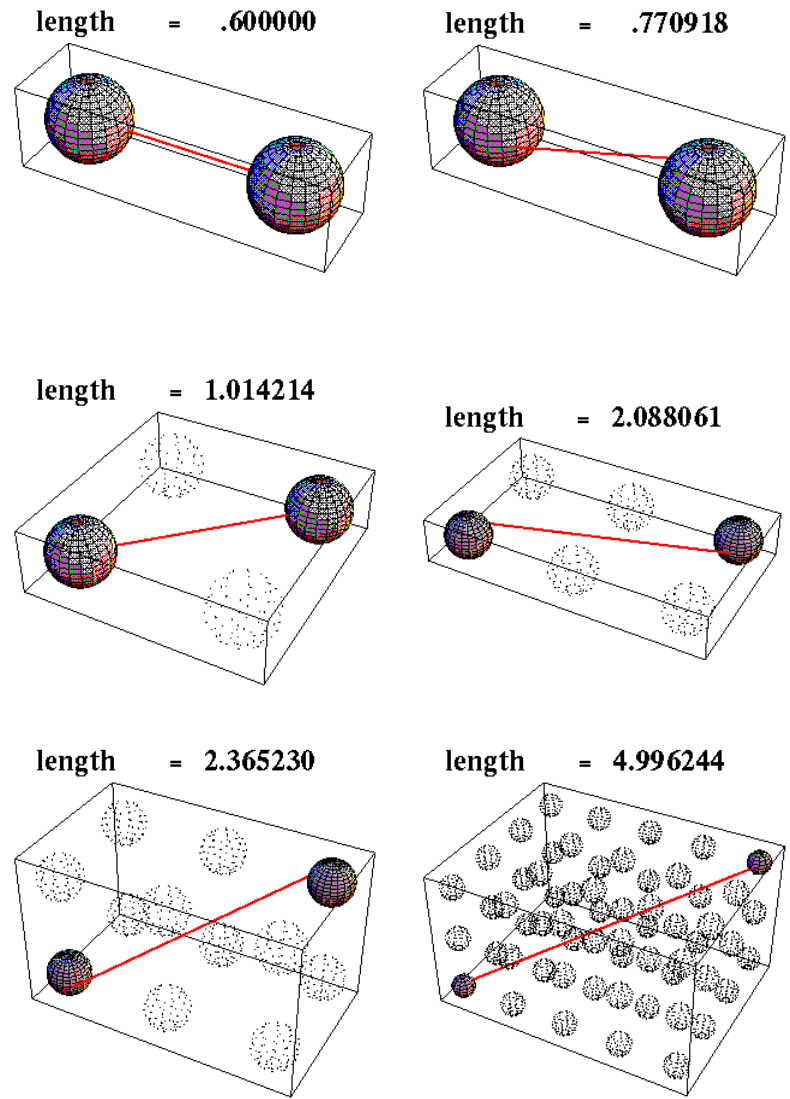


Figure 16: A sample of periodic orbits of the desymmetrized 3D Sinai billiard with  $S = 1$ ,  $R = 0.2$  with a single reflection. The periodic orbits are shown in the unfolded representation. The “full” spheres are those from which the periodic orbit reflects. The “faint” dotted spheres are those from which there is no reflection.

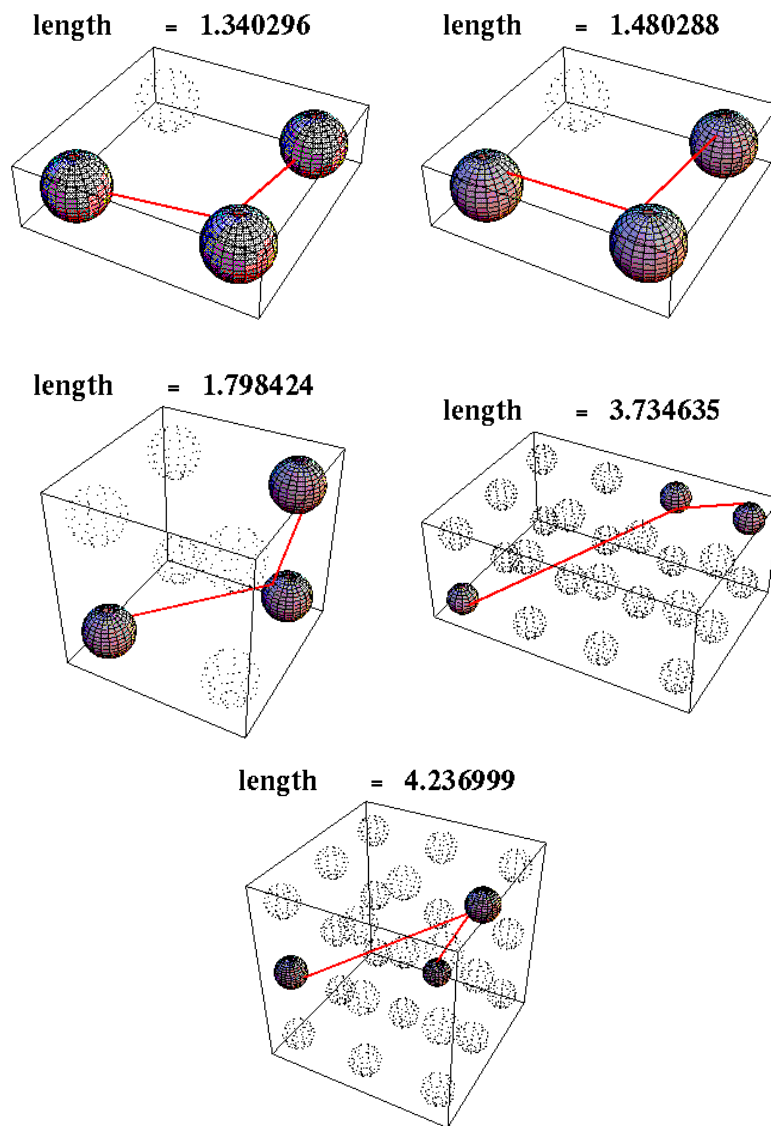


Figure 17: A sample of periodic orbits of the 3D SB with 2 reflections.

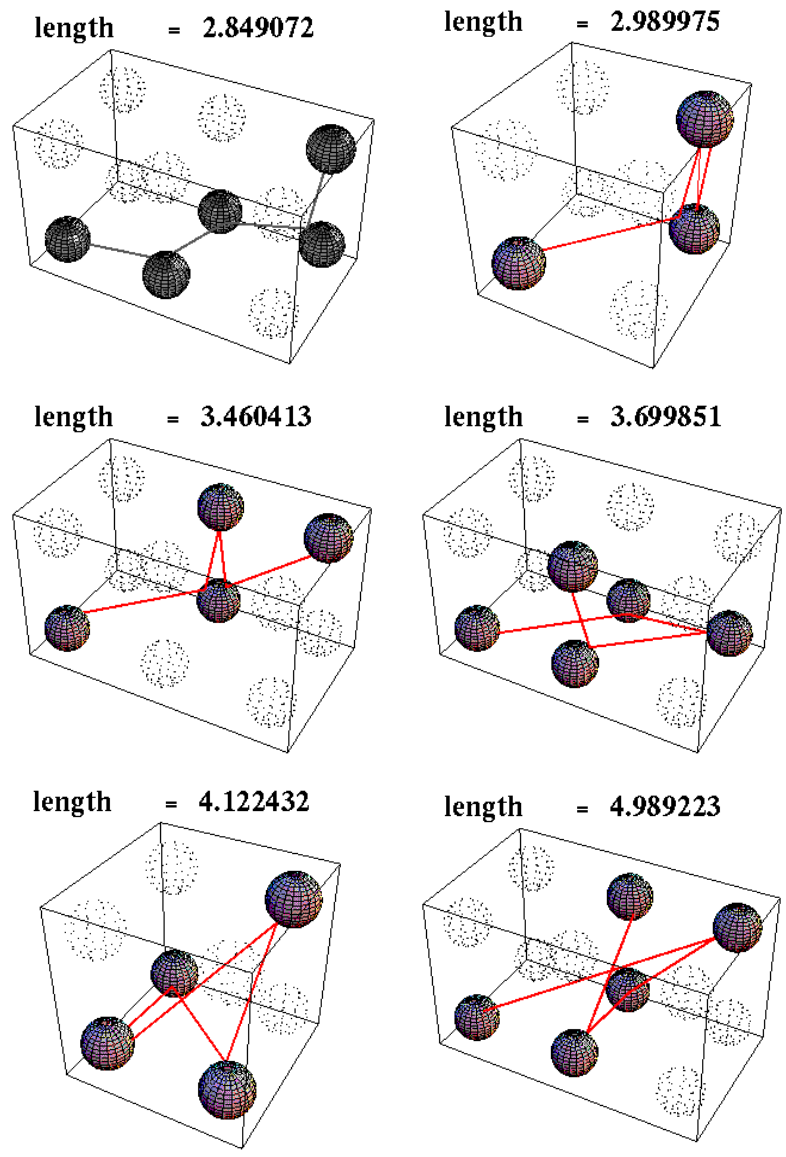
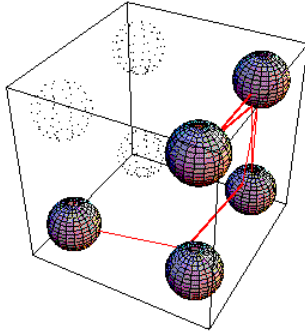
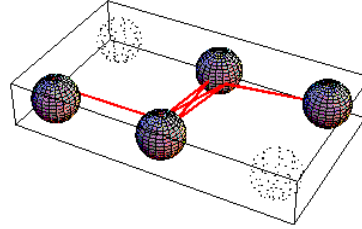


Figure 18: A sample of periodic orbits of the 3D SB with 4 reflections.

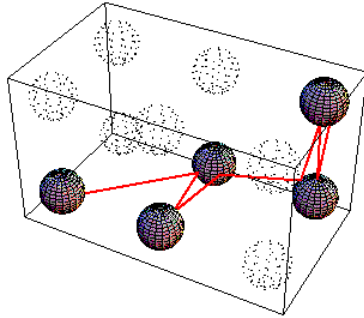
length = 4.626712



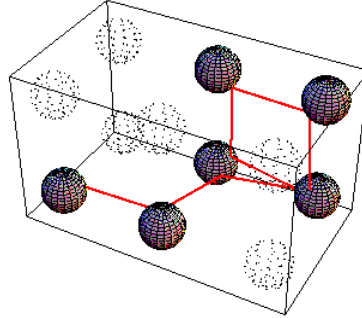
length = 4.766563



length = 4.968249



length = 4.999978



length = 4.943742

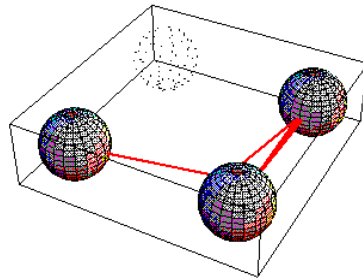


Figure 19: A sample of periodic orbits of the 3D SB with 7 reflections. The bottom periodic orbit undergoes 8 reflections.

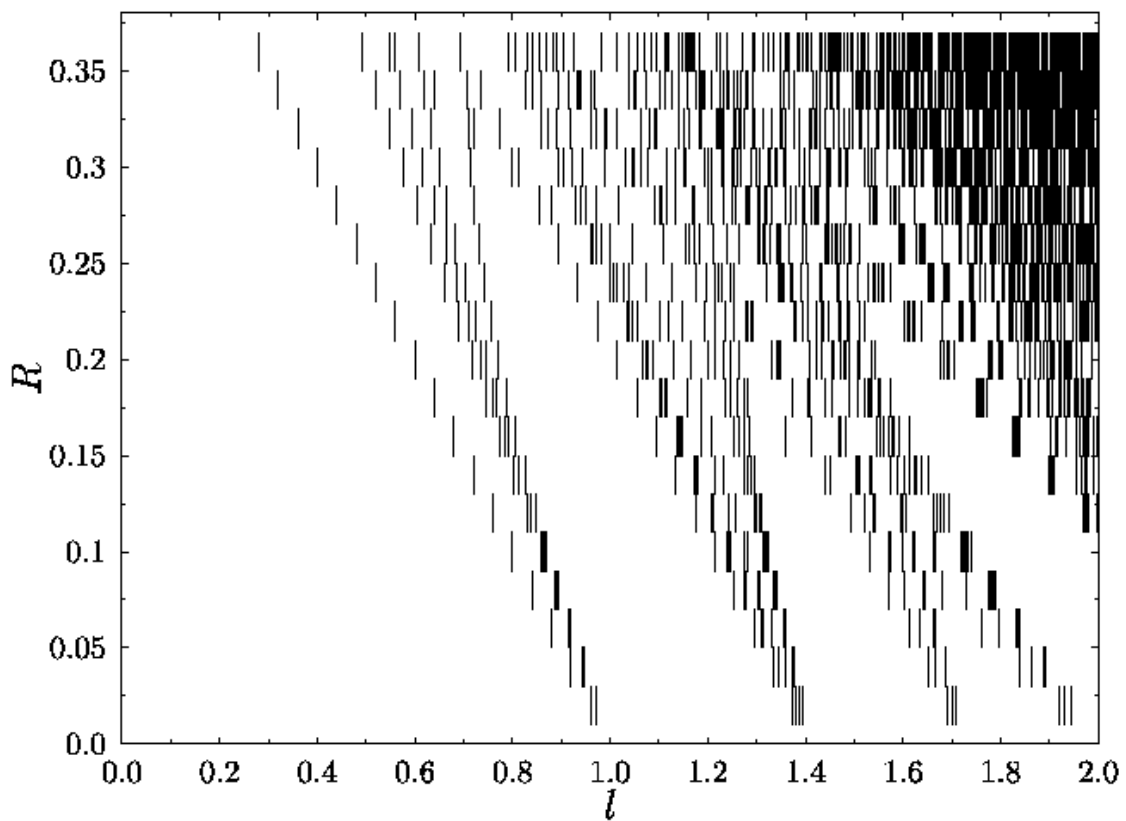


Figure 20: Length spectra of periodic orbits for Sinai billiards with  $R$  values between 0.02 and 0.36 in steps of  $\Delta R = 0.02$ . The vertical bars indicate the lengths of periodic orbits.

the above formula in our case we use the numerical data to compute:

$$\lambda_{\text{num}}(l) \equiv \frac{1}{l} \ln \left( \sum_{L_{\text{erg}} \leq L_j \leq l} L_j \right), \quad (64)$$

where  $L_{\text{erg}}$  is a length below which we do not expect universality (i.e, the law (63)) to hold. The exponential proliferation implies:

$$\lambda_{\text{num}}(l) \approx \frac{1}{l} \ln |e^{\lambda l} - e^{\lambda L_{\text{erg}}}| - \frac{\ln \lambda}{l} \rightarrow \lambda, \quad l \rightarrow \infty. \quad (65)$$

Therefore, we expect  $\lambda_{\text{num}}(l)$  to approach a constant value  $\lambda$  when  $l$  is sufficiently larger than  $L_{\text{erg}}$ . In figure 21 we show the results of the numerical computation of  $\lambda_{\text{num}}$  for the  $R = 0.2$  database and for  $L_{\text{erg}} = 2.5$ . The figure clearly indicates a good agreement between the data and the theory (65) for  $\lambda = 3.2$ .

One of the hallmarks of classically ergodic systems is the balance between the proliferation of periodic orbits and their stability weights due to ergodic coverage of phase space. This is a manifestation of the uniform coverage of phase space and is frequently referred to as the ‘‘Hannay – Ozorio de Almeida sum rule’’ [71]. It states that:

$$p(l) \equiv \sum_{\text{PO}} \frac{L_p}{|\det(I - M_j)|} \delta(l - L_j) \rightarrow 1, \quad l \rightarrow \infty, \quad (66)$$

where  $L_p$  is the primitive length and  $M_j$  is the stability (monodromy) matrix [2] (see appendix J for explicit expressions). The above relation is meaningful only after appropriate smoothing. For generic billiards the only classical length scale is the typical length traversed between reflections, and we expect (66) to approximately hold after a few reflections. In the Sinai billiard we are faced with the problem of an ‘‘infinite horizon’’, that is, that the length of free flight between consecutive reflections is unbounded. This is just another manifestation of the existence of the bouncing–ball families. According to [39, 40] this effect is responsible for a non-generic power–law tail in  $p(l)$ :

$$p(l) \approx 1 - \frac{\alpha(R)}{l}, \quad (67)$$

where  $\alpha(R)$  is a parameter that depends on the radius  $R$ . When  $R$  increases the influence (measure in configuration space) of the bouncing–balls is reduced, and we expect  $\alpha(R)$  to decrease. To check (67) we computed numerically the cumulant:

$$P(l) = \int_{L_{\text{erg}}}^l dl' p(l') \approx \sum_{L_{\text{erg}} \leq L_j \leq l} \frac{L_p}{|I - M_j|}, \quad (68)$$



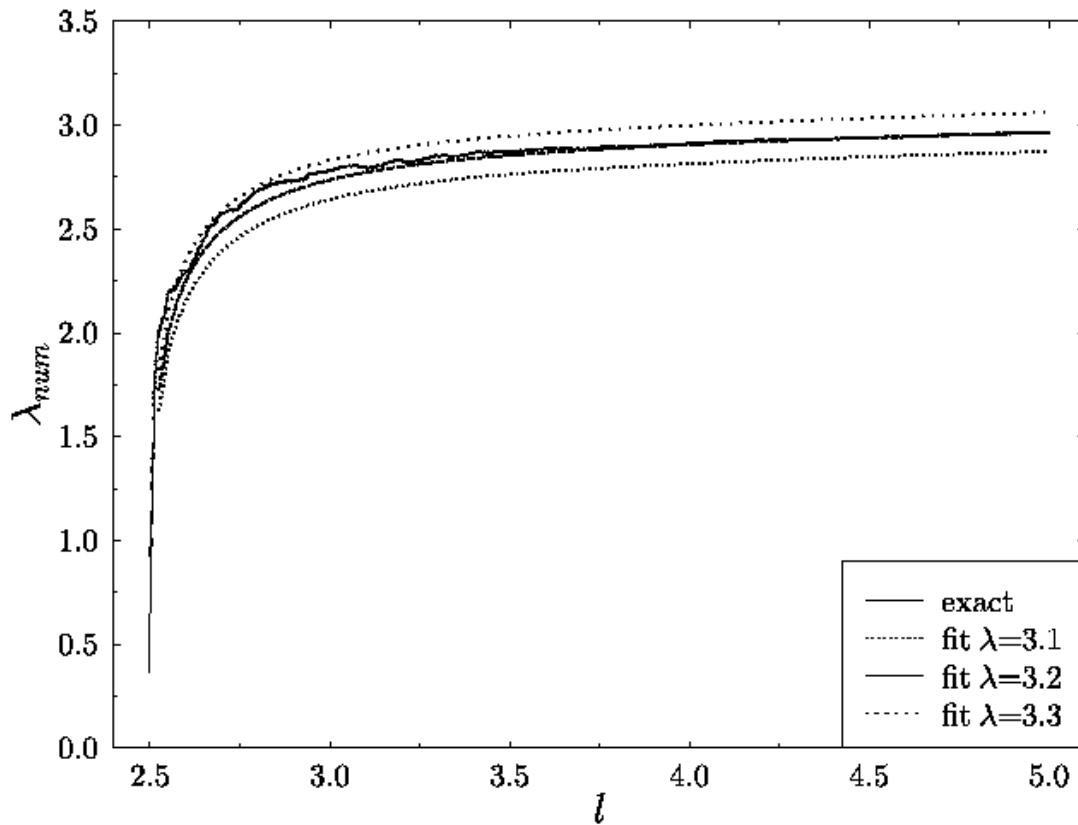


Figure 21: The quantity  $\lambda_{\text{num}}$  (c.f. RHS of equation (64)) computed from the periodic orbit database of  $R = 0.2$ . We used  $L_{\text{erg}} = 2.5$ . The theoretical fit is according to equation (65).

which should be compared to the theoretical expectation:

$$P(l) = (l - L_{\text{erg}}) - \alpha(R) \ln \left( \frac{l}{L_{\text{erg}}} \right). \quad (69)$$

The results are shown in figure 22. We considered  $R = 0.2$  and  $0.3$  and included periodic orbits up to  $L_{\text{max}} = 10$  with number of reflections  $n \leq 3$ . The restriction on  $n$  facilitates the computation and is justified for moderate values of  $l$  since the contributions from higher  $n$ 's are small. The observed deviation between the theoretical and numerical curves for  $R = 0.3$  at  $l \gtrsim 8$  is due to the fact that periodic orbits with  $n = 4$  become significant in this region. The above numerical tests confirm the validity of (67), with  $\alpha(R)$  which is a decreasing function of  $R$ . In particular, for the length interval considered here, there is a significant deviation from the fully ergodic behavior (66).

The sum-rule (66) which formed the basis of the previous analysis is an expression of the ergodic nature of the billiards dynamics. In the next subsection we shall make use of similar sum-rules which manifest the ergodicity of the Poincaré map obtained from the billiard flow by, e.g., taking the surface of the sphere and the tangent velocity vector as the Poincaré section. The resulting return-map excludes the bouncing-ball manifolds since they do not intersect the section. However, their effect is noticed because between successive collisions with the sphere the trajectory may reflect off the planar faces of the billiard an arbitrary number of times. Thus, the number of periodic orbits which bounce  $n$  times off the sphere ( $n$ -periodic orbits of the map) is unlimited, and the topological entropy is not well defined. Moreover, the length spectrum of  $n$ -periodic orbits is not bounded. These peculiarities, together with the fact that the symbolic code of the map consists of an infinite number of symbols, are the manifestations of the infinite horizon of the unfolded Sinai billiard. The return map itself is discontinuous but it remains area preserving, so the formulas which we use below, and which apply to generic maps, can be used here as well.

The classical return probability is defined as the trace of the  $n$ -step classical evolution operator (see, e.g., [72] and references therein). It is given by:

$$U(n) \equiv \sum_{j \in \mathcal{P}_n} \frac{n_{p,j}}{|\det(I - M_j)|}, \quad (70)$$

where  $n$  is the number of times the periodic orbit reflects from the sphere,  $\mathcal{P}_n$  is the set of all  $n$ -periodic orbits,  $n_{p,j}$  is the period of the primitive periodic orbit of which  $j$  is a repeated traversal. As a consequence of the ergodic nature of the map  $U(n) \rightarrow 1$  in the limit  $n \rightarrow \infty$ . However, due to the effect of the infinite horizon, the number of periodic orbits in  $\mathcal{P}_n$  is infinite, and in any numerical simulation it is important to check to what degree the available data set satisfies the sum rule. For this purpose we define the function:

$$U(l; n) \equiv \sum_{j \in \mathcal{P}_n} \frac{n_{p,j}}{|\det(I - M_j)|} \Theta(l - L_j), \quad (71)$$

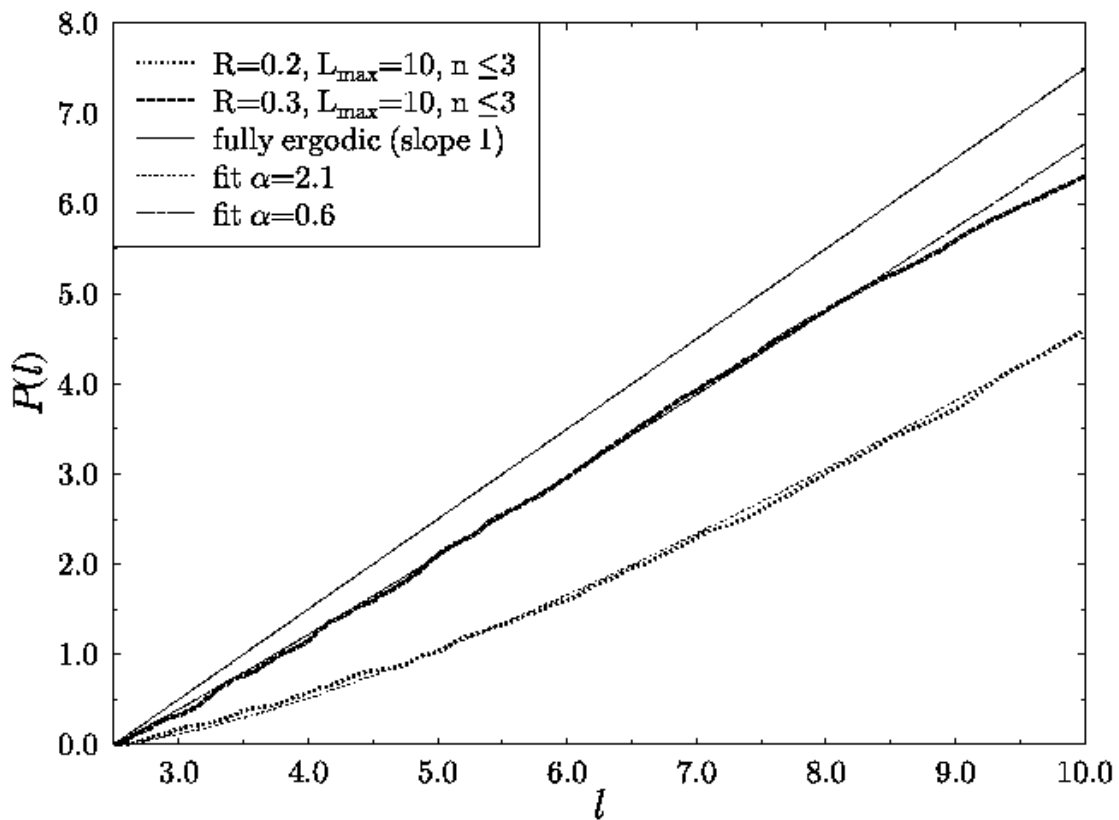


Figure 22: The function  $P(l)$  (c.f. RHS of equation (68)) computed for  $R = 0.2$  and  $0.3$  and fitted according to equation (69). We also show the asymptotic prediction (66).

which takes into account only  $n$ -periodic orbits with  $L_j \leq l$ . In figure 23 we plot  $U(l; n)$  for  $R = 0.4$  and  $n = 1, 2, 3$ . The results clearly indicate that for the present data saturation is reached, and once  $n \geq 2$  the asymptotic value is very close to 1. Even at  $n = 1$  one gets  $U(n = 1) \approx 0.8$  which is surprisingly close to 1, bearing in mind that we are dealing with the fixed points of the map! It should be noted that to reach saturation in the case  $R = 0.4$ ,  $n = 3$  one needs 536,379 periodic orbits up to  $l = 12$ , whose computation consumes already an appreciable amount of time. Thus, we are practically restricted to the few lowest  $n$ 's in our computations. As can be seen in figure 23 the function  $\partial U(l; n)/\partial l$  is mostly supported on a finite interval of  $L$  values. Its width will be denoted by  $\Delta L(n)$ .

#### 4.4 Periodic orbit correlations

In the previous subsection we discussed various aspects of the one-point statistics of the classical periodic orbits, and demonstrated their consistency with the standard results of ergodic theory. Here, we shall probe the length spectrum further, and show that this spectrum is not Poissonian. Rather, there exist correlations between periodic orbits which have far-reaching effects on the semiclassical theory of spectral statistics of the quantum billiard. The semiclassical theory will be dealt with in section 7, and here we restrict ourselves to purely classical investigations.

Above we introduced the Poincaré return map of the sphere, and have shown that the ergodicity of this map implies a sum rule for the set of  $n$ -periodic orbits of the map. We define the weighted density of lengths of  $n$ -periodic orbits as follows:

$$d_{\text{cl}}(l; n) \equiv \sum_{j \in \mathcal{P}_n} \tilde{A}_j \delta(l - L_j), \quad (72)$$

where  $\tilde{A}_j$  are given by:

$$\tilde{A}_j = \frac{n_{p,j} (-1)^{b_j}}{|\det(I - M_j)|^{1/2}}, \quad (73)$$

where  $b_j$  is the number of times the trajectory reflects from the planar boundaries. The amplitudes  $\tilde{A}_j$  are related to the standard semiclassical amplitudes  $A_j$  defined in (99) by  $\tilde{A}_j = \pi n \sigma_j A_j / L_j$ .

The density (72) is different from the density  $p(l)$  defined previously (66) since: (a) it relates to the subset of the  $n$ -periodic orbits of the return map of the sphere, (b) it assigns a signed weight to each of the  $\delta$ -functions located at a particular length, and (c) the absolute value of the weights in (72) are the square roots of the weights in (66). Densities with signed weights are not encountered frequently in spectral theory, but they emerge naturally in the present context. At this point the definition of  $d_{\text{cl}}(l; n)$  might look unfamiliar and strange, but the reason for this particular choice will become clear in the sequel.

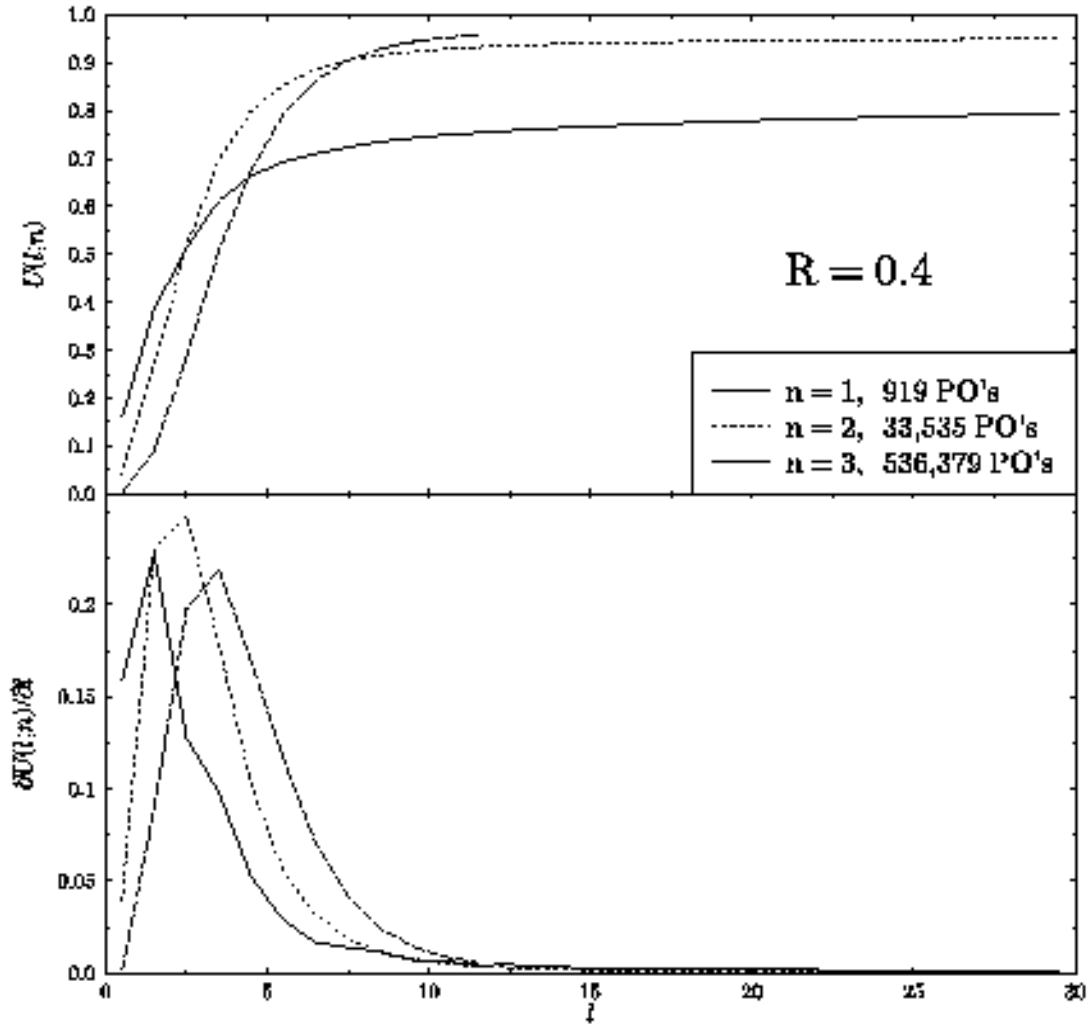


Figure 23: Upper plot: The function  $U(l; n)$  (c.f. equation (71)) for the cases  $R = 0.4$ ,  $n = 1, 2, 3$ . Lower plot: The function  $\partial U(l; n)/\partial l$  for the same cases. Both plots indicate the saturation of the classical return probability in spite of the infinitely many periodic orbits in  $\mathcal{P}_n$ .

To examine the possible existence of correlations in the length spectrum, we study the corresponding autocorrelation function:

$$R_{\text{cl}}(\delta l; n) \equiv \int_0^\infty dl d_{\text{cl}}(l + \delta l/2; n) d_{\text{cl}}(l - \delta l/2; n). \quad (74)$$

The two-point form factor is the Fourier transform of  $R_{\text{cl}}(\delta l; n)$ , and it reads explicitly as:

$$K_{\text{cl}}(k; n) = \int_{-\infty}^{+\infty} e^{ikx} R_{\text{cl}}(x; n) dx = \left| \sum_{j \in \mathcal{P}_n} \tilde{A}_j \exp(ikL_j) \right|^2. \quad (75)$$

The form factor has the following properties:

- $K_{\text{cl}}(k; n)$  is a Fourier transform of a distribution and therefore it displays fluctuations, which become stronger as the number of contributing orbits increases. Therefore, any discussion of this function requires some smoothing or averaging. We shall specify the smoothing we apply in the sequel.
- At  $k = 0$ ,

$$K_{\text{cl}}(0; n) = \left| \sum_{j \in \mathcal{P}_n} \tilde{A}_j \right|^2. \quad (76)$$

Because of the large number of periodic orbits, the sum of the signed amplitudes is effectively reduced due to mutual cancellations. Its value can be estimated by assuming that the signs are random. Hence,

$$K_{\text{cl}}(0; n) \approx \sum_{j \in \mathcal{P}_n} \left| \tilde{A}_j \right|^2, \quad (77)$$

which will be shown below to be bounded.

- At large values of  $k$ ,

$$K_{\text{cl}}(k; n) \approx \sum_{j \in \mathcal{P}_n} g_j \left| \tilde{A}_j \right|^2, \quad \text{for } k \rightarrow \infty, \quad (78)$$

where  $g_j$  is the number of isometric periodic orbits of length  $L_j$ . Since large fluctuations are endemic to the form factor, this relation is meaningful when  $k$ -averaging is applied. Comparing the last sum with (70) we can write:

$$K_{\text{cl}}(k; n) \approx \langle n_{p,j} g_j \rangle U(n), \quad \text{for } k \rightarrow \infty. \quad (79)$$

In our case of the 3D SB,  $n_{p,j} = n$  for the large majority of the periodic orbits in  $\mathcal{P}_n$ , which is the generic situation for chaotic systems. Also,  $g_j = 2$  for almost all the periodic orbits with  $n \geq 3$ . Thus, one can safely replace  $\langle n_{p,j} g_j \rangle$  with  $2n$  for large  $n$ . Moreover, as we saw above,  $U(n) \rightarrow 1$  for large  $n$ , hence  $K_{\text{cl}} \rightarrow 2n$  for large  $k$  and  $n$ .

- If the length spectrum as defined above were constructed by a random sequence of lengths with the same smooth counting function  $U(l; n)$ , or if the phases were picked at random, one would obtain the Poisson behavior of the form factor, namely, a constant:

$$K_{\text{cl}}(k; n) \approx \langle n_p g_p \rangle U(n) , \quad \text{for } k > \frac{2\pi}{\Delta L(n)} . \quad (80)$$

Here,  $\Delta L(n)$  is the effective width of the length distribution defined above.

Thus, we could identify two–point correlations in the classical length spectrum by computing  $K_{\text{cl}}(k; n)$  and observing deviations from the  $k$ -independent expression (80).

#### 4.4.1 Numerical tests

We used the periodic orbit database at our disposal to compute the form factors for several values of  $n$  and  $R$ . In each case presented we made sure that the function  $U(l; n)$  is numerically saturated. This guarantees that the (infinitely many) neglected periodic orbits have very small weight, and are thus insignificant.

In figure 24 we present the numerical results, where we plotted the function:

$$C_{\text{cl}}(k; n) \equiv \frac{1}{k - k_{\text{min}}} \int_{k_{\text{min}}}^k dk' K_{\text{cl}}(k'; n) , \quad (81)$$

designed to smooth the fluctuations in  $K_{\text{cl}}(k; n)$  [11]. We started the integration at  $k_{\text{min}} > 0$  to avoid the large peak near  $k = 0$ , which otherwise overwhelms the results. In any case, the neglected small- $k$  region is irrelevant for the semiclassical theory of quantal spectral correlations. Analyzing the results, we note that the asymptotic form factors (denoted as “Full classical form factor”) approach constant values, which are indeed close to  $2n$ , as predicted. More importantly, the deviations from the constant (Poissonian) result at low  $k$  demonstrate unambiguously the *existence of correlations* in the classical spectra. The structure of the form factor indicates that the classical spectrum is rigid on the scale of a correlation length  $\lambda(n; R)$ , which can be defined as the inverse of the  $k$  value at which the form factor makes its approach to the asymptotic value [11]. In the following we shall describe a few tests which prove that the observed correlations are real, and not a numerical artifact or a trivial consequence of the way in which the length spectral density is defined.

The spectral density  $d_{\text{cl}}(l; n)$  has an effective finite width  $\Delta L(n)$  which was defined above. The fact that the lengths are constrained to this interval induces trivial correlations which appear on the scale  $\Delta L(n)$ , and we should check that this scale is sufficiently remote from the correlation scale  $\lambda(n; R)$ . To this end, and to show that the observed classical correlations are numerically significant, we scrambled the signs of the weights  $\tilde{A}_j$  by multiplying each of them with a

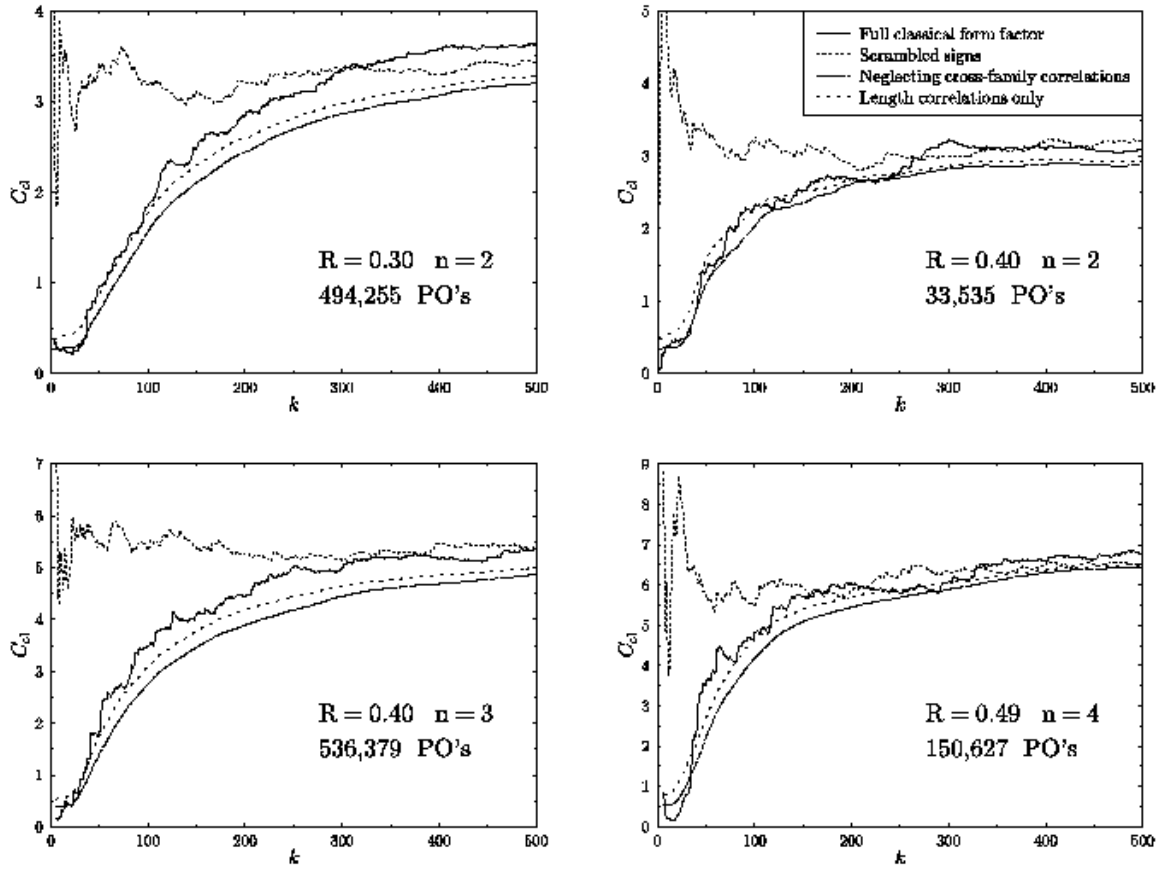


Figure 24: The averaged classical form factor  $C_{cl}(k; n)$  (c.f. (81)) of the 3D SB for several values of  $n$  and  $R$ . We also plot the averaged form factors with signs of the amplitudes scrambled, without cross-family terms, and with amplitudes averaged over family (length-correlation only). See text for details.



randomly chosen sign. We maintained, however, the time-reversal symmetry by multiplying conjugates by the same sign. The resulting form factors, shown in figure 24 (denoted as “Scrambled signs”), are consistent with the Poissonian value  $2n$  for essentially all  $k$  values, and the difference between the scrambled and unscrambled data is large enough to add confidence to the existence of the classical correlations. This indicates also that the correlations are not due to the effective width of  $d_{\text{cl}}(l; n)$ , since both the scrambled and unscrambled data have the same effective width.

On the other extreme, one might suspect that the classical correlations are due to rigidity on the scale of one mean spacing between lengths of periodic orbits. This is certainly not the case, since the typical mean length spacing for the cases shown in figure 24 is  $10^{-3}$ – $10^{-4}$ , which implies a transition to the asymptotic value for much larger  $k$ -values than observed. We therefore conclude, that the correlation length  $\lambda(n; R)$  is *much larger* than the mean spacing between neighboring lengths. This is the reason why various studies of the length-spectrum statistics [60, 73] claimed that it is Poissonian. Indeed it is Poissonian on the scale of the mean spacing where these studies were conducted. The correlations become apparent on a very different (and much larger) scale, and there is no contradiction. The coexistence of a Poissonian behavior on the short length scales, and apparent rigidity on a larger scale was discussed and explained in [11]. It was suggested there that a possible way to construct such a spectrum is to form it as a union of  $N \gg 1$  statistically independent spectra, all having the same mean spacing  $\bar{\Delta}$ , and which show spectral rigidity on the scale of a single spacing. The combined spectrum with a mean spacing  $\bar{\Delta}/N$  will be Poissonian when tested on this scale, since the spectra are independent. However, the correlations on the scale  $\bar{\Delta}$  will persist in the combined spectrum. A simple example will illustrate this construction. Take a random (Poissonian) spectrum with a mean spacing 1. Generate a shifted spectrum by adding  $\bar{\lambda} \gg 1$  to each spectral point and combine the original and the shifted spectra to a single spectrum. On the scale 1 the combined spectrum is Poissonian. However, the fact that each spectral point is (rigidly) accompanied by another one, a distance  $\bar{\lambda}$  apart, is a correlation which will be apparent at the scale  $\bar{\lambda}$  only. We use this picture in our attempt to propose a dynamical origin of the length correlations.

#### 4.4.2 The dynamical origin of the correlations

As was already mentioned, the idea that periodic orbit correlations exist originates from the quantum theory of spectral statistics which is based on trace formulas. The classical correlations are shown to be a manifestation of a fundamental duality between the quantum and the classical descriptions [9, 11]. However, the effect is purely classical, and hence should be explained in classical terms, without any reference to the quantum mechanical analogue. The essential point is to find the classical origin of the partition of the periodic orbits to inde-

pendent and uncorrelated families, as was explained in the previous section. So far, all the attempts to find the classical roots of these correlations failed, and till now there is no universal theory which provides the classical foundations for the effect. For the Sinai billiard in 3D there seems to exist a physical–geometrical explanation, which is consistent with our data, and which is supported by further numerical tests.

Consider the Sinai billiard with a sphere with a vanishingly small radius. In this case, all the periodic orbits which are encoded by words  $W$  built of the same letters  $w_i$  are isometric, independently of the ordering of the letters or the attached symmetry element  $\hat{g}$ . This phenomenon can be clearly seen in the spectrum of lengths corresponding to  $R = 0.02$  in figure 20. In this case, it is clear that the spectrum of lengths is a union of “families” of periodic orbits, each family is characterized by a unique set of building blocks  $w_i$ , which are common to the family members. When the radius  $R$  increases and becomes comparable to the linear dimension of the billiard, the approximate isometry and the resulting correlations breaks down, and one should use a more refined and restrictive definition of a family. The aim is to find a partition to families which will restrict the membership in a family to the smallest set, without losing any of the correlation features. The most restrictive definition of a family in the present context will be to include all the periodic orbits which share the same  $W = (w_1, w_2, \dots, w_n)$  part of the code and have different admissible  $\hat{g}$  symmetry elements. Words which are built of the same letters but in a different order define different families. Since there are 48 possible  $\hat{g}$ ’s, each family consists of at most 48 members and will be denoted by  $\Omega(W)$ . It should also be noted that the signs of the weights  $\tilde{A}_j$  within a family do not change with  $R$  since they reflect the parity of  $\hat{g}$ . The partition of the set of periodic orbits in families is not particular to just a few orbits, but rather, is valid for the entire set. This partition is the proposed source of the correlations that were observed in the form factor. This concept is illustrated in figure 25, and graphic representations of two families are displayed in figure 26. The most outstanding feature which emerges from figure (26) is that the orbits occupy a very narrow volume of phase–space throughout most of their length, and they fan out appreciably only at a single sphere.

The above arguments suggest that the main source of correlations are the similarities of orbits within each family  $\Omega(W)$ . To test this argument we performed a numerical experiment, in which we excluded the inter–family terms of the form factor, leaving only the intra–family terms. This excludes family–family correlations and maintains only correlations within the families. The results are shown in figure 24 (denoted by “Neglecting cross–family contributions”). The obvious observation is that the form factors were only slightly affected, proving that periodic–orbit correlations do not cross family lines! Thus, the main source of correlations is within the families  $\Omega(W)$ . We mention that very similar results are obtained if inter–family sign randomization is applied instead of the exclusion of cross–terms. We note, that in most cases a periodic orbit and its time–reversal

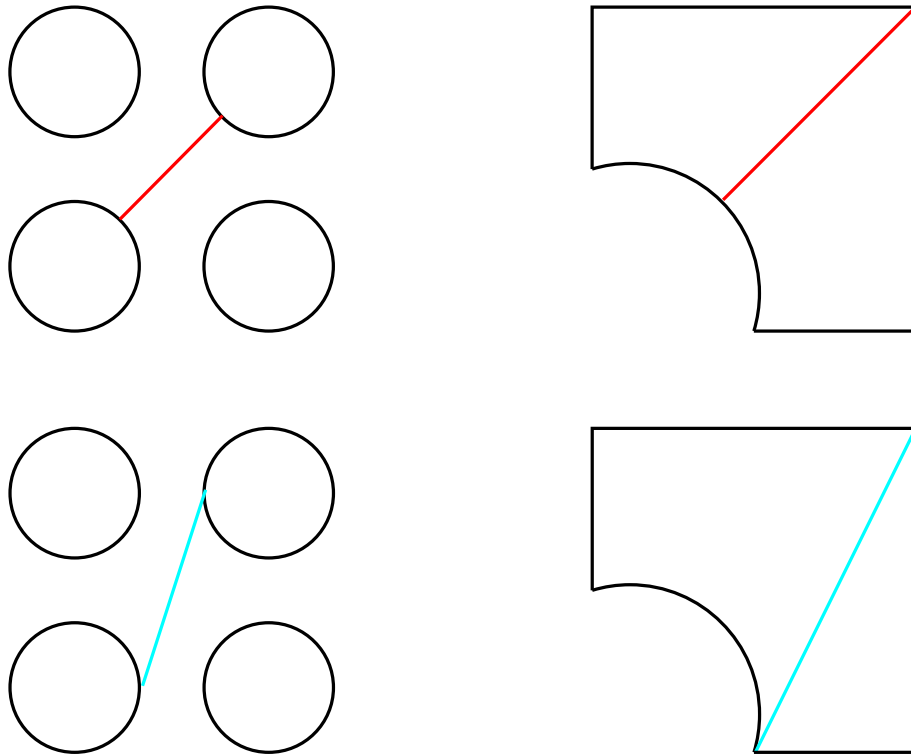
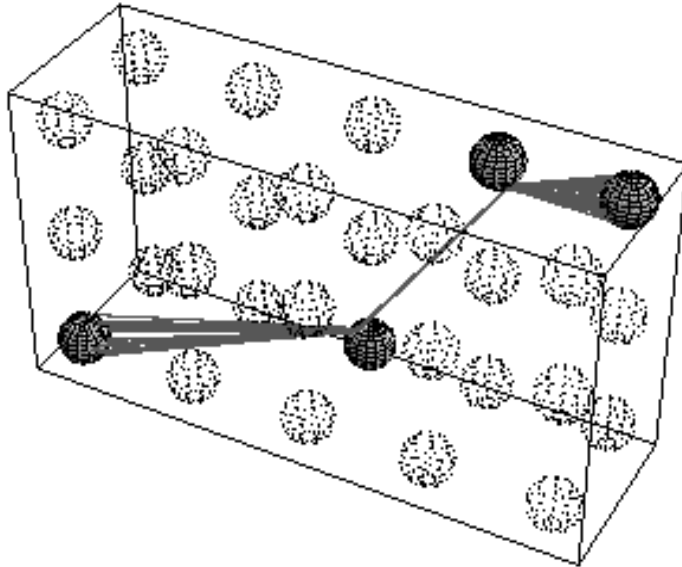


Figure 25: Two periodic orbits which are members of the same family of the quarter 2D SB. The two periodic orbits have the same  $W$ , hence they reflect off the same discs. But they correspond to two *different* symmetry elements, and hence are different. For simplicity the illustration is made for the 2D SB, but the same principle applies also to the 3D Sinai billiard. Left: Unfolded representation, right: Standard representation.

**R = 0.20 n = 3**  
**IFAM = 1000 #PO's = 46**  
**Length = 4.695204 :- 5.028641**



**R = 0.20 n = 6**  
**IFAM = 30000 #PO's = 24**  
**Length = 6.378634 :- 6.502746**

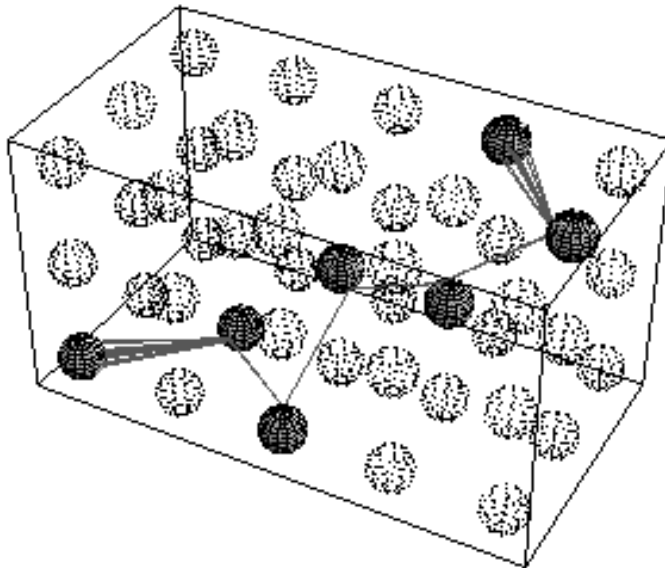


Figure 26: Two families of periodic orbits of the 3D SB, represented in the unfolded representation of the SB. The faint spheres do not participate in the code.

conjugate do not belong to the same family. Thus, neglecting the cross-family terms leads to partial breaking of time-reversal, which we compensated for by rectifying the intra-family form factor such that it will have the same asymptotic value as the full one.

It is interesting to check whether the correlations are due to the lengths or due to the size of the amplitudes. To examine that, we not only neglected the cross-family terms, but also replaced the amplitudes  $\tilde{A}_j$  within each family by constants multiplied by the original signs, such that the overall asymptotic contribution of the family does not change. The results are also plotted in figure 24 (denoted as “Length correlations only”). The resulting (rectified) form factors display slightly diminished correlations. However there is no doubt that almost all correlations still persist. This proves, that the correlations between the magnitudes of the weights play here a relatively minor role, and the correlations are primarily due to the lengths.

There are a few points in order. First, the numerical results presented here concerning the classical correlations are similar to those of reference [11]. However, here we considered the classical mapping rather than the flow, and this reduces the numerical fluctuations significantly. Using the mapping also enables the quantitative comparison to the semiclassical theory, which will be discussed in section 7. Second, it is interesting to enquire whether the average number of family members  $N_{\text{fam}}(n; R)$  increases or decreases with  $n$ . Since, if it decreases, our explanation of the origin of correlations becomes invalid for large  $n$ . The numerical results clearly indicate that  $N_{\text{fam}}(n; R)$ , computed as a weighted average with the classical weights, increases with  $n$ , which is encouraging. For example, for the case  $R = 0.4$  we obtained  $N_{\text{fam}} = 9.64, 18.31, 21.09, 28.31$  for  $n = 1, 2, 3, 4$ , respectively.

Thus, we were able to identify the grouping of orbits into “families” with the same code word  $W$  but with different symmetry  $\hat{g}$  as the prominent source of the classical correlations in the 3D Sinai billiard. In each family the common geometric part of the code  $W$  sets the mean length and the different group elements  $\hat{g}$  introduce the modulations. This pattern repeats for all the families, but the lengths of different families are not correlated. This finding conforms very well with the general scheme which was proposed to explain the typical correlations in the classical spectrum [9, 74]. However, a classical derivation of a quantitative expression for the correlations length  $\lambda$  is yet to be done.

#### 4.4.3 Length correlations in the 3-Torus

The ideas developed above about the correlations between periodic orbits in the fully chaotic billiard, have an analogue in the spectrum of lengths of periodic tori in the integrable case of the 3-torus. In section 3 we studied the quantum 3-torus of size  $S$  and showed in section 3.1.1 that due to number theoretical degeneracies, the quantum form factor is not Poissonian. The form factor displays a negative

(repulsive) correlation which levels off at  $\tau^* = 1/\gamma = 1/(2Sk)$ . This can be transcribed into an expression for the correlation length of the classical spectrum in the following way.

Expressing  $\tau^*$  in units of length we obtain:

$$L^* = 2\pi\bar{d}(k)\tau^* = \frac{S^2k}{2\pi}. \quad (82)$$

Consequently:

$$k^*(L) = \frac{2\pi L}{S^2}, \quad (83)$$

from which we read off

$$\lambda(L) = \frac{S^2}{L}. \quad (84)$$

Since the lengths of the periodic orbits are of the form  $L_j = S \times \sqrt{\text{integer}}$ , the minimal spacing between periodic orbits near length  $L$  is:

$$\Delta_{\min}(L) = \frac{S^2}{2L}, \quad (85)$$

and therefore

$$\lambda(L) = 2\Delta_{\min}(L). \quad (86)$$

In other words, the classical correlation length of the 3-torus coincides (up to a factor 2) with the minimal spacing between the periodic orbits. Therefore,  $\lambda(L)$  indeed signifies the correlation length scale between periodic orbits, which is imposed by their number-theoretical structure.

## 5 Semiclassical analysis

In the previous sections we accumulated information about the quantum spectrum and about the periodic orbits of the 3D Sinai billiard. The stage is now set for a semiclassical analysis of the billiard. We shall focus on the analysis of the semiclassical Gutzwiller trace formula [2] that reads in the case of the Sinai billiard:

$$d(k) \equiv \sum_{n=1}^{\infty} \delta(k - k_n) \approx \bar{d}(k) + d_{\text{bb}}(k) + \sum_{\text{PO}} A_j \cos(kL_j). \quad (87)$$

The quantum spectral density on the LHS is expressed as the sum of three terms. The term  $\bar{d}$  is the smooth density of states (see section I). The term  $d_{\text{bb}}$  consists of the contributions of the non-generic bouncing-ball manifolds. It contains terms of the form (31) with different prefactors (which are possibly 0) due to partial or complete shadowing of the bouncing-ball family by the sphere. The last term is the contribution of the set of generic and unstable periodic orbits, where  $L_j$  denote their lengths and  $A_j$  are semiclassical amplitudes. One of the main objective of the present work was to study the accuracy of (87) by a direct numerical computation of the difference between its two sides. This cannot be done by a straightforward substitution, since three obstacles must be removed:

- The spectrum of wavenumbers  $k_n$  was computed for the fully desymmetrized Sinai billiard. To write the corresponding trace formula, we must remember that the folding of the Sinai *torus* into the Sinai *billiard* introduces new types of periodic orbits due to the presence of symmetry planes, edges and corners. Strictly speaking, the classical dynamics of these orbits is singular, and becomes meaningful only if proper limits are taken. As examples we mention periodic orbits that bounce off a corner, or that are wholly confined to the symmetry planes. These periodic orbits are isolated and unstable, and should not be confused with the bouncing-ball families which are present both in the ST and in the SB. For periodic orbits that reflect from a corner but are not confined to symmetry planes, the difficulty is resolved by unfolding the dynamics from the SB to the ST as was described in the previous section. Periodic orbits which are confined to symmetry planes are more troublesome since there is more than one code word  $\hat{W}$  which correspond to the same periodic orbit. We denote the latter as “improper”. The 3D Sinai billiard is abundant with improper periodic orbits, and we cannot afford treating them individually as was done e.g. by Sieber [60] for the 2D hyperbola billiard. Rather, we have to find a general and systematic method to identify them and to calculate their semiclassical contributions. This will be done in the next subsection. (The semiclassical contributions of the improper periodic manifolds for the integrable case  $R = 0$  were discussed in section 3.1).

- As it stands, equation (87) is a relation between *distributions* rather than between *functions*, and hence must be regulated when dealing with actual computations. Moreover, even though our quantum and classical databases are rather extensive, the sums on the two sides of the equation can never be exhausted. We overcome these problems by studying the weighted “length spectrum” obtained from the trace formula by a proper smoothing and Fourier-transformation. It is defined in subsection 5.2.
- Finally, we must find ways to rid ourselves from the large, yet non-generic contributions of the bouncing–ball families. This was achieved using rather elegant tricks which are described in subsections 5.4, 5.5 below.

## 5.1 Semiclassical desymmetrization

To derive the spectral density of the desymmetrized Sinai billiard we make use of its expression in terms of the (imaginary part of the) trace of the SB Green function. This Green function satisfies the prescribed boundary conditions on all the boundaries of the fundamental domain, and the trace is taken over its volume. In the following we shall show how to transform this object into a trace over the volume of the entire ST, for which all periodic orbits are proper (no symmetry planes). This will eliminate the difficulty of treating the improper orbits. To achieve this goal we shall use group–theoretical arguments [31, 60, 75, 76, 77]. The final result is essentially contained in [78].

When desymmetrizing the ST into SB, we have to choose one of the irreps of  $O_h$  to which the eigenfunctions of the SB belong (see section 2.2.3). We denote this irrep by  $\gamma$ . We are interested in the trace of the Green function of the SB over the volume of the SB which is essentially the density of states:

$$T \equiv \text{Tr}_{\text{SB}} G_{\text{SB}}^{(\gamma)}(\vec{r}, \vec{r}'). \quad (88)$$

One can apply the projection operation [31] and express  $G_{\text{SB}}^{(\gamma)}$  using the Green function of the ST:

$$G_{\text{SB}}^{(\gamma)}(\vec{r}, \vec{r}') = \frac{1}{l_\gamma} \sum_{\hat{g} \in O_h} \chi^{(\gamma)*}(\hat{g}) G_{\text{ST}}(\vec{r}, \hat{g}\vec{r}'), \quad (89)$$

where  $\chi^{(\gamma)}(\hat{g})$  is the character of  $\hat{g}$  in the irrep  $\gamma$  and  $l_\gamma$  is the dimension of  $\gamma$ . It can be verified that the above  $G_{\text{SB}}$  satisfies the inhomogeneous Helmholtz equation with the correct normalization, and it is composed only of eigenfunction that transform according to  $\gamma$ . Thus:

$$T = \frac{1}{l_\gamma} \sum_{\hat{g} \in O_h} \chi^{(\gamma)*}(\hat{g}) \text{Tr}_{\text{SB}} G_{\text{ST}}(\vec{r}, \hat{g}\vec{r}'). \quad (90)$$



To relate  $\text{Tr}_{\text{SB}}$  with  $\text{Tr}_{\text{ST}}$  we use the relation:

$$G_{\text{ST}}(\vec{r}, \vec{r}') = G_{\text{ST}}(\hat{h}\vec{r}, \hat{h}\vec{r}') \quad \forall \hat{h} \in O_h \quad (91)$$

which can be proven by e.g. using the spectral representation of  $G_{\text{ST}}$ . In particular, we can write:

$$G_{\text{ST}}(\vec{r}, \vec{r}') = \frac{1}{48} \sum_{\hat{h} \in O_h} G_{\text{ST}}(\hat{h}\vec{r}, \hat{h}\vec{r}'). \quad (92)$$

Combining (92) with (90) we get:

$$\begin{aligned} T &= \frac{1}{48l_\gamma} \sum_{\hat{g}, \hat{h} \in O_h} \chi^{(\gamma)*}(\hat{g}) \text{Tr}_{\text{SB}} G_{\text{ST}}(\hat{h}\vec{r}, \hat{h}\hat{g}\vec{r}') \\ &= \frac{1}{48l_\gamma} \sum_{\hat{g}, \hat{h} \in O_h} \chi^{(\gamma)*}(\hat{h}\hat{g}\hat{h}^{-1}) \text{Tr}_{\text{SB}} G_{\text{ST}}(\hat{h}\vec{r}, (\hat{h}\hat{g}\hat{h}^{-1})\hat{h}\vec{r}') \\ &= \frac{1}{48l_\gamma} \sum_{\hat{h}, \hat{k} \in O_h} \chi^{(\gamma)*}(\hat{k}) \text{Tr}_{\text{SB}} G_{\text{ST}}(\hat{h}\vec{r}, \hat{k}\hat{h}\vec{r}'). \end{aligned} \quad (93)$$

To obtain the second line from the first one, we recall that the character is the trace of the irrep matrix, and we have in general  $\text{Tr}(ABC) = \text{Tr}(CAB)$ , therefore  $\chi(\hat{g}) = \chi(\hat{h}\hat{g}\hat{h}^{-1})$ . The third line is obtained from the second one by fixing  $\hat{h}$  and summing over  $\hat{g}$ . Since  $\hat{h}\hat{g}_1\hat{h}^{-1} = \hat{h}\hat{g}_2\hat{h}^{-1} \iff \hat{g}_1 = \hat{g}_2$  the summation over  $\hat{g}$  is a rearrangement of the group. We now apply the geometrical identity:

$$\sum_{\hat{h} \in O_h} \int_{\text{SB}} d^3r f(\hat{h}\vec{r}) = \int_{\text{ST}} d^3r f(\vec{r}) \quad (94)$$

to cast (93) into the desired form:

$$T = \frac{1}{48l_\gamma} \sum_{\hat{g} \in O_h} \chi^{(\gamma)*}(\hat{g}) \text{Tr}_{\text{ST}} G_{\text{ST}}(\vec{r}, \hat{g}\vec{r}'), \quad (95)$$

where we relabelled  $\hat{k}$  as  $\hat{g}$  for convenience. The result (95) is the desired one, since  $T$  is now expressed using traces over ST which involve no symmetry planes. Semiclassically, the formula (95) means that we should consider all the periodic orbits of the ST *modulo* a symmetry element  $\hat{g}$  to get the density of states of the SB. Therefore, the difficulty of handling improper orbits is eliminated, since in the ST all of the isolated periodic orbits are proper.

Let us elaborate further on (95) and consider the various contributions to it. A proper periodic orbit of the SB with code  $(W; \hat{g})$  has 48 realizations in the ST which are geometrically distinct. They are obtained from each other by applying

the operations of  $O_h$ . These conjugate periodic orbits are all related to the same  $\hat{g}$  and thus have the same lengths and monodromies. Consequently they all have the same semiclassical contributions. Hence, their semiclassical contribution to  $T$  is the same as we would get from naively applying the Gutzwiller trace formula to the SB, considering only proper periodic orbits. This result is consistent with our findings about classical desymmetrization (section 4.2 above). For the improper periodic orbits there is a difference, however. There are genuine semiclassical effects due to desymmetrization for unstable periodic orbits that are confined to planes or to edges, notably large reduction in the contributions for Dirichlet conditions on the symmetry planes.

To demonstrate this point, let us consider in some detail an example of the periodic orbit that traverses along the 8-fold edge  $AE$  in figure 1. For the ST (no desymmetrization) its semiclassical contribution is:

$$A_1 = \frac{R}{2\pi}. \quad (96)$$

For the SB there are 8 code words that correspond to the periodic orbit(s) which traverses along this 8-fold edge. A calculation yields for the semiclassical contribution:

$$A_8 = \frac{R}{8\pi} \left[ 2 \pm 2\sqrt{1-2\beta} \pm \beta \left( \frac{2-\beta}{1-\beta} \right) \right], \quad (97)$$

where  $\beta \equiv R/S$ . The upper sign is for the case of the totally symmetric irrep, and the lower one for the totally antisymmetric irrep. In the antisymmetric case we get for  $\beta \ll 1$ :

$$\frac{A_8}{A_1} \approx \left( \frac{\beta}{2} \right)^4, \quad (98)$$

which means that the desymmetrization *greatly reduces* the contribution of this periodic orbit in case of Dirichlet boundary conditions on the planes. For the case of our longest spectrum ( $R = 0.2$ ,  $S = 1$ ) this reduction factor is approximately  $2 \times 10^{-4}$  which makes the detection of this periodic orbit practically impossible. For Neumann boundary conditions the contribution is comparable to the ST case and is appreciable.

The formula (95) together with the algorithm described above are the basis for our computations of the semiclassical contributions of the periodic orbits of the SB. Specifically, the contribution of a code  $\hat{W}$  is given by:

$$A_{\hat{W}} = \frac{L_{\hat{W}}^{\text{po}} K_{\hat{W}} \chi^{(\gamma)*}(\hat{g}) \sigma_{\hat{W}}}{\pi l_{\gamma} r |\det(I - M_{\hat{W}})|^{1/2}}, \quad (99)$$

where  $L_{\hat{W}}^{\text{po}}$  is the length of the periodic orbit,  $K_{\hat{W}} = (\# \text{ of distinct realizations of } \hat{W} \text{ under } O_h)/48$  and  $r$  is the repetition index. The term  $\sigma_{\hat{W}}$  is due to the reflections from the spheres and is determined by the boundary conditions on them. For Neumann boundary conditions  $\sigma_{\hat{W}} = 1$ , for Dirichlet boundary conditions  $\sigma_{\hat{W}} = (-1)^n$ , where  $n$  is the number of bounces.

## 5.2 Length spectrum

Having derived the explicit expression for the semiclassical amplitudes for the SB (99), we are in position to transform the trace formula (87) to a form which can be used for numerical computations which test its validity. We define the *length spectrum* as the Fourier transform of the density of states:

$$D(l) \equiv \frac{1}{\sqrt{2\pi}} \int_{-\infty}^{+\infty} d(k) e^{ikl} dk = \frac{1}{\sqrt{2\pi}} \sum_n e^{ik_n l}. \quad (100)$$

For convenience we define  $d(-k) \equiv d(k) \implies k_{-n} = -k_n$  and the sum is carried out for all  $n \in \mathbb{Z} \setminus \{0\}$ . Using the trace formula (87) we obtain semiclassically:

$$D_{\text{sc}}(l) = \bar{D}(l) + D_{\text{bb}}(l) + \sum_{\text{PO}} \sqrt{\frac{\pi}{2}} A_j [\delta(l - L_j) + \delta(l + L_j)]. \quad (101)$$

In the above  $\bar{D}(l)$  is a singularity at  $l = 0$  which is due to the smooth density of states. The length spectrum is sharply peaked near lengths of periodic orbits hence its name. To regularize (101) such that it can be applied to finite samples of the quantum spectrum, we use a weight function and construct the weighted length spectrum [79]:

$$D^{(w)}(l; k) \equiv \frac{1}{\sqrt{2\pi}} \int_{-\infty}^{+\infty} w(k-k') d(k') e^{ik'l} dk' = \frac{1}{\sqrt{2\pi}} \sum_n w(k-k_n) e^{ik_n l} \quad (102)$$

where  $w$  is a weight function (with an effective finite support) that is concentrated at the origin. The corresponding semiclassical expression is:

$$D_{\text{sc}}^{(w)}(l; k) = \bar{D}^{(w)}(l) + D_{\text{bb}}^{(w)}(l) + \sum_{\text{PO}} \frac{A_j}{2} [\hat{w}(l - L_j) e^{ik(l-L_j)} + \hat{w}(l + L_j) e^{ik(l+L_j)}], \quad (103)$$

where  $\hat{w}(l) \equiv (1/\sqrt{2\pi}) \int_{-\infty}^{+\infty} w(k) e^{ikl} dk$  is the Fourier transform of  $w(k)$ .

In principle,  $d(k)$  and  $D(l)$  contain the same information and are therefore equivalent. However, for our purposes, it is advantageous to use the length spectrum  $D(l)$  (and in practice  $D^{(w)}(l; k)$ ) rather than the spectral density (87) for the following reasons:

- The regularized semiclassical length spectrum,  $D_{\text{sc}}^{(w)}$ , is absolutely convergent for suitably chosen windows [79] (e.g. Gaussians). This is in contrast with the original trace formula (87).
- There is an exact mathematical result [80] that states that for billiards the singular supports of  $D(l)$  and of  $D_{\text{sc}}(l)$  are the same, if the infinite spectra are considered. This exact quantum-classical result specifically relates to the length spectra. It is therefore useful to identify and treat transient effects (e.g. diffraction contributions) for finite spectra using the length coordinate.

- The trace formula (87) can be considered as a means to quantize a chaotic system, since it expresses the quantal density of states in terms of the classical length spectrum. However, in practice this is not convenient because the semiclassical amplitudes are only leading terms in asymptotic series in  $k$  (equivalently in  $\hbar$ ). For finite values of  $k$  there can be large deviations due to sub-leading corrections [6, 7] and also due to significant diffraction corrections [8, 81, 38]. Treating the trace formula the other way (“inverse quantum chaology”) is advantageous because the quantal amplitudes have all equal weights 1.
- The appearance of peaks in both  $d(k)$  and  $D(l)$  comes as a result of the constructive interference of many oscillatory contributions. Any missing or spurious contribution can blur the peaks (see figure 27 for an example with a single energy level missing). For the energy levels we have a good control on the completeness of the spectrum due to Weyl’s law (see section I). As discussed above, this is not the case for periodic orbits where we do not have an independent verification of their completeness. Hence it is advantageous to use the energy levels which are known to be complete in order to reproduce peaks that correspond to the periodic orbits.
- For the Sinai billiard the low-lying domain of the spectrum is peculiar due to effects of desymmetrization (see section 2.4). For Dirichlet boundary conditions on the planes, the levels  $k_n R < 9$  are very similar to those of the integrable case ( $R = 0$ ). The “chaotic” levels for which the semiclassical approximation is valid ( $k_n R > 9$ ) thus start higher up, which makes the semiclassical reproduction of them very difficult in practice even with the use of Berry–Keating resummation techniques [69]. On the other hand, using the quantum levels we can reproduce a few isolated length peaks, as will be seen in the sequel.

In the following we shall demonstrate a stringent test of the completeness and of the accuracy of the quantal spectrum using the length spectrum. Then we shall investigate the agreement between the quantal and the semiclassical length spectra. We shall employ a technique to filter the effects of the bouncing balls, such that only generic contributions remain.

### 5.3 A semiclassical test of the quantal spectrum

In the following we use the length spectrum in order to develop a stringent test of the completeness and integrity of the quantal spectrum. This supplements the integrity and completeness analysis of the quantal spectrum done in subsections 2.4–2.5. The idea is to focus on an isolated contribution to the length spectrum that can be compared to an analytical result. In section 3.1 we discussed the integrable billiard ( $R = 0$ ) and observed that there are contributions to the

density of states due to isolated but *neutral* periodic orbits. The shortest periodic orbit of this kind has length  $S/\sqrt{3} \approx 0.577S$  and was shown in figure 6. Its contribution must prevail for  $R > 0$  until it is shadowed by the inscribed sphere, which occurs at  $R = S/\sqrt{6} \approx 0.41S$ . Being the shortest bouncing ball, its length is distant from the other bouncing balls. As for the isolation from other generic periodic orbits, for  $R = 0.2$  there is a nearby contribution of the shortest unstable periodic orbit of length  $0.6S$ . However, for Dirichlet boundary conditions on the planes the latter is practically eliminated due to symmetry effects as was discussed in section 5.1. Since other periodic orbits are fairly distant, this shortest bouncing ball is an ideal test-ground of the length spectrum. Using (31) and a Gaussian window:

$$w(k - k') = \frac{1}{\sqrt{2\pi\sigma^2}} \exp \left[ -\frac{(k - k')^2}{2\sigma^2} \right], \quad (104)$$

one obtains the contribution of the shortest bouncing ball to the length spectrum:

$$D_{\text{sc,shortest-bb}}^{(w)}(l; k) = \frac{e^{ik(l-S/\sqrt{3})}}{(6\pi)^{3/2}} \exp \left[ -(l - S/\sqrt{3})^2 \sigma^2 / 2 \right]. \quad (105)$$

Due to its isolation, one expects that the shortest bouncing ball gives the dominant contribution to the length spectrum near its length. Thus, for  $l \approx S/\sqrt{3}$ , one has  $|D_{\text{sc}}^{(w)}| \approx |D_{\text{sc,shortest-bb}}^{(w)}|$ . The latter is independent of  $k$ . To test the above relation, we computed the quantal length spectrum  $D^{(w)}$  for  $R = 0$  and  $R = 0.2$  for two different values of  $k$ , and compared with (105). The results are shown in figure 27, and the agreement is very satisfactory.

To show how sensitive and stringent this test is, we removed from the  $R = 0.2$  quantal spectrum a *single* level,  $k_{1500} = 175.1182$ , and studied the effect on the length spectrum. As is seen in the figure, this is enough to severely damage the agreement between the quantum data and the theoretical expectation. Therefore we conclude that our spectrum is complete and also accurate to a high degree.

## 5.4 Filtering the bouncing-balls I: Dirichlet–Neumann difference

The final goal of our semiclassical analysis is to test the predictions due to Gutzwiller’s trace formula. Since the 3D Sinai is meant to be a paradigm for 3D systems, we must remove the influence of the non-generic bouncing-ball families and find a way to focus on the contributions of the generic and unstable periodic orbit. This is imperative, because in the 3D Sinai billiard the bouncing balls have contributions which are much larger than those of the generic periodic orbits. Inspecting equations (31) and (99), we find that the contributions of the leading-order bouncing balls are stronger by a factor of  $k$  than those of the generic periodic orbits. This is worse than in the 2D case, where the factor is  $\sqrt{k}$ . To show how overwhelming is the effect of the bouncing balls, we plot in figure 28

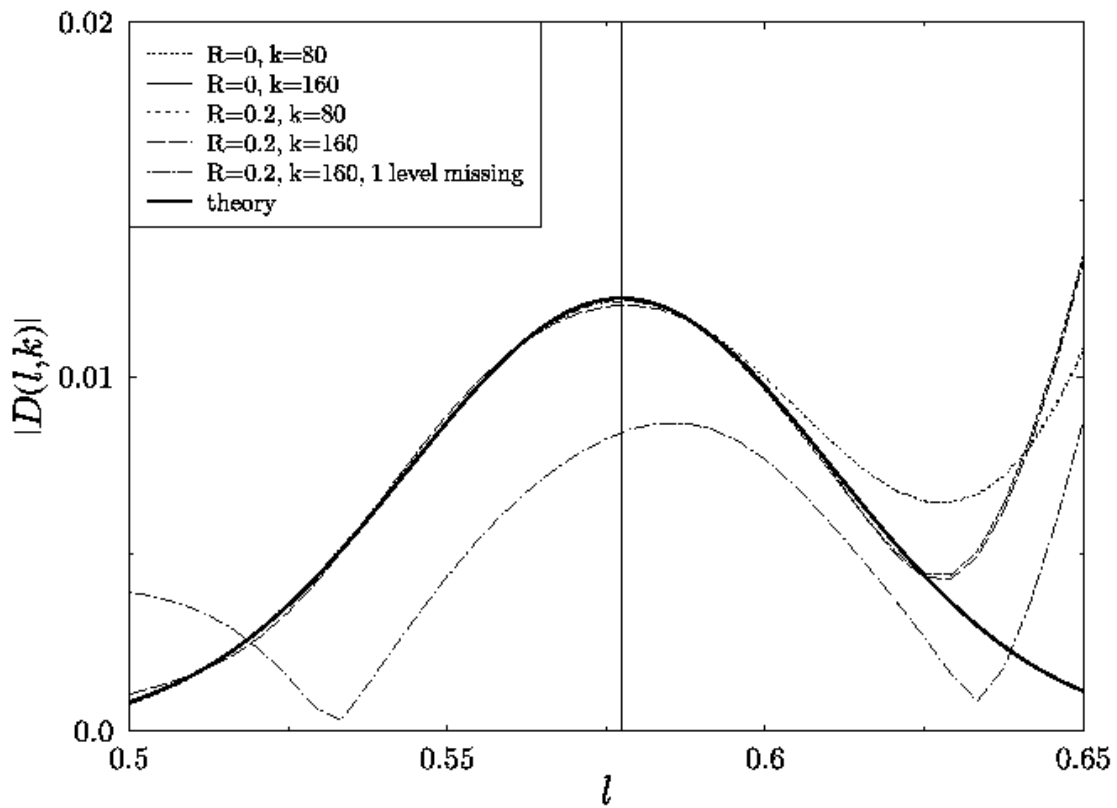


Figure 27: Absolute value of the quantal length spectra  $|D^{(w)}|$  with a Gaussian window,  $\sigma = 30$ , compared to the theoretical prediction (105). The location of the shortest bouncing ball is indicated by the vertical line.

the quantal lengths spectra  $|D^{(w)}|$  for  $R = 0$  and  $R = 0.2$  (Dirichlet everywhere) together with  $|D_{\text{sc}}^{(w)}|$  which contains contributions *only* from generic and unstable periodic orbits. One observes that all the peaks in the quantal length spectra are near lengths of the bouncing balls. Contributions of generic periodic orbits are completely overwhelmed by those of the bouncing balls and cannot be traced in the quantal length spectrum of  $R = 0.2$ . Also, we see that for  $R = 0.2$  the peaks are in general lower than for  $R = 0$ . This is because of the (partial or complete) shadowing effect of the inscribed sphere that reduces the prefactors of the bouncing balls as  $R$  increases.

In the case of the 2D Sinai billiard it was possible to analytically filter the effect of the bouncing balls from the semiclassical density of states [37, 17]. In three dimensions this is much more difficult. The functional forms of the contributions to the density of states of the bouncing balls are given in (31), but it is a difficult geometric problem to calculate the prefactors which are proportional to the cross sections of the bouncing-ball manifolds in configuration space. The desymmetrization makes this difficulty even greater and the calculations become very intricate. In addition, there is always an *infinite* number of bouncing-ball manifolds in the 3D Sinai. This is in contrast with the 2D Sinai, in which a finite (and usually quite small for moderate radii) number of bouncing-ball families exist. All this means, that an analytical subtraction of the bouncing-ball contributions is very intricate and vulnerable to errors which are difficult to detect and can have a devastating effect on the quantal-semiclassical agreement.

In order to circumvent these difficulties, we present in the following an efficient and simple method to get rid of the bouncing balls. The idea is simple: The bouncing balls are exactly those periodic orbits that *do not* reflect from the sphere. Therefore, changing the boundary conditions *on the sphere* does not affect the bouncing-ball contributions. Thus, the semiclassical density of states for Dirichlet / Neumann boundary conditions on the sphere is:

$$d_{\text{D/N}} = \bar{d}_{\text{D/N}} + d_{\text{bb}} + d_{\text{D/N}}^{(\text{osc})} . \quad (106)$$

The difference  $d_{\text{D}} - d_{\text{N}}$  is hence independent (in leading approximation in  $k$ ) of  $d_{\text{bb}}$  and has the standard form of a trace formula:

$$d_{\text{D-N}} \equiv d_{\text{D}}(k) - d_{\text{N}}(k) = [\bar{d}_{\text{D}}(k) - \bar{d}_{\text{N}}(k)] + \sum_{\text{PO}} \left( A_j^{(\text{D})} - A_j^{(\text{N})} \right) \cos(kL_j) . \quad (107)$$

Here  $A_j^{(\text{D})}$ ,  $A_j^{(\text{N})}$  are the coefficients that correspond to Dirichlet and Neumann cases, respectively. In fact, for Dirichlet, each reflection with the sphere causes a sign change, while for Neumann there are no sign changes. Therefore:

$$A_j^{(\text{D-N})} \equiv A_j^{(\text{D})} - A_j^{(\text{N})} = \begin{cases} 2A_j^{(\text{D})} & \text{odd number of reflections} \\ 0 & \text{even number of reflections} \end{cases} , \quad (108)$$

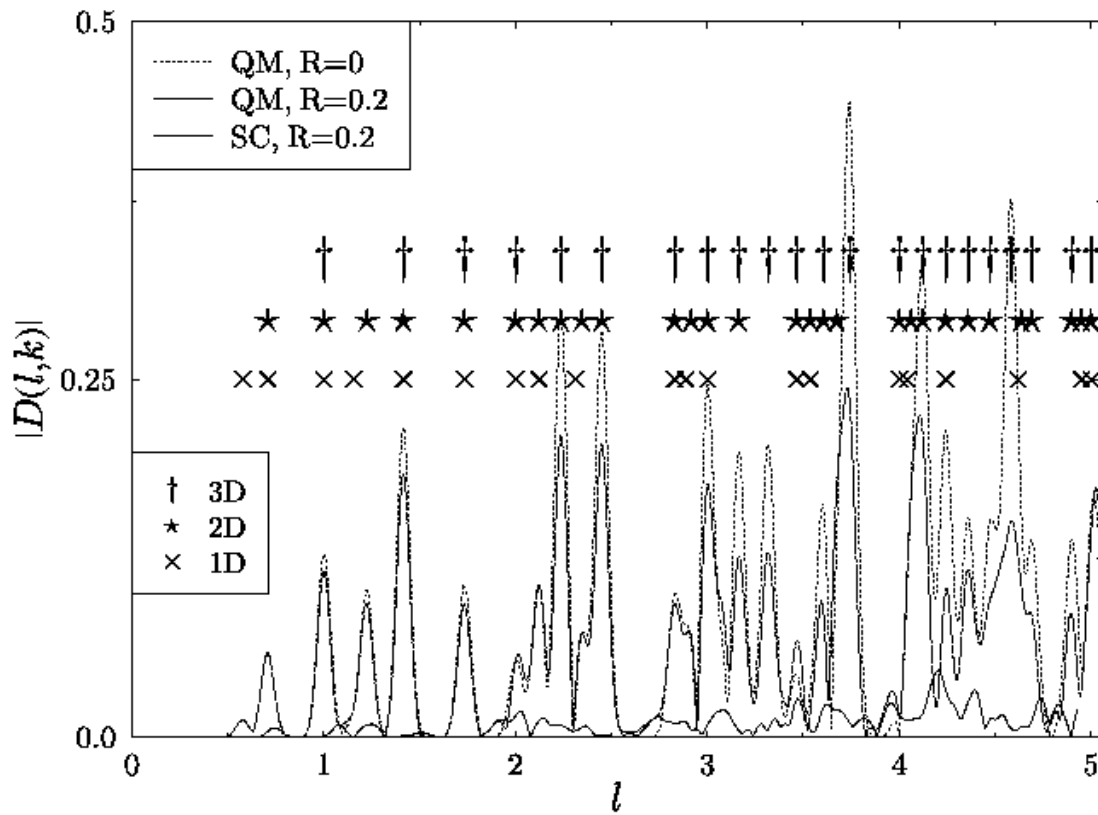


Figure 28: Quantal length spectra for  $R = 0$  and  $R = 0.2$  compared to semiclassical length spectrum for  $R = 0.2$  that contains only generic, unstable periodic orbits. In all cases  $k = 160$ ,  $\sigma = 30$ . The locations of the bouncing balls are indicated: Daggers for 2-parameters bouncing balls that occupy 3D volume in configuration space, stars for 2D bouncing balls and crosses for 1D bouncing balls.



and we expect to observe in the length spectrum of  $d_{D-N}$  contributions only due to generic periodic orbits with an odd number of reflections. The results of the numerical computations are presented in figure 29 where we compare the quantal (exact) vs. semiclassical (theoretical) length spectra. We observe on the outset that in contrast to figure 28 the quantal and semiclassical length spectra are of similar magnitudes and the bouncing balls no longer dominate. The peaks near lengths that correspond to the bouncing balls are greatly diminished, and in fact we see that the peak corresponding to the shortest bouncing ball ( $l \approx 0.577$ ) is completely absent, as predicted by the theory. Even more important is the remarkable agreement between the quantal and the semiclassical length spectra which one observes near various peaks (e.g. near  $l = 0.75, 1.25, 2$ ). Since the semiclassical length spectrum contains only generic contributions from unstable periodic orbits, this means that we demonstrated the existence and the correctness of these Gutzwiller contributions in the quantal levels. Therefore, one can say that at least as far as length spectra are concerned, the semiclassical trace formula is partially successful. There are, however, a few locations for which there is no agreement between the quantal and the semiclassical length spectra. The places where this discrepancy takes place are notably located near 3D bouncing-ball lengths. This suggest that there are “remnants” of the bouncing-ball contributions that are not filtered by the Dirichlet – Neumann difference procedure. It is natural to expect that these remnants are most prominent for the strongest (3D) bouncing balls. The origin of these remnants are the periodic orbits that are exactly tangent to the sphere. As an example, consider the 3D bouncing-ball families that are shown in figure 2 (upper part). The tangent orbits that are related to them constitute a 1-parameter family that surrounds the sphere like a “corona”. For a single tangent traversal their contributions acquire opposite signs for Dirichlet and Neumann boundary conditions on the sphere. Hence the Dirichlet – Neumann difference procedure still include these contributions which is apparent in the large discrepancy near  $l = 1$ . For two tangent traversals the Dirichlet and Neumann contributions have the same sign and hence cancel each other. This is indeed confirmed in figure 29 where we observe that near  $l = 2$  there is no discrepancy between the quantal and the semiclassical length spectra.

The above mentioned tangent orbits belong to the set of points in phase space in which the classical mapping is discontinuous. Semiclassically they give rise to diffraction effects. Tangent orbits were treated for the 2D case in our work [81, 38]. To eliminate their effects we hence need to sharpen our tools and to find a better filtering method than the present Dirichlet – Neumann difference procedure. This is performed in the following using mixed boundary conditions.

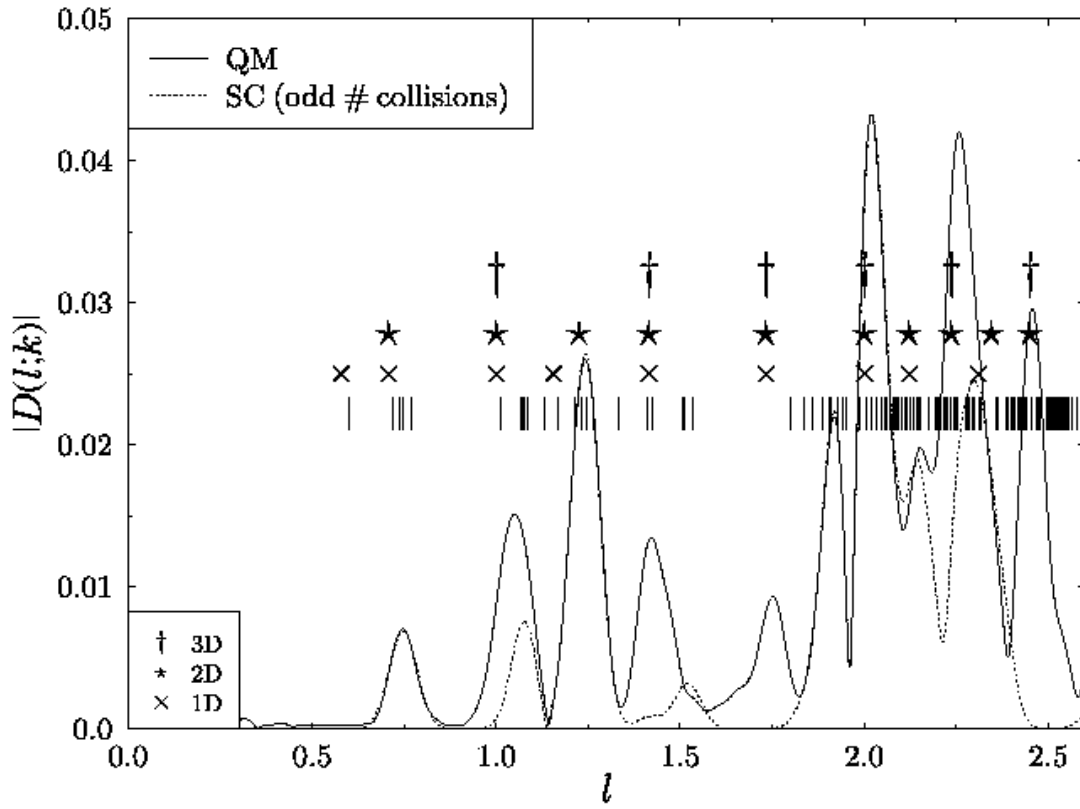


Figure 29: Dirichlet–Neumann difference length spectra for  $R = 0.2$ , with  $k = 100$ ,  $\sigma = 30$ . The semiclassical length spectrum is computed according to (108). The daggers, stars and crosses indicate the positions of the bouncing balls (refer to figure 28) and the vertical bars indicate the positions of the generic, unstable periodic orbits.

## 5.5 Filtering the bouncing-balls II: Mixed boundary conditions

The idea behind the Dirichlet–Neumann difference method was to subtract two spectra which differ only by their boundary conditions on the sphere. This can be generalized, if one replaces the discrete “parameter” of Dirichlet or Neumann conditions by a continuous parameter  $\alpha$ , and studies the differences of the corresponding densities of states  $d(k; \alpha_1) - d(k; \alpha_2)$ . In section 2.1 we discussed the mixed boundary conditions regarding the exact quantization of the 3D SB and gave the  $\alpha$ -dependent expressions for the quantal phase shifts. Mixed boundary conditions were extensively discussed in [82, 83].

To include the mixed boundary conditions in the semiclassical trace formula we generalize the results of Berry [15]. There, he derived the trace formula for the 2D Sinai billiard from an expansion of the KKR determinant in terms of traces. If one uses the 3D KKR matrix with (8) and perform a similar expansion, the result is a modification of the Gutzwiller terms as follows:

$$A_j \cos(kL_j) \longrightarrow A_j \cos(kL_j + n_j\pi + \phi_j), \quad (109)$$

$$\phi_j = (-2) \sum_{i=1}^{n_j} \arctan \left( \frac{\kappa \cot \alpha}{k \cos \theta_i^{(j)}} \right). \quad (110)$$

Here  $A_j$  are the semiclassical coefficients for the Dirichlet conditions on the sphere (c.f. equation (99)) and  $n_j$  counts the number of reflections from the sphere. The angles  $\theta_i^{(j)}$  are the reflection angles from the sphere measured from the normal of the  $j$ 'th periodic orbit. It is instructive to note that the phases (110) above are exactly the same as those obtained by a plane wave that reflects from an infinite plane with mixed boundary conditions (2). This is consistent with the local nature of the semiclassical approximation. A prominent feature of the mixed boundary conditions which is manifest in (109) is that they do not affect the geometrical properties (length, stability) of the periodic orbits. Rather, they only cause a change of a phase which depends on the geometry of the periodic orbit. This is due to the fact that the mixing parameter  $\alpha$  has no classical analogue. The invariance of periodic orbits with respect to  $\alpha$  renders the mixed boundary conditions an attractive parameter for e.g. investigations of parametric statistics. This was discussed and demonstrated in detail in [83].

We are now in a position to apply the mixed boundary conditions to get an efficient filtering of the bouncing–ball contributions. We first note that if we fix  $\kappa$ , then the levels are functions of  $\alpha$ :  $k_n = k_n(\alpha)$ . Let us consider the derivative of the quantal counting function at  $\alpha = 0$ :

$$\tilde{d}(k) \equiv \left. \frac{\partial N(k; \alpha)}{\partial \alpha} \right|_{\alpha=0} = \sum_n \left. \frac{\partial}{\partial \alpha} \Theta [k - k_n(\alpha)] \right|_{\alpha=0}$$

$$= \sum_n \left( -\frac{dk_n(\alpha)}{d\alpha} \right)_{\alpha=0} \delta(k - k_n), \quad (111)$$

where  $k_n = k_n(0)$  are the Dirichlet eigenvalues. Hence, the quantity  $\tilde{d}$  is a weighted density of states with delta-peaks located on the Dirichlet eigenvalues.

The semiclassical expression for  $\tilde{d}$  does not contain the leading contribution of the bouncing balls, since this contribution is independent of  $\alpha$ . The semiclassical contributions of the isolated periodic orbits to  $\tilde{d}$  are of the form  $A_j B_j \cos(kL_j)$ , where

$$B_j = \frac{2k}{\kappa} \sum_{i=1}^{n_j} \cos \theta_i^{(j)}. \quad (112)$$

This is easily derived from (109) and (110). Since the reflection angles  $\theta_i^{(j)}$  are in the range  $[0, \pi/2]$ , the coefficient  $B_j$  vanish *if and only if*  $\theta_i^{(j)} = \pi/2$  for all  $i = 1, \dots, n_j$ , which is an exact tangency. Therefore, exactly tangent periodic orbits are also eliminated by the derivative method. This is the desired effect of the mixed boundary conditions method that serves to further clean the spectrum from sub-leading contributions of the bouncing balls. We summarize equations (111) and (112):

$$\tilde{d}(k) = \sum_n v_n \delta(k - k_n) \approx \left( \begin{array}{c} \text{smooth} \\ \text{term} \end{array} \right) + \sum_{PO} A_j B_j \cos(kL_j), \quad v_n \equiv \left( -\frac{\partial k_n}{\partial \alpha} \right)_{\alpha=0}. \quad (113)$$

To check the utility of  $\tilde{d}$  and to verify (113) we computed both sides of (113) for  $R = 0.2$  and  $\kappa = 100$ . The quantal spectrum was computed for  $\alpha = 0.003$  and the derivatives  $v_n$  were obtained by the finite differences from the  $\alpha = 0$  (Dirichlet) spectrum. The coefficients  $B_j$  were extracted from the geometry of the periodic orbits. In figures 30 and 31 the length spectra are compared. The agreement between the quantal and the semiclassical data is impressive, especially for the lower  $l$ -values. There are no significant remnants of peaks near the bouncing-ball locations, and the peaks correspond to the generic and unstable periodic orbits. This demonstrates the utility of using  $\tilde{d}$  as an efficient means for filtering the spectrum from the non-generic effects.

The quantal-semiclassical agreement of the length spectra is not perfect, however, and it is instructive to list possible causes of this disagreement. We first recall that the semiclassical amplitudes  $A_j$  are the leading terms in an asymptotic series, hence we expect corrections of order  $1/k$  to the weights of periodic orbits. They are denoted as  $\hbar$  corrections and were treated in detail by Gaspard and Alonso [6] and by Alonso and Gaspard [7]. In our case, however,  $1/k \approx 1/100$  and these corrections are not expected to be dominant. More important are diffraction corrections which are also finite  $k$  effects that stem from the existence of a concave component (the sphere) in the billiard. Several kinds of diffraction corrections to the trace formula were analyzed for 2D billiards. Vattay, Wirzba and

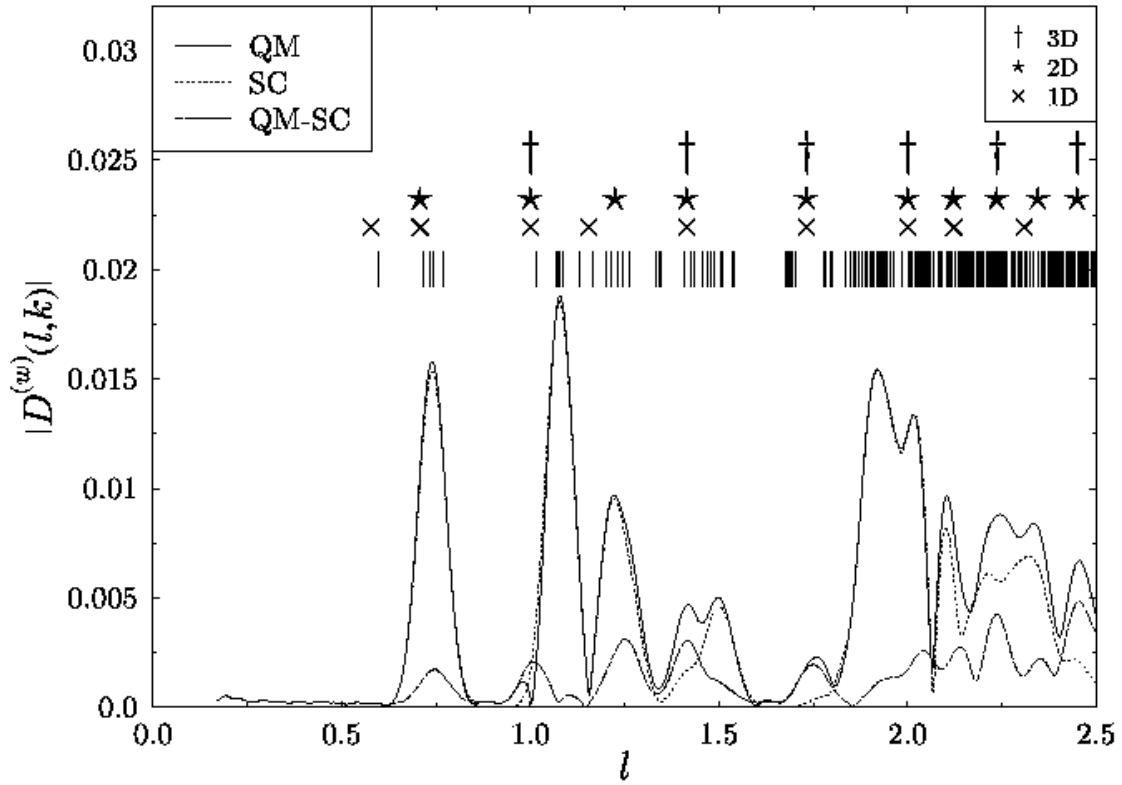


Figure 30: Length spectra for the mixed boundary conditions derivative method (113). Data are for  $R = 0.2$ ,  $k = 150$ ,  $\sigma = 30$ ,  $\kappa = 100$ . The dashed line represents  $|D^{(w)}(l) - D_{sc}^{(w)}(l)|$ . The daggers, stars and crosses indicate the positions of the bouncing balls (refer to figure 28) and the vertical bars indicate the positions of the generic, unstable periodic orbits.

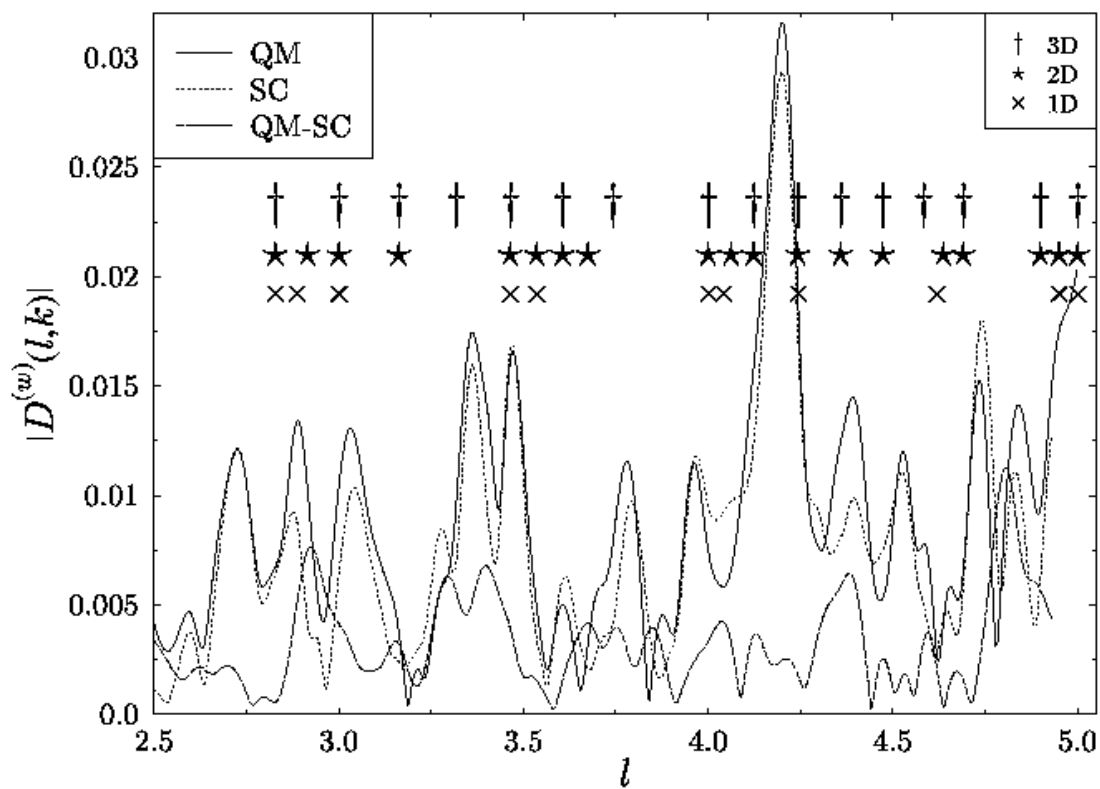


Figure 31: Continuation of figure 30 to  $2.5 \leq l \leq 5$ . We did not indicate the locations of unstable periodic orbits due to their enormous density.

Rosenqvist [8] considered *creeping orbits*, and we considered in [81, 38] *penumbra corrections*. (The penumbra is the region in phase space which is close to tangency:  $|\ell - kR| \approx (kR)^{1/3}$ , where  $\hbar\ell$  is the angular momentum.) We list the various diffraction corrections in the following:

**Creeping orbits:** These are orbits which are classically forbidden. They “creep” over concave parts of the billiard, and their semiclassical contribution is *exponentially small* in  $k^{1/3}$ , which should be negligible for the  $k$  values that we consider.

**Exactly tangent orbits:** These were already mentioned above, and we showed that their contributions are eliminated to a large extent by the mixed boundary conditions procedure. For 2D systems we found, however, that this is true in leading order only, and there are small remnants of the tangent orbits in the weighted density  $\tilde{d}$  [38]. The magnitude of the remnants in 2D is  $\mathcal{O}(1/\sqrt{k})$ , which is smaller than  $\mathcal{O}(k^0)$  of a generic unstable periodic orbit. In 3D, a similar analysis shows that the remnants of each family of tangent orbits is  $\mathcal{O}(k^0)$  which is the same magnitude as for unstable periodic orbits. Reviewing figures 30 and 31, we can observe some of the peaks of the quantal–semiclassical difference near lengths that correspond to exactly tangent orbits.

**Unstable and isolated periodic orbits that traverse the penumbra:** We have shown in [81, 38] that for periodic orbits which just miss tangency with a concave component of the billiard boundary, there is a correction to the semiclassical amplitude  $A_j$  which is of the same magnitude as  $A_j$  itself. These  $\mathcal{O}(1)$  diffraction corrections are the most important corrections to the trace formula for generic billiards. For periodic orbits which reflect at an extreme forward direction from a concave component, the amplitude  $A_j$  is very small due to the extreme classical instability. If we include diffraction corrections, the semiclassical contributions of these orbits get much larger. Therefore, the semiclassical contributions of periodic orbit that traverse the penumbra must be radically corrected. Moreover, we found that if one considers all the periodic orbits up to the Heisenberg length  $L_H \equiv 2\pi\bar{d}(k)$  (necessary to obtain a resolution of one mean level spacing), then *almost all* of the periodic orbits are vulnerable to penumbra diffraction corrections.

**Classically forbidden periodic orbits that traverse the shaded part of the penumbra:** Penumbra diffraction effects lead to semiclassical contributions from periodic orbits that slightly traverse through a concave component. Since they do not relate to classically allowed orbits, they represent new contributions to the trace formula rather than corrections of existing ones. Their magnitudes are comparable to those of generic unstable periodic orbits.

The above list of corrections, which was compiled according to studies of 2D billiards, suggests that there is a wealth of effects that must be considered if one wishes to go beyond the Gutzwiller trace formula. It is very difficult to implement these corrections systematically even for 2D billiards, and it goes beyond the scope of the present work to study them further for the 3D Sinai billiard. We mention in passing that except exact tangency, the penumbra effects are transient and depend on  $k$ .

According to the mathematical theorem [80] mentioned above, the quantal and the semiclassical length spectra are asymptotically the same. The significance of our findings in this section is that we have shown that the quantal–semiclassical agreement is achieved already for finite and moderate values of  $k$  and that the corrections are not very large (for the  $l$ -range we looked at). This is very encouraging, and justifies an optimistic attitude to the validity of the semiclassical approximation in 3D systems. However, obtaining accurate energy levels from the trace formula involves many contributions from a large number of periodic orbits. Therefore, one cannot directly infer at this stage from the accuracy of the peaks of the length spectrum to the accuracy of energy levels. There is a need to quantify the semiclassical error and to express it in a way which makes use of the above semiclassical analysis. This is done in section 6.



## 6 The accuracy of the semiclassical energy spectrum

One of the most important applications of the trace formula is to explain the spectral statistics and their relation to the universal predictions of Random Matrix Theory (RMT) [4, 5]. However, a prerequisite for the use of the semiclassical approximation to compute short-range statistics is that it is able to reproduce the exact spectrum within an error comparable to or less than the mean level spacing! This is a demanding requirement, and quite often it is doubted that the semiclassical approximation is able to reproduce precise levels for high-dimensional systems on the following grounds. The mean level spacing depends on the dimensionality (number of freedoms) of the system, and it is  $\mathcal{O}(\hbar^d)$  [3]. Gutzwiller [2] quotes an argument by Pauli [87] to show that in general the error margin for the semiclassical approximation scales as  $\mathcal{O}(\hbar^2)$  *independently of the dimensionality*. Applied to the trace formula, the expected error in units of the mean spacing, which is the figure of merit in the present context, is therefore expected to be  $\mathcal{O}(\hbar^{2-d})$ . We shall refer to this as the “traditional estimate”. It sets  $d = 2$  as a critical dimension for the applicability of the semiclassical trace formula and hence for the validity of the conclusions which are drawn from it. The few systems in  $d > 2$  dimensions which were numerically investigated display spectral statistics which adhere to the predictions of RMT as accurately as their counterparts in  $d = 2$  [53, 54, 19]. Thus, the traditional estimate cannot be correct in the present context, and we shall explain the reasons why it is inadequate.

In this section we shall develop measures for the accuracy of the semiclassical energy levels. We shall then derive formulas to evaluate these measures. Using our quantal and classical (periodic orbits) databases for the 2D and 3D Sinai billiards, we shall apply the formulas and get numerical bounds for the semiclassical errors.

The problem of the accuracy of the energy spectrum derived from the semiclassical trace formula was hardly discussed in the literature. Gutzwiller quotes the traditional estimate of  $\mathcal{O}(\hbar^{2-d})$  [2, 75]. Gaspard and Alonso [6], Alonso and Gaspard [7] and Vattay, Wirzba and Rosenqvist [8] derived explicit and generic  $\hbar$  corrections for the trace formula, but do not address directly the issue of semiclassical accuracy of energy levels. Boasman [88] estimates the accuracy of the Boundary Integral Method (BIM) [14] for 2D billiards in the case that the exact kernel is replaced by its asymptotic approximation. He finds that the resulting error is of the same magnitude as the mean spacing, in agreement with the traditional estimate. However, the dependence of the semiclassical error on the dimensionality is not established. We also mention a recent work by Dahlqvist [89] in which the semiclassical error due to penumbra (diffraction) effects is analytically estimated for the 2D Sinai billiard. The results are compatible with the ones reported here.

## 6.1 Measures of the semiclassical error

In order to define a proper error measure for the semiclassical approximation of the energy spectrum one has to clarify a few issues. In contrast with the EBK quantization which gives an *explicit* formula for the spectrum, the semiclassical spectrum for chaotic systems is *implicit* in the trace formula, or in the semiclassical expression for the spectral determinant. To extract the semiclassical spectrum we recall that the exact spectrum,  $\{E_n\}$ , can be obtained from the exact counting function:

$$N(E) \equiv \sum_{n=1}^{\infty} \Theta(E - E_n) , \quad (114)$$

by solving the equation

$$N(E_n) = n - \frac{1}{2} , \quad n = 1, 2, \dots \quad . \quad (115)$$

In the last equation, an arbitrarily small amount of smoothing must be applied to the Heavyside function. In analogy, one obtains the semiclassical spectrum  $\{E_n^{\text{sc}}\}$  as [50]:

$$N_{\text{sc}}(E_n^{\text{sc}}) = n - \frac{1}{2} , \quad n = 1, 2, \dots \quad , \quad (116)$$

where  $N_{\text{sc}}$  is a semiclassical approximation of  $N$ . Note that  $N_{\text{sc}}$  with which we start is not necessarily a sharp counting function. However, once  $\{E_n^{\text{sc}}\}$  is known, we can “rectify” the smooth  $N_{\text{sc}}$  into the sharp counting function  $N_{\text{sc}}^{\#}$  [5]:

$$N_{\text{sc}}^{\#}(E) \equiv \sum_{n=1}^{\infty} \Theta(E - E_n^{\text{sc}}) . \quad (117)$$

The most obvious choice for  $N_{\text{sc}}$  is the Gutzwiller trace formula [2] truncated at the Heisenberg time, which is what we shall use. Alternatively, one can start from the regularized Berry–Keating Zeta function  $\zeta_{\text{sc}}(E)$  [69], and define  $N_{\text{sc}} = \bar{N} - (1/\pi) \text{Im} \log \zeta_{\text{sc}}(E + i0)$ , which yields  $N_{\text{sc}} = N_{\text{sc}}^{\#}$ .

Next, in order to define a quantitative measure of the semiclassical error, one should establish a one-to-one *correspondence* between the quantal and the semiclassical levels, namely, one should identify the semiclassical counterparts of the exact quantum levels. In classically chaotic systems, for which the Gutzwiller trace formula is applicable, the only constant of the motion is the energy. This is translated into a single “good” quantum number in the quantum spectrum, which is the ordinal number of the levels when ordered by their magnitude. Thus, the only correspondence which can be established between the exact spectrum  $\{E_n\}$  and its semiclassical approximation,  $\{E_n^{\text{sc}}\}$ , is

$$E_n \longleftrightarrow E_n^{\text{sc}} . \quad (118)$$

This is to be contrasted with integrable systems, where it is appropriate to compare the exact and approximate levels which have the same quantum numbers.

The natural scale on which the accuracy of semiclassical energy levels should be measured is the mean level spacing  $(\bar{d}(E))^{-1}$ . We shall be interested here in the mean semiclassical error, and proper measures are the mean absolute difference:

$$\epsilon^{(1)}(E) \equiv \langle \bar{d}(E_n) |E_n - E_n^{\text{sc}}| \rangle_E \quad (119)$$

or the variance:

$$\epsilon^{(2)}(E) \equiv \langle (\bar{d}(E_n) (E_n - E_n^{\text{sc}}))^2 \rangle_E, \quad (120)$$

where  $\langle \cdot \rangle$  denotes averaging over a spectral interval  $\Delta E$  centered at  $E$ . The interval  $\Delta E$  is large enough so that the mean number of levels  $\Delta E \cdot \bar{d}(E) \gg 1$ . Yet,  $\Delta E$  is small enough on the classical scale, such that  $\bar{d}(E) \approx \text{constant}$  over the interval considered.

We shall now compare two different estimates for the semiclassical error. The first one is the traditional estimate:

$$\epsilon^{\text{traditional}} = \mathcal{O}(\hbar^{2-d}) \longrightarrow \begin{cases} \text{const} & , \quad d = 2 \\ \infty & , \quad d \geq 3 \end{cases} \quad \text{as } \hbar \rightarrow 0 \quad (121)$$

(c.f. section 1). It claims that the semiclassical approximation is (marginally) accurate in two dimensions, but it fails to predict accurate energy levels for three dimensions or more. We emphasize that the traditional estimate is a qualitative error measure, emerging from global error estimate of the time propagator. Hence, it cannot be directly connected to either  $\epsilon^{(1)}$  or  $\epsilon^{(2)}$ . We mention it here since it is the one usually quoted in the literature.

One may get a different estimate of the semiclassical error, if the Gutzwiller Trace Formula (GTF) is used as a starting point. Suppose that we have calculated  $N_{\text{sc}}$  to a certain degree of precision, and we compute from it the semiclassical energies  $E_n^{\text{sc}}$  using (116). Denote by  $\Delta N_{\text{sc}}$  the higher order terms which were neglected in the calculation of  $N_{\text{sc}}$ . The expected error in  $E_n^{\text{sc}}$  can be estimated by including  $\Delta N_{\text{sc}}$  and calculating the energy differences  $\delta_n$ . That is, we consider:

$$N_{\text{sc}}(E_n^{\text{sc}} + \delta_n) + \Delta N_{\text{sc}}(E_n^{\text{sc}} + \delta_n) = n - \frac{1}{2}. \quad (122)$$

Combining (116) and (122) we get (to first order in  $\delta_n$ ):

$$\delta_n \approx \frac{-\Delta N_{\text{sc}}(E_n^{\text{sc}})}{\partial N_{\text{sc}}(E_n^{\text{sc}})/\partial E} \approx \frac{-\Delta N_{\text{sc}}(E_n^{\text{sc}})}{\bar{d}(E_n^{\text{sc}})}. \quad (123)$$

In the above we assumed that the fluctuations of  $N_{\text{sc}}$  around its average are not very large. Thus,

$$\epsilon^{(1),\text{GTF}} \approx \bar{d}(E_n^{\text{sc}})|\delta_n| \approx \Delta N_{\text{sc}}(E_n^{\text{sc}}). \quad (124)$$

Let us apply the above formula and consider the case in which we take for  $N_{\text{sc}}$  its mean part  $\bar{N}$ , and that we include in  $\bar{N}$  terms of order up to (and including)  $\hbar^{-m}$ ,  $m \leq d$ . For  $\Delta N_{\text{sc}}$  we use both the leading correction to  $\bar{N}$  and the leading order periodic orbit sum which is formally (termwise) of order  $\hbar^0$ . Hence,

$$\epsilon_{\bar{N}}^{(1),\text{GTF}} = \mathcal{O}(\hbar^{-m+1}) + \mathcal{O}(\hbar^0) = \mathcal{O}(\hbar^{\min(-m+1, 0)}) . \quad (125)$$

We conclude, that approximating the energies only by the mean counting function  $\bar{N}$  up to (and not including) the constant term, is already sufficient to obtain semiclassical energies which are accurate to  $\mathcal{O}(\hbar^0) = \mathcal{O}(1)$  with respect to the mean density of states. Note again, that no periodic orbit contributions were included in  $N_{\text{sc}}$ . Including less terms in  $\bar{N}$  will lead to a diverging semiclassical error, while more terms will be masked by the periodic orbit (oscillatory) term. One can do even better if one includes in  $N_{\text{sc}}$  the smooth terms up to and including the constant term ( $\mathcal{O}(\hbar^0)$ ) together with the leading order periodic orbit sum which is formally also  $\mathcal{O}(\hbar^0)$ . The semiclassical error is then:

$$\epsilon_{\text{po}}^{(1),\text{GTF}} = \mathcal{O}(\hbar^1) . \quad (126)$$

That is, the semiclassical energies measured in units of the mean level spacing are asymptotically accurate independently of the dimension! This estimate grossly contradicts the traditional estimate (121) and calls for an explanation.

The first point that should be noted is that the order of magnitude (power of  $\hbar$ ) of the periodic orbit sum, which we considered above to be  $\mathcal{O}(\hbar^0)$ , is only a formal one. Indeed, each term which is due to a *single* periodic orbit is of order  $\mathcal{O}(\hbar^0)$ . However the periodic orbit sum *absolutely diverges*, and at best it is only *conditionally convergent*. To give it a numerical meaning, the periodic orbit sum must therefore be regularized. This is effectively achieved by truncating the trace formula or the corresponding spectral  $\zeta$  function [26, 84, 69, 90]. However, the cutoff itself depends on  $\hbar$ . One can conclude, that the simple-minded estimate (126) given above is at best a lower bound, and the error introduced by the periodic orbit sum must be re-evaluated with more care. This point will be dealt with in great detail in the sequel, and we shall eventually develop a meaningful framework for evaluating the magnitude of the periodic orbit sum.

The disparity between the traditional estimate of the semiclassical error and the one based on the trace formula can be further illustrated by the following argument. The periodic orbit formula is derived from the semiclassical propagator  $K_{\text{sc}}$  using further approximations [2]. Therefore one wonders, how can it be that *further* approximations of  $K_{\text{sc}}$  actually *reduce* the semiclassical error from (121) to (126)? The puzzle is resolved if we recall, that in order to obtain  $\epsilon_{\text{po}}^{(1),\text{GTF}}$  above we separated the density of states into a smooth part and an oscillating part, and we required that the smooth part is accurate enough. To achieve this, we have to go beyond the leading Weyl's term and to use specialized methods to calculate the smooth density of states beyond the leading order. These methods

are mostly developed for billiards [82, 91, 92]. In any case, to obtain  $\epsilon_{\text{po}}^{(1),\text{GTF}}$  we have added *additional* information which goes beyond the leading semiclassical approximation.

A direct check of the accuracy of the semiclassical spectrum using the error measures  $\epsilon^{(1)}$ ,  $\epsilon^{(2)}$  is exceedingly difficult due to the exponentially large number of periodic orbits needed. The few cases where such tests were carried out involve 2D systems and it was possible to check only the lowest (less than a hundred) levels (e.g. [60, 73]). The good agreement between the exact and the semiclassical values confirmed the expectation that in 2D the semiclassical error is small. In 3D, the topological entropy is typically much larger [50, 54], and the direct test of the semiclassical spectrum becomes prohibitive.

Facing with this grim reality, we have to introduce alternative error measures which yield the desired information, but which are more appropriate for a practical calculation. We construct the measure:

$$\delta^{(2)}(E) \equiv \left\langle |N(E) - N_{\text{sc}}^{\#}(E)|^2 \right\rangle_E . \quad (127)$$

As before, the triangular brackets indicate averaging over an energy interval  $\Delta E$  about  $E$ . We shall now show that  $\delta^{(2)}$  faithfully reflects the deviations between the spectra, and is closely related to  $\epsilon^{(1)}$  and  $\epsilon^{(2)}$ . Note, that the following arguments are purely statistical and apply to every pair of staircase functions.

Suppose first, that all the differences  $E_n^{\text{sc}} - E_n$  are smaller than the mean spacing. Then,  $|N - N_{\text{sc}}^{\#}|$  is either 0 or 1 in most of the cases (see figure 32). Hence,  $|N - N_{\text{sc}}^{\#}| = |N - N_{\text{sc}}^{\#}|^2$  along most of the  $E$  axis. Consequently,

$$\delta^{(2)}(E) \approx \langle |N(E) - N_{\text{sc}}^{\#}(E)| \rangle_E , \quad \text{for small deviations} . \quad (128)$$

The right hand side of the above equation (the fraction of non-zero contributions) equals  $\epsilon^{(1)}$ . Thus,

$$\delta^{(2)} \approx \epsilon^{(1)} , \quad \text{for small deviations} . \quad (129)$$

If, on the other hand, deviations are much larger than one mean spacing, the typical horizontal distance  $\bar{d}|E - E_n|$  should be comparable to the vertical distance  $|N - N_{\text{sc}}^{\#}|$ , and hence, in this limit

$$\delta^{(2)} \approx \epsilon^{(2)} , \quad \text{for large deviations} . \quad (130)$$

Therefore, we expect  $\delta^{(2)}$  to interpolate between  $\epsilon^{(1)}$  and  $\epsilon^{(2)}$  throughout the entire range of deviations. This behavior was indeed observed in a numerical tests which were performed to check the above expectations [93]. Moreover, it was shown in [93] that  $\delta^{(2)}$  is completely equivalent to  $\epsilon^{(2)}$  when the spectral counting functions are replaced with their smooth counterparts, provided that the smoothing width is of the order of 1 mean level spacing and the same smoothing is applied to both counting functions. That is,

$$\delta_{\text{smooth}}^{(2)} \approx \epsilon^{(2)} , \quad \text{for all deviations} . \quad (131)$$

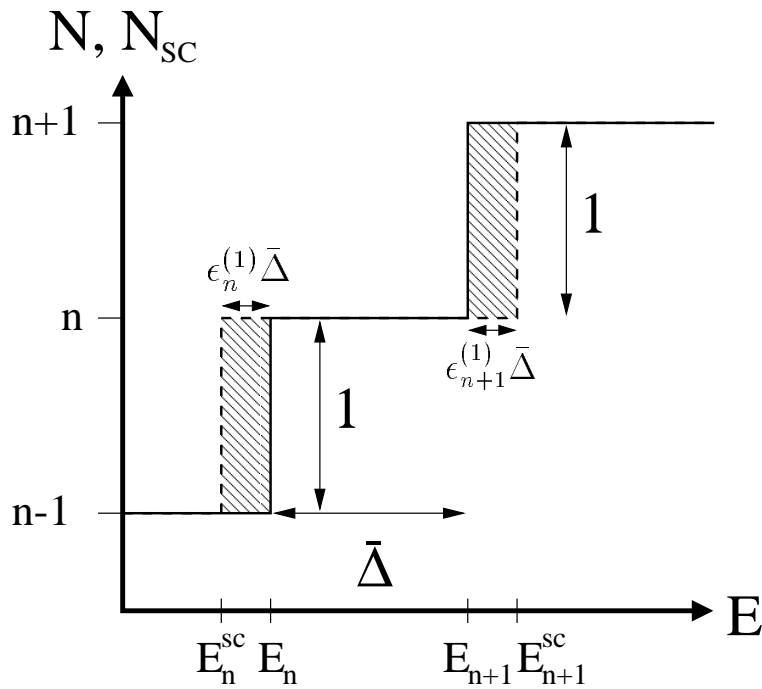


Figure 32: Illustration of  $|N(E) - N_{sc}^{\#}(E)|$  for small deviations between quantum and semiclassical energies:  $\epsilon^{(1)} \ll \bar{d}^{-1} \equiv \bar{\Delta}$ . The quantum staircase  $N(E)$  is denoted by the full line and the semiclassical staircase  $N_{sc}^{\#}(E)$  is denoted by the dashed line. The difference is shaded.

In testing the semiclassical accuracy, this kind of smoothing is essential and will be introduced by truncating the trace formula at the Heisenberg time  $t_H \equiv h\bar{d}$ . These properties of the measure  $\delta^{(2)}$ , and its complete equivalence to  $\epsilon^{(2)}$  for smooth counting functions, renders it a most appropriate measure of the semiclassical error.

We now turn to the practical evaluation of  $\delta^{(2)}$ . To perform the energy averaging, we choose a positive window function  $w(E' - E)$  which has a width  $\Delta E$  near  $E$  and is normalized by  $\int_{-\infty}^{+\infty} dE' w^2(E') = 1$ . It falls off sufficiently rapidly so that all the expressions which follow are well behaved. We consider the following counting functions that have an effective support on an interval of size  $\Delta E$  about  $E$ :

$$\hat{N}(E'; E) \equiv w(E' - E)N(E') \quad (132)$$

$$\hat{N}_{\text{sc}}^{\#}(E'; E) \equiv w(E' - E)N_{\text{sc}}^{\#}(E'). \quad (133)$$

The functions  $\hat{N}$  and  $\hat{N}_{\text{sc}}^{\#}$  are sharp staircases, since the multiplication with  $w$  preserves the sharpness of the stairs (it is not a convolution!). We now explicitly construct  $\delta^{(2)}(E)$  as:

$$\begin{aligned} \delta^{(2)}(E) &= \int_{-\infty}^{+\infty} dE' \left| \hat{N}(E'; E) - \hat{N}_{\text{sc}}^{\#}(E'; E) \right|^2 \\ &= \int_{-\infty}^{+\infty} dE' \left| N(E') - N_{\text{sc}}^{\#}(E') \right|^2 w^2(E' - E). \end{aligned} \quad (134)$$

To obtain  $\delta_{\text{smooth}}^{(2)}$  we need to smooth  $N$  and  $N_{\text{sc}}^{\#}$  over a scale of order of one mean spacing. One can, e.g., replace the sharp stairs by error functions. As for  $N_{\text{sc}}^{\#}$ , we prefer to simply replace it with the original  $N_{\text{sc}}$ , which we assume to be smooth over one mean spacing. That is, we suppose that  $N_{\text{sc}}$  contains periodic orbits up to Heisenberg time. Hence,

$$\delta_{\text{smooth}}^{(2)}(E) = \int_{-\infty}^{+\infty} dE' \left| N^{\text{smooth}}(E') - N_{\text{sc}}(E') \right|^2 w^2(E' - E). \quad (135)$$

A comment is in order here. Strictly speaking, to satisfy (131) we need to apply the same smoothing to  $N$  and to  $N_{\text{sc}}^{\#}$ , and in general  $N_{\text{sc}}^{\#, \text{smooth}} \neq N_{\text{sc}}$ , but there are differences of order 1 between the two functions. However, since our goal is to determine whether the semiclassical error remains finite or diverges in the semiclassical limit  $\hbar \rightarrow 0$ , we disregard such inaccuracies of order 1. If a more accurate error measure is needed, then more care should be practised in this and in the following steps.

Applying Parseval's theorem to (135) we get:

$$\delta_{\text{smooth}}^{(2)}(E) = \frac{1}{\hbar} \int_{-\infty}^{+\infty} dt \left| \hat{D}(t; E) - \hat{D}_{\text{sc}}(t; E) \right|^2 \quad (136)$$

where

$$\hat{D}(t; E) \equiv \frac{1}{\sqrt{2\pi}} \int_{-\infty}^{+\infty} dE' \hat{N}^{\text{smooth}}(E'; E) \exp(iE't/\hbar) \quad (137)$$

$$\hat{D}_{\text{sc}}(t; E) \equiv \frac{1}{\sqrt{2\pi}} \int_{-\infty}^{+\infty} dE' \hat{N}_{\text{sc}}(E'; E) \exp(iE't/\hbar). \quad (138)$$

We shall refer to  $\hat{D}$ ,  $\hat{D}_{\text{sc}}$  as the (regularized) quantal and semiclassical time spectra, respectively. These functions are the analogs of the length spectra  $D(l; k)$  used in section 5 for the billiard problem. The analogue becomes clear by invoking the Gutzwiller trace formula and expressing the semiclassical counting function as a mean part plus a sum over periodic orbits. We have:

$$N_{\text{sc}}(E) = \bar{N}(E) + \sum_{\text{po}} \frac{\hbar A_j(E)}{T_j(E)} \sin[S_j(E)/\hbar - \nu_j\pi/2], \quad (139)$$

where  $A_j = T_j/(\pi\hbar r_j \sqrt{|\det(I - M_j)|})$  is the semiclassical amplitude of the  $j$ 'th periodic orbit, and  $T_j, S_j, \nu_j, M_j, r_j$  are its period, action, Maslov index, monodromy matrix and repetition index, respectively. Then, the corresponding time spectrum reads:

$$\begin{aligned} \hat{D}_{\text{sc}}(t; E) &\approx \bar{D}(t; E) \\ &+ \frac{1}{2i} \sum_{\text{po}} \frac{\hbar A_j(E)}{T_j(E)} \left\{ e^{(i/\hbar)[Et + S_j(E)]} \hat{w}([t + T_j(E)]/\hbar) - \right. \\ &\quad \left. e^{(i/\hbar)[Et - S_j(E)]} \hat{w}([t - T_j(E)]/\hbar) \right\}. \end{aligned} \quad (140)$$

In the above, the Fourier transform of  $w$  is denoted by  $\hat{w}$ . It is a localized function of  $t$  whose width is  $\Delta t \approx \hbar/\Delta E$ . The sum over the periodic orbits in  $D_{\text{sc}}$  therefore produces sharp peaks centered at times that correspond to the periods  $T_j$ . The term  $\bar{D}$  corresponds to the smooth part and is sharply peaked near  $t = 0$ . To obtain (140) we expanded the actions near  $E$  to first order:  $S_j(E') \approx S_j(E) + (E' - E)T_j(E)$ . We note in passing, that this approximate expansion of  $S_j$  can be avoided altogether if one performs the Fourier transform over  $\hbar^{-1}$  rather than over the energy. This way, an action spectrum will emerge, but also here the action resolution will be finite, because the range of  $\hbar^{-1}$  should be limited to the range where  $\bar{d}(E; \hbar)$  is approximately constant. It turns out therefore, that the two approaches are essentially equivalent, and for billiards they are identical.

The manipulations done thus far were purely formal, and did not manifestly circumvent the difficult task of evaluating  $\delta_{\text{smooth}}^{(2)}$ . However, the introduction of the time spectra and the formula (136) put us in a better position than the original expression (134). The advantages of using the time spectra in the present context are the following:



- The semiclassical time spectrum  $\hat{D}_{\text{sc}}(t; E)$  is absolutely convergent for all times (as long as the window function  $w$  is well behaved, e.g. it is a Gaussian). This statement is correct even if the sum (140) extends over the entire set of periodic orbits! This is in contrast with the trace formula expression for  $N_{\text{sc}}$  (and therefore  $\hat{N}_{\text{sc}}$ ) which is absolutely divergent if all of the periodic orbits are included.
- Time scale separation: As we noted above, the time spectrum is peaked at times that correspond to periods of the classical periodic orbits. This allows us to distinguish between various qualitatively different types of contributions to  $\delta_{\text{smooth}}^{(2)}$ .

We shall now pursue the separation of the time scales in detail. We first note, that due to  $\hat{N}, \hat{N}_{\text{sc}}$  being real, there is a  $t \leftrightarrow (-t)$  symmetry in (136), and therefore the time integration can be restricted to the limits 0 to  $+\infty$ :  $\delta^{(2)} = (1/\hbar) \int_{-\infty}^{+\infty} \dots = (2/\hbar) \int_0^{\infty} \dots$ . We now divide the time axis into four intervals :

**$0 \leq \mathbf{t} \leq \Delta \mathbf{t}$ :** The shortest time scale in our problem is  $\Delta t = \hbar/\Delta E$ . The contributions to this time interval are due to the differences between the exact and the semiclassical *mean* densities of states. This is an important observation, since it allows us to distinguish between the two sources of semiclassical error — the error that emerges from the mean densities and the error that originates from the fluctuating part (periodic orbits). Since we are interested only in the semiclassical error that results from the fluctuating part of the spectral density, we shall ignore this regime in the following.

**$\Delta \mathbf{t} \leq \mathbf{t} \leq \mathbf{t}_{\text{erg}}$  :** This is the non-universal regime [65], in which periodic orbits are still sparse, and cannot be characterized statistically. The “ergodic” time scale  $t_{\text{erg}}$  is purely classical and is independent of  $\hbar$ .

**$\mathbf{t}_{\text{erg}} \leq \mathbf{t} \leq \mathbf{t}_{\text{H}}$ :** In this time regime periodic orbits are already in the universal regime and are dense enough to justify a statistical approach to their proliferation and stability. The upper limit of this interval is the Heisenberg time  $t_{\text{H}} = \hbar \bar{d}(E)$ , which is the time that is needed to resolve the quantum (discrete) nature of a wavepacket with energy concentrated near  $E$ . The Heisenberg time is “quantal” in the sense that it is dependent of  $\hbar$ :  $t_{\text{H}} = \mathcal{O}(\hbar^{1-d})$ .

**$\mathbf{t}_{\text{H}} \leq \mathbf{t} < \infty$ :** This is the regime of “long” orbits which is effectively truncated from the integration as a result of the introduction of a smoothing of the quantal and semiclassical counting functions, with a smoothing scale of the order of a mean level spacing.

Dividing the integral (136) according to the above time intervals, we can rewrite

$\delta_{\text{smooth}}^{(2)}$ :

$$\begin{aligned}\delta_{\text{smooth}}^{(2)}(E) &= \left( \int_{\Delta t}^{t_{\text{erg}}} + \int_{t_{\text{erg}}}^{t_{\text{H}}} + \int_{t_{\text{H}}}^{\infty} \right) \frac{2dt}{\hbar} \left| \hat{D}(t; E) - \hat{D}_{\text{sc}}(t; E) \right|^2 \\ &\equiv \delta_{\text{short}}^{(2)} + \delta_{\text{m}}^{(2)} + \delta_{\text{long}}^{(2)}.\end{aligned}\tag{141}$$

As explained above,  $\delta_{\text{long}}^{(2)}$  can be ignored due to smoothing on the scale of a mean level spacing. The integral  $\delta_{\text{short}}^{(2)}$  is to be neglected for the following reason. The integral extends over a time interval which is finite and independent of  $\hbar$ , and therefore it contains a fixed number of periodic orbits contributions. The semiclassical approximation provides, for each individual contribution, the leading order in  $\hbar$ , and therefore [80] we should expect:

$$\delta_{\text{short}}^{(2)} \longrightarrow 0 \quad \text{as } \hbar \longrightarrow 0.\tag{142}$$

Our purpose is to check whether the semiclassical error is finite or divergent as  $\hbar \longrightarrow 0$ , and to study whether the rate of divergence depends on dimensionality. Equation (142) implies that  $\delta_{\text{short}}^{(2)}$  cannot affect  $\delta^{(2)}$  in the semiclassical limit and we shall neglect it in the following.

We remain with:

$$\delta_{\text{smooth}}^{(2)} \approx \delta_{\text{m}}^{(2)},\tag{143}$$

which will be our object of interest from now on.

The fact that  $t_{\text{H}}$  is extremely large on the classical scale renders the calculation of all the periodic orbits with periods less than  $t_{\text{H}}$  an impossible task. However, sums over periodic orbits when the period is longer than  $t_{\text{erg}}$  tend to meaningful limits, and hence, we would like to recast the expression for  $\delta_{\text{m}}^{(2)}$  in the following way. Write  $\delta_{\text{m}}^{(2)}$  as:

$$\delta_{\text{m}}^{(2)} = \frac{2}{\hbar} \int_{t_{\text{erg}}}^{t_{\text{H}}} dt \left\langle \left| \hat{D}(t) - \hat{D}_{\text{sc}}(t) \right|^2 \right\rangle_t\tag{144}$$

$$= \frac{2}{\hbar} \int_{t_{\text{erg}}}^{t_{\text{H}}} dt \left\langle \left| \hat{D}(t) \right|^2 \right\rangle_t \times \left[ \frac{\left\langle \left| \hat{D}(t) - \hat{D}_{\text{sc}}(t) \right|^2 \right\rangle_t}{\left\langle \left| \hat{D}(t) \right|^2 \right\rangle_t} \right]\tag{145}$$

$$\equiv \frac{2}{\hbar} \int_{t_{\text{erg}}}^{t_{\text{H}}} dt \left\langle \left| \hat{D}(t) \right|^2 \right\rangle_t \times C(t)\tag{146}$$

$$= \int_{t_{\text{erg}}}^{t_{\text{H}}} \text{envelope} \times \text{correlation}$$

where the parametric dependence on  $E$  was omitted for brevity. The smoothing over  $t$  is explicitly indicated to emphasize that one may use a statistical interpretation for the terms of the integrand. This is so because in this domain, the

density of periodic orbits is so large, that within a time interval of width  $\hbar/\Delta E$  there are exponentially many orbits whose contributions are averaged due to the finite resolution.

We note now that we can use the following relation between the time spectrum and the spectral form factor  $K(\tau)$ :

$$\frac{\left\langle \left| \hat{D}(t) \right|^2 \right\rangle_t}{\hbar} dt = \frac{K(\tau)}{4\pi^2\tau^2} d\tau \quad (147)$$

where  $\tau \equiv t/t_H$  is the scaled time. The above form factor is smoothed according to the window function  $w$ . Hence:

$$\delta_{\text{smooth}}^{(2)} \approx \frac{1}{2\pi^2} \int_{\tau_{\text{erg}}}^1 d\tau \frac{K(\tau)C(\tau)}{\tau^2}. \quad (148)$$

For generic chaotic systems we expect that  $K(\tau)$  agrees with the results of RMT in the universal regime  $\tau > \tau_{\text{erg}}$  [24, 4, 65]. Therefore

$$\tau \leq K(\tau) \leq g\tau \quad \text{for } \tau_{\text{erg}} < \tau \leq 1, \quad (149)$$

where  $g = 1$  for systems which violate time reversal symmetry, and  $g = 2$  if time reversal symmetry is respected. This implies that the evaluation of  $\delta_{\text{smooth}}^{(2)}$  reduces to

$$\delta_{\text{smooth}}^{(2)} \approx \frac{g}{2\pi^2} \int_{\tau_{\text{erg}}}^1 d\tau \frac{C(\tau)}{\tau}, \quad (150)$$

where we took the upper bound  $g\tau$  for  $K(\tau)$ . The dependence on  $\hbar$  in this expression comes from the lower integration limit which is proportional to  $\hbar^{d-1}$  as well as from the implicit dependence of the function  $C$  on  $\hbar$ .

Formula (150) is our main theoretical result. However, we do not know how to evaluate the correlation function  $C(\tau)$  from first principles. The knowledge of the  $\hbar$  corrections to each of the terms in the semiclassical time spectrum is not sufficient since the resulting series which ought to be summed is not absolutely convergent. Therefore we have to recourse to a numerical analysis, which will be described in the next section. The numerical approach requires one further approximation, which is imposed by the fact that the number of periodic orbits with  $t < t_H$  is prohibitively large. We had to limit the data base of periodic orbits to the domain  $t < t_{\text{cpu}}$  with  $t_{\text{erg}} \ll t_{\text{cpu}} \ll t_H$ . The time  $t_{\text{cpu}}$  has no physical origin, it represents only the limits of our computational resources. Using the available numerical data we were able to compute  $C(t)$  numerically for all  $t_{\text{erg}} < t < t_{\text{cpu}}$  and we then *extrapolated* it to the entire domain of interest. We consider this extrapolation procedure to be the main source of uncertainty. However, since the extrapolation is carried out in the *universal* regime, it should be valid if there are no other time scales between  $t_{\text{erg}}$  and  $t_H$ .

## 6.2 Numerical results

We used the formalism and definitions presented above to check the accuracy of the semiclassical spectra of the 2D and 3D Sinai billiards. The most important ingredient in this numerical study is that we could apply the *same* analysis to the two systems, and by comparing them to give a reliable answer to the main question posed in this work, namely, how does the semiclassical accuracy depend on dimensionality.

The classical dynamics in billiards depends on the energy (velocity) trivially, and therefore the relevant parameter is the length rather than the period of the periodic orbits. Likewise, the quantum wavenumbers  $k_n$  are the relevant variables in the quantum description. From now on we shall use the variables  $(l, k)$  instead of  $(t, E)$ , and use “length spectra” rather than “time spectra”. The semiclassical limit is obtained for  $k \rightarrow \infty$  and  $\mathcal{O}(\hbar)$  is equivalent to  $\mathcal{O}(k^{-1})$ . Note also that for a billiard  $\bar{N}(k) \approx Ak^d$  where  $A$  is proportional to the billiard’s volume.

We start with the 2D Sinai billiard, which is the free space between a square of edge  $S$  and an inscribed disc of radius  $R$ , with  $2R < S$ . Specifically, we use  $S = 1$  and  $R = 0.25$  and consider the quarter desymmetrized billiard with Dirichlet boundary conditions for the quantum calculations. The quantal database consists of the lowest 27645 eigenvalues in the range  $0 < k < 1320$ , with eigenstates which are either symmetric or antisymmetric with respect to reflection on the main diagonal. The classical database consists of the shortest 20273 periodic orbits (including time reversal, reflection symmetries and repetitions) in the length range  $0 < l < 5$ . For each orbit, the length, the stability determinant and the reflection phase were recorded. The numerical work is based on the quantum spectra and on the classical periodic orbits which were computed by Schanz and Smilansky [17, 94] for the 2D billiard.

We begin the numerical analysis by demonstrating numerically the correctness of equation (142). That is, that for each *individual* contribution of a periodic orbit, the semiclassical error indeed vanishes in the semiclassical limit. In figure 33 we plot  $|D - D_{sc}|$  for  $l = 0.5$  as a function of  $k$ . This length corresponds to the shortest periodic orbit, that is, the one that runs along the edge that connects the circle with the outer square. For  $D_{sc}$  we used the Gutzwiller trace formula. As is clearly seen from the figure, the quantal–semiclassical difference indeed vanishes (approximately as  $k^{-1}$ ), in accordance with (142). We emphasize again, that this behavior does not imply that  $\delta^{(2)}$  vanishes in the semiclassical limit, since the number of periodic orbits included depends on  $k$ . It implies *only* that  $\delta_{\text{short}}^{(2)}$  vanishes in the limit, since it consists of a fixed and finite number of periodic orbit contributions. We should also comment that penumbra corrections to individual grazing orbits introduce errors which are of order  $k^{-\gamma}$  with  $0 < \gamma < 1$  [81, 38]. However, since the definition of “grazing” is in itself  $k$  dependent, one can safely neglect penumbra corrections in estimating the large  $k$  behavior of  $\delta_{\text{short}}^{(2)}$ .

We now turn to the main body of the analysis, which is the evaluation of

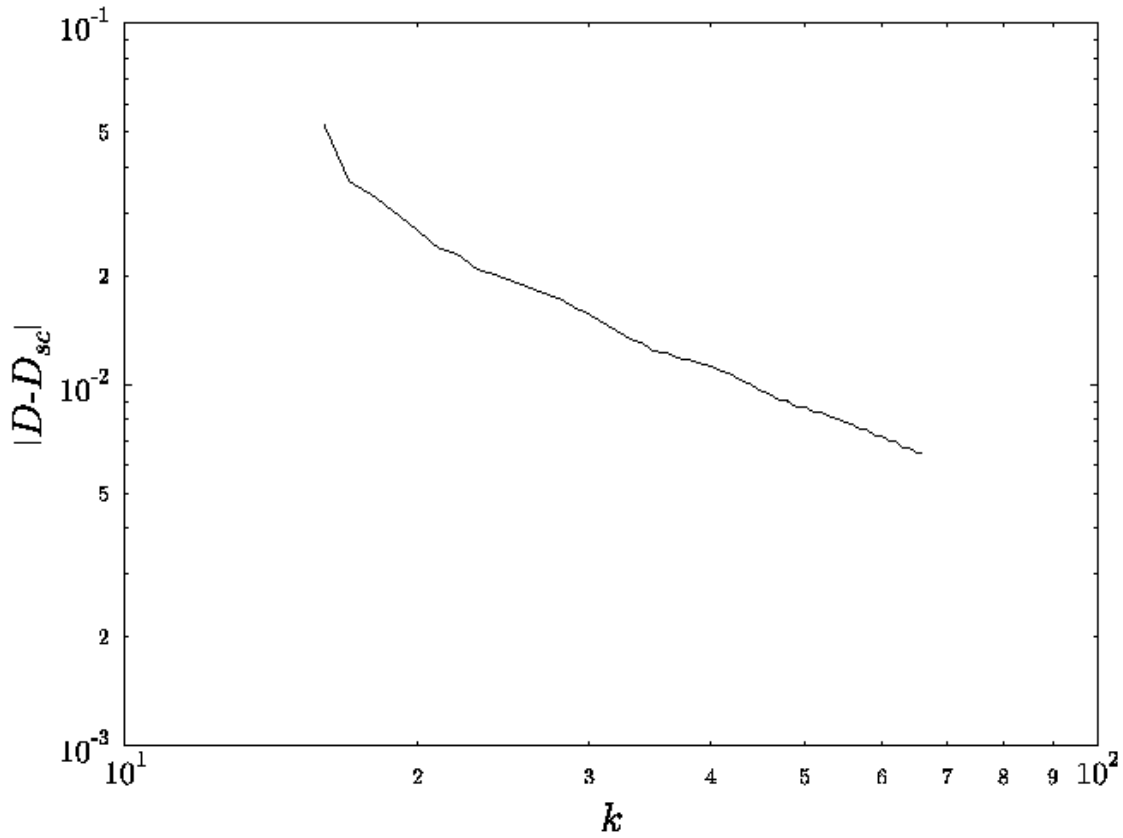


Figure 33: The absolute difference between the quantal and the semiclassical (Gutzwiller) length spectra for the 2D Sinai billiard at  $l = 0.5$ . This length corresponds to the shortest unstable periodic orbit. The average log-log slope is about  $-1.1$ , indicating approximately  $k^{-1}$  decay. The data were averaged with a Gaussian window.

$\delta_m^{(2)}$  for the 2D Sinai billiard. Based on the available data sets, we plot in figure 34 the function  $C(l; k)$  in the interval  $2.5 < l < 5$  for various values of  $k$ . One can observe, that as a function of  $l$  the functions  $C(l; k)$  fluctuate in the interval for which numerical data were available, without exhibiting any systematic mean trend to increase or to decrease. We therefore approximate  $C(l; k)$  by

$$C(l; k) \approx \text{const} \cdot f(k) \equiv C_{\text{avg}}(k). \quad (151)$$

As mentioned above, we extrapolate this formula in  $l$  up to the Heisenberg length  $L_H = 2\pi\bar{d}(k)$  and using (150) we obtain:

$$\delta_{\text{smooth}}^{(2),2D} = \frac{C_{\text{avg}}(k)}{2\pi^2} \ln(L_H/L_{\text{erg}}) = C_{\text{avg}}(k) \mathcal{O}(\ln k). \quad (152)$$

The last equality is due to  $L_H = \mathcal{O}(k^{d-1})$ . To evaluate  $C_{\text{avg}}(k)$  we averaged  $C(l; k)$  over the interval  $L_{\text{erg}} = 3.5 < l < 5 = L_{\text{cpu}}$  and the results are shown in figure 35. We choose  $L_{\text{erg}} = 3.5$  because the density of periodic orbits is large enough for this length (see figure 34) to expect universal behavior of the periodic orbits. (For the Sinai billiard described by flow the approach to the invariant measure is algebraic rather than exponential [40, 39], and thus one cannot have a well-defined  $L_{\text{erg}}$ . An any rate, the specific choice of  $L_{\text{erg}}$  did not affect the results in any appreciable way.) Inspecting  $C_{\text{avg}}(k)$ , it is difficult to arrive at firm conclusions, since it seems to fluctuate around a constant value up to  $k \approx 900$  and then to decline. If we approximate  $C_{\text{avg}}(k)$  by a constant, we get a “pessimistic” value of  $\delta^{(2)}$ :

$$\delta_{\text{smooth}}^{(2),2D}(k) = \mathcal{O}(\ln k) = \mathcal{O}(\ln \hbar) \quad \text{“pessimistic”} \quad (153)$$

while if we assume that  $C_{\text{avg}}(k)$  decays as a power-law,  $C_{\text{avg}}(k) = k^{-\beta}$ ,  $\beta > 0$ , then

$$\delta_{\text{smooth}}^{(2),2D}(k) = \mathcal{O}(k^{-\beta} \ln k) \longrightarrow 0 \quad \text{“optimistic”} . \quad (154)$$

Collecting the two bounds we get:

$$\mathcal{O}(k^{-\beta} \ln k) \leq \delta_{\text{smooth}}^{(2),2D}(k) \leq \mathcal{O}(\ln k). \quad (155)$$

Our estimates for the 2D Sinai billiard can be summarized by stating that the semiclassical error diverges no worse than logarithmically (meaning, very mildly). It may well be true that the semiclassical error is constant or even vanishes in the semiclassical limit. To reach a conclusive answer one should invest exponentially larger amount of numerical work.

There are a few comments in order here. Firstly, the quarter desymmetrization of the 2D Sinai billiard does not exhaust its symmetry group, and in fact, a reflection symmetry around the diagonal of the square remains. This means, that the spectrum of the quarter 2D Sinai billiard is composed of two independent spectra, which differ by their parity with respect to the diagonal. If we assume

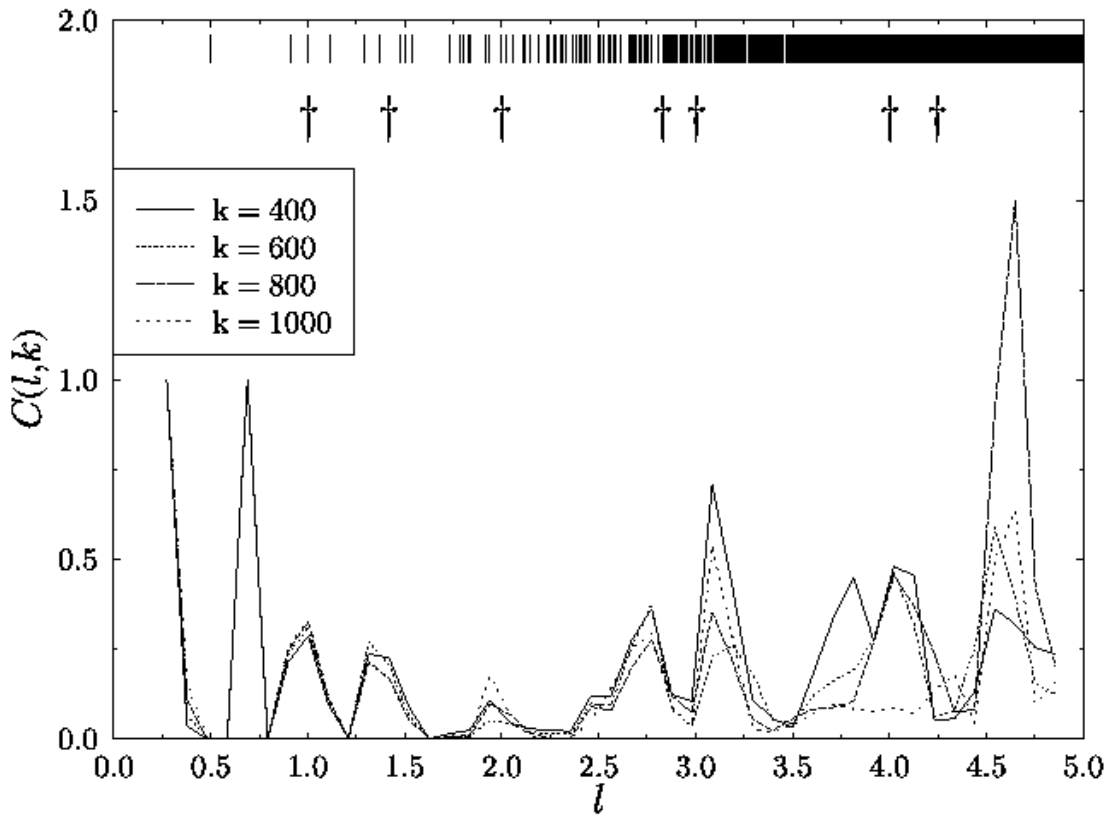


Figure 34: The functions  $C(l; k)$  for quarter 2D Sinai billiard  $S = 1, R = 0.25$  with Dirichlet boundary conditions. The window  $w(k' - k)$  was taken to be a Gaussian with standard deviation  $\sigma = 60$ . We averaged  $C(l; k)$  over  $l$ -intervals of  $\approx 0.2$  in accordance with (145) to avoid sharp peaks due to small denominators. The averaging, however, is fine enough not to wash out all of the features of  $C(l; k)$ . The vertical bars indicate the locations of primitive periodic orbits, and the daggers indicate the locations of the bouncing-ball families.

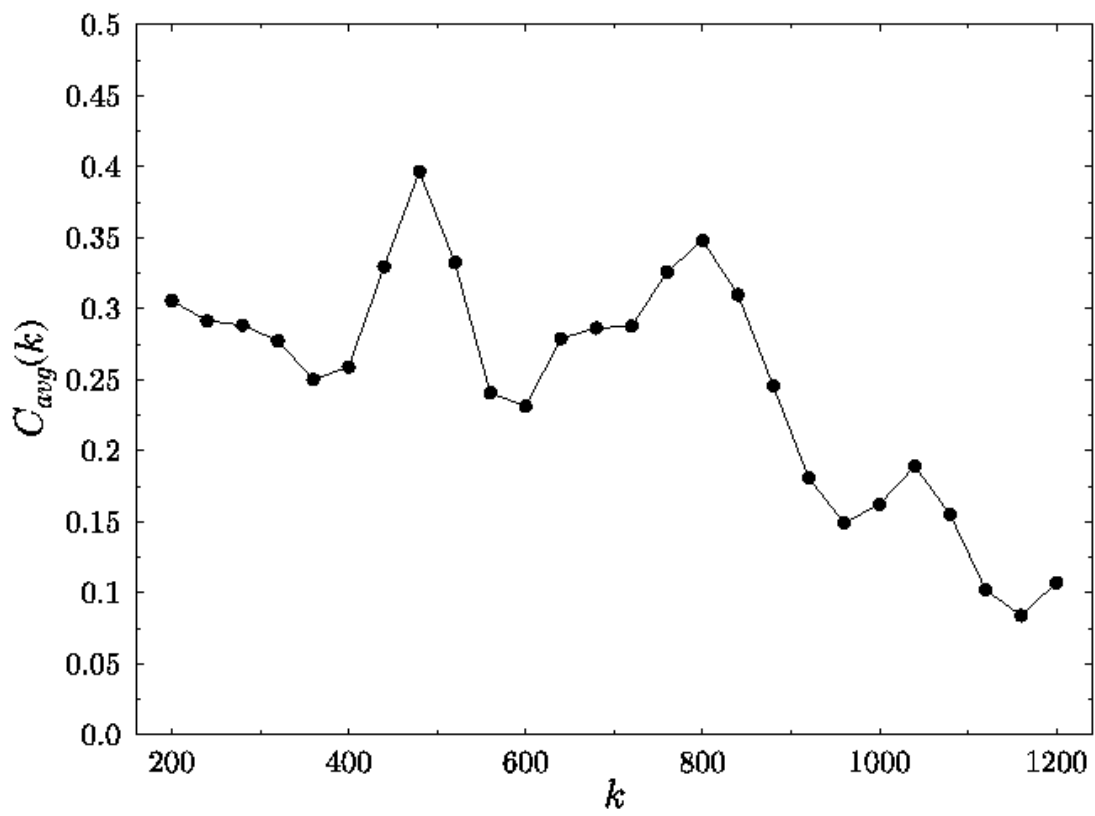


Figure 35: Averaging in  $l$  of  $C(l; k)$  for 2D Sinai billiard as a function of  $k$ .



that the semiclassical deviations of the two spectra are not correlated, the above measure is the sum of the two independent measures. It is plausible to assume also that both spectra have roughly the same semiclassical deviation, and thus  $\delta_{\text{smooth}}^{(2),2\text{D}}$  is twice the semiclassical deviation of each of the spectra. Secondly, we recall that the 2D Sinai billiard contains “bouncing–ball” families of neutrally stable periodic orbits [15, 37, 17]. We have subtracted their leading-order contribution from  $\hat{D}$  such that it includes (to leading order) only contributions from generic, isolated and unstable periodic orbits. This is done since we would like to deduce from the 2D Sinai billiard on the 2D generic case in which the bouncing–balls are not present. (In the Sinai billiard, which is concave, there are also diffraction effects [81, 38], but we did not treat them here.) Thirdly, the analogue of (147) for billiards reads:

$$\left\langle \left| \hat{D}(l) \right|_l^2 \right\rangle dl = \frac{K(\xi)}{4\pi^2 \xi^2} d\xi \quad (156)$$

when  $\xi \equiv l/L_{\text{H}}$ . In figure 36 we demonstrate the compliance of the form factor with RMT GOE using the integrated version of the above relation, and taking into account the presence of two independent spectra. Finally, it is interesting to know the actual numerical values of  $\delta_{\text{smooth}}^{(2),2\text{D}}(k)$  for the  $k$  values that we considered. We carried out the computation, and the results are presented in figure 37. One observes that for the entire range we have  $\delta_{\text{smooth}}^{(2),2\text{D}}(k) \approx 0.1 \ll 1$ , which is very encouraging from an “engineering” point of view.

We now turn to the analysis of the 3D Sinai billiard. We use the longest quantal spectrum ( $R = 0.2$ , Dirichlet) and the classical periodic orbits with length  $0 < l < 5$ .

To treat the 3D Sinai billiard we have to somewhat modify the formalism which was presented above. This is due to the fact that in the 3D case the contributions of the various non–generic bouncing–ball manifolds overwhelm the spectrum [53, 54], and unlike the 2D case, it is difficult to explicitly eliminate their (leading–order) contributions (c.f. the discussion in section 5.4). Since our goal is to give an indication of the semiclassical error in generic systems, it is imperative to avoid this dominant and non-generic effect.

We shall use the mixed boundary conditions, which were discussed in section 5.5 and were shown to largely filter the bouncing–ball effects. Specifically, we consider  $\tilde{d}$  (c.f. (113)) for our purposes. Let us construct the weighted counting function:

$$\tilde{N}(k) \equiv \int_0^k dk' \tilde{d}(k') = \sum_n v_n \Theta(k - k_n). \quad (157)$$

The function  $\tilde{N}$  is a staircase with stairs of variable height  $v_n$ . As explained above, its advantage over  $N$  is that it is semiclassically free of the bouncing balls (to leading order) and corresponds only to the generic periodic orbits [83]. Similarly, we construct from  $\tilde{d}_{\text{sc}}$  the function  $\tilde{N}_{\text{sc}}$ . Having defined  $\tilde{N}, \tilde{N}_{\text{sc}}$ , we proceed in analogy to the Dirichlet case. We form from  $\tilde{N}, \tilde{N}_{\text{sc}}$  the functions

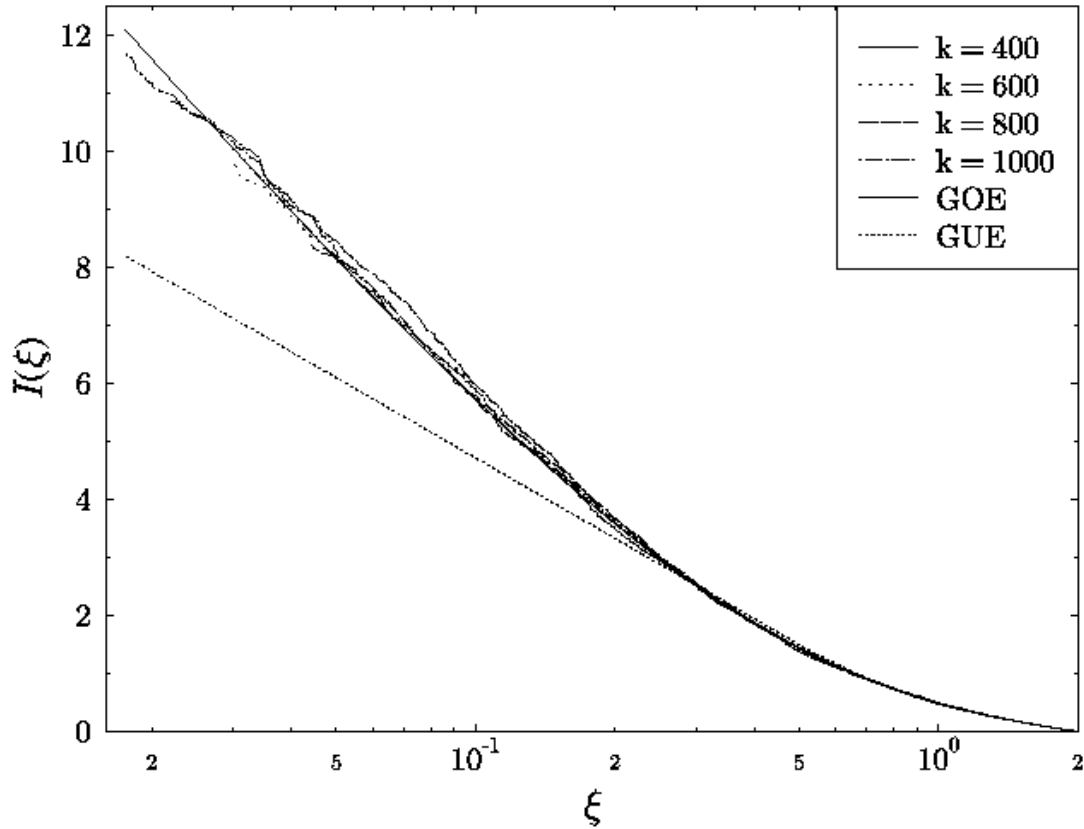


Figure 36: Verification of equation (156) for the quarter 2D Sinai billiard. We plot  $I(\xi) \equiv \int_{\xi}^2 d\xi' K(\xi')/\xi'^2$  and compare the quantum data with RMT. The minimal  $\xi$  corresponds to  $L_{\text{erg}} = 3.5$ . The integration is done for smoothing, and we fix the *upper* limit to avoid biases due to non-universal regime. Note the logarithmic scale.

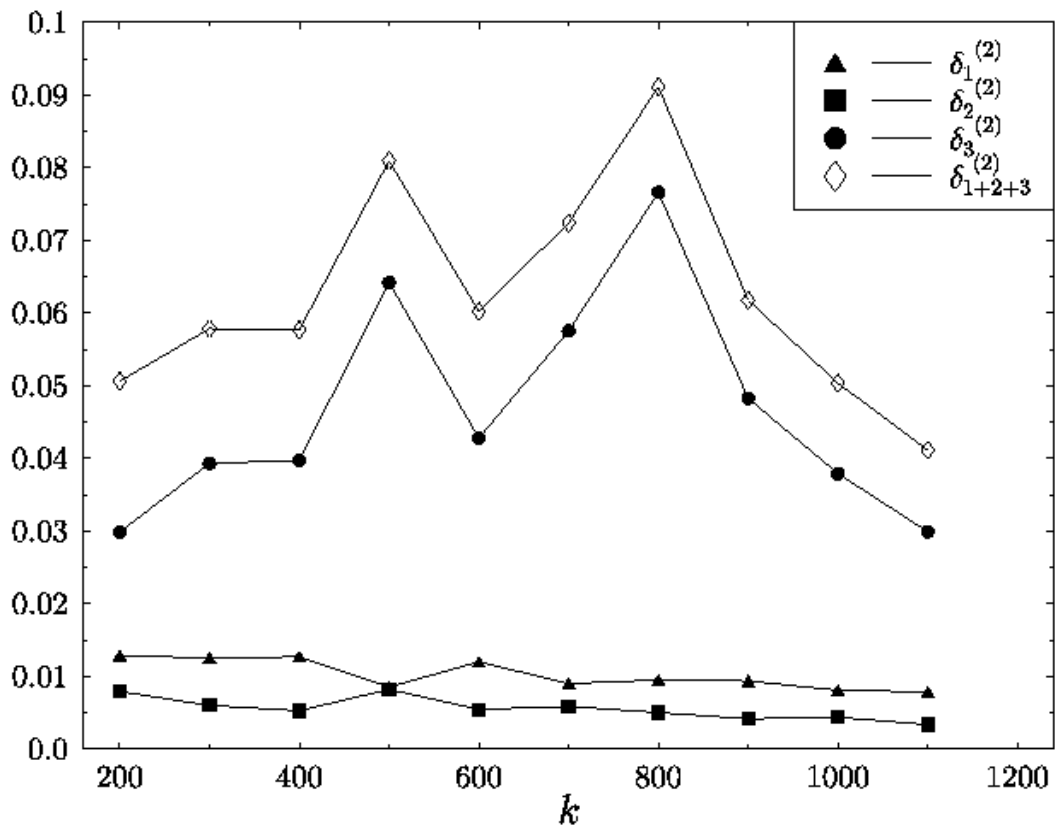


Figure 37: The numerical values of  $\delta_{\text{smooth}}^{(2)}$  for the quarter 2D Sinai billiard. We included also the contribution  $\delta_{\text{short}}^{(2)}$  of the non-universal regime. The contributions from the time interval  $t_{\text{erg}} \leq t \leq t_{\text{cpu}}$  are contained in  $\delta_{\text{m,cpu}}^{(2)}$ , and  $\delta_{\text{m,ext}}^{(2)}$  is the extrapolated value for  $t_{\text{cpu}} \leq t \leq t_{\text{H}}$  (refer to equation (141) and to the end of subsection 6.1).

$\hat{N}, \hat{N}_{\text{sc}}$ , respectively, by multiplication with a window function  $w(k' - k)$  and then construct the measure  $\delta^{(2)}$  as in (134). The only difference is that the normalization of  $w$  must be modified to account for the “velocities”  $v_n$  such as:

$$\bar{d}^{-1}(k) \sum_n v_n^2 |w(k_n - k)|^2 = 1. \quad (158)$$

The above considerations are meaningful provided the “velocities”  $v_n$  are narrowly distributed around a well-defined mean  $v(k)$ , and we consider a small enough  $k$ -interval, such that  $v(k)$  does not change appreciably within this interval. Otherwise,  $\delta^{(2)}$  is greatly affected by the fluctuations of  $v_n$  (which is undesired) and the meaning of the normalization is questionable. We shall check this point numerically.

To demonstrate the utility of the above construction using the mixed boundary conditions, we return to the 2D case. We set  $\kappa = 100\pi$ , and note that the spectrum at our disposal for the mixed case was confined to the interval  $0 < k < 600$ . First, we want to examine the width of the distribution of the  $v_n$ 's. In figure 38 we plot the ratio of the standard deviation of  $v_n$  to the mean, averaged over the  $k$ -axis using a Gaussian window. We use the same window also in the calculations below. The observation is that the distribution of  $v_n$  is moderately narrow and the width decreases algebraically as  $k$  increases. This justifies the use of the mixed boundary conditions as was discussed above. One also needs to check the validity of (156), and indeed we found compliance with GOE also for the mixed case (results not shown). We next compare the functions  $C(l; k)$  for both the Dirichlet and the mixed boundary conditions. It turns out, that also in the mixed case the functions  $C(l; k)$  fluctuate in  $l$  with no special tendency (not shown). The averages  $C_{\text{avg}}(k)$  for the Dirichlet and mixed cases are compared in figure 39. The values in the mixed case are systematically smaller than in the Dirichlet case which is explained by the efficient filtering of tangent and close to tangent orbits that are vulnerable to large diffraction corrections [81, 38]. However, from  $k = 250$  on the two graphs show the same trends, and the values of  $C_{\text{avg}}$  in both cases are of the same magnitude. Thus, the qualitative behavior of  $\delta_{\text{smooth}}^{(2)}$  is shown to be equivalent in the Dirichlet and mixed cases, which gives us confidence in using  $\delta_{\text{smooth}}^{(2)}$  together with the mixed boundary conditions procedure.

We finally applied the mixed boundary conditions procedure to compute  $\delta_{\text{smooth}}^{(2)}$  for the desymmetrized 3D Sinai with  $S = 1, R = 0.2$  and set  $\kappa = 100$ . We first verified that also in the 3D case the velocities  $v_n$  have a narrow distribution — see figure 38. Next, we examined equation (156) using quantal data, and discovered that there are deviations from GOE (figure 40). We have yet no satisfactory explanation of these deviations, but we suspect that they are caused because the ergodic limit is not yet reached for the length regime under consideration due to the effects of the infinite horizon which are more acute in 3D. Nevertheless, from observing the figure as well as suggested by semiclassical

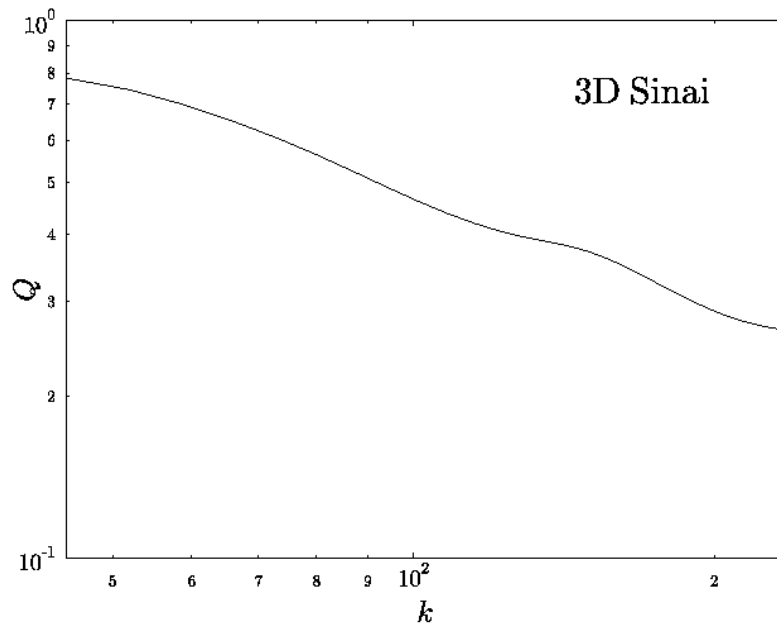
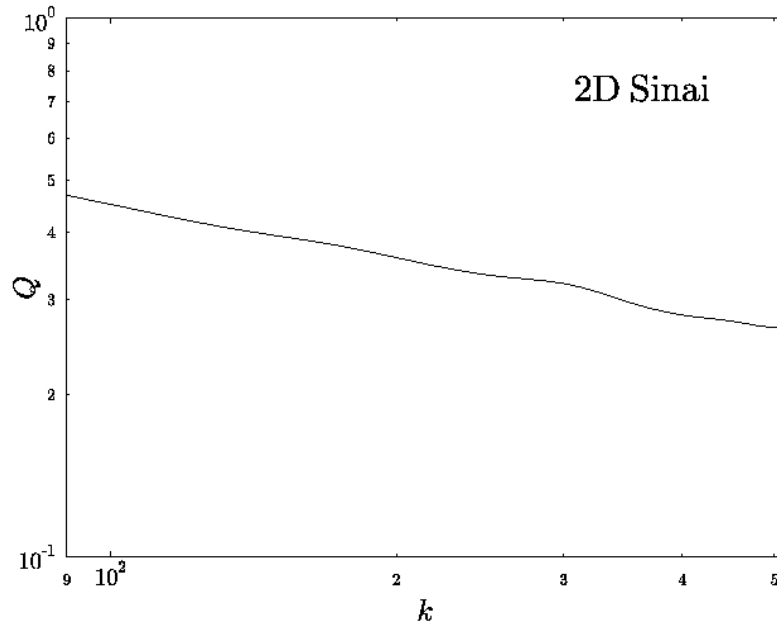


Figure 38: Calculation of  $Q \equiv \sqrt{\langle v_n^2 \rangle - \langle v_n \rangle^2} / |\langle v_n \rangle|$  for quarter 2D Sinai billiard (up) and for the desymmetrized 3D Sinai billiard (down).

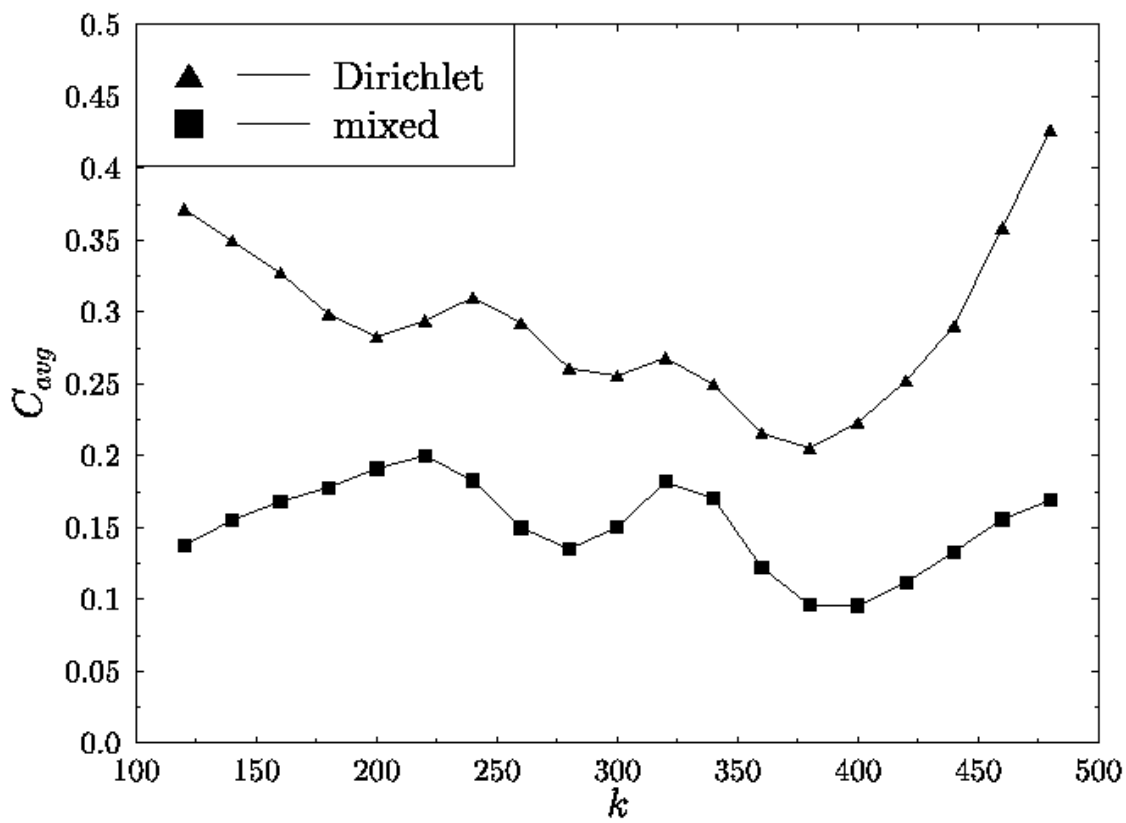


Figure 39: Comparison of  $C_{avg}(k)$  for Dirichlet and mixed boundary conditions for the quarter 2D Sinai billiard. We used a Gaussian window with  $\sigma = 40$ .

arguments, it is plausible to assume that  $K(\xi) \propto \xi$  for small  $\xi$ . Hence, this deviation should not have any qualitative effect on  $\delta^{(2)}$  according to (150). Similarly to the 2D case, the behavior of the function  $C(l; k)$  is fluctuative in  $l$ , with no special tendency (figure 41). If we average  $C(l; k)$  over the universal interval  $L_{\text{erg}} = 2.5 \leq l \leq L_{\text{cpu}} = 5$ , we obtain  $C_{\text{avg}}(k)$  which is shown in figure 42. The averages  $C_{\text{avg}}(k)$  are fluctuating with a mild decrease in  $k$ , and therefore we can again conclude that

$$\mathcal{O}(k^{-\beta} \ln k) \leq \delta_{\text{smooth}}^{(2),3\text{D}} \leq \mathcal{O}(\ln k) \quad (159)$$

where the ‘‘optimistic’’ measure (leftmost term) corresponds to  $C_{\text{avg}}(k) = \mathcal{O}(k^{-\beta})$ ,  $\beta > 0$ , and the ‘‘pessimistic’’ one (rightmost term) is due to  $C_{\text{avg}}(k) = \text{const}$ . In other words, the error estimates (155, 159) for the 2D and the 3D cases, respectively, are the same, and in sharp contrast to the traditional error estimate which predicts that the errors should be different by a factor  $\mathcal{O}(\hbar^{-1})$ . On the basis of our numerical data, and in spite of the uncertainties which were clearly delineated, we can safely rule out the traditional error estimate.

Our main finding is that the upper bound on the semiclassical error is a logarithmic divergence, both for a generic 2D and 3D systems (equations (155), (159)). In this respect, there are a few points which deserve discussion.

To begin, we shall try to evaluate  $\delta_{\text{smooth}}^{(2)}$  using the explicit expressions for the leading corrections to the semiclassical counting function of a 2D generic billiard system, as derived by Alonso and Gaspard [7]:

$$N(k) = \bar{N}(k) + \sum_j \frac{A_j}{L_j} \sin \left[ kL_j + \frac{Q_j}{k} + \mathcal{O}(1/k^2) \right] \quad (160)$$

where  $A_j$  are the standard semiclassical amplitudes,  $L_j$  are the lengths of periodic orbits and  $Q_j$  are the  $k$ -independent amplitudes of the  $1/k$  corrections. The  $Q_j$ 's are explicitly given in [7]. We ignored in the above equation the case of odd Maslov indices. If we calculate from  $N(k)$  the corresponding length spectrum  $\hat{D}(l; k)$  using a (normalized) Gaussian window  $w(k' - k) = (1/\sqrt[4]{\pi\sigma^2}) \exp[-(k' - k)^2/(2\sigma^2)]$ , we obtain:

$$\hat{D}(l; k) \approx \frac{i\sqrt{\sigma}}{2\sqrt[4]{\pi}} \sum_j \frac{A_j}{L_j} \left[ e^{ik(l-L_j) - i\frac{Q_j}{k}} e^{-(l-L_j)^2 \frac{\sigma^2}{2}} - e^{ik(l+L_j) + i\frac{Q_j}{k}} e^{-(l+L_j)^2 \frac{\sigma^2}{2}} \right]. \quad (161)$$

In the above we regarded the phase  $e^{iQ_j/k}$  as slowly varying. The results of Alonso and Gaspard [7] suggest that the  $Q_j$  are approximately proportional to the length of the corresponding periodic orbits:

$$Q_j \approx QL_j. \quad (162)$$

We can therefore well-approximate  $\hat{D}$  as:

$$\hat{D}(l; k) \approx \frac{i\sqrt{\sigma}}{2\sqrt[4]{\pi}} e^{-iQl/k} \sum_j \frac{A_j}{L_j} [\dots] = e^{-iQl/k} \hat{D}_{\text{sc-GTF}}, \quad (163)$$

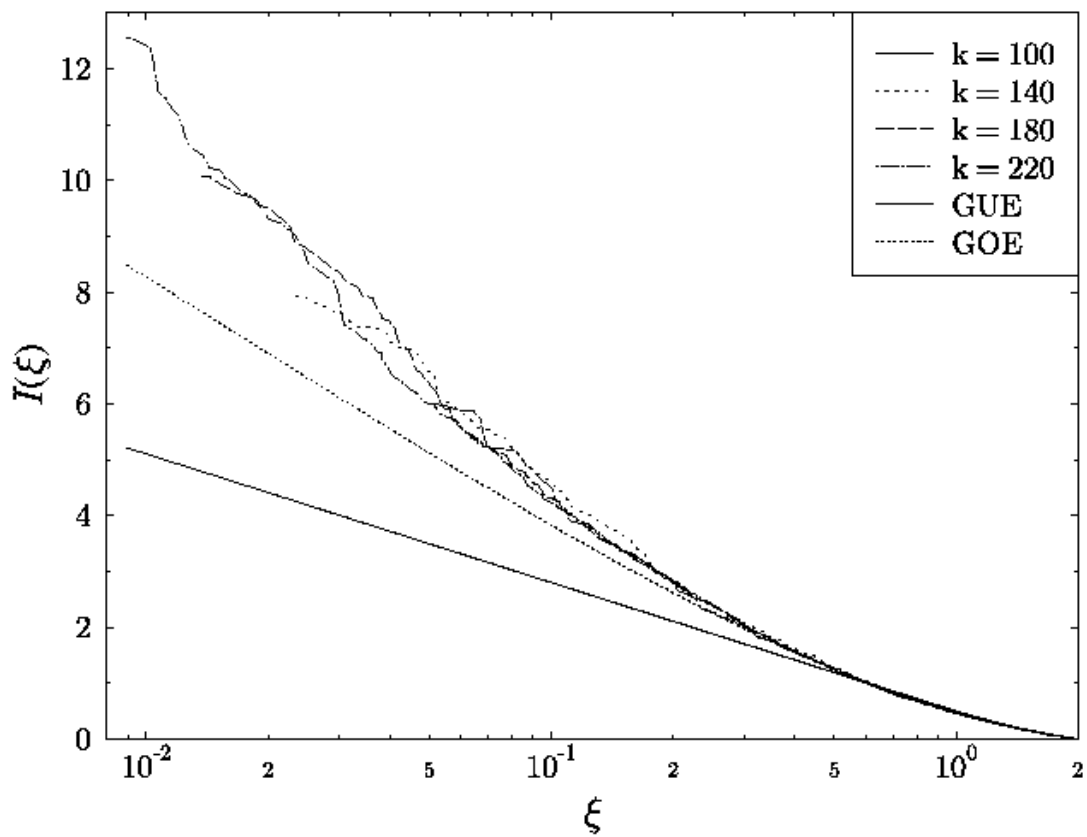


Figure 40: Check of equation (156) for the desymmetrized 3D Sinai billiard. The minimal  $\xi$  corresponds to  $L_{\text{erg}} = 2.5$ . The function  $I(\xi)$  is defined as in figure 36. Note the logarithmic scale.



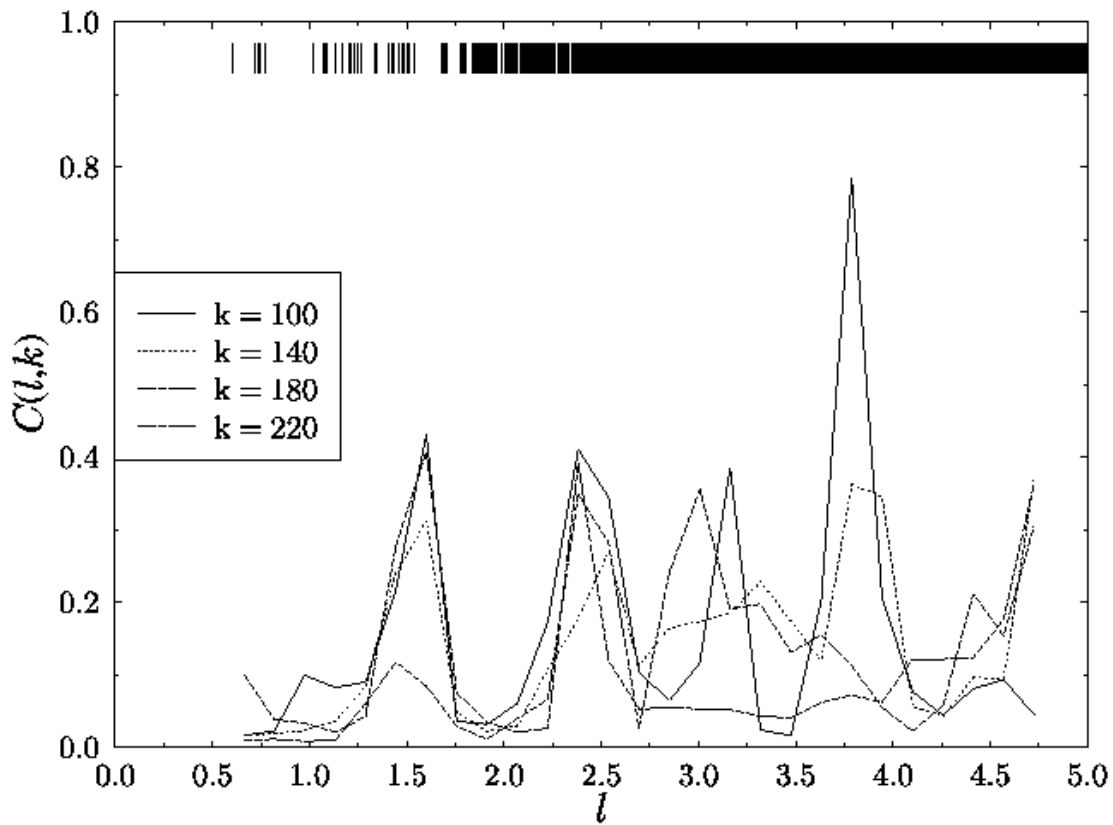


Figure 41: The functions  $C(l; k)$  for desymmetrized 3D Sinai billiard  $S = 1, R = 0.2$  with mixed boundary conditions. We took a Gaussian window with  $\sigma = 20$ , and smoothed over  $l$ -intervals of  $\approx 0.3$ . The upper vertical bars indicate the locations of primitive periodic orbits.

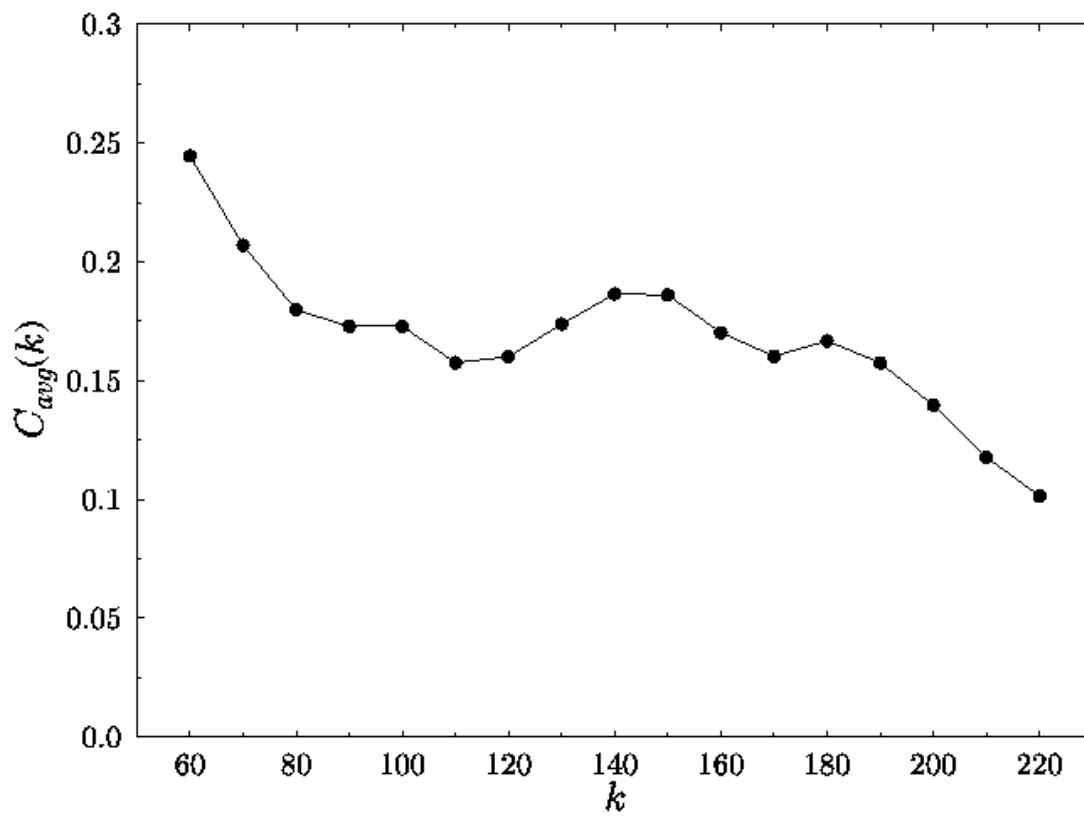


Figure 42: Averaging in  $l$  of  $C(l; k)$  for 3D Sinai billiard as a function of  $k$ . The averaging was performed in the interval  $L_{\text{erg}} = 2.5 < l < 5 = L_{\text{cpu}}$ .

where  $\hat{D}_{\text{sc-GTF}}$  is the length spectrum which corresponds to the semiclassical Gutzwiller trace formula for the counting function (without  $1/k$  corrections). We are now in a position to evaluate the semiclassical error, indeed:

$$\begin{aligned}\delta_{\text{smooth}}^{(2)}(k) &= 2 \int_{L_{\min}}^{L_{\text{H}}} dl \left| \hat{D}(l; k) - \hat{D}_{\text{sc-GTF}}(l; k) \right|^2 = \\ &= 8 \int_{L_{\min}}^{L_{\text{H}}} dl \sin^2 \left( \frac{Ql}{2k} \right) \left| \hat{D}(l; k) \right|^2.\end{aligned}\quad (164)$$

If we use equation (156) and  $K(l) \approx gl/L_{\text{H}}$  (which is valid for  $l < L_{\text{H}}$  for chaotic systems), we get:

$$\delta_{\text{smooth}}^{(2)}(k) \approx \frac{2g}{\pi^2} \int_{L_{\min}}^{L_{\text{H}}} \frac{dl}{l} \sin^2 \left( \frac{Ql}{2k} \right) = \frac{2g}{\pi^2} \int_{QL_{\min}/(2k)}^{QL_{\text{H}}/(2k)} dt \frac{\sin^2(t)}{t}.\quad (165)$$

For  $k \rightarrow \infty$  we have that

$$\int_0^{QL_{\min}/(2k)} dt \frac{\sin^2(t)}{t} \approx \int_0^{QL_{\min}/(2k)} dt \cdot t = \mathcal{O}(1/k^2)\quad (166)$$

which is negligible, hence we can replace the lower limit in (165) with 0:

$$\delta_{\text{smooth}}^{(2)}(k) \approx \frac{2g}{\pi^2} \int_0^{QL_{\text{H}}/(2k)} dt \frac{\sin^2(t)}{t}.\quad (167)$$

This is the desired expression. The dimensionality enter in  $\delta_{\text{smooth}}^{(2)}(k)$  only through the power of  $k$  in  $L_{\text{H}}$ .

Let us apply equation (167) to the 2D and the 3D cases. For 2D we have to leading order that  $L_{\text{H}} = Ak$ , where  $A$  is the billiard's area, thus,

$$\delta_{\text{analytical}}^{(2),2\text{D}}(k) \approx \frac{2g}{\pi^2} \int_0^{QA/2} dt \frac{\sin^2(t)}{t} = \text{const} = \mathcal{O}(k^0)\quad (168)$$

which means, that the semiclassical error in 2D billiards is of the order of the mean spacing, and therefore the semiclassical trace formula is (marginally) accurate and meaningful. This is compatible with our numerical findings.

For 3D, the coefficients  $Q_j$  were not obtained explicitly, but we shall assume that they are still proportional to  $L_j$  (equation (162)) and therefore that (167) holds. For 3D billiards  $L_{\text{H}} = (V/\pi)k^2$  to leading order, where  $V$  is the billiard's volume. Thus the upper limit in (167) is  $QVk/(2\pi)$  which is large in the semiclassical limit. In this case, we can replace  $\sin^2(t)$  with its mean value  $1/2$  and the integrand becomes essentially  $1/t$  which results in:

$$\delta_{\text{analytical}}^{(2),3\text{D}}(k) = \mathcal{O}(\ln k).\quad (169)$$

That is, in contrast to the 2D case, the semiclassical error diverges logarithmically and the semiclassical trace formula becomes meaningless as far as the prediction of individual levels is concerned. This statement is compatible with our numerical results within the numerical dispersion. However, it relies heavily on the assumption that  $Q_j \approx QL_j$ , for which we can offer no justification. We note in passing, that the logarithmic divergence persists also for  $d > 3$ .

Another interesting point relates to integrable systems. It can happen, that for an integrable system it is either difficult or impossible to express the Hamiltonian as an explicit function of the action variables. In that case, we cannot assign to the levels other quantum numbers than their ordinal number, and the semiclassical error can be estimated using  $\delta^{(2)}$ . However, since for integrable systems  $K(\tau) = 1$ , we get that:

$$\delta_{\text{smooth}}^{(2),\text{int}} \approx \frac{1}{2\pi^2} \int_{\tau_{\text{erg}}}^1 d\tau \frac{C(\tau)}{\tau^2}. \quad (170)$$

Therefore, for deviations which are comparable to the chaotic cases,  $C(\tau) = \mathcal{O}(1)$ , we get  $\delta_{\text{smooth}}^{(2),\text{int}} = \mathcal{O}(\hbar^{1-d})$  which is much larger than for the chaotic case and diverges for  $d \geq 1$ .

The formula (150) for the semiclassical error contains semiclassical information in two respects. Obviously,  $C(\tau)$ , which describes the difference between the quantal and the semiclassical length spectra, contains semiclassical information. But also the fact that the lower limit of the integral in (150) is finite is a consequence of semiclassical analysis. If this lower limit is replaced by 0, the integral diverges for finite values of  $\hbar$ . Therefore, the fact that the integral has a lower cutoff, or rather, that  $D$  is exactly 0 below the shortest period, is a crucial semiclassical ingredient in our analysis.

Finally, we consider the case in which the semiclassical error is estimated with no periodic orbits taken into account. That is, we want to calculate  $\langle |N(E) - \bar{N}(E)|^2 \rangle_E$  which is the number variance  $\Sigma^2(x)$  for the large argument  $x = \Delta E \bar{d}(E) \gg 1$ . This implies  $C(\tau) = 1$ , and using (150) we get that  $\delta_{\text{smooth}}^{(2)} = g/(2\pi^2) \ln(t_{\text{H}}/t_{\text{erg}})$ , which in the semiclassical limit becomes  $g/(2\pi^2) \ln(t_{\text{H}}) = \mathcal{O}(\ln \hbar)$ . This result is fully consistent and compatible with previous results for the asymptotic (saturation) value of the number variance  $\Sigma^2$  (see for instance [65, 95, 96]). It implies also that the pessimistic error bound (153) is of the same magnitude as if periodic orbits were not taken into account at all. (Periodic orbits improve, however, quantitatively, since in all cases we obtained  $C_{\text{avg}} < 1$ .) Thus, if we assume that periodic orbit contributions do not make  $N_{sc}$  worse than  $\bar{N}$ , then the pessimistic error bound  $\mathcal{O}(\ln \hbar)$  is the *maximal* one in any dimension  $d$ . This excludes, in particular, algebraic semiclassical errors, and thus refutes the traditional estimate  $\mathcal{O}(\hbar^{2-d})$ .

## 7 Semiclassical theory of spectral statistics

In section 3 we studied several quantal spectral statistics of the Sinai billiard and have shown that they can be reproduced to a rather high accuracy by the predictions of Random Matrix Theory (RMT). In the present section we would like to study the spectral two-point correlation function in the semiclassical approximation, and to show how the classical sum rules and correlations of periodic orbits, which were defined in section 4, can be used to reconstruct, within the semiclassical approximation, the predictions of RMT.

The starting point of the present discussion is the observation that the semiclassical spectrum can be derived from a secular equation of the form [26, 84]:

$$Z_{\text{sc}}(k) \equiv \det(I - S(k)) = 0, \quad (171)$$

where  $S(k)$  is a (semiclassically) unitary matrix which depends parametrically on the wavenumber  $k$ . In the semiclassical approximation, the unitary operator  $S(k)$  can be considered as the quantum analogue of a classical Poincaré mapping, which for billiard systems in  $d$  dimensions, is the classical billiard bounce map. The dimension  $N(k)$  of the Hilbert space on which  $S(k)$  acts, can be expressed within the semiclassical approximation, in terms of the phase-space volume of the Poincaré section  $\mathcal{M}$  as follows:

$$N(k) = [\mathcal{N}(k)], \quad \mathcal{N}(k) = \frac{\mathcal{M}}{(2\pi\hbar)^{d-1}}, \quad (172)$$

where  $[\cdot]$  stands for the integer value. For a billiard in two dimensions  $\mathcal{N}(k) = \mathcal{L}k/\pi$ , where  $\mathcal{L}$  is the circumference of the billiard. In the case of the fully desymmetrized 3D Sinai billiard, for which we consider the sphere return map,  $\mathcal{N}(k) = k^2 R^2/48$ . The reason why we defined the smooth function  $\mathcal{N}(k)$  will become clear in the sequel.

The eigenvalues of  $S(k)$  are on the unit circle:  $\{\exp(i\theta_l(k))\}_{l=1}^{N(k)}$ . If for a certain  $k$ , one of the eigenphases is an integer multiple of  $2\pi$ , then equation (171) is satisfied, and this value of  $k$  belongs to the spectrum. Because of this connection between the billiard spectrum on the  $k$  axis and the eigenphase spectrum on the unit circle, the statistics of  $k$ -intervals can be read off the corresponding statistics of the eigenphase intervals averaged over an appropriate  $k$ -interval where  $N(k)$  is constant [26, 84]. For this reason, it is enough to study the eigenphase statistics, and if they can be reproduced by the predictions of RMT for the relevant *circular* ensemble, the wavenumber spectral statistics will conform with the prediction of RMT for the corresponding *Gaussian* ensemble.

The spectral density of the matrix  $S(k)$  can be written as:

$$d_{\text{qm}}(\theta; k) \equiv \sum_{l=1}^{N(k)} \delta(\theta - \theta_l(k)) = \frac{N(k)}{2\pi} + \frac{1}{2\pi} \sum_{n=1}^{\infty} (e^{-in\theta} \text{tr} S^n + e^{in\theta} \text{tr} (S^\dagger)^n). \quad (173)$$

The corresponding two-point correlation function is derived by computing:

$$C_2(\eta) = \frac{2\pi}{N} \left\langle \int_0^{2\pi} \frac{d\theta}{2\pi} d_{\text{qm}}(\theta + \frac{\eta}{2}; k) d_{\text{qm}}(\theta - \frac{\eta}{2}; k) \right\rangle, \quad (174)$$

where  $\langle \cdot \rangle$  denotes an average over a  $k$ -interval where  $N(k)$  takes the constant value  $N$ . The two-point spectral form factor is defined as the Fourier coefficients of  $C_2(\eta)$ , and by substituting (173) in (174), one finds that they are equal to  $\frac{1}{N} \langle |\text{tr} S^n(k)|^2 \rangle$ . RMT provides an explicit expression:

$$\frac{1}{N} \langle |\text{tr} S^n(k)|^2 \rangle_{\text{RMT}} = K_\beta \left( \frac{n}{N(k)} \right), \quad (175)$$

where  $\beta$  is the standard ensemble label [59]. The most important fact to be noticed is that  $n$ , the ‘‘topological time’’, is scaled by  $N$ , which plays here the rôle of the Heisenberg time. For a Poisson ensemble:

$$\frac{1}{N} \langle |\text{tr} S^n(k)|^2 \rangle_{\text{Poisson}} = 1. \quad (176)$$

From now on we shall be concerned with the Circular Orthogonal Ensemble (COE:  $\beta = 1$ ). We define  $\tau_{\text{equiv}}/N$ . The function  $K_{\text{COE}}(\tau)$  is a monotonically increasing function which starts as  $2\tau$  near the origin, and bends towards its asymptotic value 1 in the vicinity of  $\tau = 1$ . For an explicit expression consult, e.g. [72]. Our aim is to show that the semiclassical expression for  $\frac{1}{N} \langle |\text{tr} S^n(k)|^2 \rangle$  reproduces this behaviour when the correlations of periodic orbits are properly taken into account.

Recalling that the unitary matrix  $S(k)$  is the quantum analogue of the Poincaré map, one can express  $\text{tr} S^n(k)$  in terms of the  $n$ -periodic orbits of the mapping. If the semiclassical mapping is hyperbolic, and the billiard bounce map is considered, one gets [72]:

$$\text{tr} S^n(k) \approx \sum_{j \in \mathcal{P}_n} \frac{n_{p,j}}{|\det(I - M_j)|^{\frac{1}{2}}} e^{ikL_j} (-1)^{b_j}. \quad (177)$$

Here  $\mathcal{P}_n$  is the set of all  $n$ -periodic orbits of the bounce map,  $n_{p,j}$  is the period of the primitive orbit of which the  $n$ -periodic orbit is a multiple. The monodromy matrix is denoted  $M_j$ ,  $L_j$  is the length, and  $b_j$  is the number of bounces from the boundaries (for a Dirichlet boundary condition). Note that when the Poincaré section consists of a part of the boundary (as is the case for the sphere return map in the 3D Sinai billiard),  $b_j$  can be different from  $n$ . Recalling the definition of the classical density  $d_{\text{cl}}(l; n)$  (72) in subsection 4.4, and realizing that the pre-exponential factors are just the  $\tilde{A}_j$  coefficients (73), we deduce that within the semiclassical approximation,

$$\int_0^{2\pi} e^{in\theta} d_{\text{qm}}(\theta; k) d\theta = \text{tr} S^n(k) \approx \int_0^\infty e^{ikl} d_{\text{cl}}(l; n) dl. \quad (178)$$

This equation is of fundamental importance, because it expresses the duality between the quantum mechanical spectral density and the classical length density via their Fourier transforms [11]. Hence, the spectral form factors of the classical and the quantum spectral distributions are also related by:

$$\frac{1}{N} \langle |\text{tr} S^n(k)|^2 \rangle = \frac{1}{N} \langle K_{\text{cl}}(k; n) \rangle = \frac{1}{N} \left\langle \left| \sum_{j \in \mathcal{P}_n} \tilde{A}_j e^{ikL_j} \right|^2 \right\rangle. \quad (179)$$

We have shown already in section 4.4 that the length spectrum as defined by the classical density (72) contains non-trivial correlations. They appear on a scale  $\lambda(n; R)$  which is inversely proportional to the value of  $k$  where the classical correlation function approaches its asymptotic value  $gn$ . What remains to be seen now is the extent by which the semiclassical expression (179) reproduces the expected universal scaling and the detailed functional dependence on the scaled topological time  $\tau = n/N$  as predicted by RMT.

The large  $k$  limit of  $K_{\text{cl}}(k; n)$  was written explicitly in (79) and verified numerically:

$$K_{\text{cl}}(k \rightarrow \infty; n) \approx \langle n_p g_p \rangle \cdot U(n) \approx 2n. \quad (180)$$

This limit corresponds to the limit  $\frac{n}{N(k)} \rightarrow 0$  so that

$$\frac{1}{N} \langle |\text{tr} S^n(k)|^2 \rangle \approx \frac{2n}{N}, \quad (181)$$

which is identical to the behavior of  $K_{\text{COE}}(\tau)$  in the small  $\tau$  limit [59]. Therefore, the classical uniform coverage of phase space guarantees the adherence to RMT in the limit  $\tau \rightarrow 0$ . This result was derived originally by Berry in his seminal paper [4]. It is the “diagonal approximation” which can be used as long as the range of  $k$  values is larger than  $\lambda(n; R)^{-1}$ . In other words, this approximation is valid on the scale on which the classical length spectrum looks uncorrelated. This observation shows that the domain of validity of the diagonal approximation has nothing to do with the “Ehrenfest time”, sometimes also called the “ $\log \hbar$  time”. Rather, it depends on the correlation length in the classical spectrum  $\lambda(n; R)$ , as displayed by the classical form factor.

Given the classical correlation function,  $K_{\text{cl}}(k; n)$ , it cannot be meaningfully compared to the COE result at all values of the parameters. This is because once  $N(k) = 1$ , one cannot talk about quantum two-point correlations, since the spectrum consists of a single point on the unit circle. In other words, this is the extreme quantum limit, where the Hilbert space consists of a single state. Therefore, the  $k$ -values to be used must exceed in the case of the 3D Sinai billiard  $k_{\text{min}} = \sqrt{96}/R$ , which corresponds to  $\mathcal{N}(k) = 2$ . Hence, the values of  $\tau = n/N$  which are accessible are restricted to the range  $0 \leq \tau \leq n/2$ .

In figure 43 we summarize our numerical results by comparing the form factor obtained from periodic orbit theory  $K_{\text{cl}}$  with the theoretical RMT predic-

tion  $K_{\text{COE}}$ . What we actually show is the running average,

$$C(\tau) \equiv \frac{1}{\tau} \int_0^\tau d\tau' \frac{\tau'}{n} K_{\text{cl}}(\tau'), \quad (182)$$

where  $K_{\text{cl}}(\tau) \equiv K_{\text{cl}}(k(\tau; n); n)$ . The corresponding COE curve (c.f. equations (175) and (179)) is given by:

$$C(\tau) \equiv \frac{1}{\tau} \int_0^\tau d\tau' K_{\text{COE}}(\tau'). \quad (183)$$

The ‘‘diagonal approximation’’ curve is obtained by replacing  $K_{\text{COE}}(\tau)$  by  $2\tau$ , namely, classical correlations are ignored. The data sets which were chosen are those for which sufficiently many periodic orbits were computed so that the sum rule  $U(n; l) \approx 1$  was satisfied. We did not include the  $n = 1$  data because they are non-generic. As clearly seen from the figure, the data are consistent with the RMT expression and they deviate appreciably from the diagonal approximation. This is entirely due to the presence of classical correlations, and it shows that the classical correlations are indeed responsible for the quantitative agreement. Note also that the data represents four different combinations of  $n$  and  $R$ , which shows that the classical scaling is indeed consistent with the universal scaling implied by RMT. In figure 44 we present essentially the same data, but integrated and plotted using the variable  $k$ , similarly to section 4. The integration started at  $k_{\text{min}}$  for a meaningful comparison with RMT. Again, we observe the quantitative agreement, which is especially good for the higher  $n$  values ( $n = 3, 4$ ).

In section 4.4 we showed that the classical correlations originate to a large extent from the  $\Omega(W)$  families of periodic orbits. Moreover, the form factor which was calculated by neglecting cross-family contributions was much smoother than the original one. It is therefore appealing to take advantage of this smoothness and compare the numerical and theoretical form factors themselves instead of their running averages. We define:

$$K_{\text{cl}}(N; n) \equiv \langle K_{\text{cl}}(k; n) \rangle_N = \frac{1}{k(N+1) - k(N)} \int_{k(N)}^{k(N+1)} dk' K_{\text{cl}}(k'; n) \quad (184)$$

which is the semiclassical ensemble average of the form factor. In figure 45 we compare  $K_{\text{cl}}(N; n)$  with  $N \cdot K_{\text{COE}}(n/N)$ . The classical form factor included intra-family contribution only, and we multiplied it by a factor such that asymptotically it will match the theoretical value  $2n$ . This factor compensates for the partial breaking of time-reversal symmetry and for the fact that the classical saturation is to values slightly below  $2n$  for the  $n$ 's under consideration. One observes that the agreement is quite good, and in any case the classical form factor is sharply different from the diagonal approximation, meaning that classical correlations are important. In figure 46 we present the same results with  $\tau = n/N$  as the



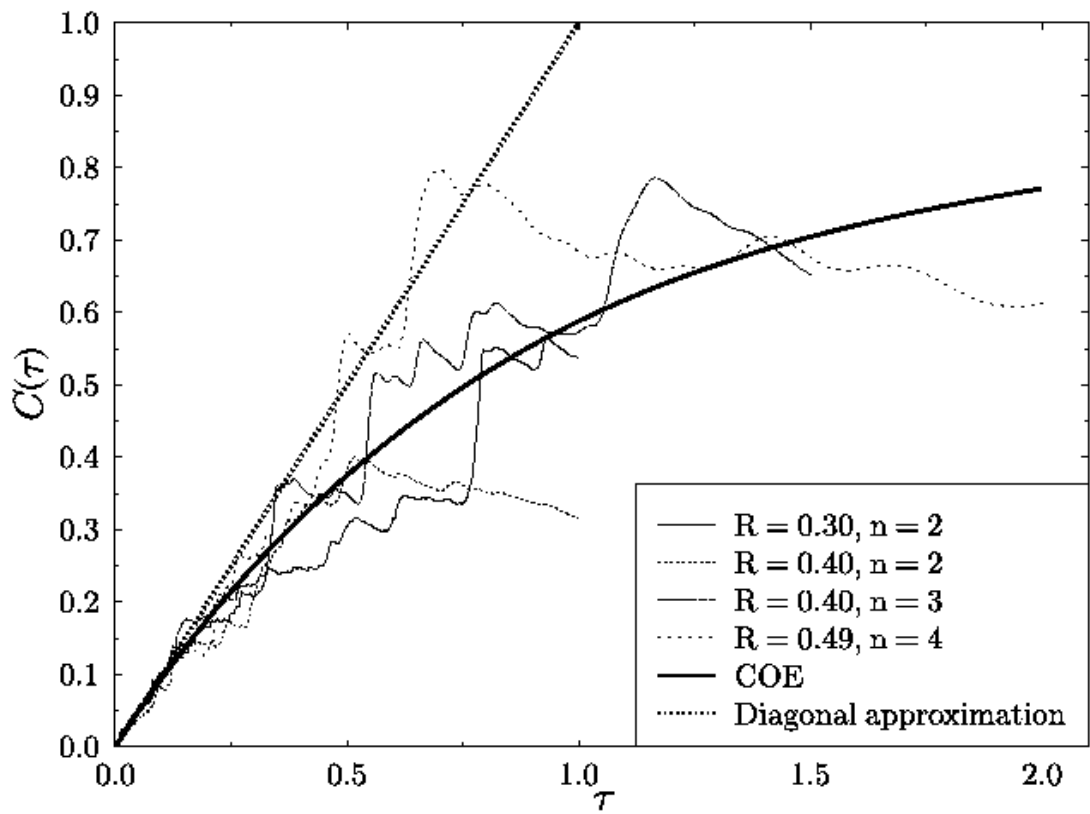


Figure 43: Comparing the classical form factor with the universal RMT predictions for various cases of the 3D SB.

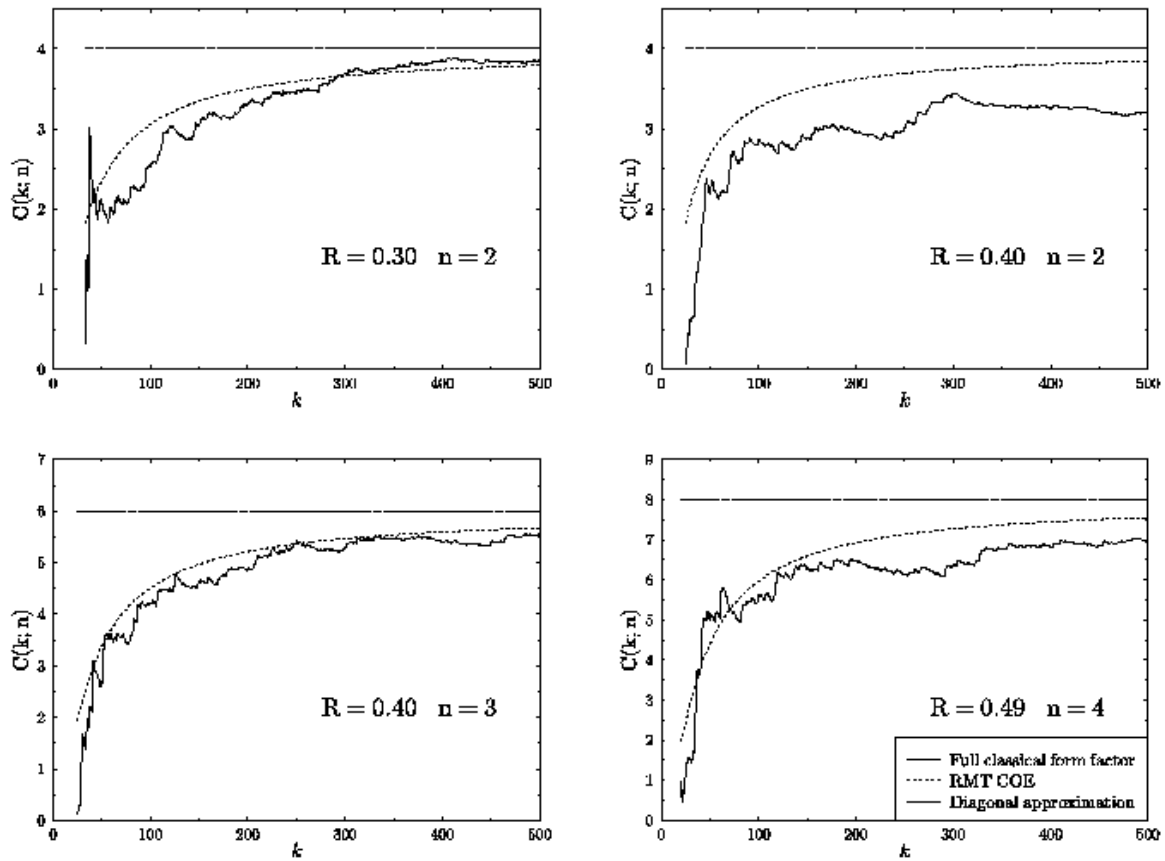


Figure 44: The classical form factor compared with the universal RMT predictions for various cases of the 3D SB in the variable  $k$ .

variable. It again shows that the classical form factor agrees with the COE expression beyond the validity range of the diagonal approximation. The range of  $\tau$  where a good agreement is observed increases with  $n$  as expected, but the estimated domain of valid comparison  $\tau < 2n$  seems to be too optimistic.

In summary we can say that the present results show that the semiclassical theory based on the Gutzwiller trace formula is capable to reproduce the COE form factor beyond the “diagonal approximation”. To do this, one has to include the classical correlations in the way which was done here, and once this is done, there is no need to augment the theory by uncontrolled “higher order” or “diffractive” corrections as was done in [85, 86] and by others. The results obtained in the present section are corroborated by a recent analysis of periodic orbit lengths correlations in billiards constructed from octagonal modular domains in the hyperbolic plane [74]. The same quality of agreement was obtained between the classical form factor and the corresponding RMT result. These billiards are in two dimensions, and therefore the scaling laws depend differently on  $k$ , and the fact that the resulting scaled quantities agree with the expressions derived from RMT gives further support to the line of thinking developed here. We have grounds to believe that the classical correlations are universal in hyperbolic systems, and have to do with the self-similar organization of the set of periodic orbits. The previous numerical studies which were conducted also on different systems support this conjecture [9, 11].

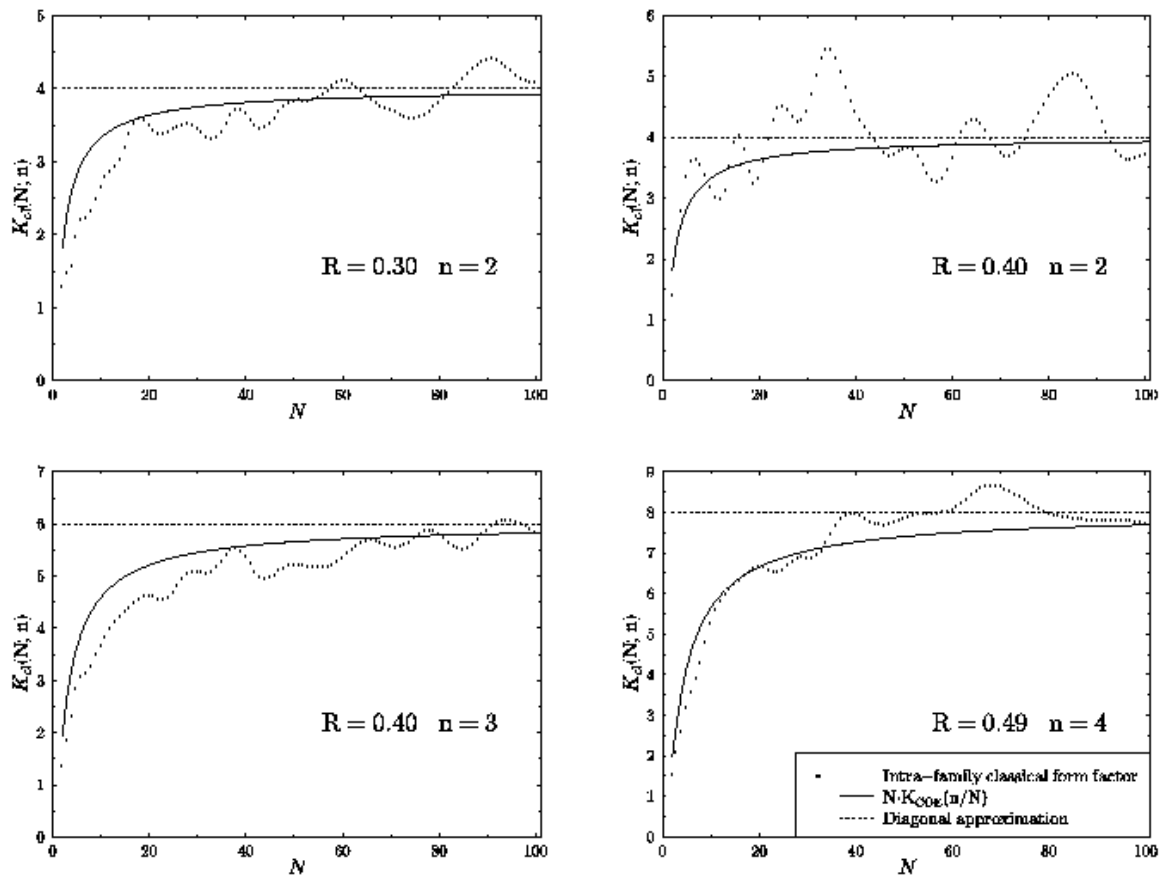


Figure 45: The intra-family classical form factor  $K_{cl}(N; n)$  compared to RMT COE. The variable is  $N$ .

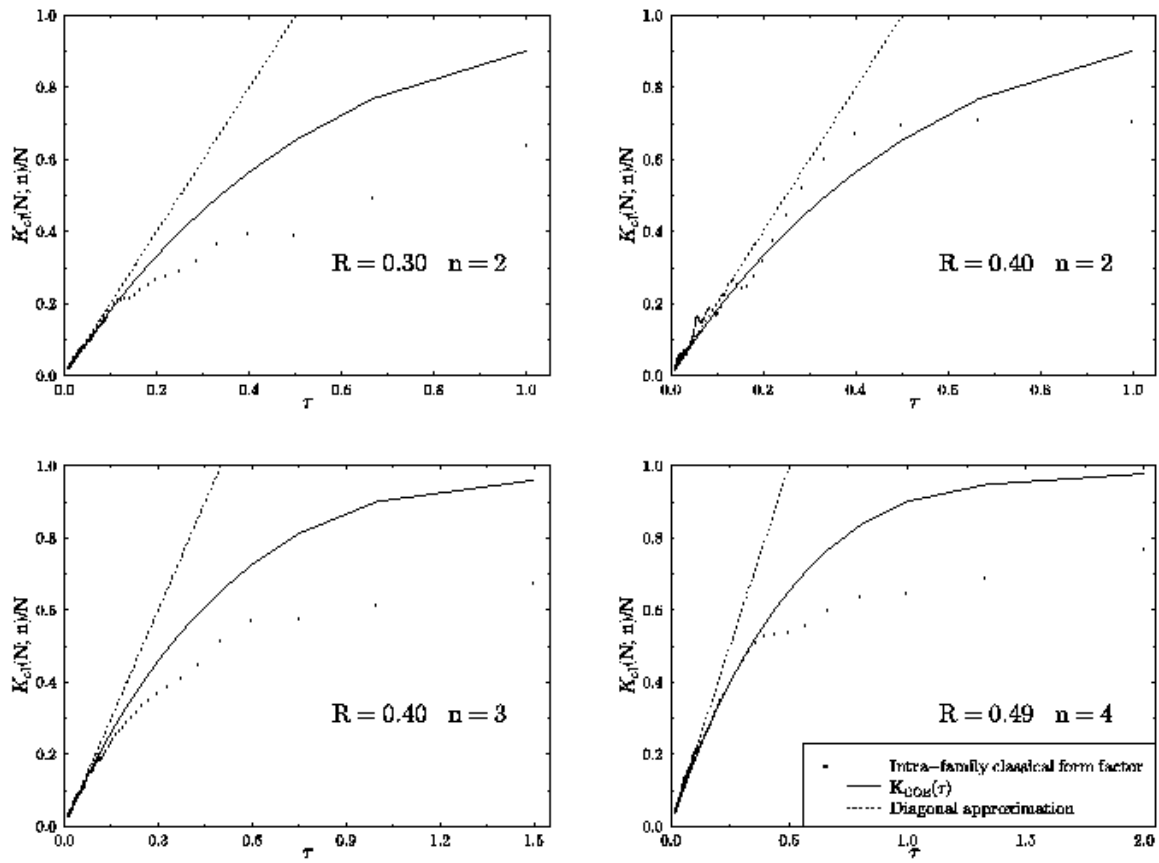


Figure 46: The intra-family classical form factor  $K_{cl}(N; n)$  compared to RMT COE. The control variable is  $\tau = n/N$ .

## 8 Summary

In the present paper we tried to provide a complete description of a paradigmatic three dimensional quantum system which is chaotic in the classical limit — the three dimensional Sinai billiard. This study is called for especially because most of the detailed investigations in the field were carried out for systems in two dimensions.

Our main purpose in this study was to emphasize and clarify issues which are genuinely related to the three dimensional character of the system. The question which concerned us most was whether the semiclassical approximation — the main theoretical tool in the field — is sufficiently accurate for the spectral analysis of systems in three dimensions.

We were able to obtain accurate and extensive data bases for the quantum energy levels and for the classical periodic orbits. These allowed us to check various properties of the quantum spectrum, and in particular to study the applicability of the semiclassical approximation. The main conclusion from our work is that contrary to various expectations, the semiclassical accuracy, measured in units of the mean spacing, does not diverge as a  $\hbar^{2-d}$ . Our numerical tests and analytical arguments indicate an error margin which at worst diverges weakly (logarithmically) with  $\hbar$ .

One of the main problems which we had to overcome was how to separate the generic features which are common to all chaotic systems, from the system specific attributes, which in the present case are the “bouncing ball” manifolds of periodic orbits. We should emphasize that in  $d$  dimensions the bouncing-ball manifolds contribute terms of order  $k^{(d-1)/2}$ , which are much larger than the order 1 contributions due to generic periodic orbits. Hence it is clear that as the dimension increases, the extracting of generic features becomes more difficult, and one has also to control higher  $\hbar$  corrections, such as, e.g., diffraction corrections to the bouncing ball contributions. We developed a method to circumvent some of these difficulties which was sufficient for the 3D Sinai billiard case, namely, we focused on the derivative of the spectrum with respect to the boundary condition. This method is a powerful means which can also be used in other instances, where non-generic effects should be excluded.

One of the issues which are essential to the understanding of trace formulae and their application, was first mentioned by Gutzwiller in his book, under the title of the “third entropy” [2]. Gutzwiller noticed that in order that the series over periodic orbits can be summed up (in some sense) to a spectral density composed of  $\delta$  functions, the phases of the contributing terms should have very special relations. The more quantitative study of this problem started when Argaman *et al.* [9] defined the concept of periodic orbit correlations. The dual nature of the quantum spectrum of energies and the classical spectrum of periodic orbit was further developed in [11]. It follows that the universality of the quantum spectral fluctuations implies that the correlation length in the spectrum of the

classical actions depends on the dimensionality in a specific way. This was tested here for the first time, and the mechanism which induces classical correlations was discussed.

Our work on the Sinai billiard in three dimensions proved beyond reasonable doubt that the methods developed for two dimensional chaotic systems can be extended to higher dimensions. Of utmost importance and interest is the study of classical chaos and its quantum implications in many body systems. This is probably the direction to which the research in “quantum chaos” will be advancing.

## Acknowledgements

The research performed here was supported by the Minerva Center for Non-Linear Physics, and by the Israel Science Foundation. Many colleagues helped us during various stages of the work. We are indebted in particular to Michael Berry, Eugene Bogomolny, Leonid Bunimovich, Doron Cohen, Barbara Dietz, Eyal Doron, Shmuel Fishman, Klaus Hornberger, Jon Keating, Dieter Klakow, Daniel Miller, Zeev Rudnick, Holger Schanz, Martin Sieber and Iddo Ussishkin for numerous discussions, for suggestions and for allowing us to use some results prior to their publication. In particular we thank Klaus Hornberger and Martin Sieber for their critical reading of the manuscript and for their remarks and suggestions. HP is grateful for a MINERVA postdoctoral fellowship, and wishes to thank Reinhold Blümel and John Briggs for their hospitality in Freiburg. The Humboldt foundation is acknowledged for supporting US stay in Marburg, Germany during the summer of 1998 when much of the work on this manuscript was carried out.



## A Efficient quantization of billiards: BIM vs. full diagonalization

In this Appendix we wish to compare two possible quantization schemes for billiards: Direct Diagonalization (DD) of the Hamiltonian matrix vs. the Boundary Integral Method (BIM) (see e.g. [14, 88]). The diagonalization is a generic method to solve the time independent Schrödinger equation, while the BIM is specialized for billiards. To compare the two methods, we estimate the complexity of computing all of the eigenvalues up to a given wavenumber  $k$ .

To find the matrix elements of the Hamiltonian we treat the billiard boundaries as very high potential walls. The linear dimension  $M(k)$  of the Hamiltonian matrix that is needed for finding eigenvalues around  $k$  is:

$$M_{\text{DD}}(k) = \mathcal{O} \left( \left( \frac{S}{\lambda} \right)^d \right) = \mathcal{O}((kS)^d) \quad (185)$$

where  $S$  is the typical linear dimension of the billiard,  $\lambda = 2\pi/k$  is the wavelength and  $d$  is the dimensionality of the billiard. The above estimate is obtained by enclosing the billiard in a hypercube with edge  $S$  and counting the modes up to wavenumber  $k$ . The numerical effort to find eigenvalues of a matrix is of order of its linear dimension to the power 3. Thus, the numerical effort to find all the eigenvalues of the billiard up to  $k$  using DD is estimated as:

$$C_{\text{DD}}(k) = \mathcal{O}(M_{\text{DD}}^3(k)) = \mathcal{O}((kS)^{3d}). \quad (186)$$

The expected number of eigenvalues up to  $k$  is given to a good approximation by Weyl's law, which for billiards reads:

$$N(k) = \mathcal{O}((kS)^d). \quad (187)$$

Thus, the numerical effort to calculate the first (lowest)  $N$  eigenvalues of a billiard in  $d$  dimension in the direct Hamiltonian diagonalization is

$$C_{\text{DD}}(N) = \mathcal{O}(N^3) \quad (188)$$

which is independent of the dimension.

As for the BIM, one traces the  $k$ -axis and searches for eigenvalues rather than obtaining them by one diagonalization. This is done by discretizing a kernel function on the boundary of the billiard and looking for zeroes of the resulting determinant. The linear dimension of the BIM matrix is

$$M_{\text{BIM}} = \mathcal{O} \left( \left( \frac{S}{\lambda} \right)^{d-1} \right) = \mathcal{O}((kS)^{d-1}) = \mathcal{O}(N^{1-1/d}). \quad (189)$$

This estimate is obtained from discretizing the boundary of the billiards which is of dimension  $d - 1$  by hypercubes of edge  $\lambda$ . The numerical effort of calculating the determinant once is:

$$c_{\text{BIM}}(k) = \mathcal{O}(M_{\text{BIM}}^3(k)) = \mathcal{O}((kS)^{3(d-1)}) . \quad (190)$$

(In practice, one often uses the SVD algorithm [58], which is much more stable than a direct computation of the determinant and has the same complexity.) Using the relation (187) we find that the numerical effort to find an eigenvalue near the  $N$ th one is estimated by

$$c_{\text{BIM}}(N) = \mathcal{O}(N^{3-3/d}) . \quad (191)$$

To get the above result we assumed that a fixed number of iterations (evaluations of the determinant) is needed to detect each eigenvalue, which is justified at least for the case where level repulsion is expected. Thus, the complexity to calculate all the eigenvalues up to the  $N$ th is

$$C_{\text{BIM}}(N) = \mathcal{O}(N)c_{\text{BIM}}(N) = \mathcal{O}(N^{4-3/d}) . \quad (192)$$

In particular:

$$\begin{aligned} C_{\text{BIM}}(N) &= \mathcal{O}(N^{5/2}), & \text{for } d = 2 \\ C_{\text{BIM}}(N) &= \mathcal{O}(N^3), & \text{for } d = 3. \end{aligned}$$

We conclude that the BIM is more efficient than DD for 2 dimensions, and for 3 dimensions they are of the same level of complexity. In practice, however, it seems that the BIM is better also in 3 dimensions, since the DD matrices can be prohibitly large, and manipulating them (if possible) can be very expensive due to memory limitations (paging). Also one has to take into account, that due to evanescent modes, the numerical proportionality factor in (189) is actually close to 1, while for (185) the factor can be large if high accuracy is desired. This is due to the fact that the off-diagonal matrix elements of the Hamiltonian decay only like a power-law due to the sharp potential and hence very large matrices are needed in order to obtain accurate eigenvalues.

## B Symmetry reduction of the numerical effort in the quantization of billiards

Consider a  $d$ -dimensional billiard which is invariant under a group  $\mathcal{G}$  of geometrical symmetry operations. We want to compare the numerical effort that is needed to compute the lowest  $N$  eigenvalues of the fully symmetric billiard with that of computing the lowest  $N$  eigenvalues of the desymmetrized billiard. In “desymmetrized” we mean the following: if  $\Omega$  is the full billiard domain, then the desymmetrized billiard  $\omega$  is such that  $\bigcup_{\hat{g} \in \mathcal{G}} \hat{g}\omega = \Omega$ . If one uses the direct diagonalization (DD) of the Hamiltonian matrix, then there is no advantage to desymmetrization, because the prefactor in (188) should not depend on the shape of the billiard if its aspect ratio is close to 1. Therefore, the numerical effort of computing the lowest  $N$  levels of either the fully symmetric or the desymmetrized billiard is more or less the same using DD. On the other hand, as we show in the sequel, desymmetrization is very advantageous within the framework of the BIM,.

We first note, that considering a particular irreducible representation  $\gamma$  of  $\mathcal{G}$  is equivalent to desymmetrization of the billiard together with imposing boundary conditions that are prescribed by  $\gamma$ . The dimension of  $\gamma$  is denoted as  $d_\gamma$  and the order of  $\mathcal{G}$  is denoted as  $N_\mathcal{G}$ . Given a complete basis of functions in which the functions are classified according to the irreps of  $\mathcal{G}$ , then the fraction of the basis functions that belong to the irrep  $\gamma$  is  $d_\gamma^2/N_\mathcal{G} \equiv F_\gamma$ . This is also the fraction of eigenvalues that belong to  $\gamma$  out of the total number of levels, when we consider a large number of levels. Using the notations of appendix A, we thus have:

$$\begin{aligned} M_{\text{BIM}}^{(\gamma)}(k) &= F_\gamma M_{\text{BIM}}(k) \\ N^{(\gamma)}(k) &= F_\gamma N(k) \end{aligned} \quad (193)$$

where the quantities with superscript  $\gamma$  correspond to the desymmetrized billiard, and the others to the fully symmetric one. Using (189) and repeating arguments from appendix A results in:

$$C_{\text{BIM}}^{(\gamma)}(N) = F_\gamma^{\frac{3}{d}} C_{\text{BIM}}(N). \quad (194)$$

In the equation above we replaced  $N^{(\gamma)} \rightarrow N$ . Thus, the decrease in the density of states is more than compensated by the reduction in the size of the secular matrix and the overall numerical effort is diminished by a factor of  $F_\gamma^{\frac{3}{d}}$ . For example, in the case of the 3D Sinai billiard and for a one-dimensional irrep, the saving factor is:

$$F_\gamma^{\frac{3}{d}} = \left(\frac{1^2}{48}\right)^{\frac{3}{3}} = \frac{1}{48} \quad (195)$$

which is a very significant one.

## C Resummation of $D_{LM}$ using the Ewald summation technique

In general, the Ewald summation technique is used to calculate (conditionally convergent) summations over lattices  $\{\vec{\rho}\}$ :

$$S = \sum_{\vec{\rho}} f(\vec{\rho}). \quad (196)$$

One splits the sum  $S$  into two sums  $S_1, S_2$  which depend on a parameter  $\eta$ :

$$S = S_1 + S_2 = \sum_{\vec{\rho}} f_1(\vec{\rho}; \eta) + \sum_{\vec{\rho}} f_2(\vec{\rho}; \eta). \quad (197)$$

This splitting is usually performed by representing  $f(x)$  as an integral, and splitting the integral at  $\eta$ . The idea is to resum  $S_1$  on the reciprocal lattice  $\{\vec{g}\}$  using the Poisson summation formula:

$$S_1 = \sum_{\vec{g}} \int d^d \rho \exp(2\pi i \vec{\rho} \vec{g}) f_1(\vec{\rho}; \eta) \equiv \sum_{\vec{g}} \hat{f}_1(\vec{g}; \eta), \quad (198)$$

and to choose  $\eta$  such that both  $S_1$  and  $S_2$  will rapidly converge.

We need to apply the Ewald summation technique to  $D_{LM}(k)$ , given explicitly in equation (5), which constitute the main computational load. This is because they include summations over the  $\mathbf{Z}^3$  lattice which need to be computed afresh for each new value of  $k$ . It is possible to apply the Ewald technique directly to each  $D_{LM}$ , but it is much simpler to take an indirect route: We shall Ewald resum the free Green function on the 3-torus, and then read off the  $D_{LM}$ 's as expansion coefficients.

We start with the free outgoing Green function on the three-dimensional torus:

$$G_0^T(\vec{q}) = -\frac{1}{4\pi} \sum_{\vec{\rho} \in \mathbf{Z}^3} \frac{\exp(ik|\vec{q} - \vec{\rho}|)}{|\vec{q} - \vec{\rho}|}, \quad (199)$$

where we took the side of the torus to be 1 for simplicity and defined  $\vec{q} \equiv \vec{r} - \vec{r}'$ . To split the sum we use an integral representation of the summands [55, 30]:

$$\frac{\exp(ik|\vec{q} - \vec{\rho}|)}{|\vec{q} - \vec{\rho}|} = \frac{2}{\sqrt{\pi}} \int_{0(C)}^{\infty} \exp\left[-(\vec{q} - \vec{\rho})^2 \xi^2 + \frac{k^2}{4\xi^2}\right] d\xi, \quad (200)$$

where the integration contour  $C$  is shown in figure 47. It is assumed that  $k$  has an infinitesimal positive imaginary part, which is taken to 0 at the end of the calculation. We now deform the contour into  $C'$  (see figure 47), such that it runs

along the real axis for  $\xi > \sqrt{\eta}/2$ , and split the integral at this point as follows:

$$G_0^T(\vec{q}) = G_1^T(\vec{q}) + G_2^T(\vec{q}), \quad (201)$$

$$G_1^T(\vec{q}) = -\frac{1}{2\pi\sqrt{\pi}} \sum_{\vec{\rho}} \int_{0(C')}^{\sqrt{\eta}/2} \exp\left[-(\vec{q}-\vec{\rho})^2\xi^2 + \frac{k^2}{4\xi^2}\right] d\xi, \quad (202)$$

$$G_2^T(\vec{q}) = -\frac{1}{2\pi\sqrt{\pi}} \sum_{\vec{\rho}} \int_{\sqrt{\eta}/2}^{\infty} \exp\left[-(\vec{q}-\vec{\rho})^2\xi^2 + \frac{k^2}{4\xi^2}\right] d\xi. \quad (203)$$

$$(204)$$

The summation in  $G_2^T$  is rapidly convergent, due to the fact that we integrate over the tails of a rapidly decaying function in  $\xi$  (faster than a Gaussian), and we start further on the tail when  $\rho$  grows. In order to make  $G_1^T$  also rapidly convergent, we need to Poisson resum it. We use the identity:

$$\sum_{\vec{\rho}} \exp[-(\vec{q}-\vec{\rho})^2\xi^2] = \frac{\pi\sqrt{\pi}}{\xi^3} \sum_{\vec{g}} \exp\left[\frac{(2\pi g)^2}{4\xi^2} + i(2\pi\vec{g})\vec{q}\right], \quad (205)$$

which is obtained by explicitly performing the integrals of the Poisson summation. Thus,

$$\begin{aligned} G_1^T(\vec{q}) &= -\frac{1}{2} \sum_{\vec{g}} \exp(2\pi i\vec{g}\vec{q}) \int_{0(C')}^{\sqrt{\eta}/2} \frac{d\xi}{\xi^3} \exp\left[\frac{k^2 - (2\pi g)^2}{4\xi^2}\right] \\ &= \sum_{\vec{g}} \frac{\exp(2\pi i\vec{g}\vec{q}) \exp\left[\frac{k^2 - (2\pi g)^2}{\eta}\right]}{k^2 - (2\pi g)^2}. \end{aligned} \quad (206)$$

The second line was obtained from the first one by performing the integrals explicitly. The expression obtained for  $G_1^T$  is also rapidly convergent, and is suitable for computations. We thus succeeded in rewriting  $G_0^T$  as two rapidly converging sums (206), (203). We note that the results (206), (203) are valid for general lattices, the cubic lattice being a special case [30].

The heart of the above resummation of  $G_0^T$  was the integral representation (200) which is non-trivial. In appendix D we present an alternative derivation of the above results using more intuitive, physical arguments.

It remains to extract the  $D_{LM}$ 's from the resummed  $G_0^T$ . The basic relation is [30]:

$$G_0^T(\vec{q}) = \sum_{LM} j_L(kq) Y_{LM}(\Omega_{\vec{q}}) \left[ D_{LM}(k) + \frac{k}{\sqrt{4\pi}} \frac{n_0(kq)}{j_0(kq)} \delta_{L0} \right]. \quad (207)$$

Using expansion theorems [56] applied to (203) and (206) one can rewrite  $G_0^T$  as:

$$G_0^T(\vec{q}) = \sum_{LM} Y_{LM}(\Omega_{\vec{q}}) \left\{ \sum_{\vec{g}} 4\pi i^L e^{k^2/\eta} Y_{LM}^*(\Omega_{\vec{g}}) j_L(2\pi gq) \frac{e^{-(2\pi g)^2/\eta}}{k^2 - (2\pi g)^2} - \right.$$

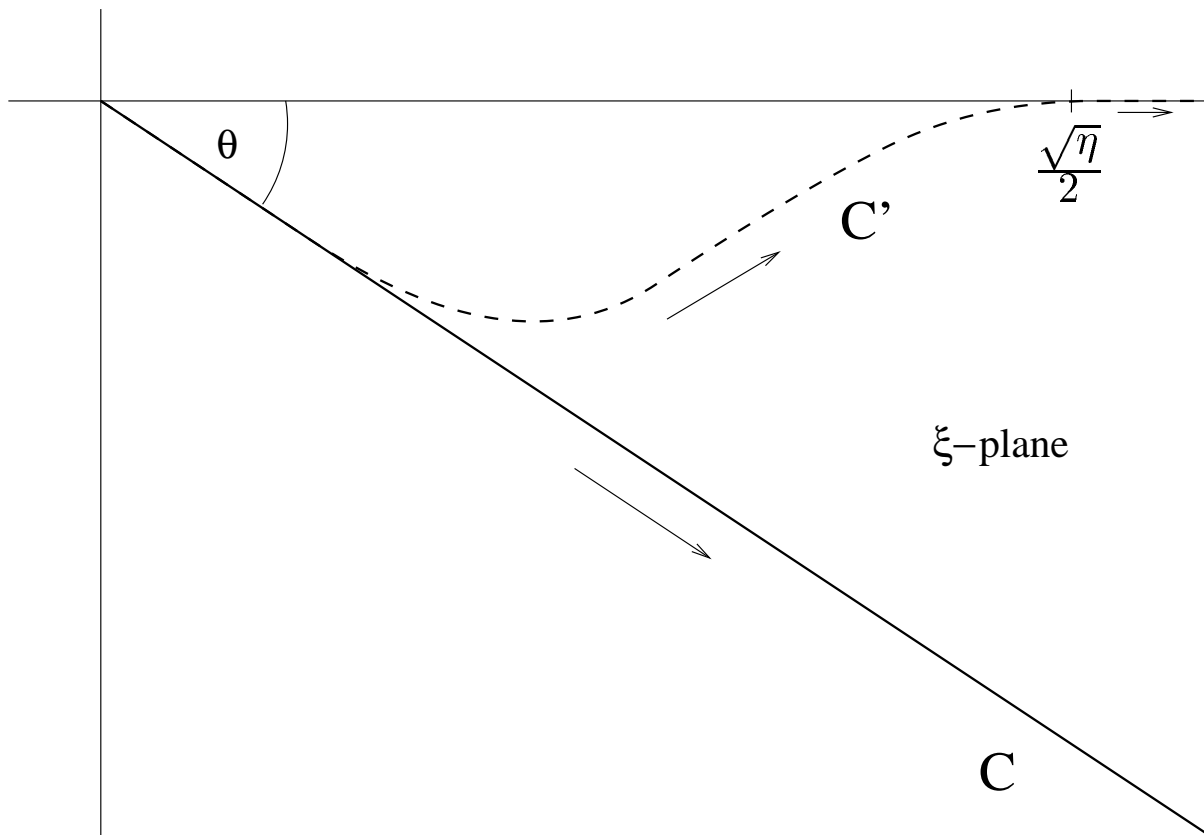


Figure 47: Contours for the integral evaluation of  $G_0^T$ . In the above  $\theta \equiv \arctan[\text{Im}(k)/\text{Re}(k)]/2 - \pi/4$ .

$$\left. \sum_{\vec{\rho}} \frac{2i^L}{\sqrt{\pi}} Y_{LM}^*(\Omega_{\vec{\rho}}) \int_{\frac{\sqrt{\eta}}{2}}^{\infty} d\xi j_L(-2i\rho q \xi^2) \exp \left[ -(\rho^2 + q^2)\xi^2 + \frac{k^2}{4\xi^2} \right] \right\}. \quad (208)$$

Comparing equations (207) and (208), and using the orthogonality of the spherical harmonics  $Y_{LM}(\Omega_{\vec{q}})$ , one obtains:

$$D_{LM}(k) = \frac{1}{j_L(kq)} \left[ \sum_{\vec{g}} \cdots + \sum_{\vec{\rho}} \cdots - \frac{k}{\sqrt{4\pi}} n_0(kq) \delta_{L0} \right]. \quad (209)$$

This is the Ewald–resumed expression of  $D_{LM}(k)$ . It has the interesting feature, that even though each of the terms explicitly depends on  $q$ , the total expression is independent of  $q$ . The same applies also to  $\eta$ . This freedom can be used to simplify the expression (209), since for  $q \rightarrow 0$  the spherical Bessel functions simplify to powers [30]:

$$j_L(aq) \longrightarrow \frac{(aq)^L}{(2L+1)!!}, \quad (210)$$

which are computationally less demanding. Taking the limit is straightforward for  $L \neq 0$ , while for  $D_{00}$  there is a complication due to the singularity of  $n_0(kq)$ . As shown in appendix E this singularity is exactly cancelled by the  $\vec{\rho} = \vec{0}$  term, resulting in a finite expression also for  $D_{00}$ . The final result is:

$$D_{LM} = D_{LM}^{(1)} + D_{LM}^{(2)} + D_{00}^{(3)} \delta_{L0}, \quad (211)$$

$$D_{LM}^{(1)} = 4\pi i^L k^{-L} e^{k^2/\eta} \sum_{\vec{g}} (2\pi g)^L Y_{LM}^*(\Omega_{\vec{g}}) \frac{e^{-(2\pi g)^2/\eta}}{k^2 - (2\pi g)^2}, \quad (212)$$

$$D_{LM}^{(2)} = \frac{2^{L+1} k^{-L}}{\sqrt{\pi}} \sum_{\vec{\rho} \neq \vec{0}} \rho^L Y_{LM}^*(\Omega_{\vec{\rho}}) \int_{\frac{\sqrt{\eta}}{2}}^{\infty} d\xi \xi^{2L} \exp \left[ -\rho^2 \xi^2 + \frac{k^2}{4\xi^2} \right], \quad (213)$$

$$D_{00}^{(3)} = -\frac{\sqrt{\eta}}{2\pi} \sum_{n=0}^{\infty} \frac{(k^2/\eta)^n}{n!(2n-1)}, \quad (214)$$

with the convention  $g^L|_{g=0, L=0} = 1$ . This completes the task of Ewald–resuming the building blocks  $D_{LM}(k)$  into rapidly convergent series.

## D “Physical” Ewald summation of $G_0^T(\vec{q})$

In this appendix we present a derivation of the results (206), (203) by a method that is different than the one used in appendix C. The present method is physically appealing and does not require the use of complicated integral representations. It is inspired by Appendix B of Kittel’s book [97] which deals with the problem of calculating Madelung constants (electrostatic potentials) of ion crystals.

In the sequel we use  $\vec{q} \equiv \vec{r} - \vec{r}'$  and adopt the following notational convention: For any quantity  $X(\vec{q})$  we add a superscript  $T$  to denote its lattice sum:

$$X^T(\vec{q}) \equiv \sum_{\vec{\rho}} X(\vec{q} - \vec{\rho}). \quad (215)$$

We start from the Helmholtz equation for  $G_0$ :

$$(\nabla_{\vec{r}}^2 + k^2)G_0(\vec{q}) = \delta(\vec{q}). \quad (216)$$

Due to linearity, the function  $G_0^T$  satisfies:

$$(\nabla_{\vec{r}}^2 + k^2)G_0^T(\vec{q}) = \delta^T(\vec{q}). \quad (217)$$

The RHS of (217) can be interpreted as a “charge distribution” which is composed of point charges on a lattice. Each such point charge  $\delta(\vec{q} - \vec{\rho})$  induces a “potential”  $G_0(\vec{q} - \vec{\rho}) = -\exp(ik|\vec{q} - \vec{\rho}|)/(4\pi|\vec{q} - \vec{\rho}|)$  which is long-ranged due to the sharpness of the charge. (This is in analogy to the electrostatic case.) Hence, the lattice sum of potentials  $G_0^T$  is conditionally convergent. To overcome this difficulty we introduce an arbitrary charge distribution  $\lambda(\vec{q})$  and rewrite (217) as:

$$G_0^T(\vec{q}) = G_1^T(\vec{q}) + G_2^T(\vec{q}), \quad (218)$$

$$(\nabla^2 + k^2)G_1^T(\vec{q}) = \lambda^T(\vec{q}), \quad (219)$$

$$(\nabla^2 + k^2)G_2^T(\vec{q}) = \delta^T(\vec{q}) - \lambda^T(\vec{q}). \quad (220)$$

We want  $\lambda(\vec{q} - \vec{\rho})$  to effectively screen the  $\delta(\vec{q} - \vec{\rho})$  charges, making  $G_2$  short-ranged. This will result in rapid convergence of  $G_2^T$ . (Note, that the equations (218)-(220) hold also for the quantities without the T superscript due to linearity.) On the other hand,  $\lambda(\vec{q})$  must be smooth enough, such that  $G_1^T$  will rapidly converge when Poisson resumed. It is hence plausible to choose a (spherically symmetric) Gaussian charge distribution for  $\lambda(\vec{q})$ :

$$\lambda(\vec{q}) = A \exp(-\alpha q^2), \quad (221)$$

where  $A$  and  $\alpha$  are yet arbitrary parameters.



We calculate first  $G_2(\vec{q})$  by rewriting the inducing charge as an integral over  $\delta$  charges, and using the fact that each  $\delta$  charge contributes  $G_0$  to the potential:

$$(\nabla^2 + k^2)G_2(\vec{q}) = \delta(\vec{q}) - \lambda(\vec{q}) = \delta(\vec{q}) - \int d^3Q \lambda(\vec{Q}) \delta(\vec{q} - \vec{Q}). \quad (222)$$

Hence,

$$\begin{aligned} G_2(\vec{q}) &= G_0(\vec{q}) - \int d^3Q \lambda(\vec{Q}) G_0(\vec{q} - \vec{Q}) \\ &= G_0(\vec{q}) \left[ 1 - A \left( \frac{\pi}{\alpha} \right)^3 e^{-\frac{k^2}{4\alpha}} \right] + \frac{A}{2\alpha q} \int_0^\infty dt e^{-\alpha(t+q)^2} \cos(kt). \end{aligned} \quad (223)$$

The first term is long-ranged due to  $G_0$ , and the second term is short-ranged due to the integral that is rapidly decreasing as a function of  $q$ . To make  $G_2$  short ranged, we thus have to set the coefficient of  $G_0$  to 0, which is satisfied if we choose

$$A = A(k, \alpha) = \left( \frac{\alpha}{\pi} \right)^3 \exp\left( \frac{k^2}{4\alpha} \right). \quad (224)$$

Therefore, we get for  $G_2^T$  a rapidly convergent sum:

$$G_2^T(\vec{q}) = -\frac{\sqrt{\alpha} e^{\frac{k^2}{4\alpha}}}{2\pi\sqrt{\pi}} \sum_{\vec{\rho}} \frac{1}{|\vec{q} - \vec{\rho}|} \int_0^\infty dt \exp[-\alpha(t + |\vec{q} - \vec{\rho}|)^2] \cos(kt). \quad (225)$$

This can be re-expressed in a more compact form using complement error functions with complex arguments:

$$G_2^T(\vec{q}) = -\frac{1}{2\pi} \sum_{\vec{\rho}} \frac{1}{|\vec{q} - \vec{\rho}|} \operatorname{Re} \left[ \exp(-ik|\vec{q} - \vec{\rho}|) \cdot \operatorname{erfc} \left( \sqrt{\alpha}|\vec{q} - \vec{\rho}| - \frac{ik}{2\sqrt{\alpha}} \right) \right], \quad (226)$$

where

$$\operatorname{erfc}(z) \equiv \frac{1}{\sqrt{\pi}} \int_z^\infty e^{-u^2} du. \quad (227)$$

To calculate  $G_1^T$  we can directly Poisson resum (225). Alternatively, we can use again the Helmholtz equation for  $G_1^T$  (219) to simplify the calculations. We expand  $G_1^T$  in the reciprocal lattice:

$$\begin{aligned} G_1^T(\vec{q}) &= \sum_{\vec{g}} \int d^3\rho \exp(2\pi i \vec{\rho} \vec{g}) G_1(\vec{q} - \vec{\rho}) \\ &= \sum_{\vec{g}} \exp(2\pi i \vec{q} \vec{g}) \int d^3\rho \exp(-2\pi i \vec{\rho} \vec{g}) G_1(\vec{\rho}) \\ &\equiv \sum_{\vec{g}} \exp(2\pi i \vec{q} \vec{g}) G_{1\vec{g}} \end{aligned} \quad (228)$$

where the second line was obtained from the first one by shifting the origin of the integration. Similarly for  $\lambda^T(\vec{q})$ :

$$\lambda(\vec{q}) = \sum_{\vec{g}} \exp(2\pi i \vec{q} \vec{g}) \lambda_{\vec{g}}. \quad (229)$$

Inserting (228, 229) into (219) and using the orthogonality of the Fourier components, we get the simple relation between  $G_{1\vec{g}}$  and  $\lambda_{\vec{g}}$ :

$$G_{1\vec{g}} = \frac{\lambda_{\vec{g}}}{k^2 - (2\pi g)^2}. \quad (230)$$

When inserted back into (228) we finally get for  $G_1^T$ :

$$G_1^T(\vec{q}) = \sum_{\vec{g}} \frac{\exp(2\pi i \vec{g} \vec{q}) \exp\left[\frac{k^2 - (2\pi g)^2}{4\alpha}\right]}{k^2 - (2\pi g)^2}. \quad (231)$$

This expression is identical with (206) if we set  $4\alpha = \eta$ . It can be shown [55] that also the expressions for  $G_2^T$ , (203) and (226) are identical. However, equation (226) is more convenient if one needs to compute  $G_0^T(\vec{q})$ , since it involves well-tabulated computer-library functions [58] and saves the burden of numerical integrations. On the other hand, the expression (203) is more convenient as a starting point for calculating  $D_{LM}(k)$ .

To summarize, we re-derived the Ewald-resummed form of  $G_0^T(\vec{q})$  using the underlying Helmholtz equation. We used a physically intuitive argument of screening potentials, that was shown to be equivalent to the more abstract integral representation of  $G_0(\vec{q})$ , equation (200).

## E Calculating $D_{00}^{(3)}$

We need to calculate (refer to equation (209) and its subsequent paragraph):

$$D_{00}^{(3)} \equiv \lim_{q \rightarrow 0} \left\{ \frac{1}{j_0(kq)} \left[ \frac{1}{\sqrt{4\pi}} \frac{\cos(kq)}{q} - \frac{1}{\pi} \int_{\sqrt{\eta}/2}^{\infty} d\xi \exp \left( -q^2 \xi^2 + \frac{k^2}{4\xi^2} \right) \right] \right\}, \quad (232)$$

where we used the explicit expression  $n_0(x) = -\cos(x)/x$ . Taking the limit of the denominator is trivial, since  $j_0(kq) \rightarrow 1$ . For  $q \rightarrow 0$  we can write,

$$\frac{1}{\sqrt{4\pi}} \frac{\cos(kq)}{q} = \frac{1}{\sqrt{4\pi}q} + \mathcal{O}(q), \quad (233)$$

which contains  $1/q$  singularity. As for the term with the integral, we expand  $\exp(k^2/4\xi^2)$  in a Taylor series, and transforming to the variable  $t = q\xi$  one gets:

$$-\frac{1}{\pi} \int_{\sqrt{\eta}/2}^{\infty} d\xi \exp \left( -q^2 \xi^2 + \frac{k^2}{4\xi^2} \right) = -\frac{1}{\pi q} \sum_{n=0}^{\infty} \frac{(kq)^{2n}}{4^n n!} \int_{q\sqrt{\eta}/2}^{\infty} dt t^{-2n} e^{-t^2}. \quad (234)$$

For  $n = 0$ :

$$\int_{q\sqrt{\eta}/2}^{\infty} dt e^{-t^2} = \left( \int_0^{\infty} - \int_0^{q\sqrt{\eta}/2} \right) dt e^{-t^2} = \frac{\sqrt{\pi}}{2} - \frac{1}{2} \sqrt{\eta} q + \mathcal{O}(q^2). \quad (235)$$

For  $n > 0$  we integrate by parts:

$$\int_{q\sqrt{\eta}/2}^{\infty} dt t^{-2n} e^{-t^2} = \frac{1}{2n-1} \left( \frac{1}{2} \sqrt{\eta} q \right)^{-2n+1} e^{-\eta q^2/4} + \mathcal{O}(q^{-2n+3}). \quad (236)$$

Collecting everything together back to (232), the  $1/q$  singularities cancel, and we remain with the finite expression:

$$D_{00}^{(3)} = -\frac{\sqrt{\eta}}{2\pi} \sum_{n=0}^{\infty} \frac{(k^2/\eta)^n}{n!(2n-1)}. \quad (237)$$

## F The “cubic harmonics” $Y_{LJK}^{(\gamma)}$

### F.1 Calculation of the transformation coefficients $a_{\gamma JK, M}^{(L)}$

We want to calculate the linear combinations of spherical harmonics that transform according to the irreducible representations of the cubic group  $O_h$ . This problem was addressed by von der Lage and Bethe [57] which coined the term “cubic harmonics” for these combinations. They gave an intuitive scheme that was used to calculate the first few cubic harmonics, but their arguments are difficult to extend for large  $L$ 's. Moreover, their method is recursive, because one has to orthogonalize with respect to all lower lying combinations. This is cumbersome to implement numerically and might result in instabilities for large  $L$ 's. The only other work on the subject that we were aware of [98] specializes in the symmetric representation and gives only part of the combinations. It also expresses the results not in terms of spherical harmonics, but rather as polynomials that are difficult to translate to  $Y_{LM}$ 's.

We describe in the following a simple and general numerical method to calculate the cubic harmonics in a non-recursive way. This is based on a general theorem, that states that a function  $f^{(\gamma)}$  transforms according to the irrep  $\gamma$  iff it satisfies [31]:

$$\hat{P}^{(\gamma)} f^{(\gamma)} = f^{(\gamma)} \quad (238)$$

where  $\hat{P}^{(\gamma)}$  is the projection operator onto the subspace that belongs to  $\gamma$ :

$$\hat{P}^{(\gamma)} = \frac{l_\gamma}{N_G} \sum_{\hat{g} \in G} \chi^{(\gamma)*}(\hat{g}) \hat{g}. \quad (239)$$

We denote by  $l_\gamma$  the dimension of  $\gamma$ ,  $N_G$  is the number of elements in the group  $G$ , and  $\chi^{(\gamma)}(\hat{g})$  are the characters. The realization of  $\hat{P}^{(\gamma)}$  as a matrix in an arbitrary basis results in general in an infinite matrix. However, in the case of the cubic harmonics, we know that  $O_h \subset O(3)$ , thus the operations of  $\hat{g} \in O_h$  do not mix different  $L$ 's. Hence, working in the  $Y_{LM}$  basis, we can write the cubic harmonics as the finite combinations:

$$Y_{LJ}^{(\gamma)}(\Omega) = \sum_{M=-L}^{+L} a_{\gamma J, M}^{(L)*} Y_{LM}(\Omega) \quad (240)$$

where  $J$  enumerates the irreps  $\gamma$  in  $L$ . For simplicity we consider 1-dimensional irreps. Applying (238), (239) to (240) and using the Wigner matrices  $\mathcal{D}^{(L)}(\hat{g})$  to express the operations of  $\hat{g}$  on  $Y_{LM}$  [56], we get the following  $(2L+1) \times (2L+1)$  linear system:

$$\sum_{M'} \left[ P_{MM'}^{(\gamma, L)} - \delta_{MM'} \right] a_{\gamma J, M'}^{(L)*} = 0 \quad (241)$$

where:

$$P_{MM'}^{(\gamma,L)} = \frac{1}{48} \sum_{\hat{g} \in G} \chi^{(\gamma)*}(\hat{g}) \mathcal{D}_{MM'}^{(L)}(\hat{g}). \quad (242)$$

The above equations are best solved using SVD algorithm [58], and the (orthonormalized) eigenvectors that belong to the zero singular values are the required coefficients  $a_{\gamma J, M'}^{(L)*}$ . For multi-dimensional irreps one needs to classify the cubic harmonics also with respect to the row  $K$  inside the irrep. This can be done by simple modification of the above procedure, using the appropriate projectors [31].

The above general procedure can be simplified for specific irreps. In the following we shall concentrate on the completely antisymmetric irrep  $\gamma = a$  and further reduce the linear system (241). We first note, that the antisymmetric cubic harmonics must satisfy per definition:

$$\hat{g} Y_{LJ}^{(a)}(\Omega) = \chi^{(a)}(\hat{g}) Y_{LJ}^{(a)}(\Omega) = (-1)^{(\text{parity of } \hat{g})} Y_{LJ}^{(a)}(\Omega) \quad \forall \hat{g} \in O_h. \quad (243)$$

We then choose a few particular  $\hat{g}$ 's for which the operations on  $Y_{LM}(\Omega)$  are simple:

$$\begin{aligned} \hat{r}_x(xyz) &\equiv (-xyz) : \quad \hat{r}_x Y_{LM}(\theta, \phi) = Y_{LM}(\theta, -\phi) = (-1)^M Y_{L-M}(\theta, \phi) \\ \hat{r}_y(xyz) &\equiv (x-yz) : \quad \hat{r}_y Y_{LM}(\theta, \phi) = Y_{LM}(\theta, \pi - \phi) = Y_{L-M}(\theta, \phi) \\ \hat{r}_z(xyz) &\equiv (xy-z) : \quad \hat{r}_z Y_{LM}(\theta, \phi) = Y_{LM}(\pi - \theta, \phi) = (-1)^{L+M} Y_{LM}(\theta, \phi) \\ p_{xy}(xyz) &\equiv (yxz) : \quad p_{xy} Y_{LM}(\theta, \phi) = Y_{LM}(\theta, \frac{\pi}{2} - \phi) = (-i)^M Y_{L-M}(\theta, \phi). \end{aligned} \quad (244)$$

Applying (243) and (244) to (240) results in the following ‘‘selection rules’’:

$$\begin{aligned} a_{aJ, M}^{(L)*} &= 0, \quad L \neq 2p + 1, M \neq 4q, \quad p, q \in \mathbb{N} \\ a_{aJ, -M}^{(L)*} &= -a_{aJ, M}^{(L)*} \end{aligned} \quad (245)$$

which reduces the number of independent coefficients to be computed by a factor of 16. The form of the projector matrix  $P^{(aL)}$  can also be greatly reduced, if we observe that the group  $O_h$  can be written as the following direct multiplication:

$$O_h = G_3 \otimes G_{16} \quad (246)$$

$$G_3 = \{\hat{e}, \hat{c}, \hat{c}^2\} \quad \hat{e} = \text{identity}, \quad \hat{c}(xyz) = (yzx) \quad (247)$$

$$G_{16} = \{\hat{e}, \hat{p}_{xy}\} \otimes \{\hat{e}, \hat{r}_x\} \otimes \{\hat{e}, \hat{r}_y\} \otimes \{\hat{e}, \hat{r}_z\} \quad (248)$$

and consequently, the projector can be written as

$$\hat{P}^{(a)} = \hat{P}_3 \hat{P}_{16} \quad (249)$$

$$\hat{P}_3 = \hat{e} + \hat{c} + \hat{c}^2 \quad (250)$$

$$\hat{P}_{16} = (\hat{e} - \hat{p}_{xy})(\hat{e} - \hat{r}_x)(\hat{e} - \hat{r}_y)(\hat{e} - \hat{r}_z). \quad (251)$$

The operator  $\hat{P}_{16}$  acts as the identity on the subspace defined by (245) and hence we need to consider only the operation of  $\hat{P}_3$ . Simple manipulations give the following set of equations:

$$\sum_{q' > 0} \left[ 2d_{4q,4q'}^{(L)} \left( \frac{\pi}{2} \right) - \delta_{4q,4q'} \right] a_{aJ,4q'}^{(L)*} = 0, \quad q > 0, \quad L = 2p + 1. \quad (252)$$

The matrices  $d_{4q,4q'}^{(L)}$  are the “reduced” Wigner matrices, which are real [56], thus the resulting coefficients are also real. The above is a square linear system, which is 8 times smaller than the general one (241).

## F.2 Counting the $Y_{LJ}^{(\gamma)}$ 's

The number of the irreps  $\gamma$  of  $O_h$  that are contained in the irrep  $L$  of  $O(3)$  is given by the formula [31]:

$$N_{\gamma L} = \frac{1}{48} \sum_{\hat{g} \in O_h} \chi^{(\gamma)*}(\hat{g}) \chi_L(\hat{g}) \quad (253)$$

where  $\chi_L(\hat{g})$  are the characters of the irrep  $L$ . An explicit calculation shows that the main contributions for large  $L$ 's come from the identity and from the inversion operations, thus:

$$N_{\gamma L} \approx [1 \pm (-1)^L] \frac{l_\gamma(2L+1)}{48}. \quad (254)$$

where the  $\pm$  corresponds to the parity of  $\gamma$ . Since for  $l_\gamma$ -dim irrep we have  $l_\gamma$  basis functions, and there are  $2L+1$  basis functions in the irrep  $L$ , the fraction of cubic harmonics that belong to  $\gamma$  is:

$$F_\gamma \approx \frac{l_\gamma^2}{48} \quad (255)$$

in accordance with the general relation:

$$\sum_{\gamma} l_\gamma^2 = 48. \quad (256)$$

Consequently, the fraction of cubic harmonics that belong to the  $K$ 'th block of  $\gamma$  is

$$F_{\gamma K} \approx \frac{l_\gamma}{48}. \quad (257)$$

## G Evaluation of $l(\vec{\rho}_p)$

### G.1 Proof of equation (10)

We need to prove the relation:

$$\sum_{\hat{g} \in O_h} Y_{LM}(\Omega_{\hat{g}\vec{\rho}}) = l(\vec{\rho}_p) \sum_{\vec{\rho}' \in S(\vec{\rho}_p)} Y_{LM}(\Omega_{\vec{\rho}'}) \quad (258)$$

where  $\vec{\rho}_p \equiv (i, j, k)$  is the unique vector in the set  $O_h \vec{\rho}$  which resides in the fundamental domain  $i \geq j \geq k \geq 0$ ,  $S(\vec{\rho}_p)$  is the collection of all distinct vectors obtained by the operations  $\hat{g}\vec{\rho}_p$ ,  $\hat{g} \in O_h$ , and  $l(\vec{\rho}_p)$  is an integer.

**Proof.** Let  $\mathcal{H}$  be the set of all  $\hat{g} \in O_h$  under which  $\vec{\rho}_p$  is invariant:

$$\hat{g}\vec{\rho}_p = \vec{\rho}_p \iff \hat{g} \in \mathcal{H}. \quad (259)$$

The set  $\mathcal{H}$  is a subgroup since:

1. The identity  $\hat{e} \in \mathcal{H}$ .
2. The set  $\mathcal{H}$  is closed under multiplication, since if  $\hat{g}_1, \hat{g}_2 \in \mathcal{H}$  then  $\hat{g}_1(\hat{g}_2\vec{\rho}_p) = \hat{g}_1\vec{\rho}_p = \vec{\rho}_p$ .
3. The set  $\mathcal{H}$  is closed under inversion:  $\hat{g}^{-1}\vec{\rho}_p = \hat{g}^{-1}(\hat{g}\vec{\rho}_p) = \vec{\rho}_p$ .

The order of (number of terms in)  $\mathcal{H}$  is denoted as  $N_{\mathcal{H}}$ . We assume that  $\mathcal{H}$  is the maximal invariance subgroup, and construct the right cosets  $\hat{g}\mathcal{H} = \{\hat{g}\hat{h}_1, \dots\}$ . According to [31] there are  $N_c = 48/N_{\mathcal{H}}$  mutually exclusive such cosets  $C_1, \dots, C_{N_c}$  (The number 48 is the order of  $O_h$ ). Their union is  $O_h$ . For each coset  $C_i$  we can define

$$\vec{\rho}_i \equiv C_i \vec{\rho}_p \quad (260)$$

which is meaningful due to the invariance of  $\vec{\rho}_p$  under  $\mathcal{H}$ .

We want to prove the following

**Lemma.**  $\vec{\rho}_i \neq \vec{\rho}_j$  iff  $i \neq j$ .

**Proof.** Assume the opposite, then in particular

$$\begin{aligned} \hat{g}_i \vec{\rho}_p &= \hat{g}_j \vec{\rho}_p \\ \Leftrightarrow (\hat{g}_j^{-1} \hat{g}_i) \vec{\rho}_p &= \vec{\rho}_p \\ \Leftrightarrow \hat{g}_j^{-1} \hat{g}_i &= h \in \mathcal{H} \\ \Leftrightarrow \hat{g}_i &= \hat{g}_j h \\ \Leftrightarrow C_i &= C_j \end{aligned}$$

in contradiction to the assumption. The last line was obtained using the rearrangement theorem [31] applied to the group  $\mathcal{H}$ . QED.

We now set

$$S(\vec{\rho}_p) = \cup_{i=1}^{N_c} \vec{\rho}_i \quad (261)$$

$$l(\vec{\rho}_p) = N_{\mathcal{H}} = \text{integer} \quad (262)$$

and since  $\sum_{\hat{g} \in O_h} = \sum_{i=1}^{N_c} \sum_{\hat{g} \in C_i}$  we proved (258). QED.

## G.2 Calculating $l(\vec{\rho}_p)$

We give an explicit expression of  $l(\vec{\rho}_p)$ . Consider  $\vec{\rho}_p = (i, j, k)$  such that  $i \geq j \geq k \geq 0$  with no loss of generality. Then

$$l(\vec{\rho}_p) = l_p(\vec{\rho}_p) l_s(\vec{\rho}_p), \quad (263)$$

$$l_p(\vec{\rho}_p) = \begin{cases} 1, & i \neq j \neq k \neq i \\ 2, & i = j \neq k \text{ or } i \neq j = k \text{ or } i = k \neq j \\ 6, & i = j = k \end{cases} \quad (264)$$

$$l_s(\vec{\rho}_p) = 2^{(\# \text{ zero indices})}. \quad (265)$$

We prove this formula in the following. First we observe, that  $O_h$  can be decomposed as

$$O_h = \mathcal{P}_3 \otimes \mathcal{S}_3 \quad (266)$$

$$\mathcal{P}_3 = \text{group of permutation of 3 numbers} \quad (267)$$

$$\mathcal{S}_3 = \{\pm \pm \pm\} = 3 \text{ sign changes.} \quad (268)$$

Let  $\mathcal{H}_P, \mathcal{H}_S$  be the subgroups of  $\mathcal{P}_3, \mathcal{S}_3$ , respectively, under which  $\vec{\rho}_p$  is invariant.

**Lemma.**  $\mathcal{H} = \mathcal{H}_P \otimes \mathcal{H}_S$ .

**Proof.** Let  $\hat{g} = \hat{p}\hat{s}$ , where  $\hat{g} \in O_h$ ,  $\hat{p} \in \mathcal{P}_3$  and  $\hat{s} \in \mathcal{S}_3$ . This representation of  $\hat{g}$  is always possible according to (266). If  $\hat{s} \notin \mathcal{H}_S$  then  $\hat{s}\vec{\rho}_p \neq \vec{\rho}_p$ , thus necessarily there is at least one sign change in  $\hat{s}\vec{\rho}_p$  with respect to  $\vec{\rho}_p$ . Consequently,  $\hat{g}\vec{\rho}_p \neq \vec{\rho}_p$ , because permutations only change the order of indices and cannot restore the different sign(s). We conclude that  $\hat{g} \notin \mathcal{H}$ . Thus,  $\hat{g} \in \mathcal{H} \Rightarrow \hat{s} \in \mathcal{H}_S$ . For every  $\hat{g} \in \mathcal{H}$  we must have therefore  $\hat{g}\vec{\rho}_p = \hat{p}\hat{s}\vec{\rho}_p = \hat{p}\vec{\rho}_p = \vec{\rho}_p$  which proves that also  $\hat{p} \in \mathcal{H}_P$ . QED.

We conclude that  $N_{\mathcal{H}} = \text{order}(\mathcal{H}_P) \cdot \text{order}(\mathcal{H}_S)$ . This is manifest in equations (263-265).



# H Number theoretical degeneracy of the cubic lattice

## H.1 First moment

The following arguments are due to J. Keating [99]. We first need to estimate the fraction of integers that can be expressed as a sum of 3 squares. The key theorem is due to Gauss and Legendre and states that:

$$q = i^2 + j^2 + k^2, \quad i, j, k \in \mathbb{N} \iff q \neq 4^m(8l + 7), \quad m, l \in \mathbb{N}. \quad (269)$$

From this we can estimate that the fraction of integers which *can not* be expressed as a sum of 3 squares of integers is:

$$\frac{1}{8} \left( 1 + \frac{1}{4} + \frac{1}{4^2} + \dots \right) = \frac{1}{6}. \quad (270)$$

In the above we used the fact (which is easily proven) that if  $q = 4^m(8l + 7)$  then  $m, l$  are uniquely determined. Therefore, asymptotically only 5/6 of the integers are expressible as a sum of three squares.

Our object of interest is the degeneracy factor  $g_\rho(\rho)$  defined as:

$$g_\rho(\rho) \equiv \#(\vec{\kappa} \in \mathbb{Z}^3 | \kappa = \rho). \quad (271)$$

The number of  $\mathbb{Z}^3$ -lattice points whose distance from the origin is between  $\rho$  and  $\rho + \Delta\rho$  is estimated by considering the volume of the corresponding spherical shell:

$$N_\rho \approx 4\pi\rho^2\Delta\rho. \quad (272)$$

Since  $\rho^2$  is an integer, the number of integers in the same interval is:

$$n_\rho \approx 2\rho\Delta\rho. \quad (273)$$

Taking into account that only 5/6 of the integers are accessible, we obtain:

$$\langle g_\rho(\rho) \rangle = \frac{N_\rho}{(5/6)n_\rho} = \frac{12\pi}{5}\rho. \quad (274)$$

## H.2 Second moment

Here we use a result due to Bleher and Dyson [100], brought to our attention by Z. Rudnick:

$$\sum_{k=1}^N g_\rho^2(\sqrt{k}) = cN^2 + \text{error}, \quad c = \frac{16\pi^2}{7} \frac{\zeta(2)}{\zeta(3)} \approx 30.8706. \quad (275)$$

Differentiating by  $N$  and considering only integers for which  $g_\rho \neq 0$  one obtains:

$$\langle g_\rho^2(\rho) \rangle \approx \frac{12}{5} c \rho^2 \approx 74.0894 \rho^2 . \quad (276)$$

Therefore,

$$\frac{\langle g_\rho^2(\rho) \rangle}{\langle g_\rho(\rho) \rangle} \approx \beta \rho , \quad \beta = \frac{c}{\pi} \approx 9.8264 . \quad (277)$$

# I Weyl's law

A very important tool in the investigation of eigenvalues is the smooth counting function, known as Weyl's law. For billiards it was thoroughly discussed e.g. by Balian and Bloch [82] and by Baltes and Hilf [91]. We construct in the following the expression for the 3D Sinai billiard. In general, it takes on the form:

$$\bar{N}(k) = N_3 k^3 + N_2 k^2 + N_1 k + N_0, \quad (278)$$

where we included terms up to and including the constant term. In fact, for the nearest-neighbour and two-point spectral statistics the constant term  $N_0$  is unimportant, since it shifts the unfolded spectrum  $x_n \equiv \bar{N}(k_n)$  uniformly. Nevertheless, for completeness we shall calculate this term. We enumerate the contributions in the case of Dirichlet boundary conditions one by one and then write down the full expression. Figure 6 should be consulted for the geometry of the billiard.

**N<sub>3</sub>:** There is only one contribution due to the volume of the billiard:

$$N_3 = \frac{\text{volume}}{6\pi^2} = \frac{1}{288\pi^2} \left( S^3 - \frac{4}{3}\pi R^3 \right). \quad (279)$$

**N<sub>2</sub>:** The contribution is due to the surface area of the planes + sphere:

$$N_2 = -\frac{\text{surface}}{16\pi} = -\frac{1}{384\pi} \left[ 6(1 + \sqrt{2})S^2 - 7\pi R^2 \right]. \quad (280)$$

**N<sub>1</sub>:** Here we have contributions due to the curvature of the sphere and due to 2-surface edges:

**curvature:**

$$N_1^{\text{curvature}} = \frac{1}{12\pi^2} \int_{\text{surface}} ds \left[ \frac{1}{R_1(s)} + \frac{1}{R_2(s)} \right] = -\frac{R}{72\pi}, \quad (281)$$

where  $R_1, R_2$  are the principal local radii of curvature.

**edges:** We have 6 plane-plane edges and 3 plane-sphere edges. Their contributions are given by:

$$\begin{aligned} N_1^{\text{edges}} &= \frac{1}{24\pi} \sum_{\text{edges}} \left( \frac{\pi}{\alpha_j} - \frac{\alpha_j}{\pi} \right) L_j \\ &= \frac{S}{144\pi} (27 + 9\sqrt{2} + 8\sqrt{3}) + \frac{R}{24\pi} \left( \frac{9\pi}{8} - \frac{95}{12} \right), \end{aligned} \quad (282)$$

where  $L_j$  are the lengths of the edges, and  $\alpha_j$  are the corresponding angles.

**N<sub>0</sub>:** There are three terms here due to square of the curvatures, 3-surface corners and curvature of the edges:

**curvature<sup>2</sup>:**

$$N_0^{\text{curvature}^2} = \frac{1}{512\pi} \int_{\text{surface}} ds \left[ \frac{1}{R_1(s)} - \frac{1}{R_2(s)} \right]^2 = 0. \quad (283)$$

**3-surface corners:** In the 3D Sinai billiard we have 6 corners due to intersection of 3 surfaces; 3 of them are due to intersection of 3 symmetry planes and the other 3 are due to intersection of 2 symmetry planes and the sphere. The corners are divided into 4 types as follows:

$$\begin{aligned} 1 \times \alpha &\equiv (45^\circ, 54.74^\circ, 36.26^\circ) \\ 3 \times \beta &\equiv (45^\circ, 90^\circ, 90^\circ) \\ 1 \times \gamma &\equiv (60^\circ, 90^\circ, 90^\circ) \\ 1 \times \delta &\equiv (90^\circ, 90^\circ, 90^\circ). \end{aligned}$$

As for the corners  $\beta, \gamma, \delta$  which are of the type  $(\phi, 90^\circ, 90^\circ)$  there is a known expression for their contribution [91]:

$$c_\phi = -\frac{1}{96} \left( \frac{\pi}{\phi} - \frac{\phi}{\pi} \right). \quad (284)$$

Therefore:

$$c_\beta = -\frac{5}{128}, \quad c_\gamma = -\frac{1}{36}, \quad c_\delta = -\frac{1}{64}. \quad (285)$$

As for the corner  $\alpha$ , we calculate its contribution from the  $R = 0$  integrable case (“the pyramid”). The constant term in the case of the pyramid is  $-5/16$  [53] and originates only from 3-plane contributions (there are no curved surfaces or curved edges in the pyramid). The pyramid has 4 corners: 2 of type  $\alpha$  and 2 of type  $\beta$ . Using  $c_\beta$  above we can therefore eliminate  $c_\alpha$ :

$$2 \cdot c_\alpha + 2 \cdot \left( -\frac{5}{128} \right) = -\frac{5}{16} \implies c_\alpha = -\frac{15}{128}. \quad (286)$$

Hence, the overall contribution due corners in the 3D Sinai is:

$$\begin{aligned} N_0^{\text{3-surface}} &= 1 \cdot \left( -\frac{15}{128} \right) + 3 \cdot \left( -\frac{5}{128} \right) + \\ &\quad 1 \cdot \left( -\frac{1}{36} \right) + 1 \cdot \left( -\frac{1}{64} \right) \\ &= -\frac{5}{18}. \end{aligned} \quad (287)$$

**curvature of edges:** We have 3 edges which are curved. They are 90° edges that are due to plane-sphere intersections. Baltes and Hilf [91] quote the constant term  $(-1/12) + (1/256)(H/R)$  for the circular cylinder, where  $H$  is the height and  $R$  is the radius of the cylinder. We conclude from this that the  $H$ -independent term  $-1/12$  is due to the curvature of the 90° edges between the 2 bases and the tube. Assuming locality, it is then plausible to conjecture that the contribution due to the curvature of a 90° edge is:

$$-\frac{1}{48\pi} \int_{\text{edge}} \frac{dl}{R(l)}, \quad (288)$$

where  $R(l)$  is the local curvature radius of the edge. When applied to our case ( $R(l) = -R$ ), we get:

$$N_0^{\text{curv. edge}} = \frac{1}{64}. \quad (289)$$

Putting everything together we get:

$$\begin{aligned} \bar{N}(k) &= \frac{1}{288\pi^2} \left( S^3 - \frac{4}{3}\pi R^3 \right) k^3 \\ &- \frac{1}{384\pi} \left[ 6(1 + \sqrt{2})S^2 - 7\pi R^2 \right] k^2 \\ &+ \left[ \frac{S}{144\pi} (27 + 9\sqrt{2} + 8\sqrt{3}) + R \left( \frac{3}{64} - \frac{11}{32\pi} \right) \right] k \\ &- \frac{151}{576}. \end{aligned} \quad (290)$$

## J Calculation of the monodromy matrix

The monodromy matrix measures the linear response to infinitesimal displacements of the initial conditions of a classical orbit. Its eigenvalues determine the stability of the orbit. Due to the symplectic form of the equations of motion, if  $\lambda$  is an eigenvalue of the monodromy matrix then also  $\lambda^*$ ,  $1/\lambda$  and  $1/\lambda^*$  [2]. Therefore, generically the eigenvalues come in groups of four:

$$\lambda = \exp(\pm u \pm iv), \quad u, v \in \mathbb{R}. \quad (291)$$

In  $d$  dimensions the monodromy has  $2(d-1)$  eigenvalues. Therefore, only for  $d \geq 3$  the generic situation (291) can take place. In two dimensions there are only two eigenvalues and consequently one obtains the following three possible situations (which are special cases of (291) with either  $u$  or  $v$  set to 0):

**Elliptic:**  $\lambda_{1,2} = \exp(\pm iv)$ , stable orbit.

**Parabolic:**  $\lambda_{1,2} = 1$  or  $\lambda_{1,2} = (-1)$ , neutrally stable orbit.

**Hyperbolic:**  $\lambda_{1,2} = \exp(\pm u)$  or  $\lambda_{1,2} = -\exp(\pm u)$ , unstable orbit.

The parabolic case with the “+” sign is denoted as “direct parabolic” and with “-” sign it is denoted as “inverse parabolic”. Similar terminology applies to the hyperbolic case. The generic case (291) is designated as “loxodromic stability” [2].

### J.1 The 3D Sinai torus case

We wish to calculate explicitly the  $4 \times 4$  monodromy matrices in the case of the 3D Sinai torus. There are (at least) two possible ways to tackle this problem. One possibility is to describe the classical motion by a discrete (Hamiltonian, area-preserving) mapping between consecutive reflections from the spheres. The mapping is generated by the straight segment that connects the two reflection points, and the monodromy can be explicitly calculated from the second derivatives of the generating function. This straightforward calculation was performed for the 2D case (for general billiards) e.g. in [72] and it becomes very cumbersome for three dimensions. Rather, we take the alternative view of describing the classical motion as a continuous flow in time, as was done e.g. by Sieber [60] for the case of the 2D hyperbola billiard. We separate the motion into the sections of free propagation between spheres and reflections off the spheres, and the monodromy matrix takes the general form:

$$M = M_{\text{prop}}^{n+1 \leftarrow n} M_{\text{ref}}^n \cdots M_{\text{prop}}^{3 \leftarrow 2} M_{\text{ref}}^2 M_{\text{prop}}^{2 \leftarrow 1} M_{\text{ref}}^1, \quad (292)$$

where  $M_{\text{prop}}^{i+1 \leftarrow i}$  describes the free propagation from sphere  $i$  to sphere  $i+1$  and  $M_{\text{ref}}^i$  describes the reflection from the sphere  $i$ . To explicitly calculate the matrices

one has to choose a well-defined (and convenient) coordinate system, which is a non-trivial task in three dimensions. If we denote the direction along the orbit by “1”, then we have two more directions, denoted henceforth “2” and “3”. Hence there is a rotation freedom in choosing the directions 2 and 3. For convenience of calculation of  $M_{\text{ref}}$  we choose the following local convention for coordinates: Near sphere  $i$  there exists the plane  $\mathcal{P}_i$  which is uniquely defined (except for normal incidence) by the incoming segment, the outgoing segment and the normal to the sphere  $i$  at the reflection point. Direction 1 is obviously in  $\mathcal{P}_i$ . We uniquely define direction 3 to be perpendicular to  $\mathcal{P}_i$  along the direction of the cross product of the outgoing direction with the normal. Direction 2 is then uniquely defined as  $\hat{e}_2 \equiv \hat{e}_3 \times \hat{e}_1$  such that a right-handed system is formed. Obviously  $\hat{e}_2$  is contained in  $\mathcal{P}_i$ . The uniqueness of the local coordinate system guarantees that the neighbourhoods of the initial and the final points of the periodic orbits are correctly related to each other. To account for the local coordinate systems we need to apply a rotation between every two reflections that aligns the “old” system to the “new” one. Hence,

$$M = M_{\text{prop}}^{n+1 \leftarrow n} M_{\text{rot}}^{n+1 \leftarrow n} M_{\text{ref}}^n \dots M_{\text{prop}}^{3 \leftarrow 2} M_{\text{rot}}^{3 \leftarrow 2} M_{\text{ref}}^2 M_{\text{prop}}^{2 \leftarrow 1} M_{\text{rot}}^{2 \leftarrow 1} M_{\text{ref}}^1. \quad (293)$$

We should also fix the convention of the rows and columns of  $M$  in order to be able to write explicit expressions. It is chosen to be:

$$\begin{pmatrix} \delta q_2 \\ \delta p_2 \\ \delta q_3 \\ \delta p_3 \end{pmatrix}_{\text{final}} = M \begin{pmatrix} \delta q_2 \\ \delta p_2 \\ \delta q_3 \\ \delta p_3 \end{pmatrix}_{\text{initial}}. \quad (294)$$

A detailed calculations gives the explicit expressions for  $M_{\text{prop}}$ ,  $M_{\text{ref}}$  and  $M_{\text{rot}}$ :

$$M_{\text{prop}}^{i+1 \leftarrow i} = \begin{pmatrix} 1 & L_{i+1 \leftarrow i}/p & 0 & 0 \\ 0 & 1 & 0 & 0 \\ 0 & 0 & 1 & L_{i+1 \leftarrow i}/p \\ 0 & 0 & 0 & 1 \end{pmatrix}, \quad (295)$$

$$M_{\text{ref}}^i = \begin{pmatrix} -1 & 0 & 0 & 0 \\ -\frac{2p}{R \cos \beta_i} & -1 & 0 & 0 \\ 0 & 0 & 1 & 0 \\ 0 & 0 & \frac{2p \cos \beta_i}{R} & 1 \end{pmatrix}, \quad (296)$$

$$M_{\text{rot}}^{i+1 \leftarrow i} = \begin{pmatrix} \cos \alpha_{i+1 \leftarrow i} & 0 & -\sin \alpha_{i+1 \leftarrow i} & 0 \\ 0 & \cos \alpha_{i+1 \leftarrow i} & 0 & -\sin \alpha_{i+1 \leftarrow i} \\ \sin \alpha_{i+1 \leftarrow i} & 0 & \cos \alpha_{i+1 \leftarrow i} & 0 \\ 0 & \sin \alpha_{i+1 \leftarrow i} & 0 & \cos \alpha_{i+1 \leftarrow i} \end{pmatrix}. \quad (297)$$

In the above  $p$  is the absolute value of the momentum which is a constant,  $L_{i+1 \leftarrow i}$  is the length of the orbit’s segment between spheres  $i$  and  $i+1$ ,  $\beta_i$  is the reflection

angle with respect to the normal of the sphere  $i$  and  $\alpha_{i+1\leftarrow i}$  is the angle that is needed to re-align the coordinate system from sphere  $i$  to  $i + 1$ . Even though the entries of  $M$  are dimensional, the eigenvalues of  $M$  are dimensionless. Hence, the eigenvalues cannot depend on  $p$ , which is the only variable with dimensions of a momentum. (All other variables have either dimension of length or are dimensionless.) Therefore, one can set  $p = 1$  for the sake of the calculations of the eigenvalues of  $M$ . The formulas above for the monodromy were verified numerically for a few cases against a direct integration of the equations of motion near a periodic orbit of the Sinai torus. We mention the work of Sieber [52] which extends the calculation of the monodromy matrix to an arbitrary billiard in three dimensions.

## J.2 The 3D Sinai billiard case

We next deal with the calculation of the monodromy matrix for the periodic orbits of the desymmetrized 3D Sinai Billiard. In principle, one can follow the same procedure as above, and calculate the monodromy as for the Sinai torus case, this time taking into account the presence of the symmetry planes. A reflection with a symmetry plane is described by:

$$M_{\text{ref}}^{\text{plane}} = \begin{pmatrix} -1 & 0 & 0 & 0 \\ 0 & -1 & 0 & 0 \\ 0 & 0 & 1 & 0 \\ 0 & 0 & 0 & 1 \end{pmatrix}, \quad (298)$$

which is simply  $M_{\text{ref}}$  with  $R \rightarrow \infty$ . This method, however, is computationally very cumbersome because of the need to fold the orbit into the desymmetrized Sinai billiard. Instead, we can use the monodromy matrix that is calculated for the unfolded periodic orbit, because the initial and final (phase space) neighbourhoods are the same modulo  $\hat{g}$ . A calculation shows, that in order to align the axes correctly, one needs to reverse direction 3 if  $\hat{g}$  is not a pure rotation:

$$M_{\hat{W}} = \begin{pmatrix} 1 & 0 & 0 & 0 \\ 0 & 1 & 0 & 0 \\ 0 & 0 & \sigma(\hat{g}) & 0 \\ 0 & 0 & 0 & \sigma(\hat{g}) \end{pmatrix} M_{\hat{W}}^{\text{unfolded}}, \quad (299)$$

where  $\sigma(\hat{g})$  is the parity of  $\hat{g}$ :

$$\sigma(\hat{g}) = \begin{cases} +1, & \hat{g} \text{ is a rotation} \\ -1, & \hat{g} \text{ is an improper rotation (rotation + inversion)} \end{cases}. \quad (300)$$

The above formulas were verified numerically for a few cases by comparing the result (299) to a direct integration of the classical dynamics in the desymmetrized Sinai billiard.



## References

- [1] \*\*\* M.-J. Giannoni, A. Voros, and J. Zinn-Justin, editors. *Proceedings of the 1989 Les Houches Summer School on “Chaos and Quantum Physics”*, Amsterdam, 1991. Elsevier Science Publishers B. V.
- [2] \*\*\* M. C. Gutzwiller. *Chaos in Classical and Quantum Mechanics*. Springer-Verlag, New York, 1990.
- [3] L. D. Landau and E. M. Lifshitz. *Quantum mechanics, non-relativistic theory*, volume 3 of *Course of theoretical physics*. Pergamon Press, 1958.
- [4] \*\*\* M. V. Berry. Semiclassical theory of spectral rigidity. *Proc. Roy. Soc. London A*, 400:229, 1985.
- [5] E. B. Bogomolny and J. P. Keating. Gutzwiller’s trace formula and spectral statistics: Beyond the diagonal approximation. *Phys. Rev. Lett.*, 77:1472–1475, 1996.
- [6] P. Gaspard and D. Alonso.  $\hbar$  expansion for the periodic orbit quantization of hyperbolic systems. *Phys. Rev. A*, 47:R3468–R3471, 1993.
- [7] D. Alonso and P. Gaspard.  $\hbar$  expansion for the periodic orbit quantization of chaotic systems. *CHAOS*, 3:601–612, 1993.
- [8] Gabor Vattay, Andreas Wirzba, and Per E. Rosenqvist. Periodic orbit theory of diffraction. *Phys. Rev. Lett.*, 73:2304, 1994.
- [9] \*\* N. Argaman, F. M. Dittes, E. Doron, J. P. Keating, A. Y. Kitaev, M. Sieber, and U. Smilansky. Correlations in the actions of periodic orbits derived from quantum chaos. *Phys. Rev. Lett.*, 71:4326, 1993.
- [10] Doron Cohen. Periodic orbits, breake-time and localization. *J. Phys. A*, 31:277, 1998.
- [11] Doron Cohen, Harel Primack, and Uzy Smilansky. Quantal–classical duality and the semiclassical trace formula. *Ann. Phys.*, 264:108–170, 1998.
- [12] Serge Tabachnikov. *Billiards*. Societe Mathematique de France, 1995.
- [13] J. R. Kuttler and V. G. Sigillito. Eigenvalues of the Laplacian in two dimensions. *SIAM Review*, 26:163–193, 1984.
- [14] M. V. Berry and M. Wilkinson. Diabolical points in the spectra of triangles. *Proc. R. Soc. A*, 392:15–43, 1984.
- [15] \*\*\* M. V. Berry. Quantizing a classically ergodic system: Sinai billiard and the KKR method. *Ann. Phys.*, 131:163–216, 1981.

- [16] E. Doron and U. Smilansky. Some recent developments in the theory of chaotic scattering. *Nucl. Phys. A*, 545:455, 1992.
- [17] \*\* H. Schanz and U. Smilansky. Quantization of Sinai's billiard – A scattering approach. *Chaos, Solitons and Fractals*, 5:1289–1309, 1995.
- [18] E. Vergini and M. Saraceno. Calculation by scaling of highly excited states of billiards. *Phys. Rev. E*, 52:2204, 1995.
- [19] Tomaz Prosen. Quantization of generic chaotic 3d billiard with smooth boundary I: Energy level statistics. *Phys. Lett. A*, 233:323–331, 1997.
- [20] Tomaz Prosen. Quantization of generic chaotic 3d billiard with smooth boundary II: Structure of high-lying eigenstates. *Phys. Lett. A*, 233:332–342, 1997.
- [21] \* Ya. G. Sinai. Dynamical systems with elastic relations. *Russ. Math. Surv.*, 25:137–189, 1970.
- [22] K. Nakamura. *Quantum Chaos*. Cambridge University Press, 1993.
- [23] Leonid A. Bunimovich and Jan Rehacek. Nowhere dispersing 3d billiards with non-vanishing Lyapunov exponents. *Commun. Math. Phys.*, 189:729–757, 1997.
- [24] \* O. Bohigas, M. J. Giannoni, and C. Schmit. Characterization of chaotic quantum spectra and universality of level fluctuations. *Phys. Rev. Lett.*, 52:1–4, 1984.
- [25] L. A. Bunimovich. Decay of correlations in dynamical systems with chaotic behavior. *Sov. Phys. JETP*, 62:842–852, 1985.
- [26] E. Doron and U. Smilansky. Semiclassical quantization of chaotic billiards — a scattering theory approach. *Nonlinearity*, 5:1055–1084, 1992.
- [27] \*\* L. A. Bunimovich. Variational principle for periodic trajectories of hyperbolic billiards. *Chaos*, 5:349, 1995.
- [28] \* W. Kohn and N. Rostoker. Solution of the Schrödinger equation in periodic lattices with an application to metallic lithium. *Physical Review*, 94:1111–1120, 1954.
- [29] J. Korrynga. On the calculation of the energy of a bloch wave in a metal. *Physica*, 13:393–400, 1947.
- [30] \*\* F. S. Ham and B. Segall. Energy bands in periodic lattices - Green's function method. *Physical Review*, 124:1786–1796, 1961.

- [31] M. Tinkham. *Group Theory and Quantum Mechanics*. McGraw-Hill Book Company, 1964.
- [32] \* Holger Schanz. On finding the periodic orbits of the Sinai billiard. In Jan A. Freun, editor, *Dynamik, Evolution, Strukturen*. Verlag Dr. Köster, Berlin, 1996.
- [33] O. Biham and M. Kvale. Unstable periodic orbits in the stadium billiard. *Phys. Rev. A*, 46:6334, 1992.
- [34] A. Bäcker and H. R. Dullin. Symbolic dynamics and periodic orbits for the cardioid billiard. *J. Phys. A*, 30:1991–2020, 1997.
- [35] Kai T. Hansen. Alternative method to find orbits in chaotic systems. *Phys. Rev. E*, 52:2388, 1995. [chao-dyn/9507003](#).
- [36] Kai T. Hansen and Predrag Cvitanović. Symbolic dynamics and Markov partitions for the stadium billiard. [chao-dyn/9502005](#), 1995.
- [37] \*\* M. Sieber, U. Smilansky, S. C. Creagh, and R. G. Littlejohn. Non-generic spectral statistics in the quantized stadium billiard. *J. Phys. A*, 26:6217–6230, 1993.
- [38] Harel Primack, Holger Schanz, Uzy Smilansky, and Iddo Ussishkin. Penumbra diffraction in the semiclassical quantization of concave billiards. *J. Phys. A*, 30:6693–6723, 1997.
- [39] Per Dahlqvist and Roberto Artuso. On the decay of correlations in Sinai billiards with infinite horizon. *Phys. Lett. A*, 219:212–216, 1996.
- [40] A. J. Fendrik and M. J. Sanchez. Decay of the Sinai well in  $d$  dimensions. *Phys. Rev. E*, 51:2996, 1995.
- [41] R. L. Weaver. Spectral statistics in elastodynamics. *J. Acoust. Soc. Am.*, 85:1005–1013, 1989.
- [42] O. Bohigas, C. Legrand, C. Schmit, and D. Sornette. Comment on spectral statistics in elastodynamics. *J. Acoust. Soc. Am.*, 89:1456–1458, 1991.
- [43] Dominique Delande, Didier Sornette, and Richard Weaver. A reanalysis of experimental high-frequency spectra using periodic orbit theory. *J. Acoust. Soc. Am.*, 96:1873–1880, 1994.
- [44] C. Ellegaard, T. Guhr, K. Lindemann, H. Q. Lorensen, J. Nygard, and M. Oxborrow. Spectral statistics of acoustic resonances in Aluminum blocks. *Phys. Rev. Lett.*, 75:1546, 1995.

- [45] C. Ellegaard, T. Guhr, K. Lindemann, J. Nygard, and M. Oxborrow. Symmetry breaking and “acoustic chaos”. In N.M. Atakishiyev, T. Seligman, and K.B. Wolf, editors, *Proceedings of VI Wigner Symposium in Guadalajara, Mexico*, pages 330–333, Singapore, 1996. World Scientific.
- [46] S. Deus, P. M. Koch, and L. Sirko. Statistical properties of the eigenfrequency distribution of three-dimensional microwave cavities. *Phys. Rev. E*, 52:1146–1155, 1995.
- [47] H. Alt, H.-D. Graf, R. Hofferbert, C. Rangacharyulu, H. Rehfeld, A. Richter, P. Schardt, and A. Wirzba. Studies of chaotic dynamics in a three-dimensional superconducting microwave billiard. *Phys. Rev. E*, 54:2303, 1996.
- [48] H. Alt, C. Dembowski, H.-D. Graf, R. Hofferbert, H. Rehfeld, A. Richter, R. Schuhmann, and T. Weiland. Wave dynamical chaos in a superconducting three-dimensional Sinai billiard. *Phys. Rev. Lett.*, 79:1026, 1997. [chao-dyn/9706025](#).
- [49] U. Dörr, H.-J. Stöckmann, M. Barth, and U. Kuhl. Scarred and chaotic field distributions in a three-dimensional Sinai-microwave resonator. submitted to *Phys. Rev. Lett.*, 1997.
- [50] R. Aurich and J. Marklof. Trace formulae for three-dimensional hyperbolic lattice and application to a strongly chaotic tetrahedral billiard. *Physica D*, 92:101–129, 1996.
- [51] Michael Henseler, Andreas Wirzba, and Thomas Guhr. Quantization of hyperbolic  $N$ -sphere scattering systems in three dimensions. *Ann. Phys.*, 258:286–319, 1997. [chao-dyn/9701018](#).
- [52] Martin Sieber. Billiard systems in three dimensions: The boundary integral equation and the trace formula. *Nonlinearity*, 11:1607, 1998.
- [53] Harel Primack and Uzy Smilansky. Quantization of the three-dimensional Sinai billiard. *Phys. Rev. Lett.*, 74:4831–4834, 1995.
- [54] Harel Primack. *Quantal and semiclassical analysis of the three-dimensional Sinai billiard*. PhD thesis, The Weizmann Institute of Science, Rehovot, Israel, 1997.
- [55] P. Ewald. *Ann. Physik*, 64:253, 1921.
- [56] D. A. Varshalovic, A. N. Moskalev, and V. K. Khersonskii. *Quantum theory of angular momentum*. World Scientific, 1988.

- [57] F. C. Von der Lage and H. A. Bethe. A method for obtaining electronic eigenfunctions and eigenvalues in solids with an application to Sodium. *Physical Review*, 71:612–622, 1947.
- [58] The Numerical Algorithm Group Limited, Oxford, England. *NAG Fortran Library Manual, Mark 14*, ©1990.
- [59] O. Bohigas. Random matrix theories and chaotic dynamics. In M.-J. Giannoni, A. Voros, and J. Zinn-Justin, editors, *Proceedings of the 1989 Les Houches Summer School on “Chaos and Quantum Physics”*, page 547, Amsterdam, 1991. Elsevier Science Publishers B.V.
- [60] \*\*\* M. Sieber. *The Hyperbola Billiard: A Model for the Semiclassical Quantization of Chaotic Systems*. PhD thesis, University of Hamburg, 1991. DESY preprint 91-030.
- [61] S. Kettemann, D. Klakow, and U. Smilansky. Characterization of quantum chaos by autocorrelation functions of spectral determinant. *J. Phys. A*, 30:3643, 1997.
- [62] M. Abramowitz and I. A. Stegun (ed.). *Handbook of Mathematical Functions*. Dover Publications, Inc., New-York, 1965.
- [63] M. V. Berry and M. Tabor. Closed orbits and the regular bound spectrum. *Proc. R. Soc. Lond. A*, 349:101–123, 1976.
- [64] M. V. Berry and M. Tabor. Calculating the bound spectrum by path summation in action-angle variables. *J. Phys. A*, 10:371–379, 1977.
- [65] M. V. Berry. Some quantum to classical asymptotics. In M.-J. Giannoni, A. Voros, and J. Zinn-Justin, editors, *Proceedings of the 1989 Les Houches Summer School on “Chaos and Quantum Physics”*, page 251. Elsevier Science Publishers B.V., Amsterdam, 1991.
- [66] Thomas Dittrich. Spectral statistics for 1-D disordered systems: A semiclassical approach. *Phys. Rep.*, 271:267, 1996.
- [67] Barbara Dietz and Fritz Haake. Taylor and Pade analysis of the level spacing distributions of random-matrix ensembles. *Z. Phys. B*, 80:153–158, 1990.
- [68] Tsampikos Kottos and Uzy Smilansky. Periodic orbit theory and spectral statistics for quantum graphs. *Ann. Phys.*, 273:1–49, 1999.
- [69] J. P. Keating. The Riemann Zeta function and quantum chaology. In G. Casati, I. Guarneri, and U. Smilansky, editors, *Proceedings of the 1991 Enrico Fermi International School on “Quantum Chaos”, course CXIX*. North-Holland, 1993.

- [70] R. Balian and C. Bloch. Distribution of eigenfrequencies for the wave equation in a finite domain III. Eigenfrequency density oscillations. *Ann, Phys.*, 69:76–160, 1972.
- [71] J. H. Hannay and A. M. Ozorio de Almeida. Periodic orbits and a correlation function for the semiclassical density of states. *J. Phys. A*, 17:3429, 1984.
- [72] \*\* Uzy Smilansky. Semiclassical quantization of chaotic billiards — A scattering approach. In E. Akkermans, G. Montambaux, and J. Zinn-Justin, editors, *Les Houches, Session LXI*. Elsevier Science B. V., 1994.
- [73] Takahisa Harayama and Akira Shudo. Periodic orbits and semiclassical quantization of dispersing billiards. *J. Phys. A*, 25:4595–4611, 1992.
- [74] J. L. Helfer, H. Kunz, and U. Smilansky. in preparation.
- [75] \* Martin C. Gutzwiller. The semi-classical quantization of chaotic Hamiltonian systems. In M.-J. Giannoni, A. Voros, and J. Zinn-Justin, editors, *Proceedings of the 1989 Les Houches Summer School on “Chaos and Quantum Physics”*, pages 201–249, Amsterdam, 1991. Elsevier Science Publishers B.V.
- [76] P. Cvitanović and B. Eckhardt. Symmetry decomposition of chaotic dynamics. *Nonlinearity*, 6:277, 1993.
- [77] B. Lauritzen. Discrete symmetries and periodic-orbit expansions. *Phys. Rev. A*, 43:603–606, 1991.
- [78] Jonathan M. Robbins. Discrete symmetries in periodic-orbit theory. *Phys. Rev. A*, 40:2128–2136, 1989.
- [79] M. Sieber and F. Steiner. Generalized periodic-orbit sum rules for strongly chaotic systems. *Phys. Lett. A*, 144:159, 1990.
- [80] K. G. Andersson and R. B. Melrose. The propagation of singularities along gliding rays. *Inventiones Math.*, 41:197–232, 1977.
- [81] Harel Primack, Holger Schanz, Uzy Smilansky, and Iddo Ussishkin. Penumbra diffraction in the quantization of dispersing billiards. *Phys. Rev. Lett.*, 76:1615–1618, 1996.
- [82] \* R. Balian and B. Bloch. Distribution of eigenfrequencies for the wave equation in a finite domain I. Three-dimensional problem with smooth boundary surface. *Ann. Phys.*, 60:401–447, 1970.

- [83] Martin Sieber, Harel Primack, Uzy Smilansky, Iddo Ussishkin, and Holger Schanz. Semiclassical quantization of billiards with mixed boundary conditions. *J. Phys. A*, 28:5041–5078, 1995.
- [84] E. B. Bogomolny. Semiclassical quantization of multidimensional systems. *Nonlinearity*, 5:805, 1992.
- [85] I. L. Aleiner and A. I. Larkin. Divergence of the classical trajectories and weak localization. *Phys. Rev. B*, 54:14423, 1996.
- [86] R. S. Whitney, I. V. Lerner, and R. A. Smith. Can the trace formula describe weak localization? cond-mat/9902328., 1999.
- [87] W. Pauli. Ausgewählte Kapitel aus der Feldquantisierung. In C. Enz, editor, *Lecture notes*, Zürich, 1951.
- [88] \* P. A. Boasman. Semiclassical accuracy for billiards. *Nonlinearity*, 7:485–533, 1994.
- [89] Per Dahlqvist. Error of semiclassical eigenvalues in the semiclassical limit: An asymptotic analysis of the Sinai billiard. chao-dyn/9812017.
- [90] B. Georgeot and R. E. Prange. Exact and quasiclassical Fredholm solutions of quantum billiards. *Phys. Rev. Lett.*, 74:2851–2854, 1995.
- [91] H. P. Baltes and E. R. Hilf. *Spectra of Finite Systems*. Bibliographisches Institut, Mannheim, 1976.
- [92] M. V. Berry and C. J. Howls. High orders of the Weyl expansion for quantum billiards: Resurgence of the Weyl series, and the Stokes phenomenon. *Proc. Roy. Soc. Lond. A*, 447:527–555, 1994.
- [93] Harel Primack and Uzy Smilansky. On the accuracy of the semiclassical trace formula. *J. Phys. A*, 31:6253–6277, 1998.
- [94] Holger Schanz. *Investigation of Two Quantum Chaotic Systems*. PhD thesis, Humboldt University Berlin, 1997. LOGOS Verlag, Berlin (1997).
- [95] E. Bogomolny and C. Schmit. Semiclassical computations of energy levels. *Nonlinearity*, 6:523–547, 1993.
- [96] R. Aurich, J. Bolte, and F. Steiner. Universal signatures of quantum chaos. *Phys. Rev. Lett.*, 73:1356–1359, 1994.
- [97] Charles Kittel. *Introduction to solid state physics*. John Wiley and Sons Inc., 1953.

- [98] Sidney Golden and Jr. Thomas R. Tuttle. Coordinate-permutable cubic harmonics and their determination. *Phys. Rev. B*, 42:6916–6920, 1990.
- [99] Jon Keating. private communication.
- [100] P. M. Bleher and F. J. Dyson. Mean square limit for lattice points in spheres. *Acta Arithmetica*, 68:383–393, 1994.